AD-A173 978   MULTIFUNCTION RADAR FOR AIRBORNE APPLICATIONS(U)   1/3
ADVISORY GROUP FOR AEROSPACE RESEARCH AND DEVELOPMENT
NEUILLY-SUR-SEINE (FRANCE)   M H CARPENTIER ET AL.
UNCLASSIFIED   JUL 86 AGARD-CP-381   F/G 17/9   NL

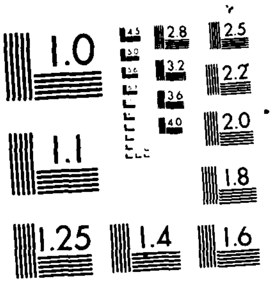

MICROCOPY RESOLUTION TEST CHART
NATIONAL BUREAU OF STANDARDS 1963-A

②

AGARD-CP-381

AGARD-CP-381

AGARD

ADVISORY GROUP FOR AEROSPACE RESEARCH & DEVELOPMENT

7 RUE ANCELLE 92200 NEUILLY SUR SEINE FRANCE

AGARD CONFERENCE PROCEEDINGS No.381

Multifunction Radar for Airborne Applications

NORTH ATLANTIC TREATY ORGANIZATION

DISTRIBUTION AND AVAILABILITY
ON BACK COVER

AGARD-CP-381

NORTH ATLANTIC TREATY ORGANIZATION

ADVISORY GROUP FOR AEROSPACE RESEARCH AND DEVELOPMENT

(ORGANISATION DU TRAITE DE L'ATLANTIQUE NORD)

AGARD Conference Proceedings No.381

MULTIFUNCTION RADAR
FOR AIRBORNE APPLICATIONS

A-1

Papers presented at the Avionics Panel Symposium
held in Toulouse, France, 14—18 October 1985.

THE MISSION OF AGARD

The mission of AGARD is to bring together the leading personalities of the NATO nations in the fields of science and technology relating to aerospace for the following purposes:

- Exchanging of scientific and technical information;
- Continuously stimulating advances in the aerospace sciences relevant to strengthening the common defence posture;
- Improving the co-operation among member nations in aerospace research and development;
- Providing scientific and technical advice and assistance to the Military Committee in the field of aerospace research and development (with particular regard to its military application);
- Rendering scientific and technical assistance, as requested, to other NATO bodies and to member nations in connection with research and development problems in the aerospace field;
- Providing assistance to member nations for the purpose of increasing their scientific and technical potential;
- Recommending effective ways for the member nations to use their research and development capabilities for the common benefit of the NATO community.

The highest authority within AGARD is the National Delegates Board consisting of officially appointed senior representatives from each member nation. The mission of AGARD is carried out through the Panels which are composed of experts appointed by the National Delegates, the Consultant and Exchange Programme and the Aerospace Applications Studies Programme. The results of AGARD work are reported to the member nations and the NATO Authorities through the AGARD series of publications of which this is one.

Participation in AGARD activities is by invitation only and is normally limited to citizens of the NATO nations.

The content of this publication has been reproduced
directly from material supplied by AGARD or the authors.

Published July 1986

ISBN 92-835-0395-3

Printed by Specialised Printing Services Limited
40 Chigwell Lane, Loughton, Essex IG10 3TZ

THEME AND OBJECTIVES

Radar is still the most important sensor in military aircraft. A number of important features make radar superior to optical systems and other sensors.

- long range performance,
- penetration of weather (fog, clouds),
- range and Doppler estimation,
- flexibility due to electronic beam steering,
- various signal processing routines,
- high resolution imaging (SAR).

Different tasks such as target search, tracking, and missile guidance can be fulfilled by radar. In a military aircraft, additional tasks such as terrain following and avoidance, mapping, Doppler navigation, and SAR imaging may be required. Since most of the output data is combined in a single on-board computer, the question of which radar functions should be integrated, and at what level, arises. Reducing size, weight, cost, and power consumption are particular goals for commonality in airborne radar systems.

However, integration of several radar tasks in one system may cause problems for the achievement of reliable overall performance. Centralized systems may be more efficient because of the integration of different functions at the same radar level, but they may be subject to catastrophic failure if proper attention is not given to design for fault tolerance and overall system reliability. Careful attention must also be given to mode timeliness and duty cycles in order that all functions can be accomplished within the operating speed and capacity of the integrated system.

In the past decade, a number of new technologies have arisen and will have decisive influence on tomorrow's radar concepts. VLSI and VHSIC will open new dimensions of digital signal processing. New analogue techniques such as SAW devices and optical methods promise new ways of analogue signal processing. Systolic processor structures can reduce operation time. On the other hand, new antenna concepts (in particular active and conformal arrays) and algorithms offer new dimensions in the performance of airborne radar such as 360 degree coverage, jammer and clutter resistance, high resolution, target tracking and multi-purpose operation.

The purpose of this symposium was to bring together specialists in the various fields in order to present the state-of-the-art in the individual topics. The development of new concepts for the design of future airborne radar systems was emphasized rather than the description of existing systems.

* * * *

Le radar est toujours le senseur primordial dans les avions militaires. Un certain nombre de caractéristiques importantes donne au radar la supériorité sur les systèmes optiques et les autres senseurs. Parmi ces caractéristiques, citons:

- la longue portée,
- la pénétration par mauvaises conditions météorologiques (brouillard, nuages),
- l'estimation de distance et l'estimation Doppler,
- la souplesse dûe à l'orientation électronique des faisceaux,
- les divers programmes de traitement de signaux,
- l'imagerie à haut pouvoir séparateur (SAR: radar à ouverture synthétique).

Différentes tâches telles que recherche et poursuite de cibles et guidage de missiles, peuvent être effectuées par radar. Dans un avion militaire, des tâches additionnelles peuvent être requises: par exemple, suivi de terrain et évitement d'obstacle, cartographie, navigation Doppler et imagerie SAR. La plupart des données de sorties étant combinées dans un seul calculateur de bord, la question qui se pose est la suivante: quelles fonctions du radar doivent être integrées et à quel niveau? La déduction des dimensions, du poids, du coût et de la consommation d'énergie représente autant d'objectifs particuliers de commonalité dans les systèmes radar aéroportés.

Toutefois l'intégration de plusieurs tâches radar en un seul système peut être cause de problèmes si l'on veut obtenir un ensemble de performances fiables. Des systèmes centralisés peuvent s'avérer plus efficaces en raison de l'intégration de différentes fonctions au même niveau radar, mais ils peuvent être sujets à des pannes catastrophiques si l'on ne consacre pas toute l'attention voulue à une conception orientée vers la tolérance aux fautes, et la fiabilité générale du système. Il importe également de prendre soigneusement en compte l'opportunité du mode et les cycles de marche afin que toutes les fonctions puissent être accomplies dans les limites de la vitesse et de la capacité de fonctionnement du système intégré.

Au cours de ces dix dernières années, un certain nombre de technologies nouvelles ont fait leur apparition; elles exercent une influence décisive sur les concepts radar de demain. L'Intégration à Très Grande Echelle (VLSI) et les Circuits Integrés à Très Grande Vitesse (VHSIC) ouvriront de nouvelles voies dans le domaine du traitement numérique des signaux. Les nouvelles techniques analogiques telles que les dispositifs SAW (à ondes stationnaires) et les méthodes optiques semblent porteuses d'avenir en matière de traitement de signaux analogiques. Les structures de processeurs systoliques peuvent réduire le temps de fonctionnement. D'autre part, de nouveaux concepts d'antennes (en particulier réseaux actifs et conformes) et de nouveaux algorithms offrent des perspectives nouvelles en ce qui concerne les performances des radars aéroportés, comme la couverture sur 360°, la résistance, au brouillage et aux signaux parasites, le pouvoir séparateur eleve, la poursuite des cibles et le fonctionnement polyvalent.

L'objectif du symposium qui vous a été présenté fut de réunir des spécialistes de domaines divers afin d'exposer l'état de l'art actuel pour les différents sujets abordés. L'accent fut mis sur le développement de nouveaux concepts pour la mise au point des futurs systèmes radar aéroportés, plutôt que sur la description des systèmes actuels.

AVIONICS PANEL

Chairman:	Dr F.I.Diamond Chief Scientist RADC/CA Rome Air Development Center Griffiss AFB, NY 13441 USA	Deputy Chairman:	Dr G.H.Hunt ADXR (E) Royal Aircraft Establishment Farnborough, Hants GU14 6TD United Kingdom

TECHNICAL PROGRAMME COMMITTEE

Dr R.Klemm (Chairman)
Forschungsinstitut für Funk und Mathematik — FFM
Bad Neuenahrer Strasse 20
5307 Wachtberg-Werthhoven
Federal Republic of Germany

Mr Y.Brault (FR)
Ing. L.Crovella (IT)
Dr F.I.Diamond (US)
Mr J.Dorey (FR)
Mr M.Jacobsen (GE)
Mr I.W.Mackintosh (UK)
Prof. E.B.Stear (GCP) (US)

HOST NATION COORDINATOR

Mr P.Cassagnaveres
47 Avenue Léon Blum
31056 Toulouse
France

PANEL EXECUTIVE

Lt Colonel M.V.Stratton

From Europe	From US and Canada
AGARD-NATO 7 rue Ancelle 92200 Neuilly sur Seine France	AGARD-NATO APO New York 09777

Tel. (Paris) (1) 47.38.57.65 Telex 610176F

CONTENTS

SESSION I – ISSUES IN MULTIFUNCTION RADAR OPERATION

SESSION II – SYNTHETIC APERTURE RADAR

SESSION III – SIGNAL/DATA PROCESSING

III-1 Clutter and Interference

---

† Abstract only
* Abstract only. The full text appears in classified publication CP 381 (Supplement)
** In classified publication CP 381 (Supplement)

III-2 Algorithms and their Implementation

III-3 Classification

---

† Abstract only
* Abstract only. The full text appears in classified publication CP 381 (Supplement)
** In classified publication CP 381 (Supplement)

Reference

SESSION IV – EQUIPMENT AND COMPONENT DESIGN

SESSION V – SIMULATION OF MULTIFUNCTION RADAR SYSTEM

---

* Abstract only. The full text appears in classified publication CP 381 (Supplement)

† Abstract only

The Coming Revolution In Radar

Verne L. Lynn
Deputy Director
Defense Advanced Research Projects Agency
1400 Wilson Boulevard
Arlington, Virginia 22209-2308 USA

Airborne radar will continue to be driven by factors which have long been critical such as cost, size, weight and power consumption. Reliability, always important, must receive new emphasis, especially in the era of highly integrated multi-function radars where well designed redundancy management and efficient resource allocation will be essential. As new technology matures, these needs will cause the continuing evolution of radars.

More importantly, two relatively new forces will drive revolutionary change. First, it is increasingly clear that detection is tantamount to negation in modern warfare. If the enemy can find a radar, he can destroy it or jam it, and high powered radars are obviously susceptible to detection and precise location with only a few seconds of radiation. In this same vein, the airborne radar's platform may be increasingly difficult for the enemy to detect as a result of attention to its radar cross section and infrared signature but, unless the radar itself is comparably reduced in detectability, it will be the "give-away." This need for radars to "hide" suggests strong new emphasis on bistatic systems, low probability of intercept (LPI) techniques and, where applications permit, the wider use of shorter wavelengths in millimeter or infrared bands.

The second force driving revolutionary change is the decreasing target signature. As radar targets shrink in visibility, the radar designer must cope with more than simple signal-to-noise reduction. Clutter rejection, deception recognition and ECCM will be vastly more difficult in the many cases where current operation is marginal.

The very difficult problems associated with detection avoidance and with dealing with lowered target signatures will lead to new and much more complex radar concepts. To a very large extent, solutions will lie in signal processing and computation.

Fortunately, a new generation of emerging technologies offer the orders of magnitude improvement in processing which will be required. New analog devices can provide gigahertz bandwidths and extraordinary time bandwidth products. Likewise, optical processing using non-linear techniques and binary components can also yield prodigious capabilities. Digital computational density continues to expand with 10^3 - 10^6 node multiprocessors coming practical at moderate costs. In addition, custom-designed VLSI will be widely available so that unique problems will be able to afford optimized solutions. Expert system technology will surely play an increasing and major role.

The challenge to the radar designer is to identify concepts and technology which will do a better job of addressing long standing needs such as cost and reliability while simultaneously responding to the new demands for avoiding detection and for coping with less visible targets.

ABOUT THE FUTURE OF AIRBORNE RADAR

by

Professor Michel H.Carpentier
THOMSON-CSF
23 rue de Courcelles
75362 Paris Cedex 08
France

1 - PRESENT SITUATION

During the last decade, has progressively being introduced a change in the design of combat aircraft. The same plane is more and more capable of being used for various different missions, and the variety of possible missions do not systematically involve a relevant variety in on-board equpments (except fot the very armament). As a consequence, the radar has become more and more polyvalent, for economical as well as operational reasons.

Technological evolution gives to a modern combat aircraft radar the possibility of instantaneously switching to be adapted to very different missions such as faraway detection of ennemy penetrating airplanes flying at low altitude, as well as accurate localization of small ships in heavy sea-clutter conditions, or detection of trucks or detection of stationnary helicopters.

However, drastical improvements obtained in the field of transmitting tubes, of antennas, of frequency generation, of signal processing have not still been sufficient enough to provide complete flexibility.

It is possible to switch from a given mode to an other one, but using simultaneously several modes, as requested by the users, is generally difficult, if not impossible. As an example it is very difficult to combate against a fighter while keeping perfect protection against the ground returns, or it is very difficult to provide a wide surveillance, while penetrating at low altitude in a terrain clearance mode.

To give an idea of the situation, I will try to recall operational needs, as they are now and as they could be imagined for the future

Roughly, as seen by the radar designer, operational needs could be classified

- depending on the nature of targets and environments, the mission of the A/C being localization and/or destruction of the targets
- depending on the auxiliary functions needed to permit the realization of the missions (terrain following, navigation informations...)

1.1. - Air targets and their environment

Their are of various types, at any altitude, at any speed ; and their equivalent echoing area (e.e.a.) is permanently reducing :

- interceptors at high altitude and high speed
- penetration A/c at very low altitude
- cruize missiles at very low altitude and low e.e.a. (0.1 m2 or less)
- helicopters at very low altitude and various speeds (including speed zero).

The aircraft equipped with the radar could also be at any altitude, above any type of earth surface, and obliged to acquire the targets in a severe environment :

1.1.1. The ground constituted by a very large number of parasitic targets, fixed or mobile, generally very powerful.

1.1.2. The E.C.M. systems, operating from very sophisticated receivers and/or an a priori knowledge of the radar characteristics.

The E.C.M. systems are of various types and several ones could be used simultaneously :

- noise jammers,
- active and passive decoys.

Active decoys become more and more clever : their mission is to make a replica of the radar signal, but slightly modified, in a manner realistic enough to either give wrong information on target characteristics (range, speed, direction, strength), or to give wrong information on the number of the targets in order to saturate signal and/or data processing of the radar, incapable of making the good choice among that large number of targets, all of them looking like real ones.

Those decoys could be borne or dropped, either by the targets themselves (or at least by some of them), or by stand-off planes, or by ground stations installed in the ennemy territory.

1.1.3. - The defense organization of the ennemy, which could be

- the air to air weapons of the targets (guns, active radar missiles, passive i.R. or antiradiation missiles)

  some ground-based weapon systems, basically of the same nature, more or less dangerous, depending on the aircraft altitude.

1.1.4. - And, finally, the existence of the other friend aircraft which produce electromagnetic pollution with their radar and/or E.C.M. equipments.

1.2. - Surface targets

1.2.1. Sea-surface targets could be very small and their acquisition should be possible in all-weather conditions (in case of rescue, for instance). Recognition of the type of ship is useful - all E C.M. protection of ships are possible, specifically use of efficient decoys.

1.2.2 - On the ground, targets are of various types : tanks, mobiles of fixed, helicopters (stationnary), fixed structures such as bridges, S.A.M. batteries. Target recognition is very often a must, in a natural very dense environment, in front of various ennemys E.C.M., including drones or ultralight airplanes which could be used for a purpose of staturation.

1.3. - Auxiliary functions

Auxiliary functions could be, for instance,

- system achieving navigation aid (correction to information given by inertial means), which generally necessitates high-resolution mapping of the terrain
- all-weather terrain following.

*

* *

Technically speaking, what is the impact of so many missions, conditions, situations on the airborne radar design ?

All existing solutions are based on the utilization of the flexibility of the transmitter (capable of transmitting different signals, owing to the use of pulse compression technics and/or to the use of transmitters capable of more than one peak power level) and are based on the use of real time very fast computers for signal and data processing.

However, in spite of the flexibility offered by modern electronic components, compromises remain necessary :

Practically, it is very often the air-to-air mission, when it is requested to be of good quality, which involves the main characteristics of an airborne radar : frequency band, transmitted power, level of parasitic radiation of the antenna, spectral quality of oscillators, etc.

Classical mechanical antennas are well-adapted to air-to-air mission (with exception for multitarget tracking), but *they are not so well adapted to air-to-surface missions (even with use of beam-switching* organization). In spite of all efforts achieved in order to reduce the inertia of mechanisms, terrain-following will only by totally efficient when electronic scanning will be used.

In France, radars presently under development are designed to provide all air-to-air, air-to-ground, air-to-sea missions, thanks to the existence of about 50 different modes. To obtain sufficient performance for every mode, transmitted signals need to be of various nature, p.r.f. varying between a few hundreds Hz and a few hundreds kHz, duty cycles varying between 2 and 1000. In those conditions it is very convenient to use a transmitter capable of different peak powers, depending on the p.r.f. and duty cycles.

The inertia of the antenna is requested to be small enough, in spite of its relatively big size. As a bonus, it is useful, for some missions,to use simultaneously several modes, such as :

- anticollision
- air-to-air search
- air-to-air tracking (s)

The advantage of electronic scanning becomes quite obvious : passive antennas in a first period of time, and then active antennas.

The antenna, whatever be its nature (classical, or electronic scanning), is strictly requested, in order to be relevant with performing Doppler modes, to provide excellent radiation patterns, the parasitic side lobes being extremely low.

Improvement of the performance reached by processings (within a given volume) leads to avoid to lose information in the receiving part of the radar : so it appears reasonable to use simultaneously

- one sumchannel
- 2 monopulse ecartometry channels
- one anciliary channel

Those 4 channels with a large linear dynamic range provide after analog to digital conversion a data rate around 500 Mbits/s, to be processed in real time.

In order to reduce volume and cost of signal processing, it is interesting to utilize one very powerful machine (1000 MFlop/s) capable of achieving simultaneously the complete processing of all the selected modes. Depending on the radar mode, the configuration, the data rate, formats vary. This machine of M.I.M.D. type present in fact a lot of problems of management, data exchange, etc.

But, in fact, if we follow the information all along the receiver, it appears, from the input to the output that the formats and the data rates are reducing : for instance,

- at the input, 500 Mbits/s with 14 bits
- at the ouput, a few kbits/s with 4 bits (air-to-air display)

So, it appears more clever to replace the single machine by a cascade (or equivalent) of more specialized machines, such as

- Systolic array
- F.F.T. organization
- S.I.M.D. machine
- M.I.M.D. machine
- Specific display interface.

In supplement to that organization of machines devoted to signal processing, a more general purpose type machine has to be added, providing

- Computation at low rate
- Management
    - of information exchanges within the radar (optical bus)
    - of information exchanges between the radar and the weapon system
    - of built-in tests.

2 - PRESENT SITUATION, EVEN EXTRAPOLATED, IS NOT SATISFACTORY

Present technologies, or at least technologies under development, will permit to realize combat aircraft radars the physical characteristics of which (volume, weight, consumming power, processing capability ...) are compatible with the basic performance which are requested.

However, if we take into account the environment of the future, it appears that the present situation is not satisfactory. Problems will probably appear in the integration of all the components of the weapon system (they exist already, and compromises are needed to solve them), and more important, significant insufficiencies could appear in hostile environment.

2.1. - Problems regarding the integration of all the components of the weapon wystem

For instance,

2.1.1. - Coexistence of the E.C.M. system and of the radar on board of the same aircraft involves obvious problems regarding volume and power supply available, installation of antennas, general compatibility.

Others sensors (infrared or visible passive detectors, laser range-finders) involve similar problems.

Active cooperation between the radar and the other components appears not to be enough taken into account in order to globaly reach a better total efficiency.

2.1.2. - Final testing in flight of the radar, within the overall system, is very long and is, in fact, limited to the test of a finite number of punctual examples, generally in an simulated environment of E.C.M.

In any case, for obvious reasons of discretion, some flight tests are not recommanded.

2.2. - Operational insufficiencies

According to me, they are essentially in two fields :

- Recognition of targets not accurate enough

- Vulnerability to E.C.M.

Both aspects are, by the way, correlated

2.2.1. - Target recognition

Regarding the air-target, present technologies, in connection with the theoritical limitations, give resolution cells, in search mode, of the order of some tens to a few hundreds of meters in range, of order of some meters per second in speed, of a few degrees in angular.

This resolution appears to be insufficient in many cases, since it could produce too many false alarms, with a risk of saturating the overall system, it could produce a range reduction, interruption of target tracking in case of complex situation.

For instance, in search mode when time for observation in short,

- The radar is not always able to distinguish a penetrating ennemy aircraft from a drone whose speed is likely and equipped with a Luneberg lens or equivalent. There are trouble to count the actual number of targets of a given raid, to separate close tracks.

- Targets generally presenting a spectral response very complex, that could involve a saturation of the data processor and/or troubles in extracting range and velocity if there are more than one target illuminated.

- Fast ground vehicles could have spectral components corresponding to speeds high enough to belong to air-targets, with a risk of producing false alarms.

Regarding ground targets or sea-targets, similar problems exist.

Using synthetic aperture radars allows to get a very good resolution on fixed (or slow) targets, but that technology is not adapted to the recognition of targets with complex spectral characteristics. (Helicopters, rotating radar antennas, tanks on battle-field ...).

2.2.2. - Vulnerability to E.C.M.

Present generation radars appear to be too much vulnerable to ennemy E.C.M. such as they could be realized in the future.

For instance,

* Peak power transmitted is low in H.F.R. radars but it could be higher in other modes, which is a real advantage strictly speaking on the radar side, but a disadvantage regarding discretion.

Otherwise, coding of the transmitted signal is generally very simple and easy to be identified for E.C.M. receiver (Barker's codes, pulse compression with linear F.M., polyphased codes ...). That code is generally fixed or at least not very variable, which facilitates the identification and the angular localization of the radar. Instantaneous copy of such codes is easy, from now, for modern equipments. In case of active decoys, the future receivers, associated with analog to digital fast encoders, will probably permit to copy, then to alterate the received signal with enough realism.

Other parameters (p.r.f. - pulse length) do not vary sufficiently, in a given mode, helping the radar identification.

At least, it is obvious that flight tests, and pilot training, present a problem, giving mode or less publicity to the radar signal.

* Instantaneous spectral width of transmitted signals is narrow. Of course the radar is capable of rapidly changing its frequency within a wide band, but this degree of agility risk to be insufficient, taking into account the improvements expected from the E.C.M. systems.

* Regarding struggle against decoys, present generation radars appear not to be protected enough :

- Passif decoys (chaffs or equivalent) are generally eliminated by Doppler radars, but new problems will arise if this type of decoys could be animated with a likely average speed. Drones and R.P.V. (possibly equipped with passive responders) are not identified as such by the radar if their speed is likely.

Active decoys will in the future reach such a sophisticated level that classical protections will become totally insufficient.

3 - IN PRINCIPLE SOLUTIONS EXIST

That situation, not enough satisfactory for the far future, is such mainly because the present state of the art in technology has not allowed the realization of more efficient solutions. Decisive improvements will be needed in the future, of which the basic principles are known, the evolution of the technology promising to permit their practical achievement.

Roughly, in my opinion, 4 basic ideas could be used :

- Drastic improvement of the range resolution as well as of the complexity of transmitted waveforms.
- Better utilization of the information contained in the received signal.
- Improvement of the angular domain covered by the radar and of the means of exploration.

- *Cooperation with the E.C.M. system on board of the aircraft and generally with the other sensors.*

3.1. - Range resolution and complexity of the transmitted waveforms

Velocity resolution is limited on one side by the characteristics of the target, on the other side by the *minimum* observation time during which the transmitted waveform remain stable enough.

That time T has to be as short as possible (let us say around one millisecond, as an example).

The velocity resolution $\Delta v = \frac{\lambda}{2T}$ is then limited (for instance 16 m/s at 9 GHz for T = 1 ms), and nothing better could be expected (except a reduction of λ, possible, for instance, for relatively short range radars).

The angular resolution is limited by the antenna size. It could be significantly improved only by spreading the antenna system all along the structure of the plane (for instance, by installing transmitting-receiving active modules on the wings to improve resolution in bearing).

The improvement of the angular resolution by processing, well known technology at the present time, is finally depending on the velocity resolution and suffers same limitations.

On the contrary, improving the range resolution is possible without basic limitations. Range resolution is proportional to the spectral width of the received signal, and improvements by 10 to 1000 could be obtained depending on the utilization and on the environment.

Only a very good range resolution could permit

- to count the targets of a raid
- to separate the "brilliant points" of a target and then to evaluate its size in order to facilitate its recognition
- to localize an active decoy on the target and then to reject it
- to identify by their size dropped active decoys
- to avoid confusion between close tracks
- to reduce significantly the level of scattered clutter.

In the same time when instantaneous spectral width has to be wide, complexity of the transmitted waveform has to be increased to make the copy of it as much difficult as possible.

3.2. - Better utilization of the received signals

Present architecture of existing radars is based on the notion of a matched filter and on the utilization of Doppler effect.

It would be stupid to forget all those basic principles, but they could be used in a more clever manner.

It could be accepted in some cases to lose in sensitivity in order to get more information on the targets ; or to recognize the decoys as such.

3.3. - Improvement of angular domain

Operationnally speaking, it is generally requested to cover a domain as high as possible in the minimum time. That time could not go below a given value, for basic physical reasons.

However, explorations means must not depend on mecanical limitations.

Electronic scanning bi-dimensional array antennas, because of their beam agility :

- make more difficult identification and localization of the radar by the ennemy E.C.M. systems, and that as much as the transmitted waveform is more agile and complex
- make possible to use simultaneously several modes, generally not compatible, such as terrain following, air-to-air surveillance, multitarget tracking, etc.
- make possible the management of the available power depending on the performance requested, by sharing the energy in various direction and then, globally improve performance in comparison with a conventional radar.

Passive phase-array antennas are possible to be used in the near future, but the real aim is to use active antennas, compatible with a wide bandwidth and reduced microwave losses. Widening of the angular domain will result from using several plane arrays or curved arrays.

3.4. - Cooperation with E.C.M. system and other equipments on board

Having in mind those new radar architectures using,

- complexity of the transmitted waveforms
- instantaneous very wide spectral bandwidth
- active array antenna

reception processing architecture capable of dealing with an enormous rate of the received information, it appears that the radar could help the E.C.M. system on board of the same aircraft.

The first idea is using the radar transmission as a self screening jamming, either in time-sharing with the very radar mode, or simultaneously by sharing the transmitted power.

Detection and localization of dangerous radars is also possible, at least in some portions of the 4 π steradians, the radar being in use or not.

Association with other sensors (in visible wavelengths or in infrared) could be generalized to give confirmation on some radar alarm and/or to complement the radar, at the limit of the radar domain. It is already known that association of tracking radar and infrared sensor provides a global efficiency much better that the efficiency of every one. In an environment of intensive E.C.M. the advantage of using equipments working at wavelengths very different from classical electromagnetic ones, is obvious.

4. - SUCH A RADAR SYSTEM IS FEASIBLE

Realization of such a system, much more clever and cooperant, is feasible in a future not too far.

It necessitates, in some manner, a kind of revolution in the technical traditions, rather than an evolution which could risk to increase complexity without enough advantages.

[illegible] concept of a radar, where technical functions are physically separated, and rigidly cascaded, [illegible] be replaced by architectures in which transmission, reception and processing will be physically mixed, [illegible] time. In that field, active array antennas are only an example

[illegible] needed is enormous - it is obviously needed in signal processing the capacity of [illegible] several times 10, but it is also needed in microwave, in I.F., in internal links [illegible] have more and more importance, compared to the present situation.

[illegible]

[illegible] decisive improvements are needed for the airborne multifunction [illegible] the difficult operational environment of the future.

[illegible] radars have to be able to be used in an ambiance of electro-[illegible] as well as from friend radars. Obviously for peace-time (or [illegible] and the radar needs to be able to adapt its configuration to [illegible] in peace-time.

[illegible] of intelligence and flexibility, while improving the [illegible] the equivalent echoing area of the targets.

[illegible] whatever be the level reached, the radar has its own physical [illegible] complete system for which exist limitation in volume, weight, con-[illegible] really implement an active cooperation between all the [illegible] make the overall action globally more efficient and eco-

[illegible]

[illegible] helping me in preparing this paper.

Solid State Multifunction Phased Array Radar

W. D. Wirth
Forschungsinstitut für Funk und Mathematik (FFM) der FGAN e.V.
D-5307 Wachtberg-Werthhoven F.R. Germany

SUMMARY

With an experimental phased array radar system ELRA operational experience has been gathered. The system was planned for solid state operation, therefore it consists of active receiving and transmitting arrays. The provisional tube power amplifiers are replaced by transistor amplifiers. This change had some implications on the multifunction operation, especially on the selection of transmitted waveforms. The necessary considerations are relevant for future solid state phased array radars. The introduction of monolithic microwave antenna modules will improve the chances of active solid state phased arrays.

1. INTRODUCTION

There is agreement in the radar society about the advantages of phased arrays already for a longer time, especially concerning the multifunction capability and the operational properties. The principal drawback preventing their introduction up to now is their high investment cost. With the development of monolithic microwave integrated circuits (MMIC) a dramatic cost reduction seems possible for the near future.

The MMIC-technology may be applied only to active arrays: each antenna element is combined with its individual module with a transmit and receive amplifier together with the phase shifter. Because there will be a high number of elements (1000 to 10.000), the low transmit powers of single modules add up in space by superposition of radiated waves. Thus, considerable effective power densities within the main beam are achieved.

2. MULTIFUNCTION OPERATION WITH SOLID STATE ARRAYS

A typical operational condition with transistor power amplifiers is their low ratio of peak-to-mean power. For bipolar transistors at S-band this may be about 2. With FET-amplifiers at X-band this ratio is even only 1. Therefore the applied waveform should result in a high duty factor to use the available mean power. On the other hand a wide variety of waveforms are applicable under the contraints of mean and peak power: short pulses with high prf or long pulses with low prf and even CW. This property has to be considered with respect to the different tasks of a multifunction radar.

Multifunction array radars are attractive likewise for future groundbased air defense and for advanced fighter aircraft.

The radar functions to be performed in the ground based case by one system may be:

- Long range search
- Medium range search with clutter suppression
- Short range search
- Horizontal search in clutter with doppler filtering
- Target acquisition with parameter estimation
- Multiple target tracking
- Target classification
- Passive jammer location.

In the airborne case there will be some alternative and additional radar functions /1/:

- High prf velocity search mode for long range
- Medium prf for look down search and multiple target tracking
  Both modes are applied against the doppler shifted ground clutter. The problem of ambignous range and doppler are solved by bursts of different p.r.f.s

- Ground mapping for navigation
- Detection of moving ground targets
- Synthetic aperture formation
- Precision velocity update for doppler navigation
- Terrain avoidance and following.

It seems very likely to me that multifunction array radars may be built in future with the same antenna modules for both mentioned areas of applications. The difference between both types of systems will confine to some special selected waveforms with their corresponding signal processing and the programs for the computer control of the radar and for the data processing. The remaining one parameter for the selection of a module type then will be the desired frequency band. Some aspects of the development for an X-band module will be treated during this conference by the presentation (No 30) of E. Langer.

3. EXPERIENCE AND RESULTS WITH THE ELRA EXPERIMENTAL SYSTEM

An experimental ground based electronic steerable radar (ELRA) has been developed and operated under computer control at FFM /2/. The experience with this active phased array multifunction radar may be useful for future airborne systems as well.

The modular construction with separate transmit and receive arrays and using the concept of an active array has proven also very suitable for such an experimental system. Modules have been added piece-wise. Repair of some modules was possible while operating the remaining part of the system. 300 transmit and 768 receive modules are distributed in thinned arrays. The operating wavellength is 11 cm (S-band). In parallel subsystems for signal processing and the programs for radar control have been extended step by step.

A multifunction operation together with a tracking computer /2/ is possible with the following individual radar functions:

- Long range search with sequential detection
- Medium range search with MTI-filter and sequential detection /3/.
- Horizontal search in fixed clutter with doppler filtering
- Target acquisition
- Target location for tracking

The parameters of all tasks can be chosen independently. Target acquisition and location with higher energy compared to the search mode results in a stabilization of initiated tracks. An example of the experiments to observe targets of opportunity is demonstrated by the Fig. 1a, b, c, which show the integrated plots in a PPI-representation during an interval of 10 min for the search, acquisition and tracking mode respectively. Remarcable is the dense series of tracking plots, resulting from the track requests of the tracking computer and performed with increased energy.

The first approach for the transmitter has been realized with individual tube amplifiers. These are meanwhile replaced by transistor amplifiers for reasons of cost and reliability. They are developed as microstrip devices. The mean and peak output powers are 5 and 10 W respectively. Fig. 2 shows the output amplifier together with the radiating dipole. The principal problem with transistors arises by the fact, their peak power may be only about twice their mean power. The most suitable operation would even be CW, which is not usable for long range radars. In Fig. 3 we indicate an example for a receiving range interval equal to the blind range resulting at a duty factor $\eta \approx 0.3$. We take that ratio as a limit for long range search. We will find by some following examles, that it is not possible to make complete use of the available mean power of transistors. But we can achieve the highest duty cycles for long range operations for search and tracking and for these cases the available power is needed most.

Of course we have to control the scanning of the agile narrow pencil beam, produced by a planar array, with a computer dedicated to the radar control. Especially it is necessary to select individually the pulse period and dwell time in each beam postion. But this is no severe problem and therefore maximum performance can be achieved with transistors for transmitting in a multifunction radar.

4. PARAMETER EXAMPLE

An electronic scanning radar is naturally very flexible and almost all parameters can be varied by computer control. Nevertheless we have to establish a set of reasonable parameters for a standard operation. At any time necessary adaptations can be initiated by the computer, but the system may be reset to this basic parameter set.

In the following we select a parameter set which is suitable for ELRA operation. The task of our radar shall be the observation of the airspace, for example for air traffic control. Indeed we want to observe targets of opportunity, that means air traffic, with our system. It follows for all targets a certain radar cross section σ, which we may assume the same for all targets at all ranges. A further arbitrary choice divides the radars load to search and tracking into equal parts, or with other words, only 50% of the available radar power is dedicated to the search function.

For the following discussion we have to look at the well known radar equation:

$$n \frac{S}{N} = \frac{n \tau P\, G_t\, G_r\, \lambda^2 \sigma}{R^4 (4\pi)^3\, kTF\, L} \qquad (1)$$

(n = number of pulses in a beam position, $\frac{S}{N}$ = signal/noise power ratio, τ = pulse length, P = transmitted peak power, G_t, G_r = antenna gain for transmitting and receiving, λ = wavelength, σ = target cross section, R = target range, kTf = noise power in unit bandwidth, L = losses).

If we let the value of the product

$$P\, G_t\, G_r\, \sigma$$

unchanged, the $\frac{S}{N}$ and therefore the conditions for signal processing and the time management, we are especially interested in, is also unchanged. In this sense the ELRA-parameters may be compared to a hypothetical operational system OS:

	ELRA:	OS:
G_t	300	2000
G_r	768	2000
P	10-300 W	0.9-2000 W
σ	10 m^2	1 m^2

Additionally we assume the same beamwidth for the pencil beams of both systems, which is achieved by adequate antenna element thinning in case of ELRA. By this assumptions we expect our results to be applicable in principle to future operational systems.

For our purpose the radar equation (1) may be compressed to

$$\frac{S}{N} = \frac{\tau P}{R^4} \cdot C$$

with C comprising all fixed parameters.

So we recognize, that to achieve a certain range R we have to apply a corresponding pulse energy τP. The pulse energy τP has to be repeated by a pulse period T, matched to the unambigous range R. So the mean power of the transmitter is $P_m = \tau/_T P$, which is in the end determining the achievable range. By considering the detection performance(P_D, P_F) and the type of signal processing we get n, the number of pulses in a beam position, or nT as the dwell time.

5. EXAMPLES FOR SEARCH:

We assume the already mentioned parameters for the radar equation and F = 4 dB, L = 8 dB (propagation, scanning and matching losses).

5.1 Long Range Search:

$$R = 200\,\text{km}, \qquad \tau = 640\ \mu\text{s}$$

By applying sequential detection /4/ we achieve with a mean test length $\bar{n} = 5$ a $P_D = 0.4$. At maximum range this results for five search periods in a cumulative detection probability of $P_C = 0.92$. The blind range is given by τ to $R_b = 96\,\text{km}$. So we can search only for targets at ranges from 96-200 km. According to Fig. 4 we have 6 beam-positions (BP) for covering a height up to 20 km. In azimuth there are 60 BPs. For T = 2 ms we get a search time

$$T_{LRS} = 6 \cdot 60 \cdot 5 \cdot 0.002 = 3.65\ \text{s}$$

The duty cycles is $\eta \approx 0.3$.

For the repetition of the long range search we select a period of $t_{LRS} = 15\,\text{s}$. A radial flying target at $v = 250\frac{m}{s}$ would have moved in 5 search periods 18.7 km, which is less then 10% of maximum range.

5.2 Medium Range Search:

This has to fill up the blind range of the long range search. But this is only necessary if there is a possibility for new targets coming up in this area. All targets coming inbound from maximum range are detected already and tracked. We may have to care only for targets at low and high altitudes ($h < 600\,\text{m}$ or $h > 20\,\text{km}$). The necessary energy may now be reduced by 2^4 and this is done by chosing $\tau = 128\mu\text{s}$ and n = 2.

The detection performance at R = 100 km is therefore the same as for R = 200 km. The blind range is now 20 km. With T = 0.8 ms and 8 BP in elevation we get a search time

$$T_{MRS} = 8 \cdot 60 \cdot 2 \cdot 0.0008 = 0.7685\,\text{s}$$

The duty cycle is only ≈ 0.16.
For the repetition of this medium range search we select $t_{MRS} = 7.5\,\text{s}$. The low altitudes are covered by the coherent search along horizon.

5.3 Coherent Search along Horizon in Ground Clutter:

This search is performed with a doppler filter to achieve adequate clutter cancellation. Therefore we select a relatively high number of pulses n = 8 and $\tau = 32\ \mu\text{s}$. This values are adequate for a range of 100 km. With T = 0.8 ms the search requires a time

$$T_{SC} = 1 \cdot 60 \cdot 8 \cdot 0.0008 = 0.38\,\text{s}$$

The repetition period is selected to $t_{SC} = 5\,\text{s}$. The duty cycle is only $\eta \approx 0.05$.
A synchroneous multiple beam operation is therefore possible, especially if there are more BPs which are occupied by clutter, e.g. weather clutter.

5.4 Short Range Search:

If necessary the blind range of the medium range search may be covered. A pulse length of $\tau = 2\mu\text{s}$ and n = 3 (MTI operation) is suggested.

With T = 0.2 ms and 13 · 60 = 780 BPs this search is performed within

$$T_{SRS} = 13 \cdot 60 \cdot 3 \cdot 0.0002 = 0.468\,\text{s}$$

The repetition period is selected $t_{SRS} = 5\,\text{s}$.

5.5 Relative Search Load:

Within an interval of 15 s the time dedicated to search can now be specified:

Long range	1 x 3.6 s	= 3.600 s
Medium range	2 x 0.768 s	= 1.536 s
Clutter, horizon	3 x 0.38 s	= 1.140 s
Short range	3 x 0.468 s	= 1.404 s
	Σ	= 7.68 s

So we end up quite accidentally with 51% search load. The mean duty cycle is $\bar{\eta} = 0.19$. So we don't make use of the available mean power with $\eta = 0.5$. We used for different search tasks different dwell times in each BP and different repetition periods. Here we recognize a fundamental advantage of a beam agile radar.

6. EXAMPLES FOR TARGET LOCATION (TRACKING)

Target Location will be applied after a search result for target acquisition or validation and for computer controlled target tracking. The energy for each location task is increased by about 5 dB compared to the search mode.

Because now the range of the target is coarsely known, the pulses may be extended to approximate $\eta \approx 0.5$ at maximum range.

6.1 Long Range Location:

For the range interval 150-200 km we select according to Fig. 3 $\tau = 1$ ms and T = 2.333 ms. In favour of doppler estimation we select n = 12. ($\eta = 0.42$).

6.2 Medium Range Location:

For the range 75-150 km we select $\tau = 500$ µs, n = 8 and T = 1.5 ms ($\eta = 0.33$).

6.3 Short Range Location:

For R 75 km we select $\tau = 16$ µs, n = 16 T = 0.6 ms ($\eta = 0.026$).

6.4 Target Location Capacity

How many targets may be located or tracked with this operational parameters? If in each area 10 targets are tracked at a rate of 1 s we arrive at a tracking load of 496 ms/s, that means 49.6% which is just compatible with our search load.

For the short range location we may apply multiplex operation and thereby increase the number of targets to be located e.g. by a factor of 5. By this means also η is increased to 0.19. Because false alarms from search by clutter residues are most likely in this area, this multiplex operation should be kept in mind. The mean duty cycle for target location is $\eta_L = 0.35$ and therefore remarkably higher compared to search. The overall mean would be $\eta_m = 0.27$.

7. CODING OF PULSES

Up to now we selected pulse length τ for each special task arbitrarily. Of course the pulses have to be modulated. For the code selection the first step is to evaluate

$$d = f_d \tau \quad = 2 f_o \frac{v}{c} \tau$$

with f_d = target dopplershift. For target velocity v = 250 m/s and f_o = 2.72 GHz (S-band) and $\tau = 100$ µs we get

$$d = 0.62$$

In most cases our pulses are even longer, so we have to choose a doppler insensitive code. The classical choice is linear frequency modulation (LFM). Pulse compression by SAW devices seems impossible for long pulses up to 1 ms. So we are led to polyphase codes as the digital approximation of the LFM. The pulse compression has to be performed after beam forming and MTI with a digital transversal filter or correlator. Recent publications of Kretschmer and Lewis /5/ describe a version of the polyphase code, called P 3, which seems most suitable:

$$\varphi_i = \frac{\pi}{K} (i - 1)^2 , \; i = 1 \ldots K$$

The phase for each subpulse φ_i is of course taken modulo 2 and K is the code length or number of subpulses. One interesting feature of the P 3 code results from the fact K to be any integer in contrast to the Frank code /6/. On the other hand this P 3 code needs a finer phase quantization compared to the Frank code: for K = 64 we would need 7 compared to 3 bit phase quantization. Some computations of the ambiguity functions of the P 3 code for a coarser quantization resulted in an only minor increase in sidelobes, if we take only the number of bits corresponding to the Frank code.

For the ELRA system a phase modulation is realized with one accurately adjusted 4 bit phase shifter operating on the rf reference signal before distribution to the 300 transmitter channels. The codelength may be chosen 1, 16 or 64 and the subpulse may be 1,2 or 10 µs. All possible combinations provide values for the pulse length of 1, 2, 10, 16, 32, 64, 128, 160 or 640 µs. The pulse compression (PC) is realized by a digital filter with appropriate flexibility. In Fig. 5 are shown examples of clutter echoes after PC with codelength 1 (unmodulated), 16 and 64 with subpulse length 1 respectively 2 µs. The amplitudes are normalized to noise after PC, so the processing gain by the PC according to the codelength is obvious for some point targets.

8. MONOLITHIC MICROWAVE INTEGRATED CIRCUITS (MMIC)

The development of MMIC circuits seems to be the real and final chance for a break through of solid state phased arrays. With our parameter example we have shown, a transmitter power of 1 W per element is plenty enough for an operational system with some thousand elements. Developments are going on for complete T/R modules at S and X-band /7/, /8/. A block diagram is shown on Fig. 6.

The main parameters of such modules are of the following orders of magnitude:

transmitting power: 1 W
transmitter gain : 20 dB
Receiving gain : 20 dB
Phase shifter : 3-5 bit (depending on sidelobe specification)
Noise Figure : 4 dB
Dynamic range of receiver : 70 dB

The bandwidth should be as large as possible. Perhaps it is possible then to use the same type of module for different radar systems.

9. AUTOMATIC TESTING OF ANTENNA MODULES

An automatic testing or monitoring of all antenna elements should be possible during radar operation. An auxiliary antenna in front of the array outside the scanning angle and an individual control of the phase shifters is a precondition for a simple and effective procedure: each channel is phase modulated individually and the resulting modulation analyzed /9/.

For 3 bit phase shifters, as used in the ELRA system, the complex sum beam output (I and Q signal component) should show eight points lying on a circle spaced 45° apart. The channels gain is tested with the circle diameter. The zero phase can be evaluated and stored for phase compensation in connection with the computation for the phase steering commands. So there is no need for hardware phase alignment. The deviation of the measured phase state from the ideal ones is also evaluated. By this means faulty channels are indicated together with the type of error.
The complete test procedure may be performed within some seconds or may be interlaced with the radar operation. A nearly continuous antenna test during field operation is therefore possible.

OUTLOOK:

No fundamental problems are existing to day for the realization of electronic scanning radars. By applying computer control to the radar functions a high flexibility is given to accomplish different radar tasks with one radar system. By the development and implementation of MMIC-technology the cost for investment and operation will decrease substantially. Ground based and airborne systems may share the same antenna module technique. By increasing the required number of modules there is a contribution to further cost reductions for hardware parts and development.

REFERENCES:

1. Roulston, J.F., Multimode Airborne Radar - A Review, p. 137, Proceedings Military Microwave Conference, London 1984

2. Wirth, W.D., Phased Array Radar with Solid State Transmitter, Proceedings International Conference on Radar, Paris 1984

3. van Keuk, G., Adaptive Computer Controlled Target Tracking with a Phased Array Radar, IEEE 1975, International Radar Conference Proceedings

4. Wirth, W.D., Signal Processing for Target Detection in Experimental Phased-Array Radar ELRA, IEE Proc., Vol. 128, Pt. F, No. 5, October 1981

5. Kretschmer, F.F. and Lewis, B.L., Doppler Properties of Polyphase Coded Pulse Compression Waveforms, IEEE Transaction AES, Vol. 19, No 4, July 1981

6. Cook, Chr.E. and Bernfeld, M., Radar Signals, Academic Press 1967

7. Pengelly, R.S., Broadband Monolithic Microwave Circuits for Military Applications, Military Microwave Conference Proceedings, London 1982

8. Langer, E., The Mixture of Different Semiconductor Technologies in Radar Modules and its Impact on Cooling Problems and Reliability, Paper No. 30 of this Conference

9. Sander, W., and Hüscheltrath, G., The ELRA Phased Array Radar with Automatic Phase Adjustment in Practive, AGARD CP 197, Den Haag 1976

Fig. 1a: Search plots

Fig. 2b: Validated Search plots

Fig. 1c: Tracking plots

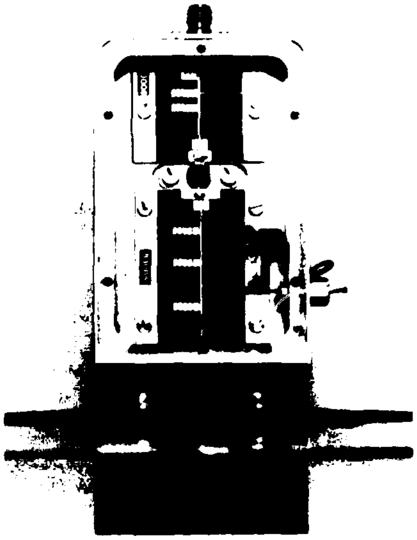

Fig. 2: Transistorampl. + dipole

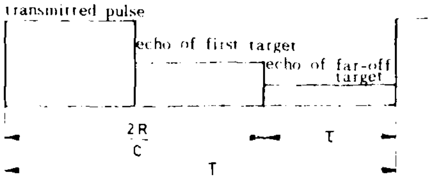

Fig. 3: Radar period and pulse length

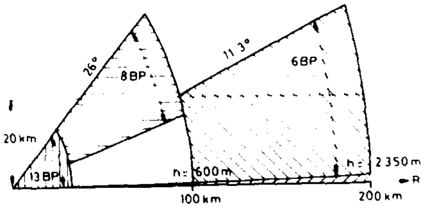

Fig. 4: Elevation Coverage

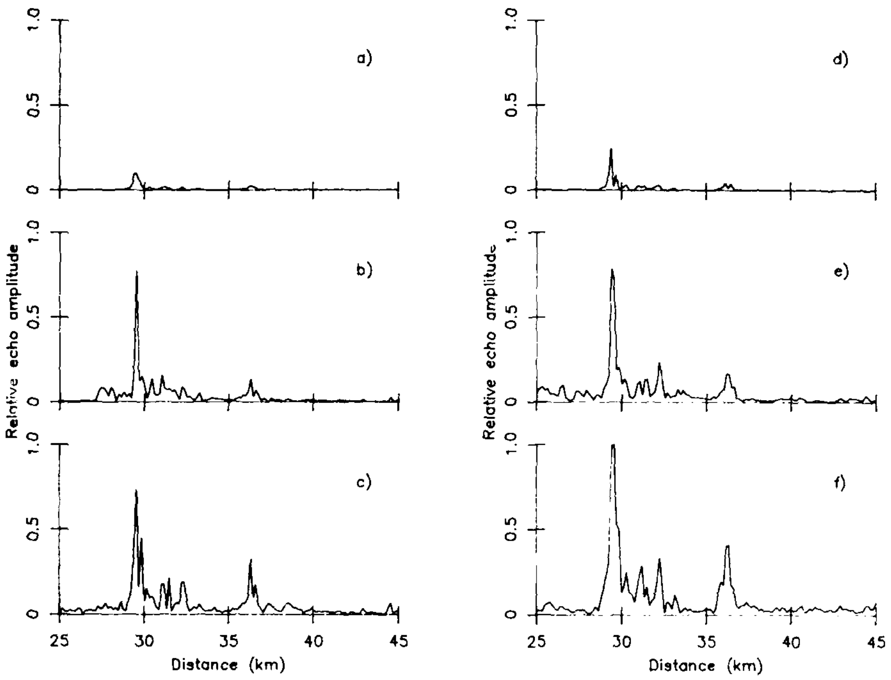

Fig. 5: Clutter signals received with ELRA-system applying polyphase pulse compression:
a,b,c: subpulse 1 µs and codelength 1,16 and 64
d,e,f: subpulse 2 µs and codelength 1,16 and 64

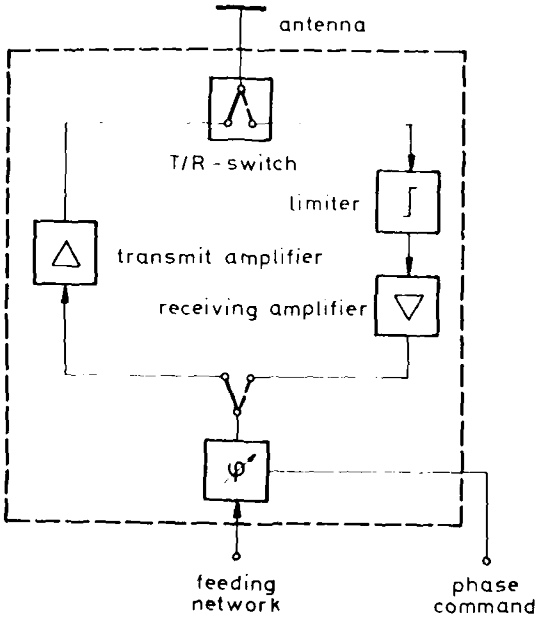

Fig. 6: T/R-module

DISCUSSION

Blinston

Efficiency of solid state modules will be important for airborne applications of electronic scanning. What is the proposed efficiency of the modules you intend to use?

Author's Reply

We hope for 20% to 25% DC to RF-efficiency.

K.Solbach

What are the definite advantages of active array radar versus passive array radar in terms of operational performance?

Author's Reply

The advantages are:

1. Prime power saving by a factor 2.
2. Redundancy of the radar antenna, e.g. 10% of modules may fail, but the system can operate without repair with reduced power (graceful degradation).
3. In future lower cost for investment and maintenance (many equal elements).

MULTIMISSION AIRBORNE RADAR FOR THE 1990s

by

Dr Thomas H.Robinson
Advanced Development Department
Advanced Programs Division
Radar Systems Group
P.O. Box 92426
Los Angeles, CA 90009
USA

ABSTRACT

The continuing trend towards the development and production of aircraft capable of multiple missions indicates that future airborne radars must provide a broad spectrum of air-to-air and air-to-ground modes. This paper investigates the modal and functional requirements of a multimode radar projected for the mid-1990s period. The paper is divided into two sections. In the first, the multimission capabilities of current radars are presented to establish trends and capabilities. In the second, the requirements of the next generation system are established.

Current multimode radars lay the basis for future systems. The experience gained on the APG-65 and APG-63/70 radars is presented and conclusions are drawn regarding their impact on future system requirements. Not only are modes and performance reviewed for these radars but also their system architecture. The discussion starts with the APG-65 radar which is the first true multimission radar with programmable signal and data processing. Following this, the evolution of the APG-63 radar, culminating with the most recent upgrading resulting in redesignation to APG-70, is presented. The incorporation of air-to-ground capabilities in the APG-70, resulting from the Dual Role Fighter program, is reviewed. Results from the Advanced Fighter Capabilities Demonstration program are presented showing how high resolution SAR was incorporated into a full weapon delivery solution.

With the context of today's systems established, the specific radar requirements for the next decade radar system are developed. This development is done in two parts. First, mode requirements are synthesized for air superiority, navigation and strike/interdiction operation. This includes low altitude penetration requirements and a review of radar timeline constraints which arise. Second, the fundamental functional requirements needed to implement the mode requirements are explored. Architectural issues and their impact on reliability and sustainability are also considered.

DISCUSSION

Dortomb

Pourquoi conserver une antenne de garde?

Quel emploi en est fait?

A quel niveau du traitement l'information de l'antenne de garde est-elle utilisée?

Author's Reply

(1) We have a guard antenna in order to reduce clutter in MPRF and for ECM reasons in current radar.

(2) In future systems more such auxiliary apertures may be used for sidelobe jammer cancellation reasons.

W.M.Boerner

(1) Have you implemented polarimetric techniques?

(2) Will you soon?

(3) What kinds of non-cooperative target identification techniques (match) are you implementing.

Author's Reply

(1) No, because full advantage of increased range and doppler processing has yet to be taken.

(2) Probably not in the next generation full control multimode radar systems.

(3) Engine modulation signatures to name one. Target motion plume exhaust identification.

R.Klemm

(1) Do you believe in the future of adaptive signal processing (e.g. for ECM or clutter reduction)?

(2) Will your signal processing be fully digital?

Author's Reply

(1) I strongly believe that adaptive signal processing will be used and understand that some of the newest large radar systems incorporate adaptive processing.

(2) Digital signal processing is expected rather than special analog processing.

E.Wölfle

For fighter aircraft there is the strong requirement for large antenna scan angles. How are you going to overcome the deficiency of phased array antennas in this respect?

Author's Reply

Inter-element spacing appropriate for scan angles of +65° are expected without giving rise to grating lobes. For larger scan angles, associated with short range tracking some grating lobes may be unavoidable.

A.Freeman

You didn't mention spotlight mode SAR as one of two options for multi-function airborne radar.

Author's Reply

Spotlight SAR will be the primary SAR mode — in fact SAR strip mapping may not be provided.

R.G.Cuthbert

The opening address suggested that quantum improvement was required in radar air-to-air performance to offset the reduction in echoing area and increase in sophistication of the threat. How do you think that this can be achieved?

Author's Reply

First, I feel that we must improve ECM resistance through techniques including increased tunable RF bandwidth. Second, we should look to improve sensitivity by superior signal processing and the expected improved efficiency of active array antennas.

MULTIFUNCTION MILLIMETRE-WAVE RADAR FOR ALL-WEATHER GROUND ATTACK AIRCRAFT

by

K.E.Potter
Royal Signals and Radar Establishment
St. Andrews Road
Malvern
Worcestershire
WR14 3PS
UK

ABSTRACT

AGARD Aerospace Applications Study No.19 (AAS-19) recently addressed the "All weather capability of combat aircraft".

The study looked at sensors and techniques required for the operations of take-off/landing, navigation to and from the battlefield, and target acquisition. The emphasis was on poor weather operation and included the threat of Warsaw Pact defences.

This paper presents details of the millimetre wave radar performance which shows that with potentially available power sources an all weather capability can be realised.

Performance is evaluated as a function of frequency and antenna size, and the use of polarimetry with wide bandwidth/coherent processing is shown to offer potential enhancement for target discrimination.

The millimetre wave radar is shown to be potentially capable of satisfying the following functions:

(i) Take off/Landing
(ii) Terrain Following
(iii) Area Correlation
(iv) Tercom
(v) Acquisition of Targets

The above roles can be achieved in an all weather environment making the millimetre wave radar a valuable multifunction airborne radar.

MULTI-MODE MULTISTATICS FOR PASSIVE/ACTIVE AIRBORNE SURVEILLANCE

by

Robert F.Ogrodnik
Rome Air Development Center (OCTM)
Griffiss AFB NY 13441-5700
USA

ABSTRACT

The increasing performance demands for air surveillance assets, as well as the necessity for continued surveillance operations in the presence of enemy jamming and Anti-Radiation Missile (ARM) attacks, have increased interest in passive surveillance, in particular multi-mode passive/active multistatic sensing. The use of noncooperative radiation as illuminators of opportunity combined with passive surveillance Electromagnetic Support Measurement (ESM) sensors opens new horizons to multistatic surveillance from a passive airborne platform. Such platforms remain secure from ARM attacks and can preserve operations in the presence of a jammming environment while employing the jammer radiation as an additional illuminator of opportunity.

Research and field tests have been conducted on ESM augmented bistatics as well as noncooperative multistatics which support the development of airborne multi-mode passive surveillance technology. This work has been conducted under such programs as the Bistatic Enhanced Altimeter Detection (BEAD) and the noncooperative multistatic Passive Coherent Location (PCL). Both BEAD and PCL technology directly support the receiver, signal processing and target location/tracking operations necessary for passive airborne surveillance. The demonstrated technologies for EM interference rejection and multistatic multi-target tracking and location under PCL provide a promising performance bench mark for passive surveillance in the presence of a complex electromagnetic environment. Passive receiver intercept performance under BEAD has provided a receiver design baseline for both look-down and look-up surveillance applications.

This paper will present the technologies under development in BEAD and PCL. It will also present the field test results and the sensor concepts. In particular, spin-off data such as bistatic look-down clutter, noise-floor limitations of noncooperative multistatics and sensitivity limitations set by passive surveillance using signal intercept techniques and illuminators of opportunity will be provided.

MOTION COMPENSATION REQUIREMENTS FOR A HIGH RESOLUTION SPOTLIGHT SAR

by

J.S.A.Hepburn
Huntec (70) Limited
Scarborough, Canada

and

G.E.Haslam and D.F.Liang
Defence Research Establishment
Ottawa, Canada

and

W.S.Widnall
Department of Aeronautics and Astronautics
Massachusetts Institute of Technology
Cambridge, MA, USA

ABSTRACT

The Canadian Department of National Defence is developing a high resolution airborne spotlight synthetic aperture radar (SAR). To attain the high contrast, high resolution and low geometric distortion objectives of the project, it is essential that very accurate motion compensation be applied to the radar returns to minimize the effects on SAR image quality of spurious antenna phase center motion. The motion compensation system being developed for the project includes a gimballed master inertial navigation system (INS) located near the center of gravity of the host aircraft, a strapdown inertial measurement unit (IMU) comprising gyroscope and accelerometer triads mounted on the radar antenna, as well as Doppler velocity and barometric altitude sensors for damping the inertial systems. The role of the master INS is to enable high accuracy alignment of the strapdown IMU. The raw sensor data are integrated using a U—D factorized Kalman filter to obtain optimal estimates of the motion of the radar antenna phase center while the SAR window is open. These data are used to adjust both the radar pulse repetition frequency and the phase and displacement of the radar returns.

Huntec (70) Limited carried out the analysis of the motion compensation requirements, leading to the specification of the motion compensation sensor configuration and accuracy. The performance of the motion compensation system has been evaluated by detailed computer simulation. This evaluation accounted for all major system error sources, including errors associated with sensors, transfer alignment and computation, with the system operating in a moderately turbulent environment.

Results of the evaluations by analysis and computer simulation are presented.

IMPLEMENTATION OF AN AIRBORNE SAR MOTION COMPENSATION SYSTEM

D. DiFilippo and D.F. Liang
Department of National Defence
Defence Research Establishment Ottawa
Ottawa, Ontario, K1A 0Z4
Canada

L. Postema
Lear Siegler, Inc., Instrument Division
Grand Rapids, Michigan, 49508
U.S.A.

B. Leach
National Aeronautical Establishment
Flight Research Laboratory
Montreal Rd., Ottawa, Ontario, K1A 0R6
Canada

ABSTRACT

The Canadian Department of National Defence has entered into the Phase II development of an airborne Synthetic Aperture Radar Motion Compensation (SARMC) system, following a Phase I feasibility study which led to the specification of the SARMC sensor configuration and accuracy.[1] This paper describes the hardware and software configurations of an airborne SARMC system implemented on board a Convair 580 research aircraft. The hardware configuration includes a gimballed LTN-51 inertial navigation system, a Decca doppler radar, a baroaltimeter and a Motion Compensation Inertial Measurement Subsystem (MCIMS). The MCIMS is a specially designed strapped-down inertial measurement unit mounted on the ring gear of the APS-506 radar antenna. Since motion compensation depends critically on knowledge of the MCIMS orientation with respect to the radar line-of-sight to the designated target, a laser alignment procedure was developed and performed to calibrate the azimuth encoder of the antenna ring gear. This procedure is discussed along with experimental results. Substantial effort was dedicated to streamlining the Kalman filter algorithms in the SARMC processing package to obtain a high degree of robustness and computational efficiency while optimally integrating the information from the motion compensation sensors. Preliminary flight trial data are presented and compared with simulation results to indicate the level of performance achievable with this optimized system.

REFERENCES

1. J.S.A. Hepburn, et al., "Motion Compensation Requirements for a High Resolution Spotlight SAR", presented in this Symposium

MM WAVE SAR SENSOR DESIGN: CONCEPT FOR AN AIRBORNE LOW LEVEL RECONNAISSANCE SYSTEM

by

Dr C.Boesswetter
DFVLR Institute for Radio Frequency Technology
8031 Oberpfaffenhofen
Germany

ABSTRACT

Airborne high resolution Synthetic Aperture Radar systems for reconnaissance applications are usually designed for high speed aircraft platforms operating in medium to large altitudes. The sensor systems in most cases are operating in X-band. This is in contrast to civil airborne remote sensing sensor systems which are designed from L- over C- to X-band, in some cases operating simultaneously in two different bands providing more degrees of freedom for evaluation.

Since some emphasis has recently been placed on imaging radar systems operating at very low altitudes and at shorter ranges the question again arises whether alternative frequency bands are useful for designing radar mapping systems to be operated under special constraints e.g. the "penetrating" radar reconnaissance system operating at very low levels day or night.

Because one of the possible carrier platforms for the penetrator sensor system is considered to be a RPV, available space and electrical power are of prime concern. This is why mm wave technology is considered for this application, although the "classical" choice of operating frequency for SAR mapping systems is at the "lower" end of the frequency scale.

In the paper the basic system design considerations for a high resolution SAR system operating at 35 GHz or 94 GHz are given.

First it is shown that only the focussed SAR concept in the side looking configuration matches the requirements and constraints. After definition of illumination geometry and airborne modes the fundamental SAR parameters in range and azimuth direction are derived. A review of the performance parameters of some critical mm wave components (coherent pulsed transmitters, front ends, antennas) establish the basis for further analysis. The power and contrast budget in the processed SAR image shows the feasibility of a 35/94 GHz SAR sensor design.

The discussion of the resulting system parameters points out that this unusual system design implies both benefits and new risk areas. One of the benefits besides the compactness of sensor hardware turns out to be the short synthetic aperture length simplifying the design of the digital SAR processor, preferably operating in real time. A possible architecture based on current state-of-the-art correlator hardware is shown. One of the potential risk areas in achieving high resolution SAR imagery in the mm wave frequency band is motion compensation. However it is shown that the short range and short synthetic aperture lengths ease the problem so that correction of motion induced phase errors and thus focussed synthetic aperture processing should be possible.

ECCM EFFECTIVENESS OF A LOW SIDELOBE ANTENNA FOR SAR GROUND MAPPING

by

Dr C.Boesswetter
DFVLR Institute for Radio Frequency Technology
8031 Oberpfaffenhofen
Germany

ABSTRACT

Airborne Synthetic Aperture Radar (SAR) Reconnaissance Systems in the strip mapping mode are susceptible to jamming. The main ECM threat is commonly understood to be the ground based sidelobe jammer which includes a sensitive intercept receiver and a tracking capability to adapt the jamming power in angle, frequency and bandwidth to the SAR system. The most important of several necessary ECCM techniques is commonly considered to be a low sidelobe SAR antenna which also improves MTI performance. To characterize the ECCM and cost effectiveness of such an expensive antenna some measures are needed.

There are two separate phases: Intercept and Jamming. Accordingly, two gains are defined: Intercept Gain and Jamming Gain. Both are based on the evaluation of the Signal-to-(Jammer plus Clutter plus Noise) Ratio in the processed SAR image for the configuration "airborne sensor-ground based jammer". Both gains describe the benefits of a low side lobe antenna in terms of jam-free flight distance (Intercept) and target contrast enhancement (Jamming).

It is shown that in the most interesting case of "heavy" jamming both intercept and jamming phases are described by the same set of equations if normalized to the pointing direction (R) of the antenna. It follows that the Intercept Ratio on the ground equals the reciprocal of the target contrast in the processed SAR image, e.g.

$$\frac{S/N_I}{S/N_R} = \frac{S/J_R}{S/J}$$

To discuss both the intercept and jamming gain performance of a given SAR antenna 3-dimensional relief plots and 2-dimensional contour plots are used. They allow the definition of both gains directly. For the parameters of a given SAR reconnaissance system the plots are calculated in an area of 120 nmi × 180 nmi (Azimuth × Range). By replacing the existing antenna with uniform weighting with an antenna with 25 dB lower sidelobe level the ECCM effectiveness in terms of intercept gain and jamming gain is shown. Since the equations are normalized to the pointing direction of the sensor antenna the results are given in relative terms. By including actual jammer parameters the ECCM effectiveness may also be given in absolute terms.

SYNTHETIC APERTURE IMAGING AIRBORNE RADAR

MARC LUCAS

THOMSON-CSF DIVISION A.V.S
178 BD GABRIEL PERI - 92240 - MALAKOFF - FRANCE

ABSTRACT

Airborne synthetic aperture radars are systems able to obtain high resolution ground images, by day or night, independant of weather conditions. Their applications are very broad, either military : reconnaissance, or civilian : mapping, remote sensing.

Following a brief technical account (synthetic aperture, pulse compression), the paper describes the operational features of an airborne radar system providing high resolution images at long range. Then a technical description is given.

This system can provide in real time, to the ground, radar images by using a high rate data link.

It consists of two main parts :

- An airborne part including the antenna, the radar transmitter-receiver, the data link unit.
- A ground station that realises in real time, data reception, synthetic aperture processing and images exploitation.

1 - INTRODUCTION

The side looking airborne radars (SLAR), using synthetic aperture technics, are systems able to obtain high resolution ground images, by day or night, independant of weather conditions. Their applications are very broad, either in the military or in the civilian domain.

In France, the first studies started in the sixty's. As for back as 1964, they allowed to have some tens meters resolution radar images. Five years later, a synthetic aperture radar, using an optical processing improved by ten the radar resolution. In 1978, a real time digital processing was sucessfully tested. All of these experimentations have allowed to get, in France, the knowledge in the synthetic aperture technics for airborne radars [1] - [5]. They resulted in the design and the realization of a side looking airborne radar, described in this paper, giving very high resolution images at long range.

Such a system ensures real time radar images visualization on ground by using a high rate data-link.

Following a brief technical account, the paper describes the operational features of this system, then a technical description is given including various up to date techlological aspects.

2 - TECHNICAL PRINCIPLES

The two dimensions of a radar image of the ground are defined respectively by the waves propagation direction and by the antenna scanning This scanning is realized by an azimuth antenna rotation for classical radar and due to the carrier displacement for the S.L.A.R..

The image quality is tied to the sensor resolution. Two kinds of resolution can be defined :

- the azimuth resolution (along track resolution) in a direction parallel to the aircraft path
- the range resolution (across track resolution) perpendicular to the first one.

For a classical SLAR the along track resolution r_a is given by :

$$r_a = D.\theta g$$

with D : radar range
θg : azimuth aperture equal to λ/L
L : antenna length
λ : wavelength

For instance D = 10 km, λ = 3 cm, L = 1 meter gives r_a = 300 meters.

The range resolution r_d is tied to the transmitted pulse length τ by the following relation :

$$r_d = \frac{c\tau}{2}$$

with c : light speed

For instance for a pulse length of 1 μs the radar range resolution is 150 meters.

The radar image quality requires the improvement of these two resolutions. This is realized by using two technics :

- synthetic aperture technics for the a long track resolution improvement
- pulse compression technics for the across track resolution improvement

2.1. Synthetic aperture technic

The synthetic aperture technic uses the radar displacement and the processing of the received signal and synthetizes a very large equivalent antenna by moving a small one.

This processing is matched to the point target signal, received by the radar during its illumination time. For a SLAR, the antenna is fixed at 90° to the aircraft course.

It is well known that the received signal characteristics are :

- an amplitude modulation which is shaped by the azimuth diagram of the antenna
- a linear Doppler frequency modulation due to the aircraft speed and with a spectral bandwidth B defined by :

$$B = \frac{2V}{\lambda}\theta g$$

with V : aircraft speed

At the output of the matched precessing the signal, in the time domain has a 3 dB width τ_a which is equal to the inverse of the Doppler bandwidth :

$$\tau_a = \frac{1}{B}$$

This width defines the along track resolution r_a that is given by :

$$r_a = V\tau_a$$

$$= \frac{V}{B}$$

$$= \frac{\lambda}{2\theta_g} = \frac{L}{2}$$

This kind of processing can be realized for instance in the time domain, by a correlation between the received signal and a reference function which has the same phase law. This law depends on the geometry of the system.

2.2. Pulse compression

Pulse compression technics is used in the SLAR systems, in order to obtain very short radar pulses and a low peak power while having high energy level

The technic is based on a long transmitted pulse, which is linearly frequency coded and on a matched filtering in the receiver.

The 3 dB pulse width, at the output of the receiver is equal to the inverse of the signal transmitted bandwidth.

This 3 dB pulse width defines the radar range (or across-track) resolution, and the transmitted high energy ensures very long detection ranges.

3 - OPERATIONAL FEATURES

The SLAR system described in this paper performs high resolution ground images, by day or nigth, independant of weather conditions. The improved image contrast, due to the good resolution, makes easy the detection of low radar cross section targets in heavy ground and sea clutter (vehicules, small, boats,...) and also permits to distinguish two clutter regions having different reflectivity coefficients σ_0 (oil spill detection on sea...). In addition, these images can be superimposed on geographical maps for different comparisons.

Due to these characteristics, this kind of system offers a lot of applications either in the military or in the civilian domain, for instance :

- high resolution mapping
- military reconnaissance
- border surveillance
- oil spill detection on the sea
- iceberg detection and localisation
- ship traffic monitoring, etc.

3.1. Architecture of the system

This system includes a side looking airborne radar (SLAR) carried by the aircraft, a data link, and a ground station.

During the mission, the SLAR illuminates the surveyed area ; the ground station receives the informations transmitted by the aircraft, performes in real time a synthetic aperture processing and presents the ground images to operators.

The performances allows the visualisation of the surveyed area, several hundreds of kilometers far from the ground station.

This system architecture proceeds from the important amount of information to manage that needs a huge processing capacity in order to obtain in real time, high resolution images.

In the airborne part, the modular design of the sub-assemblies (radar and data-link units) makes easier their installation on board different carriers. Two kinds of installations are possible:

- in a pod equipped with an air cooling fan, containing all the units and antennas

- inside the aircraft, except for the antennas

In the ground station, all equipements are sheltered inside movable and airtransportable cabins.

3.2. Description of the system

The system is based on a S.L.A.R. using a pulse compression transmitter-receiver, with a fully coherent chain, and a ground station that realizes synthetic aperture processing and images display.

The radar vidéo signal after adequate coding is sent to the data-link system, and in parallel to high density magnetic tape recorder. This recorder is used, when the data-link transmission is not possible for operational reasons (hills, mountains, aircraft altitude...). In this case, the radar signal is processed and displayed in the ground station, after aircraft landing.

In the airborne part, the data-link unit uses one transmitter and two small antennas located at the both ends of the pod. These two antennas have a 360° total azimuth cover. At any time, one of them is slaved toward the ground station, by using informations given by the aircraft inertial navigation system.

In the ground station, the received radar signal is demodulated and processed. The synthetic aperture processing is realized by a digital real time correlator. After processing the images are displayed on T.V. sets, and also stored.

3.3. Operational features

This radar is fitted with several modes that permit to visualize a ground area located on the right or on the left of the aircraft course. For each of these modes, the swath has a width of some tens of kilometers, and the resolution is a few meters for the fixed targets modes, and a few tens meters for the moving targets.

The data-link system has a maximum range of several hundreds of kilometers, depending on the aircraft altitude. The information rate is about 50 Mbits/s. The transmitted data includes the digital radar video, the radar status data and different aircraft informations (geographical coordinates,...).

In the ground station, the real time digital processing input is the direct signal received from the data-link, or the airborne tape recording.

Several modes for the exploitation are foreseen in the ground station. They allow a real time or a delayed exploitation. At the output of the digital processing, the images are sent towards two T.V. sets via two images memories.

On the screens, the operators can see the radar image of the surveyed area, moving vertically with a speed whith is proportional to the aircraft's one.

These two T.V. sets allow one operator to watch the whole surveyed area, while the other has the following possibilities.

- to examine only a part of the selected swath. For this selection the operator uses cursor. Thus it is possible to have localy on the T.V. screen the best resolution of the radar.

- to stop the image and zoom to investigate details and to obtain the geographical coordinates of an image point.

The radar images are also sent towards photographic film recorders with continuous paper development and towards an high density magnetic tape recorder.

The magnetic tape can be used :

- for a delayed exploitation of the radar images on the T.V. sets

- to achieve several images processing and make, for instance automatic targets detection, or image correlation between different flights.

4 - TECHNICAL DESCRIPTION

4.1. Side looking airborne radar

The radar is composed of several subassemblies or units, that contain all the radar functions and use high level technologies.

The transmitter-receiver unit uses SAW devices to make pulse compression. Thus it is possible to achieve a very high compression ratio.

In order to obtain a high sensitivity receiver, this unit contains a low noise microwave amplifier using field effect transistors (F.E.T.) technology. The radar signal detection is ensured by a fully coherent chain, using an ultra stable oscillator.

The power amplifier unit contains a high gain travelling wave tube (T.W.T.), associated to its own high voltage and power supply circuits.

The radar aerial is constituted of a flat slotted wave guides antenna which can be moved around the yam and roll axis. Thus it is possible to slave the antenna to the left or to the right of the aircraft path.

At the output of the transmitter-receiver unit, the radar signal is sent to a preprocessing unit. This unit includes the analog to digital converters (A.D.C.) circuits and the preprocessing filters. The A.D.C. are used to digitize the radar signal. The number of range bins digitization, defines the processed swath. This number is about ten thousand. The preprocessing filters are used to reduce the amount of informations to be transmitted and to be processed. These low-pass filters limit the received Doppler signal bandwidth, in order to keep only the useful spectrum needed by the defined along track resolution.

The data-link unit, includes a very low power travelling wave tube amplifier and also the microwave carrier generation circuits. Before amplification this carrier is modulated by a quadratic phase shift keying modulator (QPSK) which is a good compromise between the required bandwidth and the bit error rate.

4.2. The ground station

The ground station is composed of an antenna located on a turret, and of two cabins, one for the processing unit and the other for the images exploitation.

The turret ensures the passive tracking of the aircraft during the mission, and contains the data receiver and a 2 meters diameter antenna.

The synthetic aperture processing is located in a cabin, and uses a digital correlator, to compute in real time for each range bin, the correlation result between the radar signal and a reference function. This device has a powerful capacity up to the equivalent of 10^9 multiplications per second. It is composed of several modular units, that realize the processing of the swath. Each of these units includes :

- a large digital memory to store the radar video samples

- a correlator which calculates the correlation function between complex signals

- a reference function generator. These functions depends on the range

In the second cabin the exploitation of the mission is ensured by two high resolution T.V. sets (1000 x 1000 points), associated with a large memory enabling the following functions :

- image freeze

- zoom

- symbols and markers generation

The exploitation uses also two alphanumeric monitors to display all the parameters of the mission (radar modes, geographical coordinate of the aircraft or of target located on the image...). The storage of the mission is made by two kinds of recorder.

- photographic film recorders

- high density magnetic tape recorder-reproducer

Each photographic film recorder is composed of an optical block, a paper transport unit and electronic circuits. The optical block is equipped with a He - Ne Laser source with a spot diameter of 100 µm. This recorder provides a paper image with the following features :

Resolution	:	2000 spots per line
Size	:	200 mm width
Length	:	up to 150 m

CONCLUSION

The SLAR system described in this publication has high operational features associated to an up to date design that make it a very efficient product.

It has the following high-lights :

Operational aspects :

- all weater, day or night capabilities
- real time surveillance
- very high resolution mapping at long range

Technical aspect :

- synthetic aperture and pulse compression technics
- modular design for easy installation on different aircraft
- fully integrated and airtransportable ground station

ACKNOWLEDGEMENTS

I wish to thank the French Administration STTE (Servuce Technique des Telecommunications et des Equipements Aeronautiques) that has financed a part of this system development and has allowed this publication.

REFERENCES

[1] G.Rèvillon, "Radar à faisceau latéral utilisant une antenne synthètique", AGARD AVIONICS PANEL on Advanced Techniques for Aerospace Surveillance, 1967

[2] J. Génuist, "Radar à faisceau latéral utilisant une antenne synthétique", AGARD Conf. Proc. 197 on New Devices, Techniques and Systems in Radar, pp 17/1 - 17/5, 1976

[3] P. Anthouard et J.C. Baron, "Radar à antenne latérale synthétique et systèmes de traitements associes", Colloque International sur le Radar, Paris, Décember 1978

[4] P. Anthouard, "A multipurpose Synthetic Aperture Radar", Proc. of International Radar Symposium India, October 1983

[5] P. Anthouard, "Imagerie radar à ouverture synthetique : applications aéroportées et spatiales", First image symposium conference proceedings, Biarritz, France - Vol. 2 pp 723 - 734, May 1984.

Millimeter Wave Transmission through Man-Made Obscurations in a Battlefield Environment

H. Essen, E.P. Baars
Forschungsinstitut für Hochfrequenzphysik
Neuenahrer Strasse 20
5307 Wachtberg-Werthhoven
Germany

Abstract

It is quite well established that millimeter waves exhibit superior transmission features for natural obscurations, i.e. mostly adverse weather-effects, if compared to those in the IR-region. Therefore mm-wave systems are competitors for military surveillance and guidance systems.

For these applications the knowledge of the amount of degradation of mm-Systems due to obscuration in a battlefield environment has to be assessed in comparison to IR-Sensors. The results will be important as well for optimal sensor design as for the development of camouflage measures.

The data dealt with in this paper have been gathered during various measurement campaigns. They cover smoke and dust trials with mm-waves-instrumentation systems at 47 GHz and 94 GHz and experiments on screening smokes. All trials were performed in conjunction with IR-measurements.

For the dust and smoke-trials a bistatic configuration was used with transmitters and receivers located at two opposite sites across an artillery impact area. Artillery barrages of different type of ammunition were fired into the impact area and the attenuation over the path due to mud, soil, debris and smoke by the detonations was measured.

Results are discussed by means of attenuation-curves for different transmit receive-polarizations. A comparison of the results of the two employed mm-wave frequencies with the simultaneously measured IR-data is given for selected events and on a statistical basis over the whole measurement period.

For the experiments on screening smokes a monostatic configuration was chosen with a pulsed 94 GHz instrumentation radar operating over a folded transmission path against a corner reflector and armoured target vehicles. By recording the echos from a number of consecutive range gates the attenuation caused by the smoke as well as the back-scatter of the smoke cloud and the location of scattering centers within the cloud could be evaluated. Results from optical, IR and radar smokes are discussed in the paper.

A CFAR DESIGN CONCEPT FOR OPERATION IN HETEROGENEOUS CLUTTER

Harold M. Finn
ADAPTIVE SENSORS, INC.
216 Pico Blvd., Suite 8
Santa Monica, California 90405

SUMMARY

When the heterogeneous clutter field spanning the spatial sampling sliding window can be modeled as two contiguous homogeneous clutter fields with the statistical parameters of each field unknown and independent from field to field and with the transition point between fields also not known, then the cell averaging CFAR performance significantly degrades yielding target masking effects and loss of false alarm regulation. For the same defined and encountered environment spanning the sliding windows, the performance degradation effects are shown to be largely eliminated when a newly developed class of CFAR test is employed designated as Heterogeneous Clutter Estimating CFAR's (HCE-CFAR). The test initially involves the combined use of multiple hypothesis testing and maximum likelihood estimation procedures to estimate the statistical parameters of each of the two fields, and the transition point between them, and then makes use of the relevant estimated clutter field parameters to effect the final decision rule. HCE-CFAR Designs are presented for both the cases when the contiguous fields have Rayleigh first order probability distributions, and log normal probability distribution. However, the focus of the development and the conducted performance evaluation is for the Rayleigh clutter cases.

1. INTRODUCTION

For a homogeneous Rayleigh distributed clutter limiting environment, automatic target detection modes (commonly referred to as cell averaging CFARs) can be designed which provide efficient detection and constant false alarm rate (CFAR) operation by a spatial sampling of the resolution cell outputs in a sliding window surrounding the cell which is under test for the presence of a target [1,2]. The modelling constraint imposed (in the above cited references) is that the clutter field spanned by the sliding window is either a homogeneous one (that is to say, the statistical parameters in each of the resolution cells covered by the sliding window and governing the detection output of each cell are identical), or that the clutter field is a heterogeneous one but where the functions controlling the values of the statistical parameters over the parameter space are known, a-priori, within scaling constants. However, when the sliding window is spanned by two different and contiguous homogeneous clutter fields with the cell under test embedded in only one of these fields and with no a-priori assumptions introduced of the relative levels of the parameters of these two fields or at what resolution cell the transition between the two clutter fields take place, then it is shown [1,2] that the detection performance significantly degrades--false alarm regulation is no longer maintained, and serious target masking is introduced.

Motivating the subject Constant False Alarm Rate (CFAR) development is the fact that a number of frequently encountered clutter phenomena involve interfaces of clutter fields with markedly different intensities of backscattering, for example: sea to land, dry to moist terrain, non-masked to masked terrain, light to dense foliage fields, and resolution cells free of clutter to resolution cells in a rain or chaff cloud. Synchronously gated or pulsed noise jamming is another possibly encountered radar environment adhering to the same type of transition between interference fields.

A newly developed class of CFAR tests, the subject of the paper, designated as Heterogeneous Clutter Estimating CFAR's (HCE-CFAR) is free of the a-priori assumptions of the heterogeneous clutter fields introduced in the earlier work (above cited references) and overcomes the performance degradation effects noted in these references for the classes of non-uniform clutter models considered.

1.1 HETEROGENEOUS CLUTTER FIELD MODEL EMPLOYED IN THE HCE-CFAR DEVELOPMENT

The heterogeneous clutter model employed in the HCE-CFAR development is a construct of a number of contiguous homogeneous clutter fields covering the radar parameter space but with the constraint imposed that no more than two of these clutter fields span the sliding window at any one time. (One homogeneous clutter field encompassed by all the sampling cells in the sliding window is also an admissable subset of the model.) The underlying statistical parameters of each clutter field are independent of one another and are assumed to be unknown, and the transition points between fields are also assumed unknown. The sampled envelope detected outputs of all resolution cells of all the clutter fields are statistically independent, and these observed random variables are assumed to have the same form of first order probability distribution. For example, they are all Rayleigh, or log-normally distributed. The model also includes the assumption that jumps in the carrier frequency can be effected which yield statistically independent frames of data without changing the underlying statistical parameters of the modeled probability distributions.

This work was supported by the U. S. Army.

While the described heterogeneous clutter model provides an appropriate description of some radars, or radar modes, and their encountered heterogeneous clutter limiting environment, it obviously is unsuitable for others. In addition, for this initial work, the sensitivity of the HCE-CFAR designs to encountered clutter deviating from the stated heterogeneous clutter model has not been established.

1.2 BASIC CONCEPT

The concept of the HCE-CFAR design is outlined in Fig. 1. Based on the N spatial sampled outputs included in the sliding window, estimates are first made of the statistical parameters of each of the two clutter fields sampled by the N cells, and of the transition point between them. The combination of maximum likelihood estimates and multiple hypothesis tests are used to make the estimates. The statistical parameters of the relevant clutter field, that is to say, the clutter field which is estimated to have the cell under test embedded in it are then used to form the decision statistic--the function of the observables used in the final decision rule. The detection threshold is made a function of the inputed design single cell false alarm probability (P_{FA}) and the number of samples (n) which are estimated to be in the relevant clutter field.

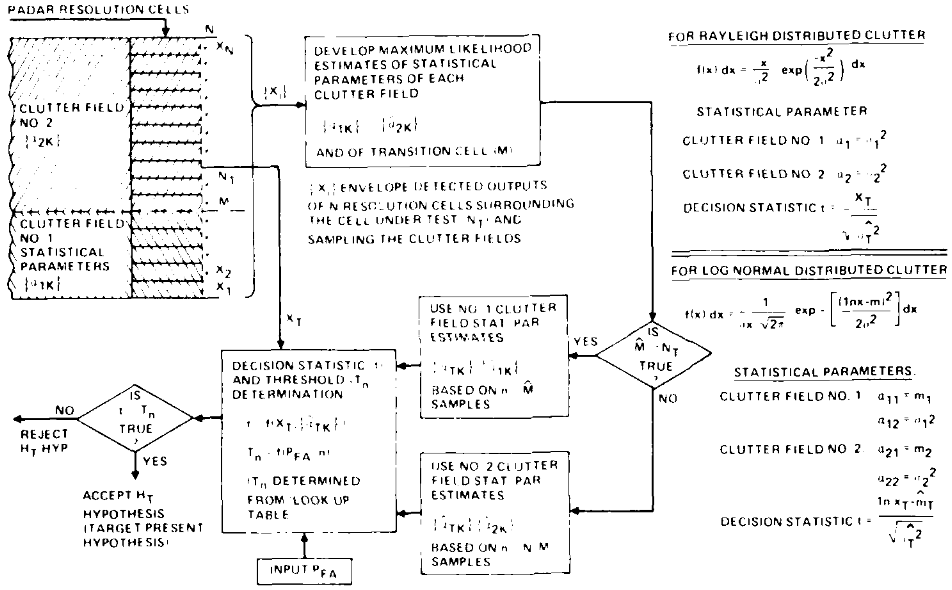

FIGURE 1 CONCEPT OF A HETEROGENEOUS CLUTTER ESTIMATING CFAR

The HCE-CFAR design concept is illustrated here for the clutter models exhibiting Rayleigh first order probability distributions describing the sampled envelope detected outputs, and also those clutter fields which are best characterized by the log-normal probability distribution. Referring to Fig. 1, it is noted that for the Rayleigh distributed clutter case, the statistical parameter estimated for each of the two clutter fields is the quantity (σ^2) which is proportional to the variance of the envelope detected output (x), and for the log-normally distributed clutter case, two statistical parameters (m and σ^2) are estimated for each of the two clutter fields. (These parameters are the mean and variance of the Normal distribution describing the natural logarithm of the envelope detected output of the sampled clutter field.)

An alternate CFAR technique [3],[4] for accommodating the two clutter fields spanning the N threshold control cells simply involves estimating the residual clutter level on each side of the cell under test, and using the greatest of these two estimates to set the detection threshold. While this procedure works well in controlling the false alarm rate when the clutter field at the edge has a lower clutter level than the clutter field encompassing the cell under test, it is not designed to overcome the significant target masking effect which results when the cells at the edge are in a clutter field with a higher clutter backscattering level than the clutter field in which the cell under test is embedded.

2. FORMULATION OF THE HETEROGENEOUS CLUTTER ESTIMATING CFAR FOR RAYLEIGH DISTRIBUTED CLUTTER

2.1 DEVELOPMENT OF THE UNBIASED VERSION OF THE HCE-CFAR DESIGN

A flow chart outlining the computational steps needed to effect an unbiased version of the HCE-CFAR test for Rayleigh distributed clutter is presented in Fig. 2.

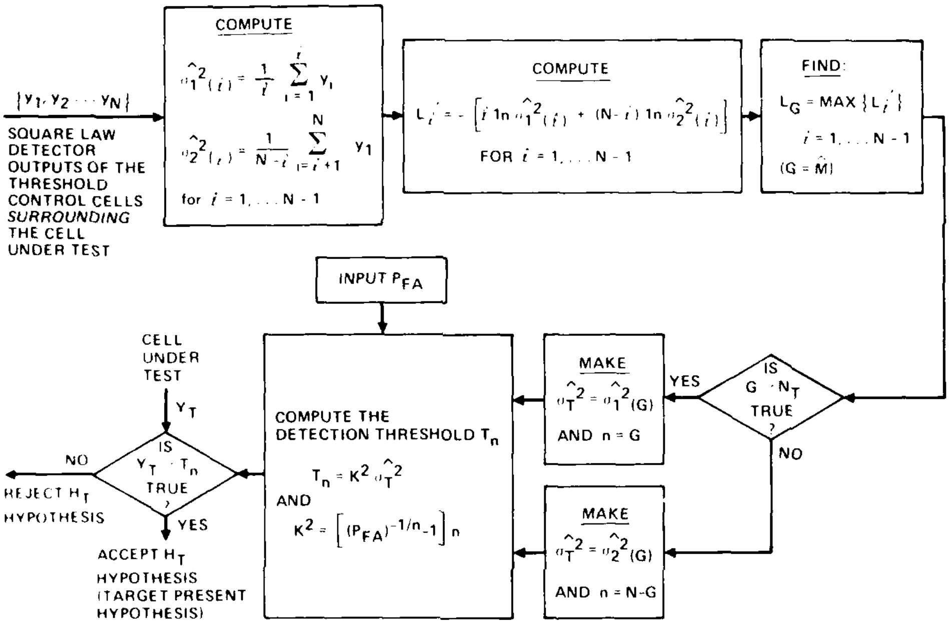

FIGURE 2 FLOW CHART OF A HETEROGENEOUS CLUTTER ESTIMATING CFAR FOR RAYLEIGH DISTRIBUTED CLUTTER UNBIASED VERSION

The N contiguous and sampled resolution cell envelope detected outputs of the sliding window y_i, i = 1,...,N are assumed to span two different clutter backscattering media. The transition from one clutter field to another takes place after the Mth resolution cells, and for i ≤ M, $\sigma_i^2 = \sigma_1^2$; and for i > M, $\sigma_i^2 = \sigma_2^2$. The heterogeneous clutter estimator involves finding estimates of σ_1^2 and σ_2^2 and the transition cell (M) based on the set of observables y_i. The development starts with the formation of the likelihood

$$L(y_{1,2},\ldots,y_N/H_{\ }) = \prod_{i=1}^{N} \exp\left[\left(\frac{-y_i}{\sigma^2_{i(\ )}}\right)\right]\frac{1}{\sigma^2_{i(\ )}} \qquad (1)$$

where H is the hypothesis that the transition of the two clutter fields takes place after the th cell. (There are N-1 hypotheses of where the transition occurs within the span of the N cells with observed outputs $\{y_i\}$). For the th hypothesis, the maximum likelihood estimates $\sigma^2_{1(\ )}$, and $\sigma^2_{2(\ )}$ are determined from the equations

$$\frac{\partial \ln L}{\partial\sigma^2_{1(\ )}} = 0 \qquad (2) \qquad \text{and} \qquad \frac{\partial \ln L}{\partial\sigma^2_{2(\ )}} = 0 \qquad (3)$$

The estimates, $\sigma^2_{1(\ )}$ and $\sigma^2_{2(\ )}$, are formulated in Fig. 2. Substituting $\sigma^2_{1(\ )}$ and $\sigma^2_{2(\ )}$ in the expression for ln L, maximizes this likelihood function for the H hypothesis. Eliminating the constant term N in ln L, yields L' (see Fig. 2) which is a monotonically related expression to the maximized likelihood L. The estimate of the sampled clutter fields may now be determined. The estimate of the transition cell M is defined as the Gth cell, and H_G is any one of the hypotheses $\{H\}$ which maximize the likelihood expression, or

$$L'_G = \text{Max}\,\{L'_i\} \qquad i = 1,2,\ldots,N-1 \tag{4}$$

The corresponding estimates σ_1^2 and σ_2^2 are

$$\sigma_{1(G)}^2 = \frac{1}{G}\sum_{i=1}^{G} y_i \quad (5) \qquad \text{and} \qquad \sigma_{2(G)}^2 = \frac{1}{N-G}\sum_{i=G+1}^{N} y_i \tag{6}$$

Thus, a complete description of the sampled clutter fields has been achieved. The estimated field partition point (after the G^{th} cell) is then compared with the position of the cell under test (N_T) in order to determine the relevant clutter field for the CFAR test (i.e., the one which has the cell under test embedded in it), and, also the number (n) of statistically independent samples of the clutter field employed in making the estimate σ_T^2. The alternate hypothesis test for the presence or absence of a target return in the cell under test involves a comparison of the test cell output y_T with the threshold $K^2\sigma_T^2$. The threshold proportionality constant K^2 is determined for a specified single cell false alarm probability P_{FA}. If the estimate of the partition point between the two fields was exact, then the false alarm probability expression developed in Ref. [2] would apply

$$P_{FA} = \left[\frac{1}{1+\frac{K^2}{n}}\right]^n \tag{7}$$

with the number of cells n interpreted as in the preceding discussion and yielding the expression of K^2 presented in Fig. 2.

In this manner, if the partitioning point of the two clutter fields spanned by the N *threshold control cells is accurately estimated*, the false alarm probability will be close to the design value.

Only a single frame of the N resolution cells sampling the clutter fields has been assumed to be available for the HCE-CFAR formulated here. If, in fact, N_F statistically independent frames of the N resolution cell outputs *are available for* use in the HCE-CFAR design, the number of statistically independent samples in each resolution cell is increased from unity to N_F, and the values, for example, of G, N and n in the presented equations must now each be multiplied by the number N_F.

2.2 BIASED VERSION OF THE HCE-CFAR DESIGN

The unbiased HCE-CFAR design described in the preceding section involves giving equal weights to each of the hypotheses of where the transition from one field to another takes place. However, to make the HCE-CFAR concept provide a satisfactory control of the false alarm rate, especially when only a single carrier frequency is employed, it is necessary to 'bias' the multiple hypothesis test in favor of the hypothesis that the cell under test is embedded in the more intense clutter field.

The rationale for the biased version of the test is made clear by viewing (see Fig. 3) the cases of the cell under test being in the more and less intense clutter fields and the consequence of transition point estimating errors for each case. In both cases, the transition point error can erroneously 'place' the cell under test in the wrong clutter field. When the cell under test is in the more intense clutter field (the upper sketch), an error placing it in the less intense clutter field will yield a highly probable false alarm event, causing an increased false alarm rate. On the other hand, the reverse situation, (depicted in the lower sketch) yields a highly probable false dismissal (or target masking) event, which does not appreciably affect the overall detection probability. Since CFAR control is, typically, of paramount concern, the test is biased towards a regulation of the *false alarm probability at the expense of some masking events* but with the target detection performance still substantially better than that obtained with the conventional cell averaging CFAR for the same non-uniform clutter fields.

The desired modification is effected by introducing a test of the alternate hypotheses of whether the cell under test is *in the more intense clutter field or not* and 'biasing' this alternate hypothesis test in the direction of accepting the hypothesis that the cell under test is in the more intense clutter. (The test is designated here as the [illegible](+)/[illegible](-) test.) The developed alternate hypothesis test is again based on the use of the observed square law detected outputs of the N surrounding threshold control cells and involves computing the ratio of the maximum likelihood that the cell under test is in the *more* intense clutter field to the maximum likelihood that it is not. The ratio of these maximum likelihoods is then compared to a fixed number, and if greater than or equal to the constant, the more intense clutter field hypothesis is accepted, and the clutter field estimates used in developing the maximum likelihood under the hypothesis that the cell under test is in the more intense clutter are used in establishing the threshold. If the ratio is not greater than the constant, then the estimates of the clutter field yielding the maximum likelihood under the hypothesis that the cell under test is in the less intense clutter field are employed in the threshold control procedure. The 'bias' to the test is introduced by setting the constant to a value less than unity. Since logarithms of these

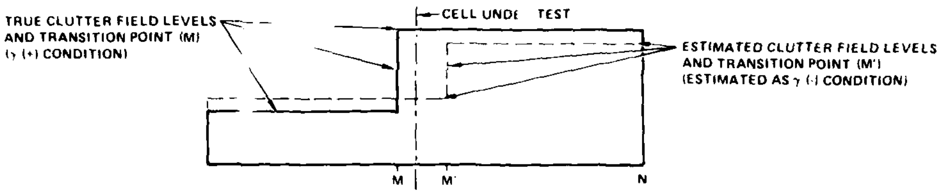

RESULTS IN A TOO LOW ESTIMATE OF THE CLUTTER LEVEL (AND REQUIRED THRESHOLD) FOR THE CELL UNDER TEST – YIELDS A HIGHLY PROBABLE FALSE ALARM EVENT.

– CAN SIGNIFICANTLY DEGRADE CFAR PERFORMANCE –

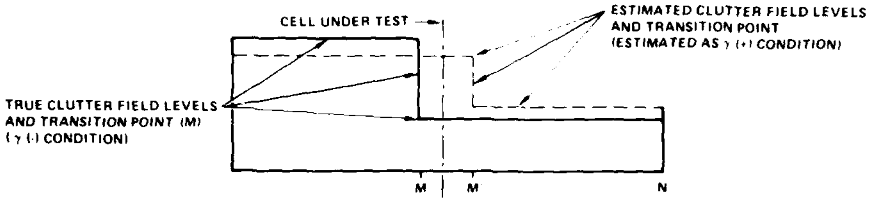

RESULTS IN A TOO HIGH ESTIMATE OF THE CLUTTER LEVEL (AND THE REQUIRED THRESHOLD) FOR THE CELL UNDER TEST – YIELDS A HIGHLY PROBABLE FALSE DISMISSAL (TARGET MASKING) EVENT.

– MORE BENIGN EFFECT ON OVERALL DETECTION PROBABILITY –

FIGURE 3 SKETCH OF CLUTTER FIELD ESTIMATING ERROR EVENTS (WHEN THE TRANSITION POINT OCCURS NEAR THE CELL UNDER TEST) YIELDING FALSE REPORTS IN THE HCE CFAR DESIGN. (RATIONALE FOR THE $\gamma(+)/\gamma(-)$ 'BIASING' HYPOTHESIS TEST, AND MULTIPLE FREQUENCY OPERATION.)

maximum likelihoods are employed in the development, the ratio becomes a difference of the two likelihood quantities, and the constant value less than one becomes a negative number. [Since the introduction of such an added biasing test, in effect, distorts the estimate of the encountered non-uniform clutter field, it would not be included in a clutter 'mapping' function of the radar.]

A flow chart describing the development of this alternate hypothesis test of where the cell under test is located--the more or less intense clutter field, and how it is employed in the CFAR test is presented in Fig. 4. The CFAR procedure described in the flow chart of Fig. 4 also includes the alternate hypothesis test of whether the N threshold control cells are sampling one uniform clutter field or two completely independent clutter fields. If the one field hypothesis is accepted, then the detection procedure reverts to the simple cell averaging CFAR procedure. [This test is designated here as the U/H test.] If the two field hypothesis is accepted, then the alternate hypothesis test of whether the target cell is in the more or less intense clutter field is conducted.

If the thresholds of the $\gamma(+)/\gamma(-)$ and U/H alternate hypothesis tests are set to unity, (or zero for the logarithmic versions), then the HCE-CFAR design reverts to the unbiased version described in Sec. 2.1 and the flow chart of Fig. 2, with the uniform clutter field hypothesis (the transition point at M=0) added to the N-1 hypotheses of where the transition between the two clutter fields takes place.

Moreover, while the subject 'biasing' tests are formally introduced here as the addition of separate alternate statistical hypothesis tests, they can also be interpreted and implemented by applying the appropriate weights to the multiple hypothesis maximum likelihood heterogeneous clutter field estimation procedure descrited in Sec. 2.1 and the flow chart of Fig. 2.

3. DERIVING PERFORMANCE DATA FOR THE HCE-CFAR AND 'CELL AVERAGING' CFAR WHEN BOTH ARE OPERATING IN THE SAME NON-UNIFORM CLUTTER ENVIRONMENT

3.1 HCE-CFAR EVALUATION METHOD

In Sec. 4, a performance evaluation of the biased version of the HCE-CFAR (described in Sec. 2.2) is presented. The evaluation involves a comparison with the conventional cell averaging CFAR design when both are operating in the same 'split field' Rayleigh distributed clutter environment, and the target to be detected is modeled as a Swerling Case #1 Type.

For the inputed partitioned two-clutter field statistically defined environment, embraced by the N threshold control cells, each replication involves the generation of the

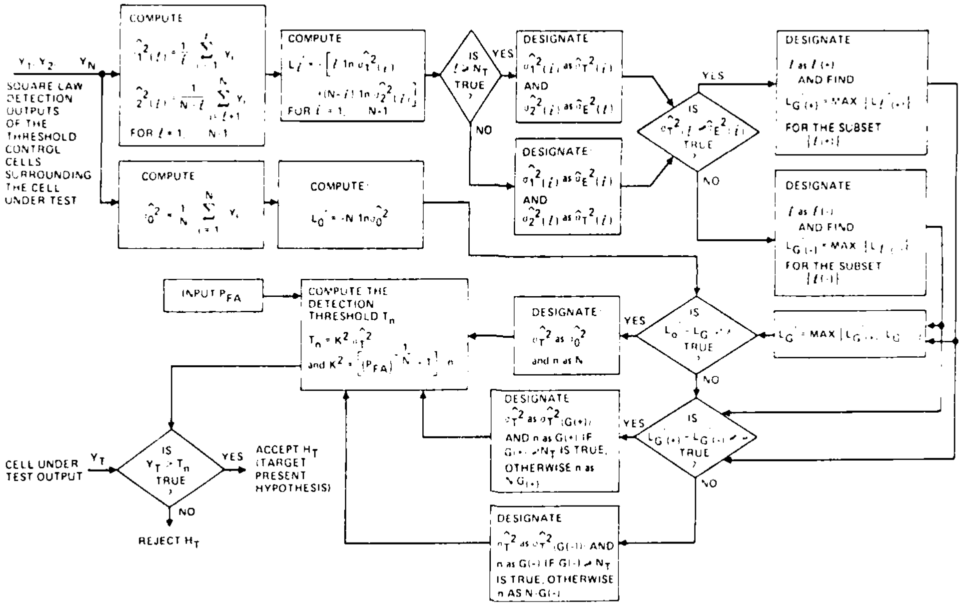

FIGURE 4. FLOW CHART OF A HETEROGENEOUS CLUTTER ESTIMATING CFAR FOR RAYLEIGH DISTRIBUTED CLUTTER WITH INCORPORATED LIKELIHOOD RATIO TESTS FOR THE ALTERNATE HYPOTHESES: UNIFORM VS NON-UNIFORM CLUTTER; AND IF NON-UNIFORM, WHETHER THE TARGET CELL IS IN THE MORE OR LESS INTENSE CLUTTER FIELD

$N(N_F)$ statistically independent Rayleigh distributed envelope detected outputs of the N threshold control cells spanning the two clutter fields and the N_F frames each assumed to be developed at a different carrier frequency and yielding statistically independent sets of N returns. The heterogeneous clutter field estimating CFAR procedure, as outlined in Sec. 2.2 and Fig. 4, is then employed to determine the estimate (σ_T^2) and the number n of samples employed in sampling what is 'tagged' to be the relevant clutter field. The threshold $T = K^2 \sigma_T^2$ is computed with the value of K^2 determined, as decribed in Sec. 2.2 as a function of both the inputed design false alarm probability and the number of samples n used in estimating σ_T^2 on that replication. The computed threshold T for each replication is then used to determine, analytically, a conditional probability of false alarm and detection on the hypothesis that the computed threshold is T. For the single variate detection of a Rayleigh distributed target (Swerling Case #1) with a received signal to noise ratio of $\bar{X}$, the conditional detection probability is expressed as

$$P'_D = \exp\left[-\frac{T}{\sigma_T^2(1+\bar{X})}\right] \tag{8}$$

and the corresponding value of the single cell false alarm probability

$$P'_{FA} = \exp\left[-\frac{T}{\sigma_T^2}\right] \tag{9}$$

with σ_T^2 defined as the inputed true value of the statistical parameter (σ^2) of the clutter field with the test cell embedded in it. The final estimate of P_D and P_{FA} are obtained by taking the average over all replications of the defined P'_D and P'_{FA} obtained on each replication.

The P_D and P_{FA} of the HCE-CFAR, when operating with the two Rayleigh fields spanning the window, are independent of the clutter level σ_T^2 of the cell under test, but can be a function of the clutter parameters, M and γ. ($\gamma = \frac{\sigma_T^2}{\sigma_E^2}$ and σ_E^2 is the Rayleigh parameter for the output of a cell in the edge field.) Therefore, the performance evaluation is conducted as a function of M and γ. The HCE-CFAR is exactly a CFAR detector when only one homogeneous Rayleigh distributed field spans the window. For this case, M has the value of zero and γ of one. (The HCE-CFAR detection efficiency relative to that of a cell averaging CFAR for this one field case is also presented in Sec. 4.)

3.2 CELL AVERAGING CFAR EVALUATION METHOD

Using the analysis procedure of Ref. 2 (Appendix 5) (applied for the Swerling Case #3 Target Type), it is easy to show for the Swerling Case #1 Target Type, that the detection probability of a cell averaging CFAR for the situation when the N sampled cells span two different Rayleigh clutter fields may be expressed as

$$P_D = \frac{\left[\frac{\iota}{\iota + \iota}\right]}{(1+\iota)^{N-M}} \qquad (10) \qquad \text{with} \qquad \iota = \frac{K^2}{N(1+\bar{X})} \qquad (11)$$

($\bar{X}$ is the signal to noise ratio.) From Eq. (10), the corresponding expression for the single cell false alarm probability can be obtained by setting $\bar{X}$ equal to zero yielding

$$P_{FA} = \frac{\left[\frac{\iota}{\iota + \frac{K^2}{N}}\right]^M}{\left(1 + \frac{K^2}{N}\right)^{N-M}} \qquad (12)$$

Equations (10) and (12) express cell averaging CFAR performance for the case when a single frame of N resolution cell samples of the clutter fields is used to estimate the clutter level and set the threshold. When more than one statistically independent frame of the N cell outputs is employed for this function (say, N_F frames), then the value of N in these equations must be replaced by the product of N and N_F, and similarly the value of M must be replaced by the product of M and N_F.

4. PERFORMANCE EVALUATION OF THE HETEROGENEOUS CLUTTER ENVIRONMENT CFAR

Detection and false alarm probabilities for a wide domain of the modeled non-uniform clutter conditions are presented for three representative HCE-CFAR designs and corresponding cell average CFAR designs. (See Figs. 5 through 12.) In general, the HCE-CFAR designs are noted to overcome the performance degradations--target masking and increased false alarm rates--experienced by the cell averaging CFAR when encountering the non-uniform clutter environment. If ι is defined as the ratio, expressed in dB, of the clutter level of the cell under test to the level existing at the edge, it is noted that for *positive* ι's,--the condition of the cell under test being in the more intense clutter--the cell averaging CFAR false alarm probability *increases* unacceptably from its design value, especially at the value of positive ι becomes large and as the transition point M between the two fields approaches the cell under test. On the other hand, each of the three illustrated heterogeneous clutter estimaging CFAR designs are noted to effect a control of the false alarm probability for the same encountered non-uniform clutter conditions.

When the cell averaging CFAR encounters a clutter field of negative ι (i.e., when the clutter field at the edge of the threshold control cells are in the more intense clutter than the clutter field encompassing the cell under test), the detection probability is

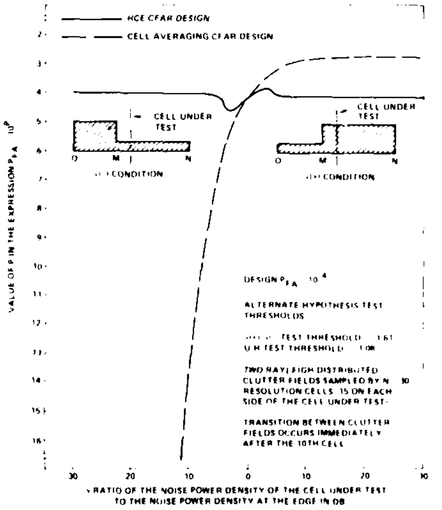

FIGURE [illegible]. AN HCE CFAR DESIGN BASED ON FOUR STATISTICALLY INDEPENDENT FRAMES OF THE SAMPLED CLUTTER FIELDS SINGLE CELL FALSE ALARM PROBABILITY P_{FA} AS A FUNCTION OF THE RATIO OF CLUTTER LEVELS FOR A FIXED TRANSITION POINT BETWEEN THE CLUTTER FIELDS (M = 10)

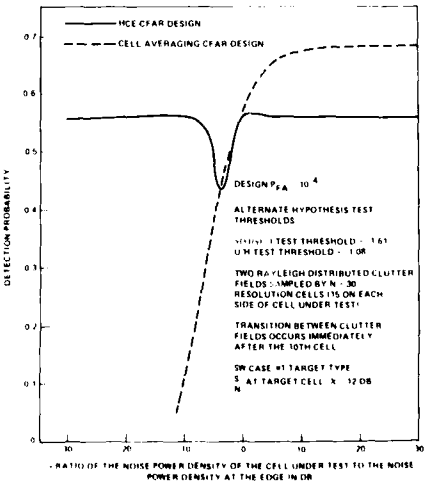

FIGURE [illegible]. AN HCE CFAR DESIGN BASED ON FOUR STATISTICALLY INDEPENDENT FRAMES OF THE SAMPLED CLUTTER FIELDS [illegible] DETECTION PROBABILITY AS A FUNCTION OF THE RATIO OF CLUTTER LEVELS FOR A FIXED TRANSITION POINT BETWEEN THE CLUTTER FIELDS (M = 10)

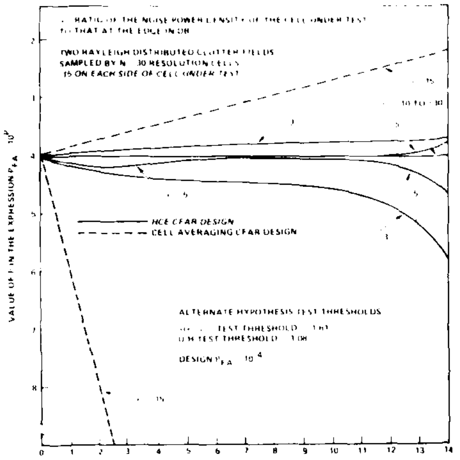

[illegible] AN HCE-CFAR DESIGN BASED ON FOUR STATISTICALLY INDEPENDENT FRAMES OF THE SAMPLED CLUTTER FIELDS [illegible] FALSE ALARM PROBABILITY (P_{FA}) AS A FUNCTION OF THE TRANSITION POINT M BETWEEN THE CLUTTER FIELDS WITH THE RATIO OF CLUTTER LEVELS AS A FIXED PARAMETER

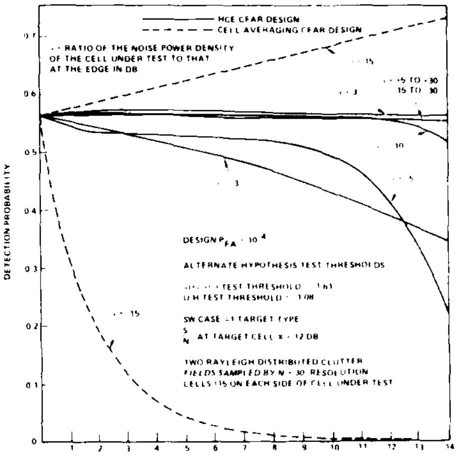

[illegible] AN HCE-CFAR DESIGN BASED ON FOUR STATISTICALLY INDEPENDENT FRAMES OF THE SAMPLED CLUTTER FIELDS DETECTION PROBABILITY AS A FUNCTION OF THE TRANSITION POINT M BETWEEN THE CLUTTER FIELDS WITH THE RATIO OF CLUTTER LEVELS AS A FIXED PARAMETER

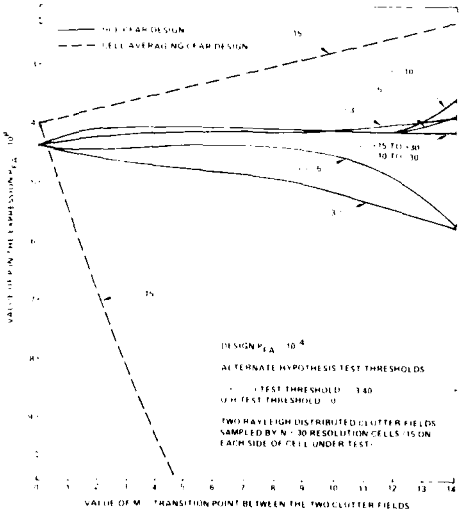

[illegible] AN HCE-CFAR DESIGN BASED ON TWO STATISTICALLY INDEPENDENT FRAMES OF THE SAMPLED CLUTTER FIELDS SINGLE [illegible] FALSE ALARM PROBABILITY (P_{FA}) AS A FUNCTION OF THE TRANSITION POINT M WITH THE RATIO OF CLUTTER LEVELS AS A FIXED PARAMETER

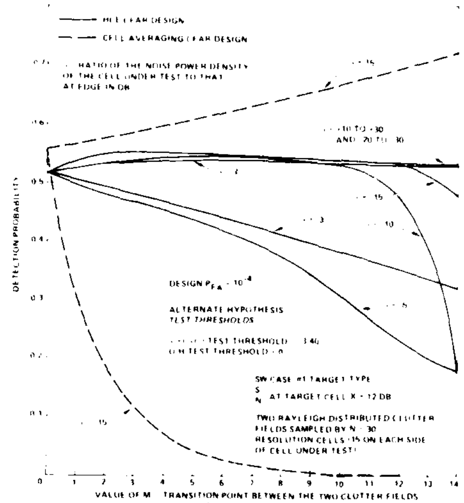

FIGURE 10 AN HCE-CFAR DESIGN BASED ON TWO STATISTICALLY INDEPENDENT FRAMES OF THE SAMPLED CLUTTER FIELDS DETECTION PROBABILITY AS A FUNCTION OF THE TRANSITION POINT M BETWEEN THE CLUTTER FIELDS WITH THE RATIO OF CLUTTER LEVELS AS A FIXED PARAMETER

drastically reduced with targets essentially completely masked for a wide domain of non-uniform clutter conditions. Conversely, the representative HCE-CFAR designs when encountering the same non-uniform clutter environments maintain a relatively good detection capability for most of the non-uniform clutter fields considered (see Figs. 6, 8, 1 and 12). [The relatively high detection probabilities of the cell averaging CFAR, when encountering a positive non-uniform clutter condition, is achieved at the expense of unacceptable large increases in the false alarm probability over the design value.]

Each of three representative HCE-CFAR designs involves the use of a different number of statistically independent frames of the sampled non-uniform clutter fields. A single, two, and four-carrier frequency design are represented. For the multiple frequency design, the incremental change in carrier frequency from one transmission--or group of transmissions in the MTI radar case--to another is assumed to yield statistically independent clutter returns, but with no perturbation of the underlying statistical parameters.

An intuitively satisfying result is that of the three presentative HCE-CFAR designs presented, the best performing one (see Figs. 5 through 8) is the one based on the most frequencies of operation (or statistically independent frames of data) namely four. The second best performing design (see Figs. 9 and 10) involves the two frequency operation

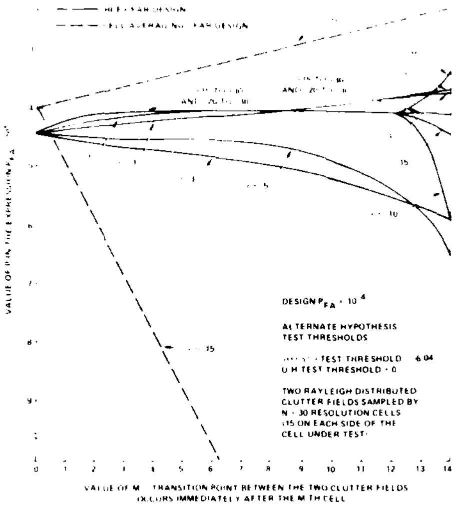

[illegible] FAR DESIGN BASED ON A SINGLE FRAME OF THE SAMPLED CLUTTER FIELDS [illegible] FALSE ALARM PROBABILITY (P_{FA}) AS A FUNCTION OF THE TRANSITION POINT (M) WITH THE RATIO OF THE CLUTTER LEVELS AS A FIXED PARAMETER

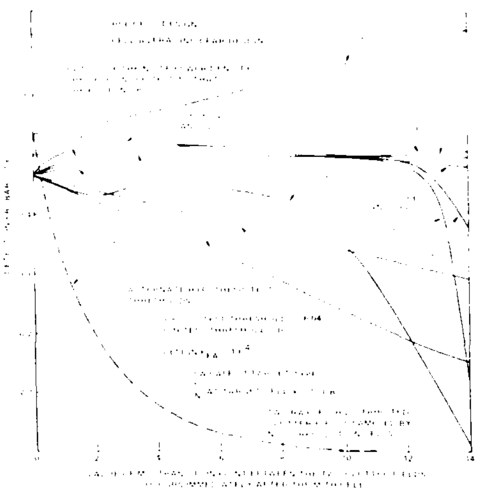

[illegible]

case. Obviously, as the number of statistically independent frames of the N cells sampling the non-uniform clutter field increases, a more accurate estimate can be made of the encountered non-uniform clutter field, leading to a more effective HCE-CFAR design. A view of the RMS and mean errors made in the estimation of the transition point between the two clutter fields (Figs. 13 and 14) also illustrates this behavior. A significant reduction in these errors is noted to take place when the number of statistically independent frames of data is increased. Since in many radar applications, frequency hopping is employed, any way, to force a decorrelation of the target and clutter returns for improved detection, the additional frames of statistically independent clutter returns may be available for use in an HCE-CFAR design.

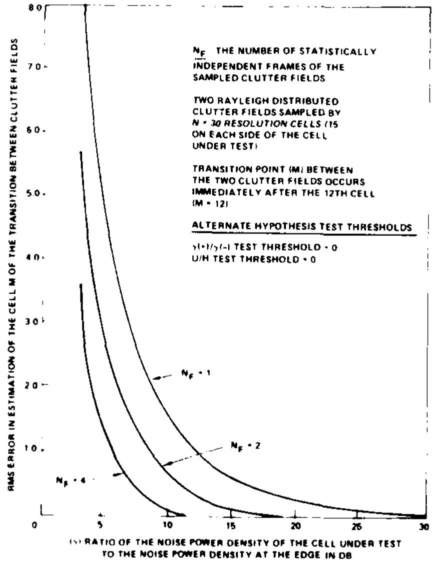

FIGURE 13. RMS ERROR OF THE CLUTTER FIELD TRANSITION POINT (M) ESTIMATE AS A FUNCTION OF THE RATIO OF THE CLUTTER LEVELS OF THE TWO CLUTTER FIELDS

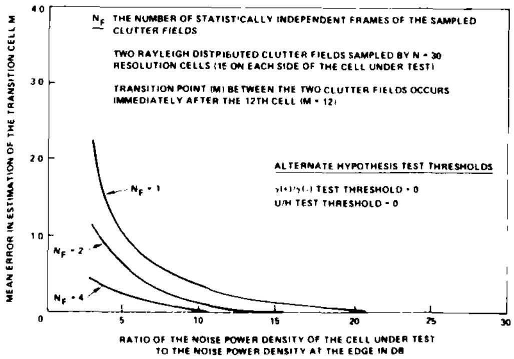

FIGURE 14. MEAN ERROR OF THE CLUTTER FIELD TRANSITION POINT (M) ESTIMATE AS A FUNCTION OF THE RATIO OF THE CLUTTER LEVELS OF THE TWO CLUTTER FIELDS

The transition point estimated errors are also noted (see Figs. 13 and 14) to rapidly decrease as the absolute value of , increases. (The more marked the jump in clutter levels at a transition point, the easier it is to 'see' the transition point and accurately estimate it.) This behavior should result in better performance of the HCE-CFAR design for large values of .. And, in fact, the best performance for each of the three designs is noted to be obtained at the largest positive and negative values of . for which the detection and false probabilities were determined (± 30 dB). On the other hand, the performance of the cell averaging CFAR is noted to degrade rapidly as the absolute value of . increases, and exhibits its worst performance at these largest values of ..

The detection performance in uniform clutter of the HCE-CFAR designs and the corresponding cell averaging CFAR designs is obtained for the case of M--the transition point--made equal to zero. For the four frequency HCE-CFAR design, the detection efficiency in uniform clutter is determined to be within .048 dB of that achievable with a four frequency cell averaging CFAR design. The additional CFAR loss of the two and one frequency HCE-CFAR designs relative to that of corresponding two and one frequency HCE-CFAR designs is 0.58 dB and 0.85 dB respectively. In uniform clutter, the HCE-CFAR designs are also shown to be exactly CFAR in performance.

When the performance is presented of an HCE-CFAR design based on the use of multiple statistically independent frames of data--assumed to be achieved by multiple frequency operation, the accompanying cell averaging CFAR performance is based on the use of the same number of frequencies. However, only a single statistically independent target sample is employed in the computation of the detection probability for the multiple frequency HCE-CFAR and cell averaging CFAR designs. Consequently, these multiple frequency results are applicable for the evaluation of each stage of an M of N detection scheme. N transmissions, each at a different carrier frequency are assumed, the received data in each resolution cell are stored, and the detection decision at each stage is deferred until the HCE-CFAR thresholds based on the N statistically independent frames of clutter return data are received.

5. HETEROGENEOUS CLUTTER ESTIMATING CFAR APPLIED TO LOG-NORMALLY DISTRIBUTED CLUTTER

The case of log-normally distributed clutter is used to illustrate the application of the HCE-CFAR concept to a two-parameter distributed clutter. A flow chart summarizing the steps involved is presented in Fig. 15. The spatial sampling of the encountered clutter is assumed to encompass two different homogeneous clutter fields but with each one log-normally distributed, and with the cell under test embedded within one of the two clutter fields. The approach again involves estimating the statistical parameters of the two clutter fields sampled and the transition point between these fields, and then to use the statistical parameter estimates of the relevant clutter field (the one in which the target cell is embedded) to make the CFAR detection test.

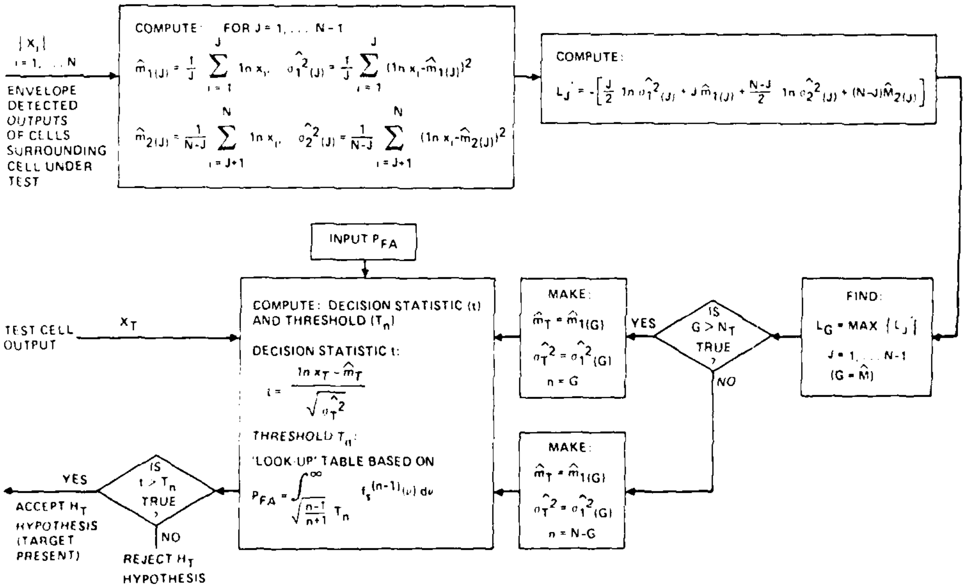

FIGURE 15 FLOW CHART OF A HETEROGENEOUS CLUTTER ESTIMATING CFAR FOR LOG-NORMALLY DISTRIBUTED CLUTTER

The heterogeneous clutter estimating procedure is developed in a manner similar to that used for the Rayleigh distributed fields. The observables are the N envelope detected outputs $\{X_i\}$ which are employed in the threshold control procedure. For each x_i, the probability density function

$$f(X_i)dx_i = \frac{1}{\sigma_i x_i \sqrt{2\pi}} \exp\left[-\frac{(\ln x_i - m_i)^2}{2\sigma_i^2}\right] dx_i \quad . \qquad (13)$$

The subject CFAR procedure involves first obtaining maximum likelihood estimates of $m_1, \sigma_1^2, m_2, \sigma_2^2$, and the transition cell M. H_J is the hypothesis based on the set of the N observables that the transition takes place after the J^{th} cell. There are N-1 such hypotheses, and for each one, the set of maximum likelihood parameter estimates $(m_{1(J)}, \sigma_{1(J)}^2; m_{2(J)}, \sigma_{2(J)}^2)$ are generated. They are formulated in Fig. 15. The estimates $(m_{1(J)}, \sigma_{1(J)}^2; m_{2(J)}, \sigma_{2(J)}^2)$ are then used to compute the set $\{L_J'\}$. L_J' can be shown to be monotonically related to the maximum of the likelihood on the condition of the H_J hypothesis and is expressed in Fig. 15. The maximum of the set $\{L_J'\}$ is now found

$$L_G' = \underset{J = 1,\ldots,N-1}{\mathrm{Max}} \left\{L_J'\right\}$$

G then becomes the estimate of the M^{th} transition cell (G=M), and H_G is any one of the hypothesis $\{H_J\}$ which yields a maximum of the set $\{L_J'\}$. Consequently, clutter field #1, with parameter estimates $m_{1(G)}$ and $\sigma_{1(G)}^2$, is estimated to extend from the first cell to the G^{th} cell, and clutter field #2 with the statistical parameter estimates $m_{2(G)}$ and $\sigma_{2(G)}^2$ is estimated to embrace the cells from the G+1 cell to the N^{th} cell. The relevant estimated clutter field for use in the illustrated CFAR test statistic is the one in which the cell under test (X_T) is embedded. The decision statistic (t) for this heterogeneous clutter estimating log-normal CFAR test (see Fig. 15) was introduced earlier [5] for effecting CFAR operation in a homogeneous log normally distributed clutter environment.

This formulation of the HCE-CFAR test for log-normally distributed clutter involves the application of an unbiased multiple hypothesis test. Just as the HCE-CFAR designs for Rayleigh distributed clutter were determined to yield improved performance with the addition of 'biasing' alternate statistical hypothesis tests of the $\gamma(+)/\gamma(-)$ and U/H type, it is anticipated that similar biasing tests added to the presented log-normal HCE-CFAR test would also lead to improved performance.

REFERENCES

1. Finn, H. M., "Adaptive Detection in Clutter," Proc. National Electronics Conference, Vol. XXII, 1966, page 562.

2. Finn, H. M., and R. S. Johnson, "Adaptive Detection Mode with Threshold Control as a Function of Spatially Sampled Clutter-Level Estimates," RCA Review, Vol. 29, No. 3, page 414.

3. Hansen, V. G., "Constant False Alarm Rate Processing in Search Radars," Proc. of IEEE 1972 International Radar Conference, London, 1973.

4. Hansen, V. G. and J. H. Sawyers, "Detectability Loss Due to Greatest of Selection in a Cell Averaging CFAR," IEEE Trans. of Aerospace and Electronic Systems, Jan. 1980, AES-16, page 115.

5. Goldstein, G. B., "False Alarm Regulation in Log-Normal and Weibull Clutter," IEEE Transactions on Aerospace and Electronic Systems, Vol. AES-9, Jan. 1973, page 84.

ACKNOWLEDGMENT

The competent and dedicated efforts of Mr. Chester Stone in developing all of the computer programs employed in the conducted evaluations is gratefully acknowledge. The reviews of the paper and insightful comments of Dr. Lawrence Brennan and Dr. Allan Tarbell are also very much appreciated.

DISCUSSION

W.L.Simkins

Can you provide a qualitative assessment of how sensitive your technique is to the assumption that the two fields have the same statistics but 2 different means? That is, if the first field was Rayleigh and the second field was non-Rayleigh, how would the CFAR performance change as the second field's statistics increasingly deviated from Rayleigh?

Author's Reply

The HCE-CFAR design has been configured to date for the case where both independent fields within the sliding window are each single parameter distributed (Rayleigh); and also for the case where both clutter fields within the window are two-statistical parameter distributed. This latter HCE-CFAR design also applies to Weibull distribution clutter.

For the case of the HCE-CFAR designed for Rayleigh distributed clutter, I believe there could be substantial degradation of performance if one of the fields is two-parameter distributed — especially if it is the field with the test cell embedded *in* it. On the other hand, the HCE-CFAR designed for 2-parameter distributed clutter, since it is applicable to Weibull distributed clutter, could accommodate the case where one field is Rayleigh distributed and the other field is Weibull distributed, since the Rayleigh distribution is one case of the Weibull distribution. This test is an inefficient one, however, if both fields are Rayleigh distributed. So that, if the question is one of real practical interest, perhaps the latter approach would be to further develop the HCE-CFAR concept to accommodate the field differences described.

A.Biggs

The view-foils indicate results of heterogeneous clutter which were not in the AGARD pre-print. Can you include these as part of the discussion phase which will appear in the finalized copy of the AGARD proceedings?

Author's Reply

I believe that the pre-print of the paper contains all of the HCE-CFAR performance results, and that no new results were presented in the talk. A fuller presentation of the results and analytical development is scheduled for publication in the IEEE Proceedings of Aerospace and Electronics.

C.Boesswetter

Is there any connection between the theory of design for CFAR systems and *radiometric resolution*, which is one of the important design parameters for imaging radar antenna, to separate between two distributed clutter fields?

Author's Reply

The theory which I presented is mainly for target detection. However, it could probably also be applied for imaging clutter fields.

HIGH-RESOLUTION MTI WITH SAR

Dr. A. Freeman
Marconi Research Centre
West Hanningfield Road
Great Baddow
Chelmsford
Essex. CM2 8HN. England.

ABSTRACT:

Moving Target Imaging (MTI) using Synthetic Aperture Radar (SAR) offers considerable potential as an all-weather surveillance tool, monitoring the movement of vehicles on the ground. The purpose of the work described in this paper is to investigate techniques of producing high-resolution images of such moving objects using the radar signals received by an existing airborne SAR system.

The first step in the MTI Method adopted is the production of a rather crude image of such moving targets as exist in the data. This can be achieved by application of a simple prefilter (for clutter-cancellation prior to the conventional azimuth (doppler) processing. The image can then be used for initial detection of the targets. In such images, well-behaved moving targets are distorted by their motions in a particular manner and the parameters of the target motions can be estimated from their shape and other properties. These parameters are measured and then used to construct a 2-dimensional filter 'matched' to the response for each target, for use in the azimuth (doppler) processing. This technique can be shown to produce high-resolution images of the moving targets with the resolution being comparable to that of the conventional airborne SAR images of the ground.

A SEQUENTIAL ADAPTATION TECHNIQUE
AND ITS APPLICATION TO THE MARK XII IFF SYSTEM

John S. Bailey
John D. Mallett
Adaptive Sensors, Incorporated
216 Pico Boulevard, Suite 8
Santa Monica, California 90405

Duane J. Sheppard
F. Neal Warner
USAERADCOM
CS&TA Laboratory
Fort Monmouth, New Jersey 07703

Robert Adams
Technology Service Corporation
2950 31st Street
Santa Monica, California 90405

SYNOPSIS

Sequential adaptation uses only two sets of receivers, correlators, and A/D converters which are time multiplexed to effect spatial adaptation in a system with (N) adaptive degrees of freedom. This technique can substantially reduce the hardware cost over what is realizable in a parallel architecture.

A three channel L-band version of the Sequential Adapter was built and tested for use with the MARK XII IFF system. In this system the sequentially determined adaptive weights were obtained digitally but implemented at RF. As a result, many of the post RF hardware induced sources of error that normally limit cancellation, such as receiver mismatch, are removed by the feedback property. The result is a system that can yield high levels of cancellation and be readily retrofitted to currently fielded equipment.

SEQUENTIAL ADAPTATION TECHNIQUES

Identification and Significance of the Problem

Military communication systems can be severely degraded by enemy jamming or, in some cases, by unintentional interference. Adaptive antennas are used in some communication and radar systems to automatically place nulls *at the angles of jammers* or interference sources. When N jammers are present, at least N adaptive degrees of freedom are required to provide N simultaneous nulls. The cost and complexity of a conventional adaptive nulling system increases with the number of degrees of freedom.

It is also important to minimize the cost and complexity of future systems. One possible method of simplifying these systems is to use a sequential algorithm for updating one adaptive weight at a time, i.e., multiplexed control of N weights using a single circuit for adaptive weight computation.

Technical Objectives

Adaptive Sensors, Inc. and its subcontractor, Technology Service Corporation, have had two major contracts to explore utilizing a Least Mean Square algorithm and multiplexed control of several adaptive weights using a single circuit for weight updating. Three important problems arise in designing a system with these properties, viz.:

a. Configuration of the LMS system. In an LMS adaptive system, the weights on antenna elements are controlled to achieve a least mean square match between the array output and some reference signal. The specific reference signal used varies from system to system. If a pilot signal is transmitted by the source during some time interval, and both the temporal structure and timing of the pilot are known at the receiving site, this pilot signal can be generated locally and used for array lock-up. This is the basic LMS array concept originally described by Widrow[1]. Its time multiplexed sequential version is depicted in Fig. 1.

In some systems the reference signal at the receiving array can be set to zero and the array adapted to minimize the output power. This technique can be used during the adaptation interval if the desired source is turned off for intervals known *a-priori* at the receiving site. The experimental test bed is an example of such a system. In some systems using spread spectrum coding with a large ratio of signal bandwidth to information bandwidth, the desired signal is so small that a zero pilot signal can be used for adaptation. The Global Positioning System fits into this category.

b. Convergence Rate in a Sequentially Adapted Array. When a single weight computing circuit is used to sequentially update several weights in an adaptive nulling system, some slowing of convergence to a good adaptive antenna pattern must be expected. Systems in which N separate weighting circuits are used to compute the N weights will generally provide faster adaptation. ASI investigated the convergence rate in a sequentially adapted system for a variety of configurations and numbers of jammers. The worst case convergence time increases by a factor approximately equal to the number of channels multiplexed over what would be obtained with a parallel LMS architecture.

c. Method of Computing Updated Weights. In an adaptive array with N adaptive weights which are updated in sequence, using a single multiplexed weight computing circuit, a variety of different methods can be used to obtain the weights. These include both analog

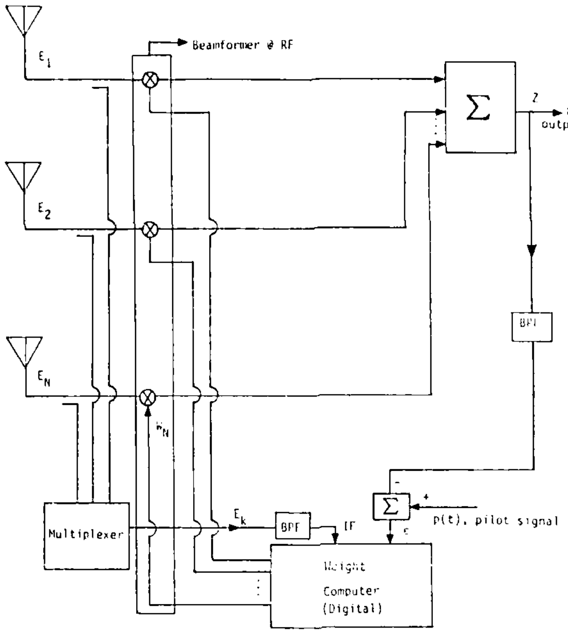

Figure 1. Adaptive Nulling Antenna with Multiplexed Control (MARK XII variation)

and digital techniques. The major emphasis of the studies was the comparison of several likely candidate methods of computing the adaptive weights or incremental weights. Digital determination of the weights was selected for implementation on the MARK XII adaptive array experimental system.

BACKGROUND

During 1983 and 1984, ASI investigated methods of simplifying the adaptive circuitry in large receiving array antennas with the requirement for nulling many wide bandwidth jammers. A sequential method of controlling subsets of element weights in a large array was evaluated. A functional block diagram of this technique is shown in Fig. 2. A subset of array elements is selected for adaptation elements k1, k2, and k3 in Fig. 2. Separate receivers are required for the main array output and for these 3 channels. The receiver outputs are A/D converted at a rate equal to the bandwidth, retaining both in-phase and quadrature components. The sample covariance matrix algorithm [2] is used in the digital processor to compute optimum increments for the 3 weights. The corresponding array weights are then incremented by the computed values of ΔW, selected to minimize this jammer power in the output.

The option of updating a single weight at each iteration was investigated during the study. One typical result is shown in Fig. 3. The upper curve in Fig. 3 shows the antenna patterns before and after adaptation. The initial pattern for the 30-element linear array with Chebyschev illumination is shown by the dashed curve. Five jammers are present in the simulation as indicated on the upper curve, and nulls are obtained at the 5 jammer angles after adaptation as shown by the solid curve. The lower curve shows the transient response obtained with sequential adaptation. In this example, a single weight is otpimized at each iteration. The ten elements with adapted weights are shown on the lower curve (viz., 29, 30, 6,...). After 40 weight iterations, during which each of the 10 selected weights are incremented four times, the output power is reduced to 4 dB above the receiver noise level. A total of 10 independent samples was used for computing each weight increment. This example illustrates the ability of a system with a multiplexed single weight processor to null multiple jammers, in this case 5 jammers.

During the study, a series of cases were run with a single weight updated per iteration. As expected, the convergence slowed as the number of jammers increased. The effect of varying the number of samples used in the sample covariance matrix was investigated as in an Applebaum-Howell system. It was found that convergence is much slower when jammers of unequal power are present.

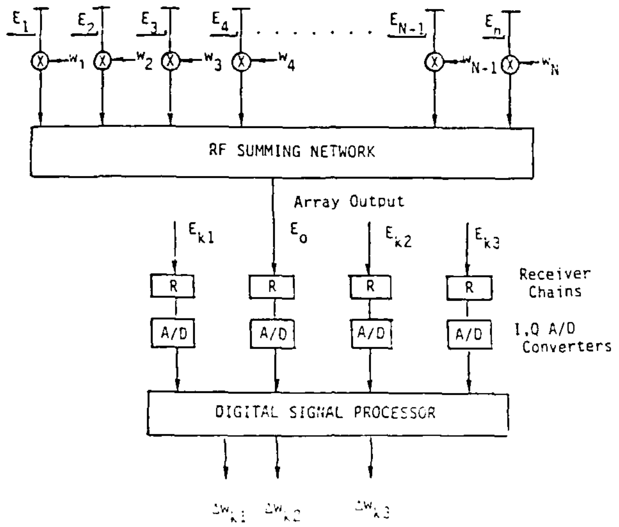

Figure 2. Hybrid Adaptive Arrays with Sequential Control of Element Weights

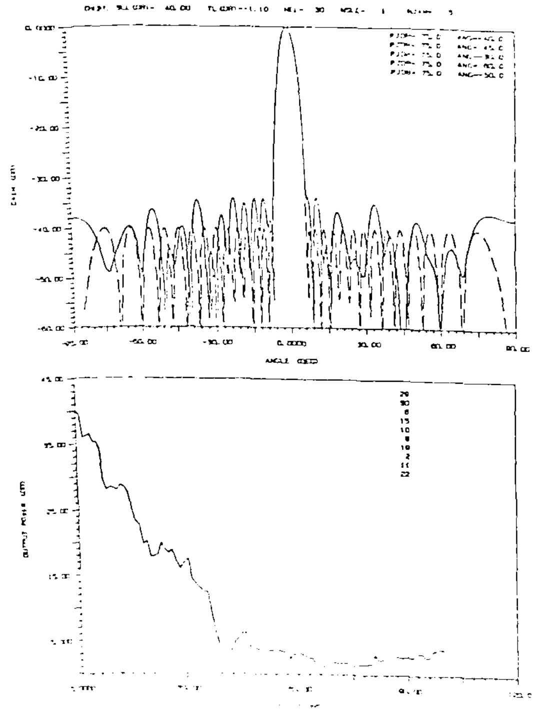

Figure 3. Sample Covariance Matrix: 10 Samples, 5 Jammers, 1 Auxiliary Channel

1.4

MARK XII SYSTEM

The basic concept is to provide an adaptive beamformer that is completely autonomous from the existing MARK XII IFF receiver, as depicted in Fig. 4. By providing an adaptive output at RF, it is feasible to replace the present antenna with an adaptive array which feeds a self-contained adaptive beamformer whose RF output (B) replaces the RF output of the present antenna (A). This approach lends itself to potential retrofitting of currently fielded systems with no modification to the extant hardware. The viability of this concept has been demonsrrated by ASI and TSC, on a laboratory demonstration model developed by the U.S. Army on Contract Nos. DAAK20-82-C-0140 and DAAK20-84-C-0157 for the L-band MARK XII IFF transceiver. A field version of that system is scheduled to be tested at Ft. Huachuca during October, 1985. Its important properties are:

- Autonomous Retrofitting. As indicated above, the adaptive antenna sybsystem is made essentially autonomous to the MARK XII IFF transponder by providing an adaptive RF output.

- Time Multiplexed Adaptation. ASI TSC have developed a unique time multiplexing adaptive algorithm that significantly reduces the hardware complexity and the concommitant cost of the adaptive array. In this approach only two receivers are required, independent of the number of auxiliary antennas. As shown in Fig. 5, (N) auxiliary channels are time multiplexed into one channel and the adaptive beam output is serviced by the second receiver. On any given iteration, the adaptive weight (w_i) for the multiplexed channel (#i) is incrementally updated by $(\Delta w)_i$ which is obtained by the implicit inversion of a (2x2) covariance matrix (which yields the 'best' $(\Delta w)_i$ for that iteration). This is equivalent to a multiplexed two channel LMS array where the gain and time constant are optimized. Simulations indicated that 4-8 samples are optimum for obtaining $(\Delta w)_i$ at each iteration.

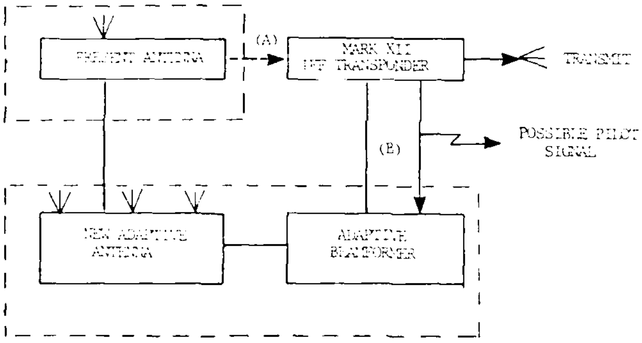

NEW HARDWARE
(Replaces present antenna)

- Adaptation at RF
- Autonomous adaptation
- Suitable for retrofitting

Figure 4. Adaptive Antenna Solution

SYSTEM ARCHITECTURE

ASI/TSC built and tested a test bed for ERADCOM, Ft. Monmouth, NJ (monitored by Mr. Duane Sheppared, Contract DAAK20-84-C-0878). Under this contract, ASI/TSC have designed, built and tested an adaptive nulling antenna for the MARK XII IFF system. The objective of the program is to obtain a simple system which can be retrofitted to existing airborne IFF transponders at minimum cost. This adaptive antenna uses a single signal processing circuit with multiplexing to sequentially update the weights on two of the three elements in the array. The system block diagram is the same as in Fig. 1, with the pilot signal in Fig. 1 set to zero. In addition to designing the adaptive system, ASI has simulated the circuitry in detail to determine the tolerances on all hardware components and the transient response of the adaptive array. The adaptive system was built and has been bench tested by Technology Service Corporation, under subcontract from ASI. This system will be field tested at Ft. Huachuca under the current contract.

The signal processing circuit used in the IFF adaptive array is hybrid--the array output and the output of one element channel are cross-correlated in an analog circuit, the correlator output is A/D converted and the updated weight is computed digitally. This weight is then D/A converted and applied to the selected element. The two variable weights are updated in sequence using a multiplexer to switch the element outputs alternately into the signal processing circuit.

Figure 6 depicts a block diagram of the complete system and Figures 7a-7f give details of the hardware configuration.

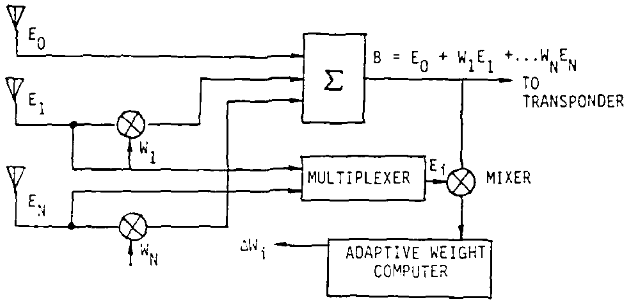

W_1W_2 are complex - phase and amplitude control

Updated sequentially - $\Delta W_i \doteq \dfrac{\overline{E_i^*B}}{|E_i|^2}$; $W_i = W_{i-1} + \Delta W_i$

Figure 5. Functional Diagram of Adaptive Receiving Antenna

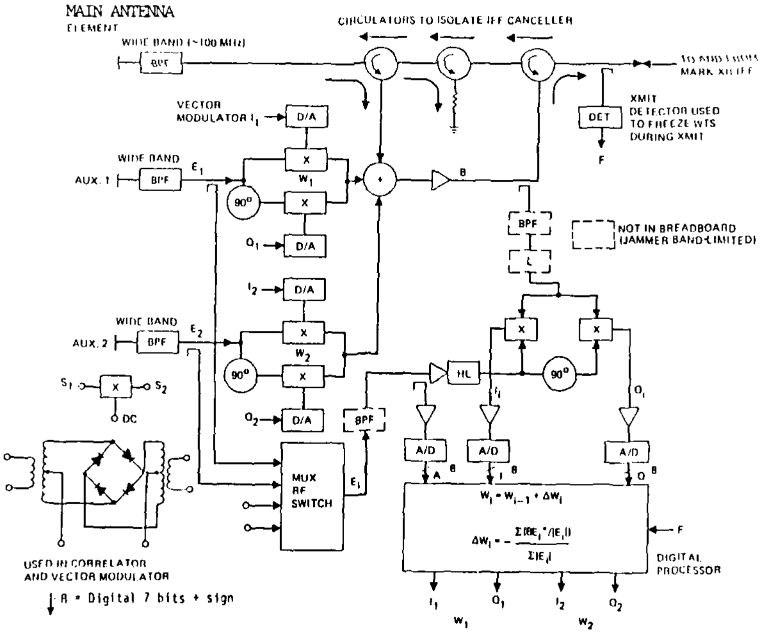

Figure 6. Adaptive Array Block Diagram

PERFORMANCE

Limitations on Cancellation

Analog beamformers at IF or digital have inherent limitations on the achievable cancellation due to sources of error introduced by the hardware itself. One of the most important of these error sources is receiver mismatch. Since only one complex weight is applied to each channel, the match between two receivers can only be exact at one frequency in the passband. Mismatch across the passband between two receivers results in residual noise power residue at the output of the cancellor as shown in Fig. 8. Figure 9 indicates the required RMS phase and amplitude match across the passband for a given level of cancellation. Note that in order to aspire to 45 dB of cancellation, less than .2° RMS phase error is tolerable, which is impractical to achieve in a relatively narrow band system (~5 MHz).

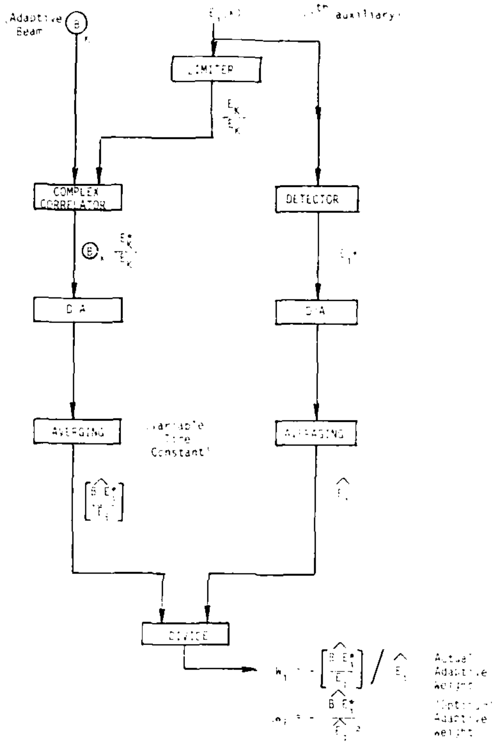

Figure 7a. Weight Computation with Limiting

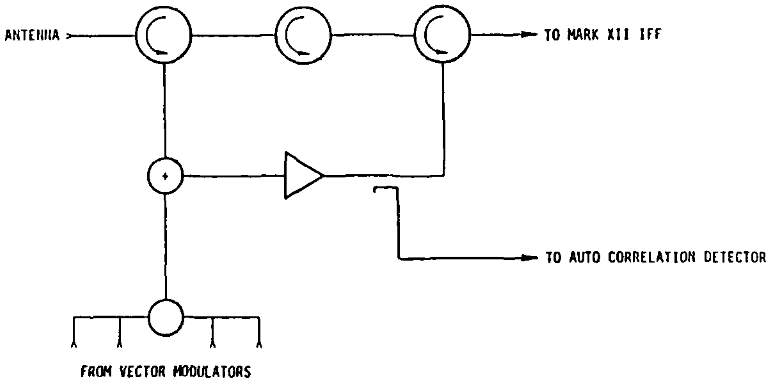

Figure 7b. Front End Block Diagram

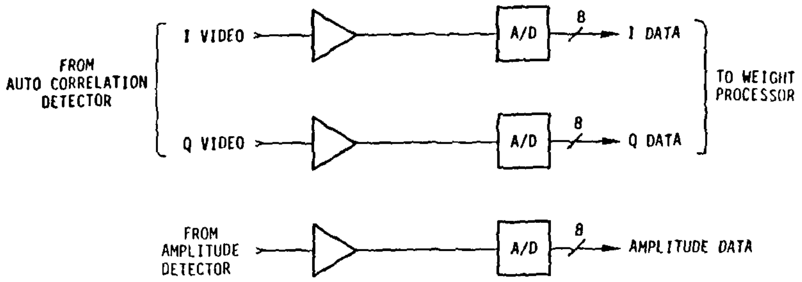

Figure 7c. Video Amplifiers - A/D Converters
Block Diagram

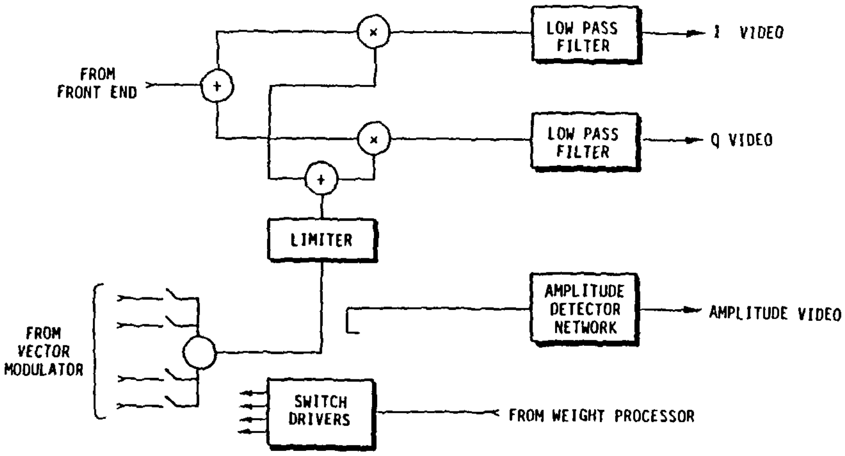

Figure 7d. Auto Correlation Detector Block Diagram

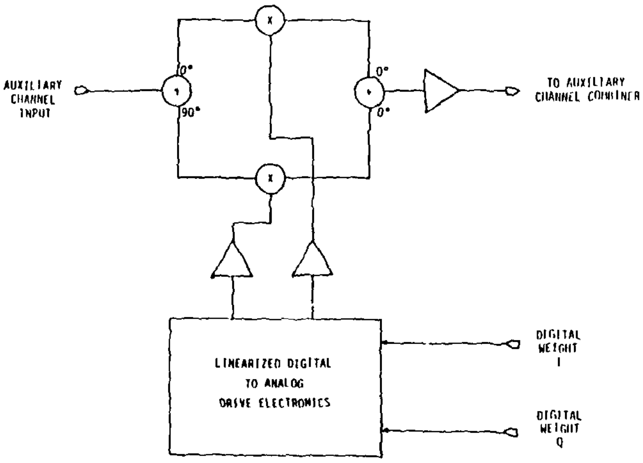

Figure 7e. Vector Modulator

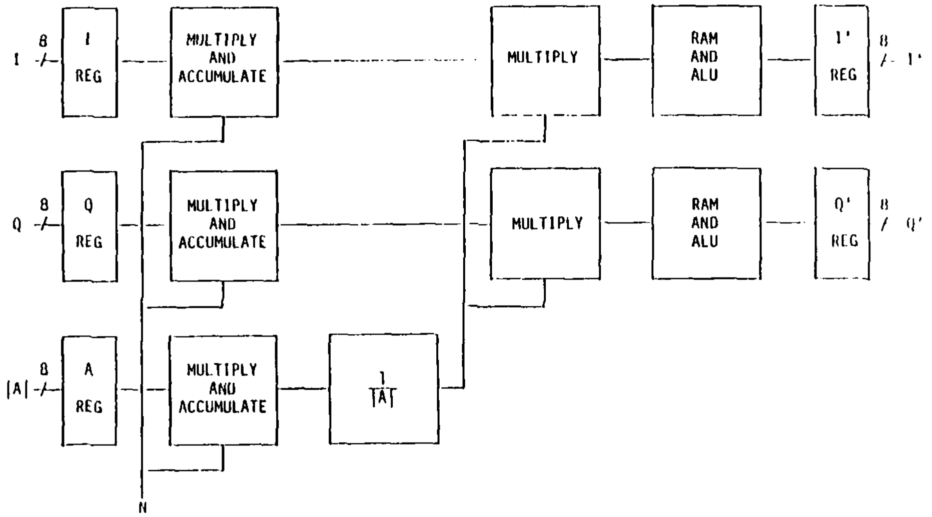

Figure 7f. Weight Processor

ADAPTATION AT RF

By applying the adaptive weights at RF at ~100 MHz bandwidth, (even though they were determined narrowband digitally) the receiver mismatch constraint is essentially removed. It is required that the cancellor perform over a very wide dynamic range of input signal levels. It is difficult for a correlator to operate over such a wide dynamic range without introducing bias errors *that would not be removed by the feedback loop. This is* solved by introducing sufficient gain in the muxed auxiliary channel to force limiting. Figure 7a shows the slight modification to the 'optimum' adaptive incremental weight that is introduced by this limiting operation.

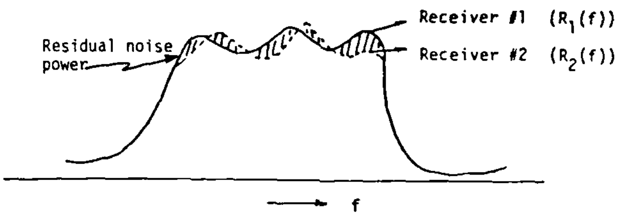

$$\frac{\min\limits_{W} \int_{-\infty}^{\infty} |R_1(f) - WR_2(f)|^2 \, df}{\int_{-\infty}^{\infty} |R_1(f)|^2 \, df} = C_R$$

Figure 8. Receiver Mismatch

SIMULATION AND TEST RESULTS

Figures 10-14 depict typical simulations of convergence rate and null depth that were corroborated in laboratory tests. Figures 10 and 11 depict the transient response to two jammers with zero and 25 dB of eigenvalue spread, while Figs. 12 and 13 show 3 and 4 jammers respectively for a hypothesized system with more adaptive degrees of freedom than actually implemented in the demonstration model. Of particular interest is the effect of various error sources in the system.

The important point to note is that all error sources except bias errors, as shown in Fig. 14, do not limit the level of cancellation. The bias error phenomenon is eliminated as shown in Fig. 7a by limiting the auxiliary channel.

CANCELLATION RATIO LIMITATION AS A FUNCTION OF RECEIVER MISMATCH IN AMPLITUDE AND PHASE

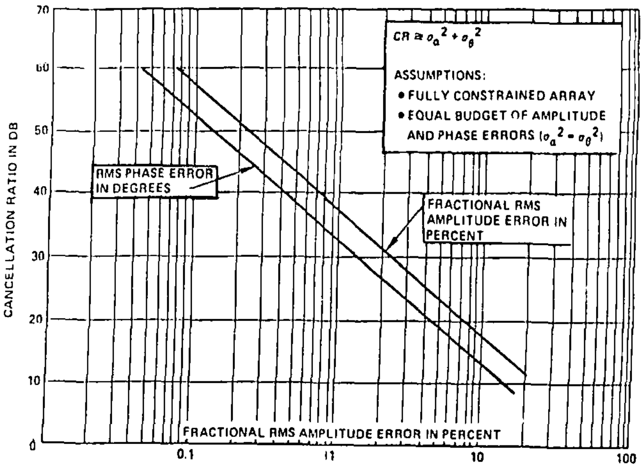

Figure 9. Cancellation vs. RMS Error

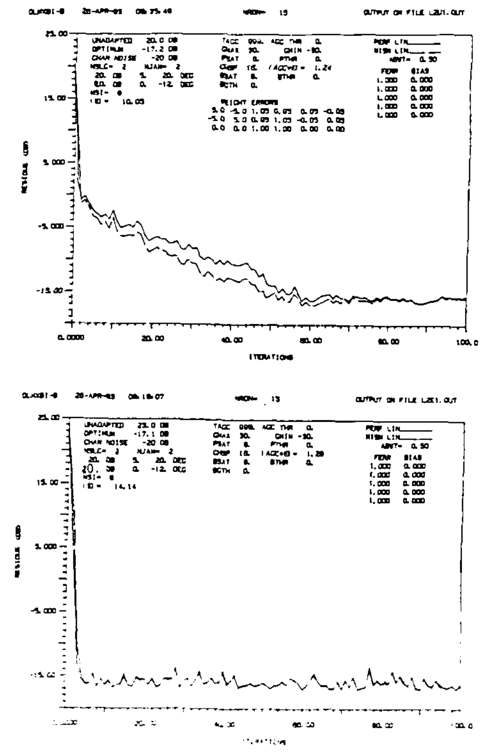

Figure 10. Weight Realization Errors

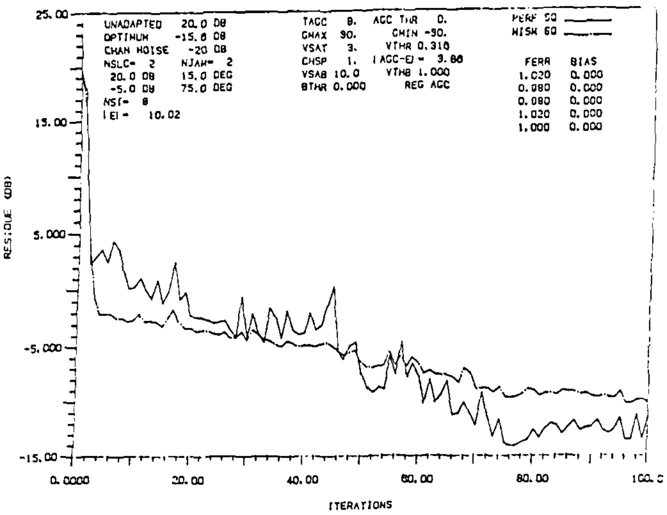

Figure 11. Eigenvalue Spread

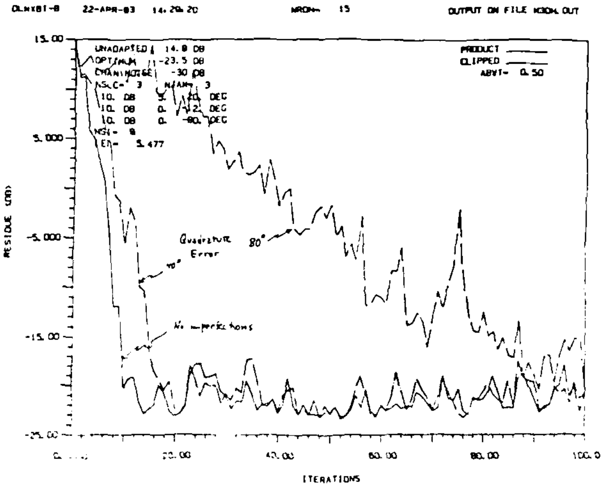

Figure 12. Effect of Quadrature Errors

In effect the only penalty for errors is a slowing of the convergence time. This results from the fact that the adaptive weighting is performed at RF prior to hardware induced sources of error such as receiver mismatch, soft limiting and imperfect quadrature.

This system has been demonstrated in the laboratory to provide 40-45 dB of cancellation against two jammers over a wide dynamic range of input signals.

REFERENCES

1. B. Widrow et al., "Adaptive noise cancelling: principles and applications," *Proc. IEEE*, vol. 63, no. 12, pp. 1692-1716, Dec. 1975.

2. Reed, I. S., J.D. Mallett, and L.E. Brennan, "Rapid Convergence Rate in Adaptive Arrays", *IEEE Trans. AES*, pp. 853-863, Nov. 1974.

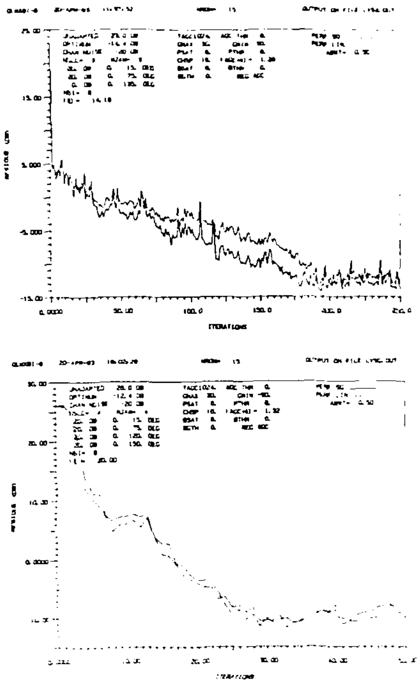

Figure 13. Comparison of Square Law and Linear Detectors

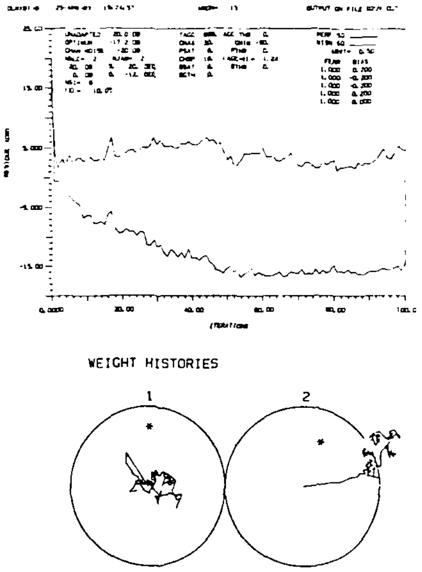

Figure 14. Effect of Bias Mismatch

HIGH RESOLUTION SIGNAL PROCESSOR FOR LIMITED APERTURE MULTIMODE RADAR

Robert L. Nevin
General Electric Company
Aerospace Electronic Systems Department
Utica, New York 13503, USA
and
M.R. O'Sullivan
O'Sullivan Consulting, Inc.
30466 Via Cambron
Rancho Palos Verdes, California 90274, USA

ABSTRACT

The maximum attainable point target detection capability of a search radar in a receiver noise limited situation is fundamentally limited by the radar's power-aperture product. However, the degree to which practical systems approach this maximum performance may be limited by processor power (i.e., processor throughput, resolution, etc.). Furthermore, in clutter limited situations, such as air-to-air look-down search modes, greater processor resolution, in both range and doppler, can reduce the effective size of the clutter cell competing with the target, and thereby improve subclutter visibility. Recent and ongoing developments have contributed to the application of high-resolution, high-throughput signal processing to multimode, multifunction airborne radars. Both air-to-air and air-to-ground modes benefit in performance from increased processing power and flexibility.

The solution to the high resolution processor is based on the experimental Modular Survivable Radar developed by General Electric *in the late 1970s, and extended to airborne multimode radar projects*. This modular, reconfigurable pipeline consists of high-efficiency stages, each with a narrow range of assigned functions, cascaded to form the full signal processor. Experience in system integration and testing has proven the adaptability of this architecture, which can be particularly useful to achieve the detection range requirements in a small fighter aircraft where physical space and cooling capability limit the power and aperture available to the radar.

The architecture of a programmable signal processor (PSP) currently in development for future application is described. This architecture allows processing elements (PE's) and memory elements to be configured into parallel pipelines. The PE's are designed to perform linear and nonlinear operations at the same high throughput rate. These features make it highly suitable for integration into the radar signal processor.

With respect to this integration, the degree of flexibility required at different points in the pipeline is considered. The nonlinear and bandwidth reduction processing which comes between the linear processor and the target data processor has the greatest variety of function. *The linear processor, and in particular the FFT or spectrum analyzer, has a more consistent function* over various radar modes. The baseline architecture is very receptive to replacement of any section by a PSP. In fact, replacement of all post FFT processing by a PSP, while maintaining the reconfigurable pipeline for the linear processing, is shown to be a very efficient near term solution. Replacement of the linear stages can follow as improvements in the PSP functional efficiency make it worthwhile.

INTRODUCTION

Modern airborne multimode radars for fighter type aircraft require a wide range of air-to-air and air-to-ground modes. A typical suite of required modes for such an application is presented in Table 1, along with representative performance requirements and an indication of the type of waveform used to implement each mode.

In some applications, aircraft constraints impose limits upon the size of the antenna aperture area available for the radar. This creates difficulties in achieving the required performance since, for most modes, antenna aperture and related antenna parameters (e.g., gain, beamwidth, etc.) are strong determinants of the achievable performance. In many instances, however, increased processing capacity can compensate, to a significant degree, for a shortfall in available aperture. In what follows, this tradeoff (i.e., available aperture versus processor capacity) will be illustrated for the specific case of a medium PRF search mode.

A summary of the types of processing functions required to implement the modes listed in Table 1 is presented, followed by a description of a high resolution, high throughput signal processor developed at General Electric Company which has found application in one such case. The requirements for programmability at various points in the processor are analyzed, with a view towards staged incorporation of a programmable signal processor. A Programmable Signal Processor under development at General Electric to meet these processing requirements is described, along with a plan to integrate it into a multimode radar in stages.

Medium PRF Search Mode Design

The range performance of a volume search radar, operating in a receiver noise limited environment with a fixed constraint on scan time may be expressed as [1, pp. 50]:

$$R^4 = \frac{\overline{P}\, T_{sc}\, A_e\, \sigma_t\, L}{4\pi\, K T_s\, (S/N)_{Req}\, \Psi} \qquad (1)$$

where: $\overline{P}$ = average transmitted power
T_{sc} = time to complete one scan of the search volume
A_e = effective antenna aperture
σ_t = target radar cross section
L = total loss factor
K = Boltzman's constant
T_s = system noise temperature
$(S/N)_{req}$ = signal-to-noise ratio required for detection
Ψ = total solid angle of the scan volume.

Equation (1) assumes that the radar processing approximates matched filter processing. A processing loss, L_p, constitutes one of the factors in L, and measures the degree to which the processing is imperfectly matched. From Equation (1) it is seen that the fundamental

TABLE 1. MULTIFUNCTION RADAR MODE SUMMARY

Mode	Waveform	Representative Performance Requirement
AIR-TO-AIR		
Range While Search	Low PRF/Look Up Med PRF/Look Down	30 nmi detection of 5 m^2 target 18 nmi detection of 5 m^2 target
Velocity Search	High PRF/Look Down	23 nmi detection of 5 m^2 target
Track While Scan	Med PRF	8 simultaneous targets
Single Target Track	Med PRF	Angle accuracy, 4 mr Range accuracy, 100 ft or 1% of range
Air Combat	Med PRF	Detection range, 1000 ft to 10 nmi
AIR-TO-GROUND		
Real Beam Ground Map	Low PRF	4° azimuth resolution
Dop. Beam Sharpening	Low PRF	20:1 beam sharpening ratio
Sea Search	Low PRF	30 nmi detection on 50 m^2 target - SS #1 25 nmi detection on 50 m^2 target - SS #4
Ground Moving Target Indication	Low PRF	Detect tank at 15 nmi
Ground Moving Target Track	Low PRF	Angle accuracy, 4 mr Range accuracy, 50 ft or 0.35% of range
Air-to-Ground Ranging	Low PRF	Accuracy, 50 ft or 0.5% of range

radar parameter determining the maximum achievable range performance in noise is the radar's power-aperture product. The processing loss, however, measures the degree to which a given processing implementation causes the radar performance to fall short of that inherent in its power-aperture product. Improving the processing efficiency can reduce the processing losses and thus cause the radar performance to more closely approach the maximum potential of its power-aperture product.

The average transmitter power for an airborne radar is typically limited by the prime power and cooling available from the aircraft (e.g., 200 watts average RF power is a reasonable figure for modern lightweight fighters). When the available aperture is also tightly limited, the only reasonable alternative available to achieve adequate performance is to expand processor capacity to achieve greater processing efficiency and thereby reduce the processing loss, L_p

Medium PRF mode design is driven primarily by the requirement to detect small airborne targets while looking down into intense ground clutter, and to determine their range, azimuth, and velocity coordinates unambiguously. Thus, over and above the foregoing considerations pertaining to detection in noise, a number of additional factors related to clutter discrimination directly affect the waveform selection and signal processing structure. Nonetheless, the final structure typically reflects the attempt to approach matched filter processing as nearly as possible, while implementing the necessary clutter rejection and ambiguity resolving functions.

The principal design features driven by the need to accommodate ground clutter are as follows:

- A significant portion of the doppler spectrum, containing ground clutter and ground moving targets is rejected
- The PRF values are chosen high enough so that the doppler rejection is not an excessive fraction of the doppler spectrum, but still low enough to permit substantial range discrimination
- The time-on-target is broken up into a number (i.e., typically eight or nine) of coherent bursts of transmitted pulses, with PRF variation from burst-to-burst, to reduce range and doppler eclipsing and permit range and doppler ambiguity resolution
- The number of pulses transmitted in each coherent burst exceeds the number to be processed in order to allow for "clutter settling" (i.e., to allow for returns from long range clutter to establish coherency)
- The processor must maintain a high dynamic range, to accommodate ground clutter, through the linear stages of processing (i.e., up to the point at which mainlobe clutter is rejected)
- Cell averaging CFAR is employed to adaptively set thresholds in response to sidelobe clutter, which can exceed receiver noise over local regions in the range doppler plane

Comparison of MPRF Mode Parameters

Table 2 presents representative parameters for two medium PRF mode designs for a tactical fighter application. The first or baseline system assumes a 24 inch diameter aperture. The second is a reduced aperture system in which the baseline aperture has been reduced by a factor of two in the vertical dimension. Table 3 presents representative processing losses for the two designs presented in Table 2. Note that the total processing losses for the baseline design are a substantial 8.5 dB, allowing considerable room for improvement through more efficient processing. The reduced aperture design has total losses of 5.8 dB, a net reduction of 2.7 dB, nearly compensating the 3 dB reduction in power aperture product. In what follows, each of the processing losses will be discussed for these two designs and the manner in which added processing power can reduce the processing losses will be illustrated.

TABLE 2. MEDIUM PRF MODE PARAMETERS

Parameter	Baseline	Reduced Aperture
Average Transmitted Power	200 W	200 W
RF Wavelength	0.1 ft	0.1 ft
Peak Antenna Gain	33 dB	30 dB
Average PRF	10 kHz	10 kHz
Average Compressed Pulse Width	1 μsec	0.25 μsec
Antenna Half Power Beamwidth	4°	4° az by 8° el
Number of Doppler Filters (i.e., FFT Size)	64	128
Number of Clutter Settling Pulses	10/CPI	10/CPI
Doppler Filter Bandwidth	PRF/64 ≈ 150 Hz	70 Hz
Average Number of Range Bins	64	512
CFAR Window Size	16 cells	128 cells
Receiver Noise Figure	3 dB	3 dB
Scan Rate	70°/sec	35°/sec
Time on Target	57 msec	114 msec
Mainlobe Clutter Rejection Ratio	60 dB	48 dB
Clutter Backscatter Coefficient	0.15	0.15
Target Cross Section	5 m^2	5 m^2
Mainlobe Clutter and GMT Rejection Bandwidth	4 kHz	4 kHz
False Alarm Rate	1/minute	1/minute
Antenna Frame Time	3.8 sec*	3.8 sec

*For a 2 bar × 60° Raster Scan.

TABLE 3. REPRESENTATIVE MPRF PROCESSING LOSSES

	24" Aperture	Reduced Aperture
M/N Loss	2.2 dB	2.2 dB
Clutter Settling Loss	0.6 dB	0.3 dB
Range Filter Mismatch Loss	0.9 dB	0.9 dB
Range Gate Straddle Loss	0.7 dB	0.2 dB
Doppler Filter Mismatch Loss	1.8 dB	1.2 dB
Doppler Filter Straddle Loss	0.7 dB	0.8 dB
CFAR Loss	1.6 dB	0.2 dB
Total Processing Losses	8.5 dB	5.8 dB

M/N Loss

The M/N loss for Medium PRF radars occurs for two reasons:

- The need to switch PRF values during the time-on-target to reduce blind zones and to resolve ambiguities
- The signal processor typically limits the amount of coherent integration that is possible.

Consider now the impact, on the baseline design presented in Table 2, of a factor of two reduction in antenna aperture. To simplify the discussion, it is assumed that the reduction is predominantly in the vertical aperture dimension. The effect of such a reduction would be to reduce antenna gain by 3 dB and broaden the elevation beamwidth by a factor of two. The increased elevation beamwidth makes it possible to scan the search volume with a single elevation bar, rather than two bars, which effectively doubles the time-on-target, if frame time is kept invariant, as is necessary for a valid comparison between the two designs. To utilize the increased time-on-target efficiently, however, without incurring added M/N or noncoherent integration loss, requires doubling the length of each coherent processing interval (CPI), thereby doubling* both the number of pulse returns being coherently processed and the FFT size required. The net result is that the M/N loss is the same for both designs, but the reduced aperture system achieves twice the doppler resolution by doubling the FFT size to 128 points.

Clutter Settling Loss

Clutter settling loss is a measure of the fraction of transmitted pulses which are "wasted" to establish clutter coherence on each CPI before the received signal return can be processed. The number of settling pulses required at a 10 kHz PRF is approximately 10, which should be adequate to "cohere" clutter at ranges up to 80 nautical miles. The resulting loss is therefore

$$10 \log \left\{ \frac{N_{FFT}}{N_{FFT} + 10} \right\} \quad \begin{cases} 0.6 \text{ dB, Baseline System} \\ 0.3 \text{ dB, Reduced Aperture System} \end{cases} \tag{2}$$

Since the reduced aperture system processes twice as many pulses coherently in each CPI as the baseline system, the number of clutter settling pulses represents a smaller fraction of the number of pulses transmitted in each coherent burst. Consequently, the clutter settling loss is smaller for the reduced aperture system.

---

*When clutter settling pulses are included, the total time on-target increases by slightly less than a factor of two, since the number of settling pulses required is a constant.

Range Filter Mismatch Loss

In pulse compression systems, the compression stage is frequently weighted to reduce the time sidelobes of the compressed pulse. The amount of weighting, typically determined by the requirement to distinguish a small target in close range proximity to a large target, is unaffected by the reduction in aperture. Consequently, this component of processing loss has the same value for both the baseline system and the reduced aperture system.

Range-Straddling Loss

Range-straddling loss is presented in Figure 1 as a function of range sample spacing for both an unweighted, compressed chirp signal and for the same signal with cosine weighting applied to reduce range sidelobes. The straddling loss listed in Table 3 for the baseline system (i.e., 0.7 dB, assumed weighted chirp with a 1/B sample spacing). By increasing the sampling rate by a factor of two (i.e.,reducing the sample spacing to 1/2 B), the straddling loss can be reduced to 0.2 dB for the reduced aperture system, a net gain of 0.5 dB.

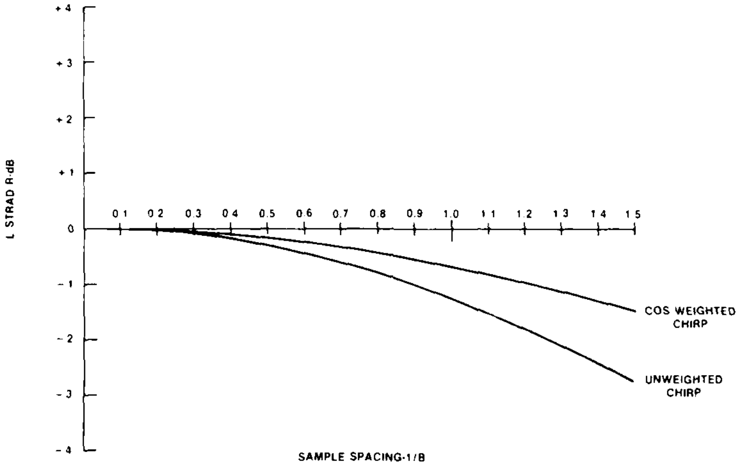

Figure 1. Range Straddling Loss Versus Sample Spacing

Doppler Filter Mismatch Loss

Doppler filter mismatch loss is a function of the amount of time domain weighting applied to the sequence of coherently processed pulses, in the FFT processor. The severity of the weighting required is determined by the clutter-to-noise spectral density ratio of the coherent spectrum at this stage. Let us examine the behavior of this quantity as the aperture is reduced.

Since the aperture reduction is confined to the vertical dimension, the spectral width of mainlobe clutter will be relatively unaffected. Consequently, the clutter-to-noise spectral density ratio will vary proportionately to the IF clutter-to-noise ratio.

Receiver and A/D converter dynamic range is determined by the received clutter-to-noise ratio, which can be expressed as:

$$P_C / P_N = K \left(\frac{G\sigma^2 L}{B} \right) \qquad (3)$$

where: K a factor containing a number of radar parameters being held constant here
B transmitted signal bandwidth

Since the aperture, and hence gain, has been halved, the clutter-to-noise ratio and dynamic range requirement have been reduced by 6 dB. If we additionally increase the range resolution (and transmitted signal bandwidth) by a factor of four, the dynamic range will be reduced by an additional 6 dB. Thus, the requirement on doppler clutter rejection, and hence on doppler filter sidelobes, is reduced by 12 dB, with the result that filter weighting can be reduced and hence filter weighting loss will also be reduced by approximately 0.6 dB as shown in Table 3.

Doppler-Straddling Loss

As the amount of doppler filter weighting is reduced, the mainlobe of the doppler filter transfer function narrows, so that doppler straddling loss increases slightly, to 0.8 dB.

CFAR Loss

CFAR loss is a strong function of the number of cells composing the CFAR average. The size of the range/doppler region over which averaging is beneficial is, however, limited by the lobing structure of sidelobe clutter. By increasing the range resolution (i.e., reducing the range cell size) by a factor of four and the doppler resolution by a factor of two, the total number of cells averaged can be increased by a factor of eight (from 16 to 128) without changing the size of the averaging region. The resulting reduction in CFAR loss, assuming a false alarm probability of 10^{-6}, can be seen from Figure 2 to be approximately 1.4 dB, as previously presented in Table 3.

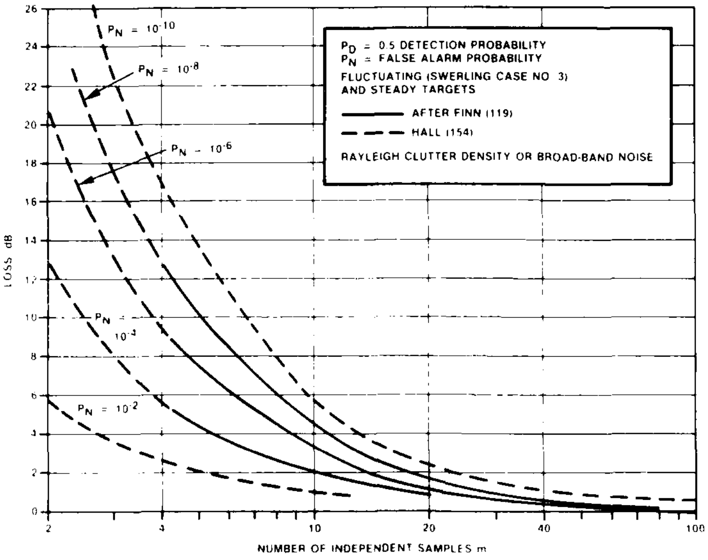

Figure 2. CFAR Loss Versus Number of Samples

Processing Loss Summary

As illustrated in Table 3, the total processing losses for the reduced aperture design have been reduced to 5.8 dB, a 2.7 dB reduction from the processing loss total for the baseline, 24 inch aperture design. Thus, a substantial fraction of the 3 dB lost due to aperture reduction has been regained. This has been accomplished primarily through increased processor capacity, that is, the range resolution has been quadrupled, the range sampling rate increased by a factor of eight, and the doppler resolution doubled. High resolution, high throughput processors capable of accomplishing these improvements are described in the remainder of this paper.

GE Pipeline Processor

The General Electric pipeline processor began with development and flight testing of its experimental Modular Survivable Radar, shown in Figure 3 and described in (2). The MSR features a distributed, reconfigurable signal processor. The signal processor elements are constructed principally from custom MOS LSI circuits designed and produced by General Electric. The radar elements, including the various signal processing elements, are controlled from a central radar controller by means of a multiplexed digital data bus.

The MSR flight test included many radar functions similar or identical to required multimode radar functions, such as Ground Moving Target Indication (GMTI) and Doppler Beam Sharpening (DBS). In these tests, the flexibility of the processor architecture was proven; thus, it became the basis for design of a multimode radar [3]. With the LSI microcircuits in place and a basic processor architecture proven, the system development time was shortened significantly.

Modular Pipeline Approach

Table 4 presents a summary of the processing functions required to implement each of the modes which were previously presented in Table 1. Note that Table 4 distinguishes between linear processing functions (e.g., pulse compression, complex multiplication for motion compensation, and filtering) and the more diverse and mode dependent nonlinear processing operations which follow the linear stages of processing. This table suggests that an extremely efficient modular processor can be provided for the most computationally intensive case - the look down air-to-air mode - whose parameters can then be modified to provide the majority of the processing required for any other mode.

Each of the major pipeline functions is implemented by a hardware element. This element has a standard input-output timing relationship. Elements with complex internal timing have their own timing and control generators. In this fashion, each processing element is a stand-alone module, requiring only parametric control and minimal timing triggers from the previous element. The result is a modular pipeline which can be easily reconfigured via the parametric controls.

Figure 4 shows the linear signal processing portion of the pipeline. The processing elements required are universal to modern coherent radar [3,4,5], with only the parameters and details of implementation varying between radar type and mode.

The waveform generator and pulse compressor are devices matched to each other. When used together, they allow higher duty cycle, hence higher average transmit power, without sacrificing range resolution [6, chapter 20]. The doppler compensation removes the primary effect of ownship motion from the received signal. The MTI canceller eliminates most of the ground clutter from the signal to reduce spectral leakage and dynamic range problems in the FFT. The FFT is used as a spectrum analyzer to separate the received signal into its doppler frequency components. The final step of the linear processing is a rescaling, to adjust the signal dynamic range for the processing steps which follow.

Figure 5 shows the nonlinear and bandwidth reduction processing. The primary radar modes require a constant search for processed target video in the range doppler matrix represented by the FFT output. This is mechanized by searching for cells whose video magnitude

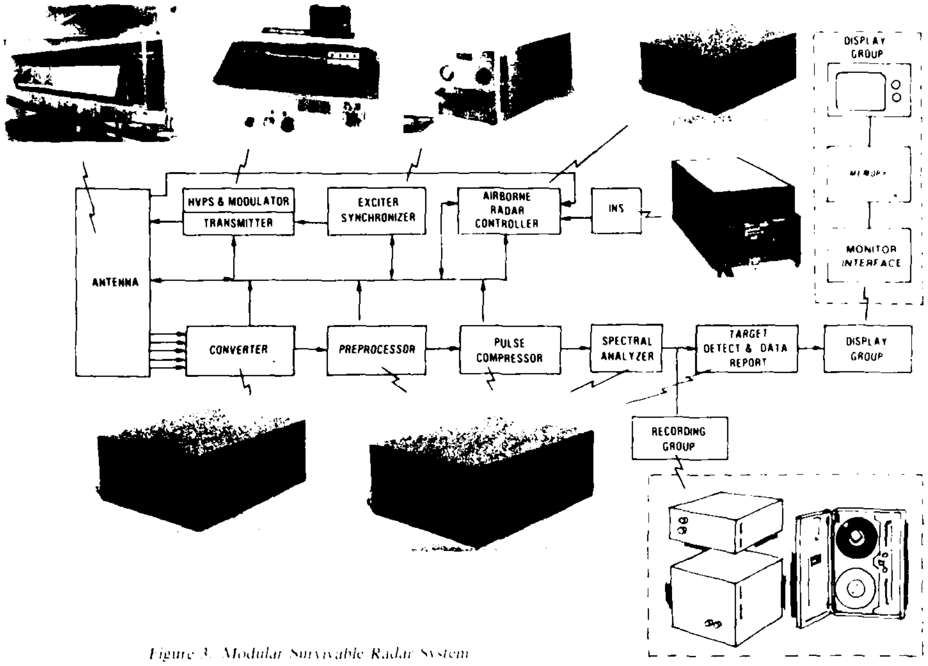

Figure 3. Modular Survivable Radar System

TABLE 4. PROCESSING FUNCTION VS MODE

Mode	Linear Processing Functions					Nonlinear Processing Functions					
	Pulse Comp.	Mot Comp.	MTI	Filtering FFT	Env Det	Δ Σ	CFAR	PDI	M N	Linear Regress.	Beam Splitting
RWS	X	X	X	X	X		X		X		
VS		X	X	X	X		X		X		
TWS	X	X	X	X	X		X				X
STT	X	X	X	X	X	X	X				
ACM		X	X	X	X		X	X			
RBGM	X				X			X			
DBS	X	X		X	X			X			
GMTI	X	X	X	X	X		X				
GMTT	X	X	X	X	X	X	X				
AGR	X					X	X	X		X	
SEA1	X				X						
SEA2	X	X	X	X	X		X		X		
TF TA	X					X	X	X		X	

substantially exceeds that of neighboring range-doppler cells, by a background averaging and thresholding process [7]. Under some conditions this is followed by a preprocessing stage which resolves the range ambiguity resulting when the pulse repetition interval is less than the echo time [5, pp. 442-444]. Target reports are then given to the Track Computer for full post-processing. Another bandwidth reduction stage selects sum and difference monopulse video for a tracked target, to be used in post-processing for angle error measurements.

Display processing is included in this category also. After the complex video is magnitude-detected, it is smoothed by integration along range and azimuth dimensions for best display readability. The same averaging mechanism is used in the DBS display processing to average several looks at a particular range-angle cell.

Table 5 shows the computational and memory capacities in the various signal processor modules. Computational capacity is shown in equivalent real integer additions and multiplications on the basis that either is a "one-chip" operation with current LSI circuits. It should be noted that the computationally intensive modules do not correspond to the memory intensive modules. The ability to provide the resources needed at the point where they are needed is an inherent advantage of the reconfigurable pipeline processor over the typical current programmable signal processor.

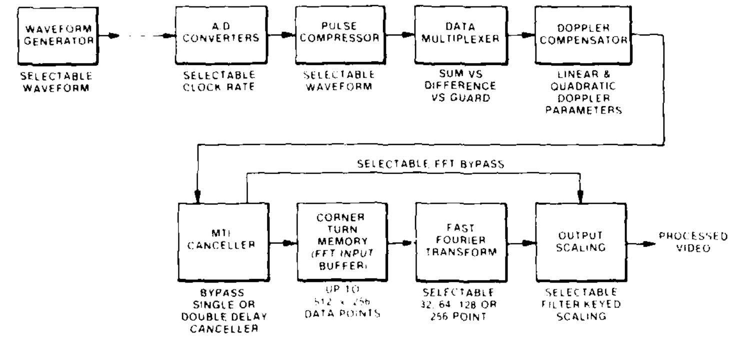

Figure 4. Linear Signal Processing

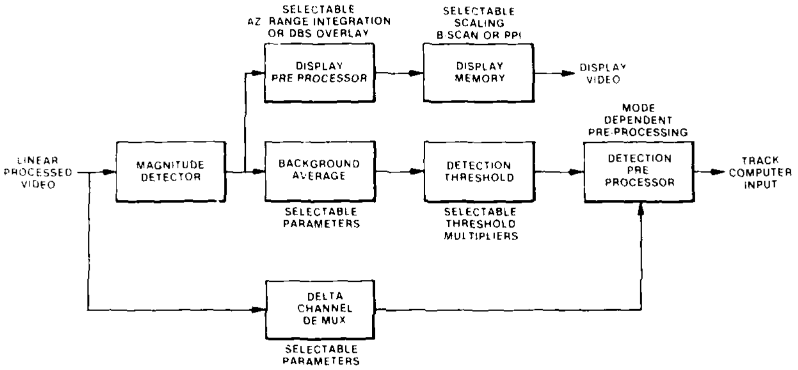

Figure 5. Nonlinear and Bandwidth Reduction Processing

TABLE 5. SIGNAL PROCESSOR CAPACITIES

Processor Stage	Equivalent Real Op/Sec	Equivalent Memory Bytes
Pulse Compressor	144M	
Doppler Compensator	36M	
MTI Canceller	8M	2K
Corner Turn Memory		256K
Fast Fourier Transform	512M	4K
Scaling Multiplier	8M	
Magnitude Detector	4M	
Background Averaging	16M	8K
Delta Channel Demux		8K
Display Preprocessor	8M	1K
Display Memory		32K
TOTAL	736M	311K

Programmable Signal Processor Integration

In the current multimode radar market, many systems have been or are being modified to incorporate a programmable signal processor (PSP). The definition and the applications of the PSP vary widely from system to system. This section will show one approach to defining a PSP and incorporating it into a multimode radar.

Flexibility Requirements vs Processor Stage

A generic radar processor consists of a linear signal processor, followed by a nonlinear and bandwidth reduction pipeline processor, which in turn feeds the stored-program postprocessor.

The linear portion can be divided into the FFT and the preprocessor. *The FFT operates in a different dimensionality* than the elements that precede it (e.g., the pulse compressor and the MTI), thus it is segregated by what we call a corner-turn memory. The FFT is generally the last linear processing stage. The FFT is a very efficient circuit, and could not be replaced with current PSP elements without giving up packaging density. Furthermore, the only variable parameter is its size, and possibly *weighting coefficients, so the PSP flexibility* is not needed.

The remainder of the linear processor is *not as tightly inflexible as the FFT*, but generally uses the same type of processing for each radar mode. Major pieces are the pulse compressor and the MTI canceller (which may also be used for presumming in Doppler Beam Sharpening (DBS)). These will vary from mode to mode in their parameters, and are generally insensitive to order, with a minimum of new functions to be expected as new modes are added. As a candidate for PSP *application, this section rates a "medium"*, for required flexibility and for packaging efficiency.

On the other hand, *the processes which follow the FFT are many and varied*. It is at this point where information is extracted from the processed video. This information is then fed to the computers, and its exact nature is highly dependent on the radar mode. In the basic search modes, CFAR target detection and range ambiguity resolution are required. In the dedicated track and air-to-ground ranging modes, the processor must extract monopulse information. *In the map modes, the raw video (in the case of real beam mapping)* or the FFT processed video (for DBS or Synthetic Aperture Radar (SAR)) must be integrated, overlayed, and otherwise readied for display. Modes for terrain following avoidance require more extensive processing of monopulse data than air-to-ground ranging, in order to achieve the required angular coverage. In all of these cases, specially tailored pipeline processing is necessary, *with a required throughput* beyond the capability of the stored program target data computer.

In general it is seen that the maximum flexibility is required of the signal processor in its latter stages. These stages are beyond the linear processing section, where the ugly work, between signal processing and computing, must be done. This conclusion may also be drawn by looking at implementation efficiency. The linear portion of the APG-67 signal processor pipeline, particularly the FFT, is more compact than a programmable signal processor capable of doing the same job. However, *the nonlinear processing is about at* the crossover, where a PSP which changes function with mode, can replace the existing special purpose stages with no increase in space, and provide flexibility for future growth. It is anticipated that as the capability and functional density of the PSP grows, and as the required radar signal processor front end functions grow, the PSP installation ahead of the FFT will also become worthwhile, and eventually the FFT itself.

PROGRAMMABLE SIGNAL PROCESSOR DEVELOPMENT

In order to realize a highly efficient signal processing configuration, the architecture must be well suited to the data flow encountered in the intended applications. A "general purpose" type of architecture, which provides for "random" data flows between processing elements and memory elements, is not efficient in a radar signal processing application where the data flow is generally well structured and predictable.

Figure 6 shows an architecture developed by General Electric which takes advantage of this data flow [8]. The configuration shown *illustrates the basic concept of a parallel pipeline architecture using small, high speed programmable* Processing Elements (PEs). The communication between the parallel pipelines is realized using a ring network. Buffer storage of large data blocks, such as is done by the Corner Turn Memory, takes place in the memory modules. Each PE contains Local Memory, so that functions not requiring mass storage can be implemented in the pipeline.

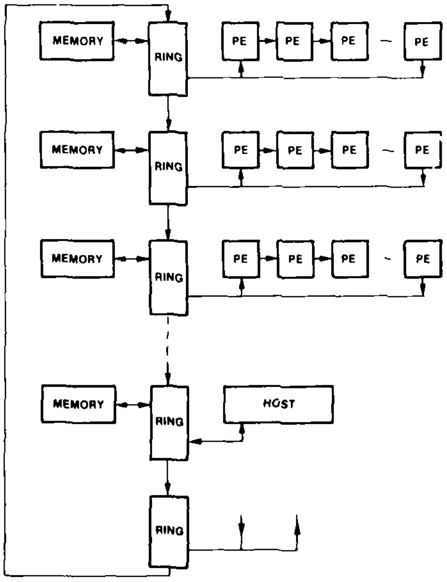

Figure 6 Programmable Signal Processor Architecture

The Processing Elements execute independent programs with program controlled synchronization interlocks. Each PE includes internal hardware controllers which allow instruction execution on a data vector to proceed concurrently with data transfers into and out of the PE, instruction fetches, and main memory transfers. Figure 7 shows how the multiport Local Memory Unit is interconnected with the processing and input/output devices to form the PE.

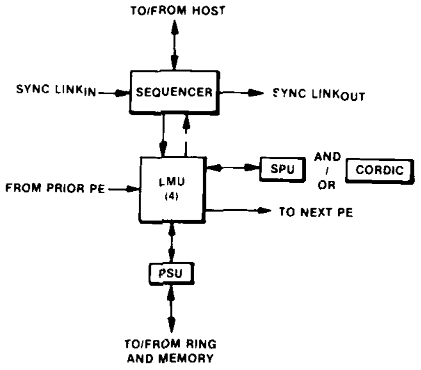

Figure 7. Processing Element (PE) Functional Partitioning

The diagram shows two processing devices in the PE. For any processing step, the data may be passed through either the Signal Processing Unit (SPU) or the Coordinate Rotational Digital Computer (CORDIC). The SPU is used for linear and logical operations such as add, multiply, and/or, and maximum/minimum, and can perform complex arithmetic in a single pass. The CORDIC is a digital differential analyzer, which can calculate nonlinear functions at the same throughput rate, such as sine/cosine, magnitude/phase of a complex number, divide, and square root. The inclusion of the CORDIC provides the PE with the capability needed to perform many more of the functions required in the nonlinear portion of the radar signal processor at the high rate required.

PSP Integration Into Multimode Radar

The nature of the PSP described above makes it very useful for piecewise integration into an existing multimode radar, because the architecture provides for a number of identical, relatively simple processing elements. Coupling these together in parallel pipelines allows them to be configured according to system processing needs. In contrast, a PSP architecture which depends on one super-fast processing element must deal with two problems. One is that the processor capability will nearly always be substantially different from the needs of an arbitrary system. The other is that contention for resources will be a never ending problem in allocating the time of processor and peripherals.

The concept for staged integration of the PSP into the General Electric Multimode Radar is shown in Figure 8. The area of most serious need has been identified as the downstream end of the pipe. The current system architecture is very amenable to introduction of a PSP at that point, without disturbing the remaining pipeline. This will allow flexibility and expansion of detection, integration, and data reduction functions which are the most changeable. The second stage will be introduction of the PSP into the upstream end of the pipeline. Flexibility in this area will allow such functions as spotlight SAR preintegration and focusing. Because the pipeline stages carry data in PRI or CPI batches, and carry the timing cues with it, the upstream PSP can also be accomplished without major disturbance. The final stage to be converted to PSP operation will be the FFT, at such time as the PSP stages become more efficient, or more likely, when the benefit of a total PSP outweighs the inefficiency.

SUMMARY

Radar requirements for a small high performance airplane with Air-to-Air and Air-to-Ground missions often place constraints on the radar power and aperture. These constraints make it more difficult to meet specified performance requirements. To some degree, these can be compensated by increased processor throughput, with particular attention to reducing mismatch losses.

This paper has described a high resolution radar signal processor designed in response to this situation, using high density LSI logic and a very efficient pipeline architecture. We have also described how this processor is to be changed by evolution to meet the needs of the small fighter airplane of the next decade.

REFERENCES

1. Nathanson, F.E., RADAR DESIGN PRINCIPLES, *McGraw-Hill*, New York, 1969.

2. Hofmeister, E.L., et al., "Modular Survivable Radar for Battlefield Surveillance Applications", *IEE-Radar 82*, London, October 1982.

3. Nevin, R.L. and K.A. Miller, "Distributed Signal and Data Processing in the AN/APG-67 Multimode Radar", *NAECON-85*, Dayton, Ohio.

4. Kuchinski, L.J. and T.R. Patton, "The APG-66 Radar and its Derivative Applications", *6th Digital Avionics Systems Conference*, Baltimore, MD, December 1984.

5. Stimson, G.W., "Introduction to Airborne Radar", *Hughes Aircraft Company*, El Segundo, CA, 1983.

6. Skolnik, M.I., ed., RADAR HANDBOOK, *McGraw-Hill*, New York, 1970.

7. Finn, H.M. and R.S. Johnson, "Adaptive Detection Mode with Threshold Control as a Function of Spatially Sampled Clutter Level Estimates", *RCA Review*, Vol. 29, No. 3, September 1968, pp. 414-464.

8. Ennis, W.G. and H.A.F. Spaanenburg, "High Performance Programmable Signal Processors", *NAECON '85*, Dayton, Ohio, May 1985.

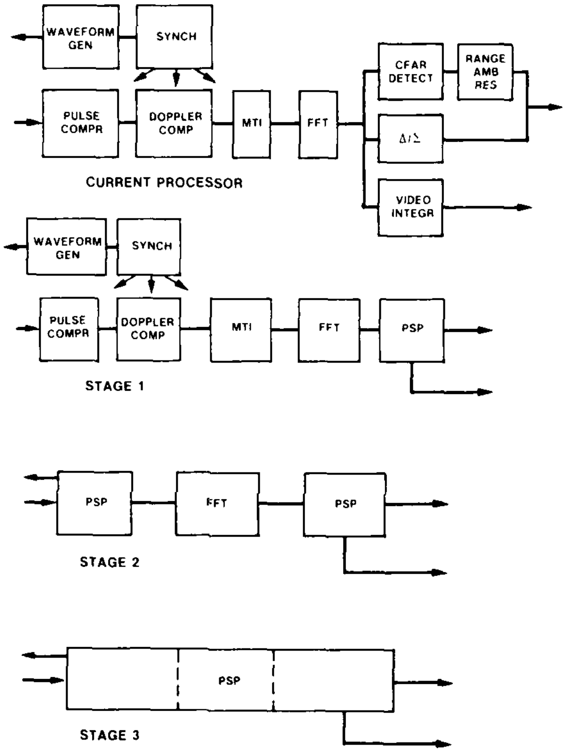

Figure 8. Staged Integration of PSP

DISCUSSION

Lazzareschi

(1) What type of pulse compression is utilized?

(2) The number of instructions shown is for the 1 or 0.25 μs pulse?

Author's Reply

(1) It is not specified, only the BI product is defined.

(2) 0.25 μseconds but without oversampling.

Angular Super-Resolution with Array Antennas - Application to Seeker-Heads

U. Nickel
Forschungsinstitut fur Funk und Mathematik der FGAN (FFM-FGAN)
D-5307 Wachtberg 7, F.R. Germany

Abstract

Monopulse seeker-heads can give large errors due to closely spaced targets or even completely wrong directions in the case of cross-eye deception. The effective countermeasure against these errors is resolution enhancement. Super-resolution methods offer the possibility to resolve targets closer than the antenna beamwidth. Such methods are favourable for seeker-head applications, because the target separation as well as the signal-to-noise ratio increases as the missile approaches the target.
All effective super-resolution methods require an antenna array with access to the single element outputs. Thus mechanical scanning is replaced by electronical scanning. Depending on the type of missile (SAM, AAM, ARM), sometimes antenna pattern restrictions have to be tolerated. Among all super-resolution methods the parametric target model fitting (PTMF) method seems to be most appropriate for this application. This method tries to fit a completely parameterised target model directly to the measured data. It can be rather easily computed (compared with other powerful methods like eigenvector decomposition), and it is the only method which can resolve completely correlated targets, which arise in the case of multipath and cross-eye deception. For seeker-heads with few antenna elements an implementation with digital signal processor chips is most suited. Computer simulations and experiments with measured data using the DESAS test equipment at FFM show that two targets separated at 0.3 beamwidth can be resolved in azimuth and elevation and that the switch from conventional monopulse to two-target estimation (super-resolution), which is crucial for the approaching missile, can be done by a reliable automatic test procedure.

DYNAMIQUES ET ALGORITHMES DE TRAITEMENT DU SIGNAL DANS LES MODES RADAR A HAUTE FREQUENCE DE RECURRENCE

par

Philippe LACOMME
THOMSON-CSF
Division Equipements Avioniques
Département RCM
173, avenue Pierre Brossolette
92120 MONTROUGE
FRANCE

RESUME

Le problème de la dynamique importante des signaux à traiter est particulièrement ardu dans le cas des modes radars à haute fréquence de récurrence (HFR). La dynamique de réception et de traitement du signal nécessaire sera d'abord définie et évaluée dans un cas typique. Les effets de la quantification sont ensuite analysés aux différentes étapes de la chaîne de traitement du signal (codage, filtre réjecteur, transformée de Fourier). Il est montré que les bruits de quantification dépendent beaucoup des algorithmes de traitement utilisés. Ainsi, la présence d'un filtre réjecteur des échos de sol peut indirectement accroître les problèmes de troncature dus aux éléments situés en aval de ce filtre. De même, les différents algorithmes de calculs de la transformée de Fourier (Fast Fourier Transform (Cooley et Tukey) ou Winograd Fourier Transform) ont un comportement très différent vis-à-vis des troncatures effectuées dans les opérateurs. Le choix des algorithmes de traitement devra donc prendre en compte, outre leurs performances en nombres d'opérations élémentaires, leur sensibilité aux bruits de quantification.

1 - DYNAMIQUES DES SIGNAUX DANS LES MODES HFR

1.1. Dynamique totale et dynamique instantanée

On a représenté sur la figure 1 l'évaluation des variations de la puissance des échos de sol et de la puissance de l'écho de cible, en fonction de la distance, lorsque la cible, centrée dans le lobe de l'antenne, se trouve à proximité du sol. Cette évaluation correspond à un cas typique de mode HFR (puissance crête : 3 KW - cible 5 m² - fréquence de récurrence : 200 KHz - altitude porteur : 5000 ft).

La dynamique totale des signaux (contraste entre la puissance minimale de la cible et la puissance maximale du sol) dépasse 100 dB. Toutefois, ces niveaux extrêmes ne sont pas reçus dans la même configuration (les sites antenne sont différents).

Le contraste le plus élevé entre la puissance du sol et la puissance de cible reçus simultanément est obtenu pour une cible en limite de portée (distance maximale). Ce contraste instantané est alors de 55 dB.

La dynamique instantanée nécessaire pour traiter correctement ces signaux doit être supérieure à ce contraste. En effet :

- le signal minimal détecté est supérieur au bruit thermique (typiquement 5 dB) après traitement Doppler,
- le signal maximal doit être reçu et traité sans saturation. Il est nécessaire de prendre une garde de 10 dB pour tenir compte des fluctuations.

La dynamique instantanée nécessaire (rapport entre le bruit thermique et le signal maximal traité sans saturation) est de l'ordre de 70 dB.

1.2. Evaluation des parasites maximaux

Les traitements effectués dans le radar introduisent des signaux parasites par effet de saturation ou par effet de quantification. Ces parasites ne sont pas en général des bruits blancs et se traduisent par des faux échos localisés. Le niveau tolérable de ces échos parasites, donné par la courbe de probabilité de détection du radar (voir figure 2), doit être tel que la fausse alarme dans la case fréquence considérée relève d'une façon insensible la fausse alarme globale. On admet que ce niveau se situe environ à 10 dB sous le signal minimal, soit environ 5 dB sous le bruit thermique. Ce parasite doit donc être de l'ordre de 75 dB sous le signal maximal, ce qui fixe le taux d'élimination du radar et donc la dynamique des traitements.

2 - DYNAMIQUE DE CODAGE ET DE TRAITEMENT

2.1. Généralités

Il est bien connu que le bruit de quantification a une puissance égale à $\frac{q^2}{12}$, où q est la valeur de l'échelon de quantification. Toutefois, ce "bruit" de quantification n'est pas toujours blanc et la densité spectrale de bruit se présente souvent sous forme de raies parasites dans lesquelles toute l'énergie de bruit est concentrée.

Nous allons étudier une chaîne de traitement classique composée (voir figure 3) :

- d'un convertisseur analogique-numérique (CAN),
- d'un filtre de simple annulation (SA) dont le rôle est la réjection partielle du lobe principal,
- d'une transformée de Fourier rapide (FFT) implantée dans un calculateur travaillant en 16 bits fixes,
- d'un dispositif de compensation du gain de la SA et de blanking des zones inutiles.

2.2. Influence du codage

Choix du poids du LSB (least significant bit)

La théorie indique qu'en présence de bruit gaussien de valeur efficace (écart type) σ, le pas de quantification maximal est $q = 2\,\sigma$.

Les figures 4, 5 et 6 nous montrent une analyse spectrale du bruit de quantification (différence entre le signal quantifié et le signal d'origine) en fonction de $\frac{\sigma}{q}$ pour un codeur sans défaut, le signal codé étant composé de bruit gaussien superposé à une sinusoïde de grande amplitude (σ constant).

Le bruit de quantification, constant en valeur relative pour $\frac{\sigma}{q} = 1$ (figure 4) et $\frac{\sigma}{q} = \frac{1}{2}$ (figure 5), produit de nombreuses raies parasites pour $\frac{\sigma}{q} = \frac{1}{4}$ (figure 6).

En fait, les codeurs ne sont pas parfaits et les tolérances admises ($\pm \frac{1}{2}$ LSB) peuvent entraîner, localement, des variations de la valeur de q dans la dynamique de codage. De telles variations induisent des raies parasites (voir figure 7) qui peuvent être masquées en accroissant $\frac{\sigma}{q}$.

De plus, le gain de la chaîne de réception pouvant varier de quelques dB, le pas de codage maximal doit être $q \leq \frac{\sigma}{2}$.

Dynamique de codage

Le traitement Doppler effectué (FFT) accroît le contraste entre le bruit codé et le signal de 25 dB environ (FFT 512 points).

La contrainte de codage étant $q = \frac{\sigma}{2}$, la dynamique minimale de réception étant de 70 dB et le codeur devant prendre en compte les valeurs crêtes (et non les valeurs efficaces), la dynamique minimale de codage doit être 70 - 25 + 6 + 3 = 54 dB, ce qui est obtenu avec un codeur 10 bits (9 bit + signe).

En fait, ce choix impose que la dynamique totale du codeur soit en permanence utilisée ce qui ne peut être obtenu qu'en régulant le gain de la chaîne de réception par une boucle de contrôle automatique de gain (CAG) précise.

Si on souhaite s'affranchir de cette boucle (sensible aux brouillages), la dynamique de codage doit être supérieure à 12 bits.

2.3. Influence du filtre de simple annulation

Le rôle de la simple annulation (SA) est de réduire la puissance des échos de sol avant FFT pour diminuer la dynamique de traitement de ceux-ci.

Avec une dynamique de codage d'environ 12 bits et un calculateur de traitement du signal travaillant en 16 bits fixes, il n'y a pas a priori de problème de troncature au niveau de cette simple annulation.

En fait, l'effet de filtrage de la simple annulation atténue le niveau de bruit radar pour les faibles fréquences (modulo FR). La figure 8 représente le spectre d'une sinusoïde superposée à du bruit blanc codé avec $q = \frac{\sigma}{2}$ après simple annulation et FFT sans troncature.

En réalité, le calculateur de traitement du signal (16 bits fixes) comporte un multiplieur qui tronque le résultat. Le bruit de troncature (équivalent à un bruit de quantification) se présente comme un bruit blanc superposé au bruit radar comme le montre la figure 9. Pour les faibles valeurs de fréquence, ce bruit est supérieur au bruit radar et désensibilise le radar. La figure 10 montre le résultat obtenu après compensation du gain de la SA.

La solution à ce problème est de remonter le gain entre la SA et la FFT pour que le bruit de troncature du multiplieur devienne négligeable vis-à-vis du bruit radar même pour les plus basses fréquences utiles (voir figure 11). Ceci réduit évidemment la dynamique des signaux de cibles traités.

2.4. Influence de l'algorithme de transformée de Fourier

Il existe différents algorithmes pour calculer la transformée de Fourier du signal dont les performances en temps de calcul sont importantes pour le dimensionnement des processeurs de traitement du signal. La transformée de Fourier de Winogad (WFT) par exemple assure un gain de calcul supérieur à 50 % par rapport à l'algorithme classique de FFT (algorithme de Cooley - Tukey) pour l'application considérée (N ≃ 500 points).

Par contre, le comportement de ces algorithmes vis-à-vis des problèmes de troncatures liés aux multiplieurs utilisés dans les processeurs est très différent. Ainsi, l'algorithme de WFT est beaucoup plus sensible aux troncatures. De plus, même pour l'algorithme de WFT, l'ordre d'exécution des transformées de Fourier élémentaires est important comme le prouvent les figures 12 et 13 qui montrent le signal en sortie de WFT 504 points effectué dans l'ordre 7-9-8 (figure 12) et dans l'ordre 8-7-9 (figure 13). Pour ces deux exemples, le signal d'entrée est composé d'une sinusoïde superposée à du bruit blanc (codées avec $\frac{\sigma}{q} = 2$) et le résultat a été moyenné sur 10 tirages pour mettre mieux en évidence les raies parasites générées dans le cas 7-9-8.

L'algorithme FFT (512) est dans ce cas préférable même s'il est moins optimisé en temps de calcul.

3 - CONCLUSIONS

La dynamique des signaux à traiter dans les modes à haute fréquence de récurrence des radars aéroportés impose des contraintes sévères au niveau de la réception et du traitement de ces signaux.

Après avoir évalué la dynamique strictement nécessaire vis-à-vis des signaux de retour de sol, de cibles et de parasites, nous avons abordé le problème des bruits et parasites de quantification aux différentes étapes de la chaîne de traitement. Le but de cette étude est de permettre le cadrage de la dynamique utile dans la dynamique disponible donnée par un processeur de traitement du signal travaillant en 16 bits fixes.

Il a été montré que l'étude des bruits de quantification est primordiale dans le choix des algorithmes de traitement du signal et que les solutions à retenir ne sont pas toujours les solutions optimales en temps de calcul.

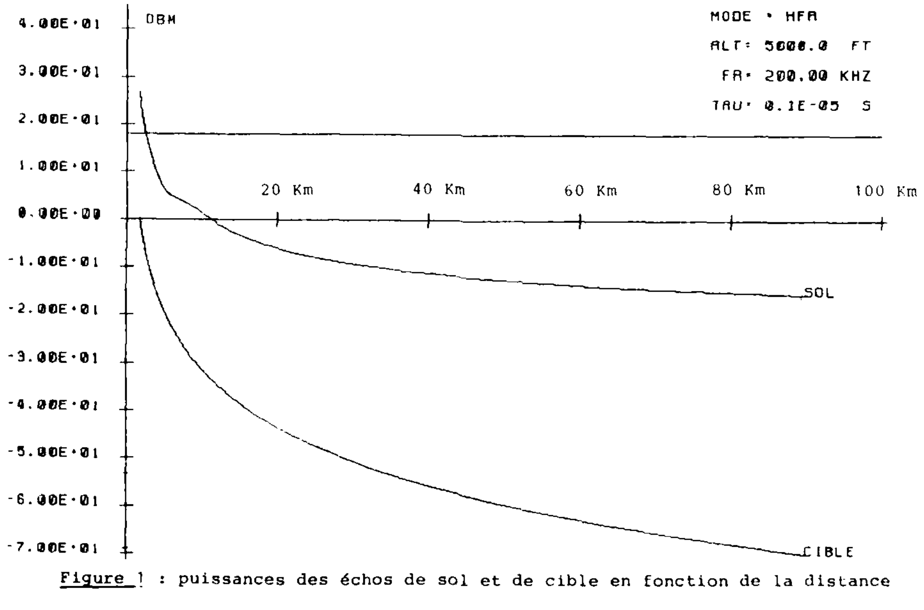

Figure 1 : puissances des échos de sol et de cible en fonction de la distance

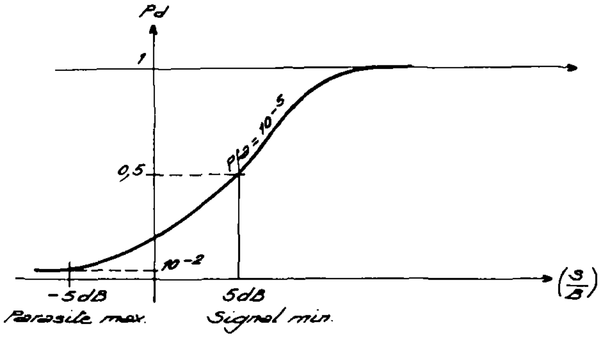

Figure 2 : évaluation de la cible minimale et du parasite maximal sur la courbe de détection (sortie FFT)

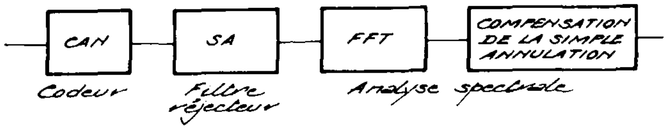

Figure 3 : chaîne de traitement du signal HFR

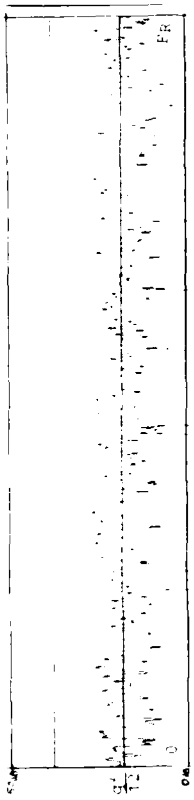

Figure 4 : bruit de quantification pour $\frac{\sigma}{q} = 1$ - codeur parfait

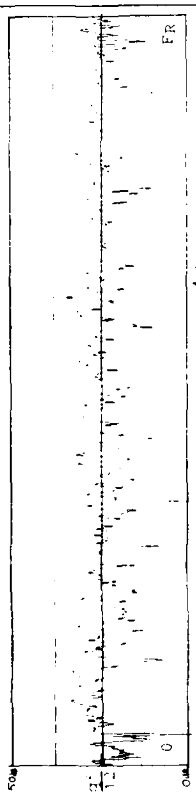

Figure 5 : bruit de quantification pour $\frac{\sigma}{q} = 1/2$ - codeur parfait

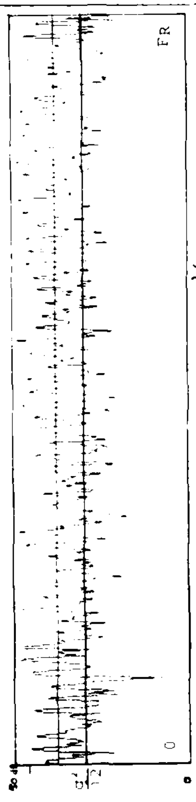

Figure 6 : bruit de quantification pour $\frac{\sigma}{q} = 1/4$ - codeur parfait

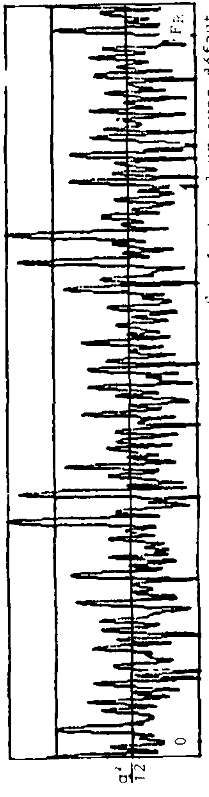

Figure 7 : bruit de quantification pour $\frac{\sigma}{q} = 1$ et codeur avec défaut ($\pm \frac{1}{2}$ LSB)

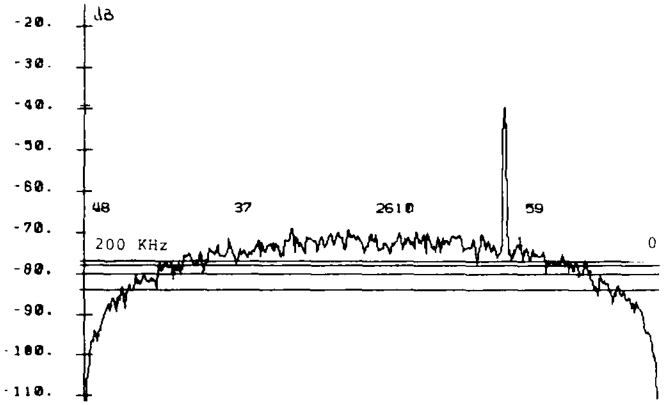

Figure 8 : influence de la SA sur le spectre (FFT sans quantification)

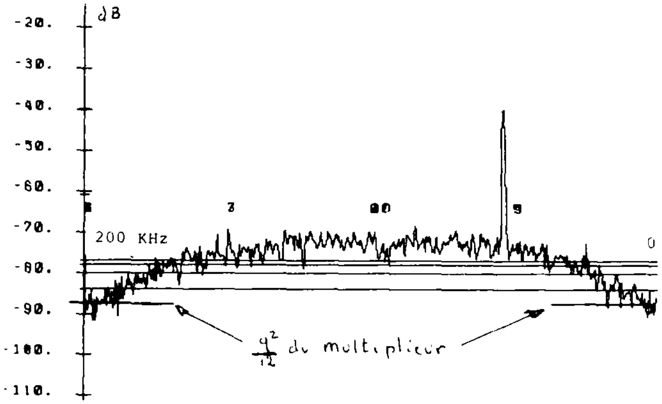

Figure 9 : influence du bruit de troncature du multiplieur pour les basses fréquences

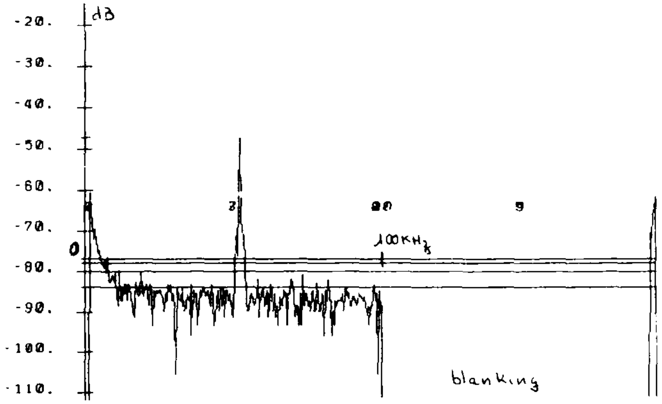

Figure 10 : bruit de troncature du multiplieur après compensation de la SA

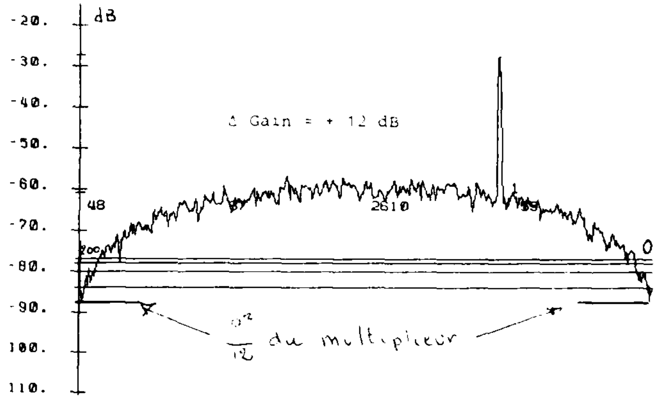

Figure 11 : réduction du bruit de troncature par adjonction d'un gain après la SA

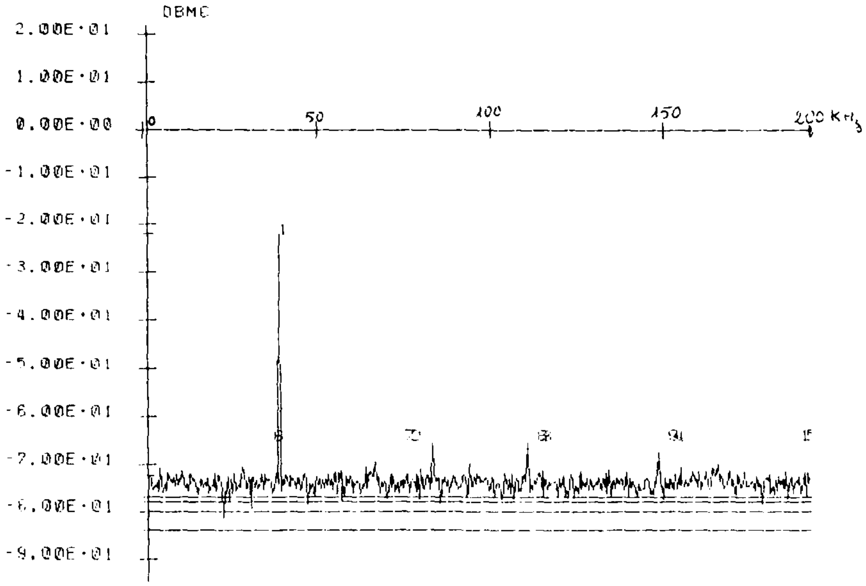

Figure 12 : spectre avec WFT 504 points 7-9-8

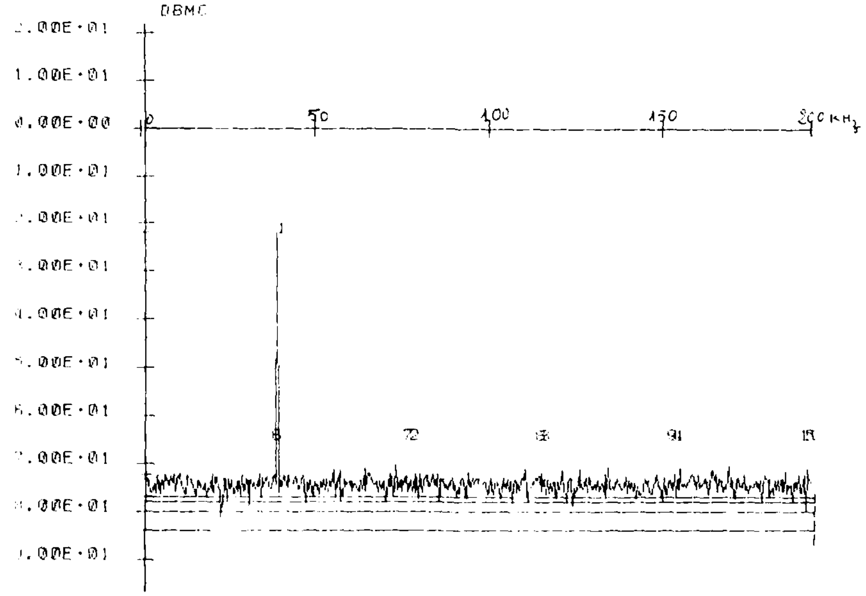

Figure 13 : spectre avec WFT 504 points 8-7-9

DIGITAL AND OPTICAL SYSTOLIC ARCHITECTURES FOR AIRBORNE ADAPTIVE RADARS

by
Stanley Lis
Vincent C. Vannicola
John A. Graniero
Surveillance Division
Rome Air Development Center
Griffiss Air Force Base, New York 13441-5700, USA

Barry P. Medoff
Advanced Processor Technology Laboratory, ESL
495 Java Drive, PO Box 3510
Sunnyvale, CA 94088-3510, USA

William A. Penn
Military Electronic Systems Operations, General Electric Company
Syracuse, NY 13221-4840, USA

SUMMARY

Systolic architectures for digital and analog, electronic and optical signal processing are presented along with specific applications to adaptive nulling. It is shown how the various architectures provide for the implementation of adaptive algorithms and how technologies affect performance. Their effects on adaptive degrees of freedom, convergence time, null depth, signal to noise ratio are presented along with size, weight, and required power. Adaptive algorithms covered are of two basic types: feedback/iterative and direct methods. Examples of each include the Least Mean Square (LMS) for the iterative type and the QU factorization based on the Givens Method for the direct method.

Simulation results have verified the performance of the least squares and the systolic array for QU factorization by Givens Method. Improved performance was obtained using the modified minimum variance distortionless response algorithm based on the maximum likelihood criteria. An optical implementation of the least squares algorithm over a continuously adaptive multi-path was experimentally evaluated. Thus far, 24 dB of cancellation was achieved over a 7 micro-second multi-path window for 10 mega-Hertz instantaneously bandwidth.

Adaptivity in the spatial, temporal, and Doppler domains are illustrated and their embodiment into the various architectures are presented. For example, an analog optical processor which generates weights in the spatial and temporal (multi-path) domains for broadband systems is shown. Also shown is a digital systolic architecture which is applied to a direct decomposition method for generation of adaptive weights in the spatial and Doppler domains. A description of brassboard models representing both type architectures that will be tested in RADC (Rome Air Development Center) laboratories is included.

THE ELECTROMAGNETIC AIRBORNE RADAR ENVIRONMENT

A typical radar system contains a large steered array that alternately transmits and receives RF pulses. The array is focused so that energy is directed primarily in a single direction, and so that the array has maximum receiving gain for returns from the same direction. Returning pulses have power proportional to r^{-4} while jamming and other forms of active interference have power proportional to r^{-2} where r is the distance from the airborne radar to the emitter. Returning pulses also have a Doppler shift proportional to the relative velocity between the radar and the target. A typical air based radar is shown in Figure 1. Many signal processing techniques have been developed for receiving desired radar returns in the presence of jamming, clutter, and multi-path ([1] Applemaum 1966, [2] Brennan and Reed 1973, [3] Masak, Kowalski, Lackey and Saggio 1980). These techniques employ adaptive spatial filtering to reject signals from other than the look direction, adaptive spectral nulling to discriminate between desired and undesired signals on the basis of Doppler shift, and adaptive time delay equalization to cancel delayed replicas of these noise like signals due to multi-path environments.

In order to achieve such multi-domain nulling, radar systems usually combine the received signal from the main array with signals from one or more low gain auxiliary elements as illustrated in Figure 2. In practice, the auxiliary elements may physically be a subset of the large number of omnidirectional low gain antennas that comprise the main array. Because the auxiliary elements are low gain and the desired returns are very weak (due to the r^{-4} attenuation), the signals from these elements are dominated by jammer, clutter, and multi-path and can therefore be used to compute the adaptive weights.

The paper focuses on algorithms and architectures for combining the signals from the auxiliary and the main array so as to separate the desired returns from sources of interference caused by clutter, jammers and associated multi-path.

ADAPTIVE ARRAY PROCESSING

We shall now review the standard mathematical model that is used in adaptive array processing. Figure 3 illustrates the generic adaptive array processing problem. In the basic model, an array of sensors receives a linear superposition of multiple signals and noise. The adaptive signal processor separates the signals, and generates as output the waveforms or parameters of one or more of the signals.

An adaptive array processor typically is based on an adaptive linear combiner of the type shown in Figure 4. The processor forms an estimate of a desired signal as a linear combination of a set of mp samples received at m sensors at p different times. This linear combination is determined by a set of mp coefficients that are generated by an adaptive signal processing algorithm.

The tapped delay line structure of the linear combiner allows for discrimination among signals on the basis of their spectral or time delay characteristics. This is important when the frequency range of interest is large compared with the carrier or center frequency (the wide-band case). In narrow band problems it is sufficient to combine only one sample from each sensor. A single wide-band problem can often be separated into a large number of distinct narrow-band problems by Fourier transforming the data that is received at each sensor.

The optimal weight vector is given as the solution to the discrete Weiner-Hopf equation, $R\,w = d$, where R is the covariance matrix of the incomming signals taken across each element and d is the cross correlation between the received data x(t) and the unknown desired signal, s(t). The covariance matrix, R, and cross correlation vector, d, are unknown quantities, and thus it is not possible to compute the optimum weight vector. However, an approximation to the optimal weight vector can be found by solving the deterministic least squares problem, minimize $\|Aw - b\|$, where A is the snapshot matrix of the time sequence of all the array elements and b is the so called desired response. Constraints may be introduced to the least squares problem in the form of $Cw = e$ where C and e are defined as a complex matrix and a complex vector respectively and are based on apriori knowledge, e.g. the look direction. Combining the deterministic data and constraints leads to the formulation of the soft-constraint least-squares problem that will be the subject of the algorithm and architecture discussed later. In this case, we find a weight vector, w, that minimizes

$$\|Aw - b\|^2 + \|Cw - e\|^2$$

The solution to the soft constraint problem will not satisfy either the normal equations determined by the data, or the constraint equation, but will in effect be a compromise between the two.

We will assume that the columns of A are linearly independent which guarantees that the LS problem has a unique solution. This unique LS solution is given by $w = A^{+}b$ where A^{+} is the $m \times M$ generalized inverse of A. The LS solution of $Aw = b$ is also the unique solution of the normal equations

$$A^H Aw = A^H b$$

Under our assumptions that the columns of A are linearly independent, the $m \times m$ matrix, $A^H A$ is nonsingular, and therefore the LS solution is given by

$$w = (A^H A)^{-1} A^H b$$

In computing the LS solution, it is best not to form the normal equations. The LS solution can be found with better accuracy and less computation through a factorization of the data matrix A of the form, $A = QU$ where Q is an $N \times m$ matrix with orthonormal columns, $Q^H Q = I$, and U is an $m \times m$ upper triangular matrix. There are well known procedures for computing a factorization $A = QU$ based on Gram-Schmidt orthogonalization, Givens rotations and Householder reflections (GVL).

It has been shown by [4] B.P. Medoff et al that a soft-constraint formulation of the LS problem includes as a special case a related hard-constraint LS problem. The hard-constraint problem is as follows: minimize $\|Aw\|$ subject to $d^H w = 1$ where A is an $n \times m$ complex data matrix as before, and d is an n element column vector. The equation $d^H w = 1$ is a so-called hard constraint. It is easily verified that the solution to the hard-constraint LS problem is given by

$$w = \frac{1}{\alpha}(A^H A)^{-1} d$$

where $\alpha = d^H A^H A\, d$

To obtain this vector as the solution of a LS problem with soft constraints, consider minimizing the cost

$$J(w) = \|Aw - b\|^2 + \|Cw - e\|^2$$

where $b = 0 \qquad C = d^H \qquad e = 1$

The solution to the unconstrained problem can be written (Medoff et al) as

$$w = (A^H A + dd^H)^{-1} d = \frac{1}{1 + d^H A^H A\, d}(A^H A)^{-1} d$$

This is a scalar multiple of the solution to the hard constrained problem.

We have shown that both the soft-constraint LS problem, minimize $\|Aw - b\|^2 + \|Cw - e\|^2$ and the hard-constraint LS problem, minimize $\|Aw\|$ subject to $d^H w = 1$, can be embedded in a larger unconstrained LS problem. Many algorithms for solving unconstrained LS problems have been investigated. We will concentrate on the QU factorization based on the Givens Method since this method has both superior numerical properties and an excellent systolic implementation. We start with the Gram-Schmidt algorithm as a basis from which we go into the Givens Method.

MODIFIED GRAM-SCHMIDT (MGS) ALGORITHM

The Gram-Schmidt algorithm computes a factorization of the data matrix, $A = QU$, where U is an $m \times m$ complex upper triangular matrix with positive real diagonal elements, and Q is an $N \times m$ complex matrix with orthonormal columns, $Q^H Q = I_{m \times m}$, a unit matrix. The MGS algorithm generates the columns of Q by sequentially processing the columns of A. Let a_i denote column i of A,

$$A = [a_1\ a_2\ .\ .\ .\ a_m]$$

and let q_i denote column i of Q

$$Q = [q_1\ q_2 \cdot \cdot \cdot q_m]$$

Let the elements of the upper triangular matrix, U, be

$$U = \begin{bmatrix} \alpha_{11} & \beta_{12} & \beta_{13} \cdot & \cdot & \beta_{1m} \\ & \alpha_{22} & \beta_{23} & & \cdot \\ & & \alpha_{33} & & \cdot \\ \cdot\ \cdot & 0 & \cdot\ \cdot & \cdot & \cdot \\ & & & & \alpha_{mm} \end{bmatrix}$$

The factorization generated by MGS can be used to solve the LS problem as follows. Substitute $A - QU$ in the original equation $Aw = b$ to obtain $QUw = b$, or $Uw = Q^H b$. The solution is found by comupting $e = Q^H b$ (matrix multiply) and then solving $Uw = e$ for w (backsubstitution).

GIVENS METHOD

Givens Method is a QU algorithm that computes the LS solution of $Aw = b$ without explicitly forming the matrix $A^H A$ that apears in the normal equations. Instead, the algorithm applies a sequence of 2×2 complex Givens rotations that transform the matrix **A** into an upper triangular matrix **U** with a positive real diagonal. The matrix U is related to A by an orthogonal transformation Q such that A = QU where the columns of Q are orthonormal, $Q^H Q = I$. Note that

$$A^H A = U^H Q^H Q U = U^H U$$

We conclude that **U** is the same upper triangular matrix that is obtained by applying the Cholesky algorithm to $A^H A$.

We will first state the complex Givens algorithm for determining the upper triangular matrix U. The algorithm applies plane rotations that are defined as follows. Given a complex number, x, and a real number, ℓ, we define a 2×2 complex matrix, $M(x,\ell)$ by

$$M(x,\ell) = \begin{bmatrix} c & \mu \\ -\mu & \bar{c} \end{bmatrix}$$

with elements c and μ such that

$$\begin{bmatrix} c & \mu \\ -\mu & \bar{c} \end{bmatrix} \begin{bmatrix} x \\ \ell \end{bmatrix} = \begin{bmatrix} \rho \\ 0 \end{bmatrix}$$

where μ and ρ are real. The quantities ρ, c, and μ are given by

$$\rho \leftarrow (\ell^2 + |x|^2)^{1/2}$$

$$\bar{c} \leftarrow x/\ell$$

$$\mu \leftarrow \ell/\rho$$

It is easily verified that **M** is an orthogonal matrix, $M^H M = MM^H = I$. To simplify the algorithm we will assume that the last row of A is zero. The algorithm overwrites the elements of A forcing zeroes below the diagonal starting from the left column and the last row. The triangular factor, **U**, is left in the first m rows of **A**.

ALGORITHM REALIZATION

Algorithms that form the sample covariance matrix, $A^H A$, solve a problem that is more sensitive than the problem solved by algorithms that work directly with the data matrix, **A**. The sensitivity of the first problem is governed by the ratio [5] Golub 1983 of the maximum eigenvalue to the mimimum eigenvalue of the covariance matrix. On the other hand, the sensitivity of the second problem is governed by the ratio [6] Elden 1980 of the maximum singular value of **A** to the minimum singular value of **A**. Because the first problem can be much more sensitive than the second problem, this increased sensitivity means that methods which form $A^H A$ can require twice as many bits of precision to achieve the same accuracy as methods that process A directly.

Of the methods that process A directly, two methods -- Gram-Schmidt and Givens Method -- are QU methods: that is, they compute a factorization A = QU where Q has orthonormal columns, $Q^H Q = I$. In QU methods, the input data is subjected to orthogonal linear transformations. Because an orthogonal transformation preserves angles between vectors and the lengths of the vectors, no large numerical values can occur at intermediate stages of the computation. In addition, no ill-conditioned matrices can be created if the input is well conditioned. The absence of large intermediate results is essential to control the introduction of roundoff errors. The preservation of conditioning prevents unnecessary growth in the effect of roundoff. The numerical stability of QU algorithms is well established in the numerical analysis literature. The stability of the Givens Method is shown by [5] Golub and Van Loan (GVL) and [7] Wilkinson (AEP). See also [8] Gentleman 1973 and [9] Hammarling 1974. The stability of the Modified Gram-Schmidt is shown by [10] Bjorck 1967.

The MSG algorithm selected here works within the dynamic range, r, of the input data. Hence fixed point precision of r bits is adaquate. However, the use of floating point arithmetic representation will greatly simplify the design by eliminating the need for complicated scaling thus allowing hardware flexibility for problems of varying size and dynamic range.

HARDWARE REALIZATION

The QU factorization based on Givens Method has both superior numerical properties and an excellent systolic implementation. The general characteristics of systolic arrays are well documented in the literature [11] Kung 1980.

Reliability and Fault Tolerance:

The important issue of reliability and fault tolerance is common to all of our systolic designs. We will consider two approaches to fault tolerance in systolic arrays: reconfigurable arrays, and fault tolerant algorithms. In the reconfigurable array approach a defective cell is bypassed. The bypass requires staging registers, but there is no increase in interconnection length. For a unidirectional linear array, 100% utilization of live cells is achieved for any number of failures as illustrated in Figure 5. For two-dimensional arrays, a reasonably good utilization of live cells can be achieved if the faulty cells can be bypassed to create a smaller two-dimensional array as in Figure 6.

An alternative approach is based on fault tolerant algorithms. These algorithms use error correcting codes--similar to checksums--that are preserved by the matrix computation of the array. A low-cost weighted checksum scheme can detect and correct single errors. The hardware and time penalties are minimal. Figure 7 shows that if a properly encoded matrix, A, having two checksum vectors is multiplied by a similarly encoded matrix, B, the matrix multiplication preserves the checksums. If the checksum indicates an error, a simple correction algorithm is invoked. The checksum technique is applicable to matrix addition, multiplication, various decompositions, transposition, and scalar matrix products.

Hardware System Architecture:

A block diagram of the signal processing system is shown in Figure 8. Signals received at the antennas are down converted to an intermediate frequency, then digitized and stored in a buffer memory. The digital processing system is divided into two parts; the Systolic Weight Computer (SWC) which reads blocks of data from memory and computes an optimal weight vector and the Digital Weight Applier (DWA) which computes complex dot products between a weight vector and the data from the sensor array.

The same architecture, and all of our Systolic Weight Computer designs given below, are applicable to a hybrid system that uses an analog weight applier. We believe, however, that an all digital approach has many advantages. The digital weight applier does not suffer from the phase and gain inaccuracies that are inherent in an analog beamformer. Furthermore, by digitizing and buffering the data, non-causal processing is possible. The weights can be applied to the same data from which they were calculated.

We assume that all processing is done on blocks of N snapshots. The system memory must accommodate at least three blocks of size N: one being filled with new data from the sensors, one holding data from which a weight vector is being computed, and one from which outputs are being formed (it may be possible to overlap the input and output blocks). In addition, if we assume that the system is pipelined with k stages, the memory must be capable of storing data for d distinct problems. Thus roughly 3kNm complex integers must be stored. Note that the number of bits per word is the number of bits provided by the analog-to digital converter.

VLSI/VHSIC Chips:

ESL has studied the use of custom VLSI chips and commercial VLSI chips in their hardware designs. The characteristics of these chips are summarized in Table I. All of the floating point chips (labeled FP) in Table I are applicable to the Systolic Weight Computer. The remaining chips are fixed point and are applicable to the Digital Weight Applier.

The ESL Systolic Chip is a custom VLSI chip that has been specifically designed for use in systolic arrays. The chip is a high speed floating point multiply/adder designed to support both complex and real arithmetic. A functional floor plan of the chip is shown in Figure 9. Chip operands are 32 bit IEEE format floating point numbers. In complex mode, successive operands are treated as the real and imaginary parts of complex numbers. In real mode, each floating-point operand is treated as a distinct real number. The chip has 3 input data ports (A, B, and C) and 2 output data ports (BD and CD) operating at 10 Mhz. All 5 data ports are 1 byte (9 bits) wide requiring 4 consecutive 1-byte data transfers to complete a real operand transfer. The principal operation performed by the systolic chip is to accept 3 input operands (A, B, and C) and produce 2 results (BD, and CD) such that

$$BD \longleftarrow B$$

$$CD \longleftarrow A*B + C$$

Control lines are provided that can selectively invert and or conjugate the A, B, and C inputs. The BD output, a delayed version of the B input, is useful for interchip data propagation within a systolic array. Special input and output controls are provided for interchip synchronization. The chip employs extensive pipelining to achieve high throughput. It is implemented in a 1.5 micron CMOS process with approximately 55,000 transistors. Power dissipation will be approximately 2 watts at the 50 ns maximum clock rate. Finally, we point out that the ESL Systolic Chip meets the VHSIC I functional throughput specification of 5×10^{11} GATE-Hz/cm^2.

Systolic Weight Computer:

The Systolic Weight Computer (SWC) reads data from the data memory and computes an optimal weight vector using the Givens Method as follows.

1. Form $\mathring{A} \longleftarrow \begin{bmatrix} C \\ A \end{bmatrix}$

   $\mathring{b} \longleftarrow \begin{bmatrix} e \\ b \end{bmatrix}$

2. Form $\bar{A} \longleftarrow \begin{bmatrix} \mathring{A} & \mathring{b} \end{bmatrix}$

3. Apply Givens algorithm to $\bar{A}$ to obtain

$$Q^H\bar{A} = \begin{bmatrix} U & Q^H\mathring{b} \end{bmatrix}$$

4. Solve $Uw = Q^H \mathring{b}$ for w by backsubstitution.

The hardware implementation of Givens Method makes use of two systolic arrays. The first systolic array which we will refer to as the QU array, applies an orthogonal transformation Q to a large matrix formed from A, b, C and e as follows.

$$Q^H \begin{bmatrix} C & e \\ A & b \end{bmatrix} = \begin{bmatrix} U & f \\ 0 & g \end{bmatrix}$$

where U is an $m \times m$ upper triangular matrix with positive real diagonal, 0 denotes a $(N-m) \times m$ matrix of zeroes, and f is an m element vector. The optimum weight vector is the solution to the triangular system

$$Uw = f$$

The second systolic array is therefore a backsolve array which solves for the optimal weight vector. Figure 10 shows a block diagram of the SWC with the two systolic arrays that are used in Givens Method. We will describe both systolic arrays in detail. For each array we will give the cell definition and interconnection, and then consider tradeoffs in cell implementation.

The QU factorization array is based on a design given by [8] Gentlemen and Kung (1981), and on extensions given by [12] Schreiber and Kuekes (1982). The basic QU array is triangular with m rows and m+1 columns. The topology of a 12×13 array is illustrated in Figure 11. The arrays contain cells of two types: boundary cells (circles) which generate plane rotations, and internal cells (squares) which apply plane rotations. Data is clocked into the array from the top. The upper triangular matrix U and vector f are computed in the array. Figure 12 depicts the operation of the boundary and internal cells in more detail. The boundary cell reads a complex input value, x, and stores internally a real number, ℓ. It computes real numbers, ρ and μ and a complex number, c, as

$$\rho \longleftarrow (\ell^2 + |x|^2)^{1/2}$$

$$c \longleftarrow \bar{x}/\rho$$

$$\mu \longleftarrow \ell/\rho$$

All cells in the array change state with a clock input. Thus if ℓ is the current state of the boundary cell, ρ is taken as the next state (by state we mean the value stored in the cell). The quantities c and μ define a 2×2 rotation such that

$$\begin{bmatrix} c & \mu \\ -\mu & \bar{c} \end{bmatrix} \begin{bmatrix} x \\ \mu \end{bmatrix} = \begin{bmatrix} \rho \\ 0 \end{bmatrix}$$

The internal cell applies a 2×2 rotation to a two element complex vector. The cell stores a complex number, y, internally. It reads a complex number, x, from the cell above, and the quantities, c and μ, from the cell to the left. The internal cell computes the quantities, y and z as

$$\begin{bmatrix} y \\ z \end{bmatrix} \leftarrow \begin{bmatrix} c & \mu \\ -\mu & \bar{c} \end{bmatrix} \begin{bmatrix} x \\ y \end{bmatrix}$$

The rotation, c and μ is passed to the cell on the right, z is passed to the cell below, and y becomes the next state of the cell.

The operation of the QU array is best understood by the following inductive explanation. Let $\mathbf{A}$ be an $N \times m$ matrix and suppose that we have an $m \times m$ upper triangular matrix $\mathbf{U}$ such that $\mathbf{A} = \mathbf{QU}$ where $Q^H Q = I$. Let $\mathbf{A}$ be the $(N+1) \times m$ matrix formed by adding an additional row x^H to $\mathbf{A}$.

$$\bar{A} = \begin{bmatrix} x^H \\ A \end{bmatrix}$$

Given $\bar{\mathbf{A}}$ and $\mathbf{U}$, we want to find an upper triangular matrix $\bar{U}$ such that $\bar{\mathbf{A}} = \bar{\mathbf{Q}}\bar{\mathbf{U}}$ where $\bar{Q}^H \bar{Q} = I$. In order to find $\mathbf{U}$ we form the $(m+1) \times m$ upper Hessenberg matrix

$$\mathring{U} = \begin{bmatrix} x^H \\ U \end{bmatrix}$$

This matrix has real nonzero values on the first sub-diagonal. Although it is not triangular, it is related to $\mathbf{A}$ through an orthogonal transformation $\mathbf{A} = Q\ U$ where

$$\mathring{Q} = \begin{bmatrix} 1 & 0 \\ 0 & Q \end{bmatrix}$$

The upper triangular matrix $\bar{U}$ is easily computed from $\mathring{U}$ by applying a sequence of m Givens rotations, each of which zeros one element on the subdiagonal of $\mathbf{U}$. With Q_i^H denoting the rotation that zeros $u_{i+1,i}$ we have

$$\begin{bmatrix} \bar{U} \\ 0 \end{bmatrix} = Q_m^H \cdots\cdot Q_1^H \begin{bmatrix} x^H \\ U \end{bmatrix}$$

Figure 13 shows the operation of the QU array in more detail. The input data are skewed in time so that at each internal cell a rotation arrives from the left at the same time as the corresponding input value arrives from the top. A single snapshot is read in on m consecutive clocks, and an additional m clocks are needed to update the entire array. Thus, $N+2m$ clocks are needed to compute the $m \times m$ triangular factor for a matrix of size $N \times m$.

This concludes the subject on digital systolic arrays. Simulation results are contained in [4]. Next we shall describe the Acousto Optic Adaptive Processor.

ACOUSTO-OPTIC ADAPTIVE PROCESSOR

This particular sidelobe canceller lends itself to radar operating in an interference multi-path environment and is configured using an optical signal processing approach. Optimum weights, distributed over the time domain, are generated through the use of Bragg cells, a liquid crystal spatial light modulator and an optical detector.

Major effort has been applied toward the cancellation of interfering/jamming signals incident on radar/communications systems [13]-[18]. The most frequently occurring situation is the reception of interfering signals through the antenna sidelobes. To cancel such forms of interference, an auxiliary set of antenna elements, co-located with the main antenna, are electronically weighted and applied to the antenna output in such a manner so as to continuously place pattern nulls in the directions of interference. In general, one complex weight must be applied to the antenna system for each source of interference located in the electromagnetic environment.

Normally, one interference source as seen by the system may consist of a noiselike signal via the direct path propagation from its radiating element. In narrow band systems, the direct path and all associated multi-paths provide a superposition of correlated replicas of the interfering signal to the system. The net effect is the presence of one interfering signal despite the fact that each replica was received from a different direction. One complex adaptive weight is required to cancel such an interfering signal. For wide band systems the situation is different. As shown in Figure 14 each multi-path propagation gives rise to a delayed replica of interference, which becomes time decorrelated with respect to the direct path. In order to provide for cancellation against such complex interfering environments, one may be required to deploy and weight (1) additional auxiliary antenna elements, or (2) taps off delay lines each driven by an antenna element per independent interferor as illustrated in Figure 15. In the case of time decorrelation due to multi-path, the delay line approach is more desirable since it eliminates the need for additional auxiliary antennas. When deploying such a large number of weights, the circuitry and tap delay spacing become very unwieldy. This is due to the fact that a tap is required at every time delay increment corresponding to the bandwidth rate of the system. For realistic multi-paths, the number of weighted taps can easily become greater than one hundred.

An acousto-optic (AO) version of the canceller shown in Figure 15 was perceived by Dickey [19] in 1975. This original suggested architecture was developed by Rhodes and Brown [20] and more recently by Penn [21] [22]. In such a system, the set of tapped delay lines across the auxiliary channels are implemented through a set of Bragg cells as shown in Figure 16. Each Bragg cell corresponds to a tapped delay line in which the tap spacing is continuously distributed. The reference signal containing the interference enters from the auxiliary channel whereupon it is delayed along the first Bragg cell and multiplied by the main channel signal. The multiplication is the interaction of the optically modulated light diffracted by the stresses set up in the Bragg cell due to the acoustic wave excited by the interference signal. This occurs at reference plane A.

Next, the product of the system output and the delayed auxiliary channel are integrated at the optical image detector integrator and mapped as an image on the surface of a liquid crystal spatial light modulator at plane B in Figure 16. Typically, the integrator weighting function, $\rho_T(t)$ is an exponential decay such as illustrated in Figure 17 with typical storage times from 10-100 ms. The image appearing at the liquid crystal surface represents the weights which must be applied across the second distributed tapped delay line shown at plane C in Figure 16. At this delay line, the interference signal entering from the auxiliary channel is delayed and multiplied by the weight pattern which has been imaged on a second laser beam reflected off the surface of the spatial light modulator. Summing of the weighted delayed interference signals is accomplished through the lens, L4. This optical sum is then detected and subtracted from the input of the main channel. This completes the canceller loop.

One can write the following relation between the detector output and the light modulating input for the entire optical chain as follows:

$$\bar{m}_{me} = 4\,\alpha\,\beta\;{}_D\,P_{TO}\,I_{SO}\,|a_o|^2\,\frac{A_S}{A_T}\int \left\langle \int \bar{r}_{me}(\lambda)\,\bar{a}^*_m\left(\lambda - \frac{x}{v_a}\right)\rho_T(t-\lambda)\,d\lambda \right\rangle \bar{a}_m\left(t - \frac{x}{v_a}\right)\rho_X(x)\,dx \qquad (1)$$

where α, β, and ${}_D$ are gain parameters of the laser modulator, integrator, and output detector, respectively; P_{TO} is the input laser power; I_{SO} is the space correlator laser intensity; A_T, A_S are the aperture areas in planes A and C of figure 3; and $\rho_X(x)$ is the spatial weighting function in plane C.

The entire operation of the optical architecture is displayed in this equation. The inner integral *represents a coherent cross-correlation between the input* $\bar{r}_{me}$ *and the reference signal* $\bar{a}_m$ *with time offset* x/v_a. This represents the weight function as a function of x, which corresponds to multi-path time offset. This weight function, in turn, is multiplied into the reference signal $\bar{a}_m(t - x/v_a)$ in the manner of a transversal filter. This represents a summation of all interference inputs over all possible multi-path offset times.

From the generic diagram in Figure 15, or the more specific optical diagram in Figure 16, it can be recalled that the residue signal, r(t), is formed by the subtraction of the predicted signal, $\bar{m}$ (t), form the input main channel signal, m(t). By this subtraction the loop is closed. Thus,

$$m(t) = r(t) + \bar{m}(t) \qquad (2)$$

By combining this relation with equation (1), the integral equation is generated which describes precisely the dynamics of the closed loop. The equation is general enough to include the case of uncorrelated noise in a(t) or m(t). Uncorrelated noise means that the noise component in either m(t) or a(t) does not correlate with the signal components in these two channels and also does not correlate with the noise component in the other channel. With a given m(t), the integral equation (2) provides a general solution for r(t). This equation is not solvable in analytic form for any but the simplest forms of m(t) and a(t).

Experimental System:

In our present experimental system, a Galium Aluminum Arsenide (GaAlAs) semiconductor diode laser provides the illumination for the time integrating correlator. Such diode lasers can be amplitude modulated to bandwidths in the 1 GHz region. Typically, the output radiation of such lasers is at the optical wavelength of 830 nano-meters (nm).

In the original design, which was reported earlier [23], an optically non-coherent mode was planned for the space integrating correlator, using a birefringent effect of the second delay line and using cross polarizers around this delay line to achieve the desired amplitude modulation. Results with the non-coherent correlator were disappointing, and it is believed that the primary reason for this is the poor efficiency of delay line modulation of non-coherent light.

The solution to the difficulties associated with the non-coherent light losses is to convert the space integrating correlator to the optically coherent mode. In the coherent mode the delay line, which can now be of Bragg mode thickness, acts as a volume hologram with much superior efficiency. Essentially all of the coherent illuminating laser light can be delivered to the output detector with a loss incurred by the modulating factor only.

Coherent operation requires an image detector-integrator, i.e. the output device of the time integrating first correlator, which also serves as a coherent spatial laser light modulator. The combined function of square-law detection, optical integration, and coherent spatial output modulation can be provided by a single device or a combination of devices. The device which provides all the needed functions is the liquid crystal light valve (LCLV), manufactured by Hughes Aircraft [24]. This device was selected both for its integration time, which is approximately 30 ms, and its ability to modulate coherent light, which is then used as input to the space integrating correlator. This device detects an input image as an intensity pattern. It transfers the image electronically to a liquid crystal layer which modulates a uniformly collimated laser beam which is brought into the rear, or liquid crystal layer. The modulation achieved is proportional to a time integrated history of the input intensity pattern. The input and output planes are optically isolated from each other by a light blocking layer, so that the only coupling between the planes is the electrical one referred to previously.

One major problem encountered with the introduction of the LCLV in the time integrating correlator is an optical wavelength incompatibility. Figure 18 shows the spectral response of the LCLV CdS photoconductive input film. [25]. As seen in this graph, the response peaks at an optical wavelength of about 530 nm, and has virtually no response beyond 600 nm. For this reason, an image converter which was part of the original design was left in the new system with the LCLV. The image converter being used has an S-25 "extended red" photoemitter which has appreciable response at 830 nm.

The time integrating correlator now operates at 830 nm (GaAlAs laser). The output correlator image is received by the image converter, which converts the light carrying the pattern to a wavelength of 530 nm, obtained from a P20 phosphor radiator (non-coherent broad-band). This intensity image, in turn, is imaged to the input plane of the LCLV which is almost perfectly matched to the 530 nm radiation. The beam which illuminates the LCLV is taken from a HeNe laser at a wavelength of 633 nm. Thus the entire space integrating correlator operates coherently at 633 nm.

A new phase is planned in which the system will operate at 515 nm throughout, this wavelength being obtained from an argon ion laser. The argon beam will be used to illuminate both correlators. The time modulation which is currently performed by electrical current modulation of the GaAlAs laser diode will be performed by an AO modulator external to the laser. This arrangement will produce a time integrating correlator output which is directly compatible with the LCLV, eliminating the necessity of using an image converter. The cancellation ratio and S/N is expected to be quite superior.

The promise of an LCLV using a silicon receptor, with a response well beyond 830 nm, offers the possibility of returning to the semiconductor laser, but now this wavelength of 830 nm could be used throughout the system. The advantages of a laser diode with its small size, and convenient modulation mode, as compared to a gas laser/external modulator is obvious.

Experimental results prove the concepts described. Figure 19 shows the spatial pattern developed on the detector-integrator when a CW carrier waveform is applied to both the time modulator (laser source) and the first delay line. This is a spatial presentation of the auto-correlation function of the sine wave carrier, which is itself a sine wave. The spatial frequency observed correctly corresponds to the carrier temporal frequency, which was 37 MHz, scaled by the delay line acoustic propagation speed. Figure 20 displays the auto-correlation of a pulse modulated carrier. The envelope of the spatial carrier is a triangular function, for which the width is twice the pulse length of 0.25 μ sec. When the electronic detector output is amplified and fed back to the subtractor, the system becomes a closed loop adaptive processor.

The final experimental result to be shown is a demonstration of such closed loop cancellation. Here a single CW carrier is applied to both delay lines, and the laser main channel signal simultaneously. In Figure 21a, the electronic output signal is displayed, with the feedback removed. In Figure 21b, the same signal is observed with the feedback connected. The amplitude cancellation ratio observed here is 16:1, or 24 dB. A number of flaws in the optical system have been discovered, and with correction of these, improvement in the cancellation ratio has been steady.

CONCLUSIONS

The soft-constraint least-squares algorithm and systolic array for QR factorization by Givens Method has been presented. The algorithm is taylored to the needs of a particular application through the choice of input data and constraints.

Simulations have demonstrated the use of soft constraints. At first, the simulations were chosen to implement the conventional minimum variance distortionless response (MVDR) algorithm. When the algorithm proved to give less than optimal performance, a different choice of constraints [4] was used to implement a Modified MVDR algorithm that gave improved performance.

An optical implementation of the time domain adaptive processor as perceived by Dickey [19] has also been the subject of this paper. In this configuration the required operations of multiplication and time delay are provided by AO delay lines. The required time integration is carried out by an image detector having a suitable time constant. In the optical realization, each resolvable optical element along the AO delay lines, used as input modulators, represents an additional delay time degree of freedom. Thus, a continuum of correlation weights is developed spatially along the AO delay line which is analagous to an infinite number of time delay taps. The optical dimension transverse to the direction of acoustic propagation can be used to provide for other array elements.

The electro-optical architecture which has been described offers an efficient, compact, and eventually economical realization of a multiple correlation loop adaptive canceller. Further effort will result in a reliable design which should provide a high cancellation ratio for a large number of independent interference sources in a distributed multi-path environment.

REFERENCES

[1] S. P. Applebaum, "Adaptive Arrays", IEEE Trans. AP, vol. AP-24, no. 5, pp. 585-598, Sept. 1976 (Originally published as Syracuse University Technical Report SURC TR 66-001, Aug. 1966).

[2] L. E. Brennan and I. S. Reed, "Theory of Adaptive Radar", IEEE Trans. AES, vol. AES-9, no. 2, pp. 237-252, March 1973

[3] R.J. Masak, A.M. Kowalski, R.J. Lackey, R.J. Saggio, "An Adaptive Time Delay Module", Hazeltine Corp., Feb. 1980, RADC-TR-79-322.

[4] B.P. Medoff, et al, ESL Inc., Sunnyvale, CA, "High Speed Adaptive Signal Processing", ESL-ER458, RADC-TR-85-53, Final Rechnical Report, March 1985.

[5] G.H. Golub, C.F. Van Loan, "Matrix Computations", Baltimore, Maryland: The Johns Hopkins University Press, 1983.

[6] L. Elden, "Algorithms for the Regularization of Ill-Conditioned Least Squares Problems", BIT, vol. 17, pp. 134-145, 1977.

[7] J.H. Wilkinson, "The Algebraic Eigenvalue Problem", Oxford: Clarendon Press, 1965.

[8] W.M. Gentleman, H.T. Kung, "Matrix Triangularization by Systolic Arrays", Proc. SPIE, vol. 298: Real-Time Signal Processing IV, T.F. Tao, Ed., Bellingham, Washington: SPIE, 1981, pp. 19-26.

[9] S. Hammarling, "A Note on Modifications to the Givens Plane Rotation", J Inst Math Appl, vol 13, pp 215-218.

[10] A. Bjorck, "Solving Linear Least-Squares Problems by Gram-Schmidt Orthogonalization", BIT, vol. 7, 1967, pp. 1-21.

[11] H.T. Kung, C.E. Leiserson, "Algorithms for VLSI Processor Arrays", in Introduction to VLSI Systems, L.A. Conway, Ed., Reading, MA: Addison-Wesley, 1980.

[12] R. Schreiber, P.J. Kuekes, "Systolic Linear Algebra Machines in Digital Signal Processing", in VLSI and Modern Signal Processing, H. Whitebouse, Ed., Prentice Hall, 1984 (presented at the USC Conference on VLSI and Signal Processing, Nov. 1982.

[13] P. W. Howells, "Intermediate Frequency Side-Lobe Canceller", Patent 3202990, Aug. 24, 1956 (filed May 4, 1959).

[14] P. W. Howells, "Explorations in Fixed and Adaptive Resolution at GE and SURC", IEEE Trans. AP, Vol. AP-24, No. 5, Sept. 1976, pp. 575-584.

[15] S. P. Applebaum, "Adaptive Arrays", Syracuse University Research Corp. Rep. SPL-709, June 1964, reprinted in IEEE Trans. on Antennas and Propagation, Vol. AP-24, pp. 573-598, Sept. 1976.

[16] B. Widrow, et. al., "Adaptive Antenna Systems", Proc. IEEE, Vol. 55, pp. 2143-2159, Dec. 1967.

[17] R. A. Monzingo, T. W. Miller, Introduction to Adaptive Arrays, John Wiley & Sons, New York, 1980.

[18] B.Widrow, et. al., "Adaptive Noise Cancelling: Principles and Applications", Proc. IEEE, Vol. 63, pp. 1692-1716, Dec. 1975.

[19] F. R. Dickey, Jr., "Photo-electric Acoustic Adaptive Signal Processor", General Electric Co., Heavy Military Equipment Dept., Syracuse, NY, Report No. R75EMH9, March 1975.

[20] J. F. Rhodes, D. E. Brown, "Adaptive Filtering with Correlation Cancellation Loops", Proceedings of SPIE, Vol 341, paper no. 18, Real Time Signal Processing, Joel Trimble, Chairman/Editor, May 4-7, 1982, Arlington, VA.

[21] W. A. Penn, et al, "Acousto-Optic Adaptive Processing (AOAP)", General Electric Co., Rome Air Development Center, RADC-TR-83-156, Dec 1983, AF Contract F30602-81-C-264.

[22] W. A. Penn, "A Coherent Optical System for Adaptive Cancelling", PhD Dissertation, Syracuse University, Syracuse, New York, 1984.

[23] W. A. Penn, "Acousto-Optic Adaptive Signal Canceller", Laser Institute of Amer., ICALEO Conf. Proc., Boston, MA, Sept. 20-23, 1982, Vol. 34, Lasers and Electro-Optics, pp. 9 - 17.

[24] W. P. Bleha, et. al., "Application of the Liquid Crystal Light Valve to Real Time Optical Data Processing", Optical Engineering Vol. 17, No. 4, July August 1978, pp. 371 -384.

[25] Data obtained from Hughes Aircraft.

ACKNOWLEDGEMENTS

The research was supported by Rome Air Development Center and Defense Advanced Research Projects Agency under projects 4600, 4506, 4519 and DARPA Order 4842. The work was performed at ESL and at the General Electric Company.

CHIP	FORMAT	TECHNOLOGY	THROUGHPUT	OPS
WEITEK WTL 1032	32-bit FP	NMOS 1.5w	8 MHz real	8 MFLOPS
WEITEK WTL 1064	32-bit FP	NMOS 2w	5 MHz real	5 MFLOPS
ANALOG DEVICES ADSP 3210	32-bit FP	CMOS .4w	10 MHz real	10 MFLOPS
ANALOG DEVICES ADSP 3220	32-bit FP	CMOS .4w	10 MHz real	[illegible] MFLOPS
TSI	32-bit FP	CMOS 2w	1.25 MHz complex 2.5 MHz real	10 MFLOPS

FP FLOATING POINT
OPS OPERATIONS PER SECOND

Table 1

Characteristics of Non VHSIC VLSI Chips

for Systolic Arrays

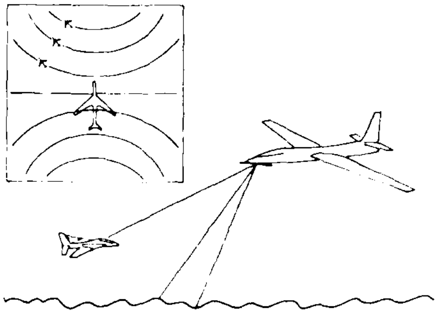

Fig 1 AIR BASED RADAR

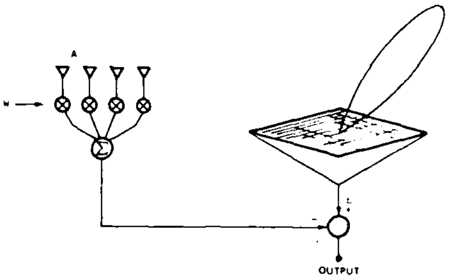

Fig. 2 RADAR BEAMFORMER

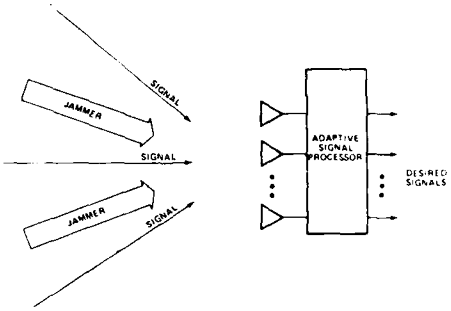

Fig 3 THE ADAPTIVE ARRAY PROCESSING PROBLEM

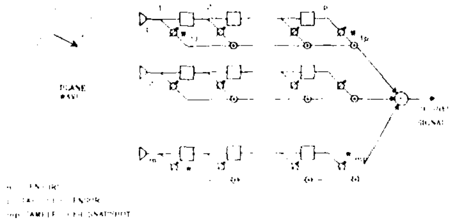

Fig 4 AN ADAPTIVE ARRAY

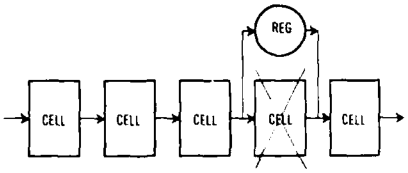

Fig. 5 BYPASS OF A DEFECTIVE CELL IN A LINEAR ARRAY

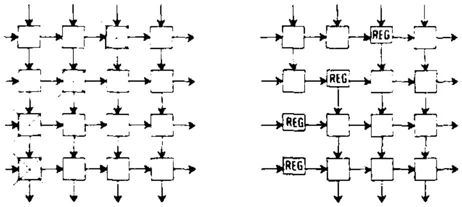

Fig 6 BYPASS OF DEFECTIVE CELLS IN A TWO-DIMENSIONAL ARRAY

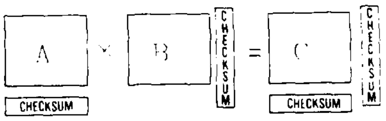

Fig. 7 ALGORITHM BASED FAULT TOLERANCE - CHECKSUM METHOD

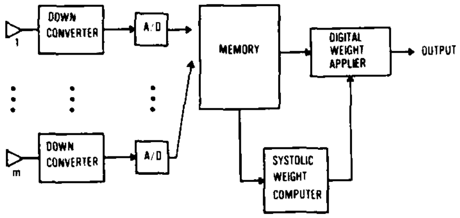

Fig. 8 THE SIGNAL PROCESSING SYSTEM

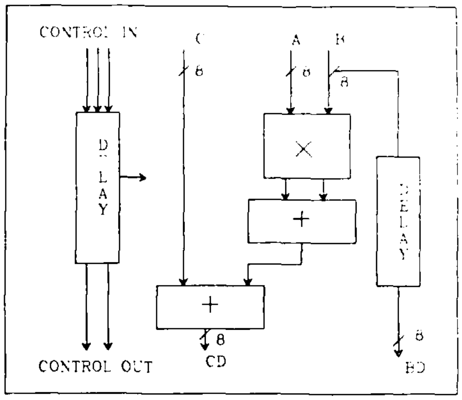

Fig. 9 FUNCTIONAL FLOOR PLAN OF THE ESL SYSTOLIC CHIP

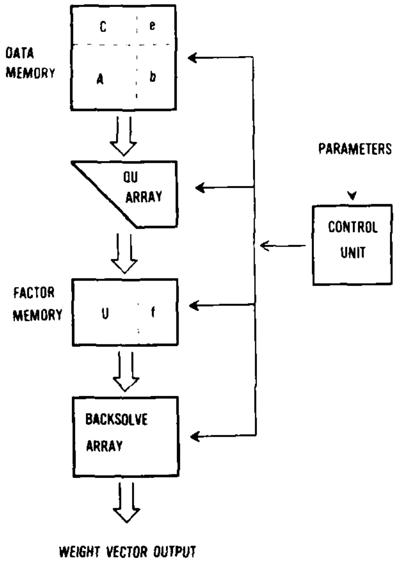

Fig. 10 BLOCK DIAGRAM OF THE SYSTOLIC WEIGHT COMPUTER

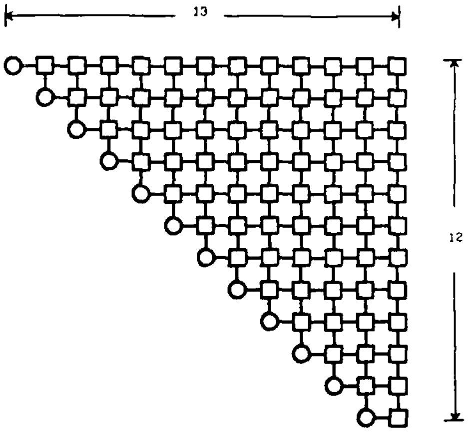

Fig. 11 A QU FACTORIZATION ARRAY

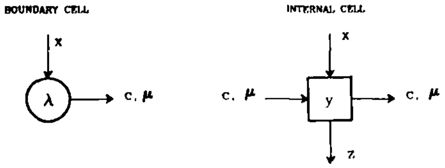

$$\rho \leftarrow \sqrt{\lambda^2 + |x|^2}$$

$$c \leftarrow \bar{x}/\rho$$

$$\mu \leftarrow \lambda/\rho$$

$$\lambda \leftarrow \rho$$

$$y \leftarrow cx + \mu y$$

$$z \leftarrow -\mu x + \bar{c}y$$

Fig. 12 CELLS IN THE QU ARRAY

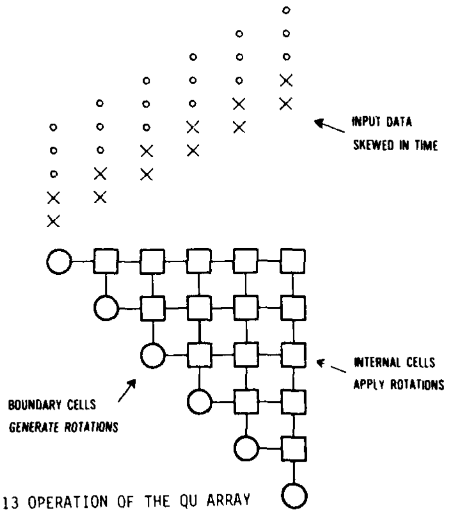

Fig 13 OPERATION OF THE QU ARRAY

TYPICAL OPERATIONAL SITUATION

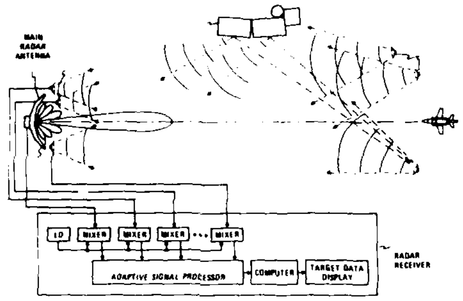

Fig. 14

ACOUSTO-OPTICAL ADAPTIVE CANCELLER

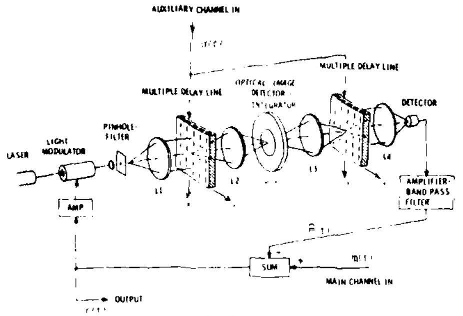

Fig. 16

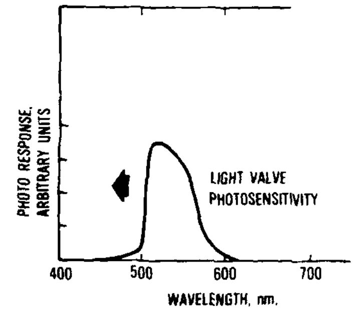

Fig. 18 LIGHT VALVE PHOTO RESPONSE CHARACTERISTICS

CONVENTIONAL ARRAY OF ADAPTIVE LOOPS

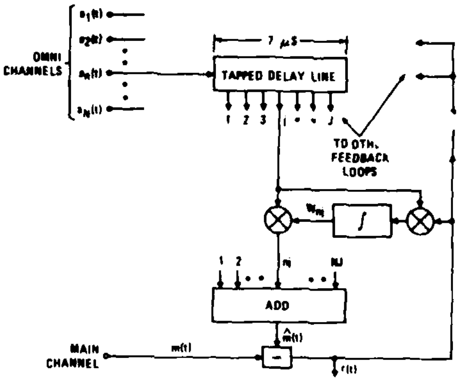

Fig. 15

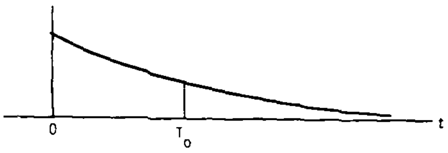

Integration weighting function corresponding to exponential decay

Fig. 17

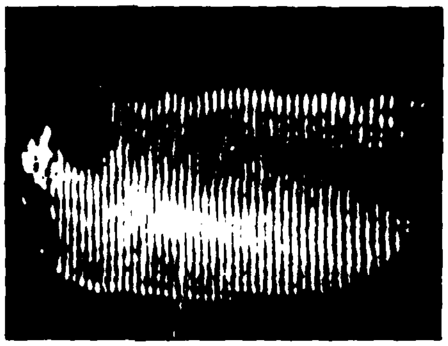

Auto-Correlation of CW Input

Fig. 19

Figure 20. Auto-Correlation of pulsed input

Figure 21a. Feedback disconnected

Figure 21b. Feedback connected

Figure 21. Cancellor Output

The Application of Multi-dimensional Access Memories to Radar Signal Processing Systems

David Hayes and Bill Strawhorne

Signal Processing Design Department,
Research Laboratory,
GEC Avionics Limited,
Elstree Way, Borehamwood
Hertfordshire, England.

ABSTRACT

A multi-dimensional access memory (MDAM) allows a word to be accessed from store either *in* the *manner* it *was* entered or as part of a bit slice of equally spaced or contiguous words. Conceptually, data may be regarded as being stored in an 'n' dimensional hypercube of side length equal to the word length that usefully maps onto a wide range of signal processing operations, (e.g. FFTs, matrix inversion, multiple moments, distance metrics, sorts, searches and correlation decodes), when associated processing units that can carry out both bit parallel and bit serial arithmetic are used. The mapping of the natural multi-dimensionality of a signal processing task onto the MDAM structure is shown to be particularly useful when bit serial, word parallel processors are employed. In these circumstances the facilities of the MDAM make possible a range of useful operations that could only be implemented with great inefficiency using conventional memories.

Furthermore, the MDAM considerably simplifies address generation for the I/O of real and complex words (e.g. the corner turn of incoming samples) while allowing useful permutations, such as barrel shifts, to be applied on each memory access for a insignificant cost in extra circuitry.

Highly efficient and deeply pipelined, implementations of MDAM/processor structures are discussed that are particulary well suited to VLSI methodologies, in that very wide bandwidth interconnection networks of high complexity can be achieved at relatively low gate and pin counts, (at both super/sub-micron levels). Thus it is possible to form highly parallel multi-MDAM/processor structures that support very high levels of concurrency, identified as necessary for future radar signal processing systems. Moreover these structures translate over classes of operations that are not normally associated with each other (e.g. histogramming and FFTs). Consequently, these forms can be made extremely general and modular to produce powerful and compact processing kernels for programmable systems that embody high level signal processing constructs in their VLSI fabric and lead to high performance at the minimum silicon cost.

On a Single Step Technique for Adaptive Array Processing

Josef Worms
Forschungsinstitut fur Hochfrequenzpuhysik der FGAN e.V.
5307 Wachtberg-Werthhoven, W-Germany

ABSTRACT

An improved adaptation algorithm designed for real time signal processing in antenna arrays is presented. The method is used for determining the filter weights in a sidelobe cancellation system. The Wiener filter equation is solved by using the well known Gauss - Seidel method and a sample matrix estimate. This algorithm (SSM - Single Step Method) combines rapid convergence and numerical stability. Compared with the direct SMI-technique and the Widrow LMS-algorithm, the properties of the proposed algorithm lead us to the conclusion that it is especially well suited for airborne antenna array applications.

INTRODUCTION

Due to progress in digital technology it appears feasible now to process digitally real - time data of adaptive antenna arrays in airborne radar applications. The popular gradient technique proposed by Widrow, Griffiths e.a. (Applebaum Loops, Widrow - Hoff Algorithm) is not the appropriate algorithm for solving the optimal filter equation by adaptive arrays in the following cases:

- a rapid change of the interference environment due to antenna scanning or blinking of noise sources
- different jammer directions with different power

The reasons for slow convergence are given by the facts that

- iteration methods are only approximations of the optimal solutions
- the "Widrow-Algorithm" does not lead to a consistent estimator (Ungerboeck 1972 /1/)

Looking for other methods, it can be shown, that the SMI-method /2/ has excellent convergence properties, but may lead to severe numerical problems.
Here an algorithm is considered which - based on the Gauss-Seidel method - employs a sample covariance matrix estimate. An application of a modified Gauss-Seidel method on clutter processes has already been described /3/. This paper quantifies the performance of the proposed algorithm in terms of convergence rate and statistical properties. It will be shown that in contrast to the LMS-algorithm the proposed algorithm is a consistent estimation of the optimal filter. The paper presents a comparison of the LMS-, SMI- and the SSM-method by computer simulation. It turns out that in spite of less mathematical operations (multiplications and additions) the SSM-algorithm performs nearly as well - in terms of convergence rate - as the SMI method.

DESCRIPTION OF THE METHOD

There are several mathematical methods leading to the solution of the well known classical optimization problem of Gauss-Markov, which finds an application for example in the sidelobe canceller as a spatial filter (fig. 1). The received array signals establish a data vector $\underline{X}^*$, which has to be weighted by a set of coefficients $\underline{W}$, in order to build the best approximation of the $\overline{\text{interfering}}$ processes x_0 in the radar antenna. Assuming that the target signals are not processed in the array we know that the minimization task

$$\varepsilon^2 = E\left(|x_0 - \underline{W}^* \underline{X}|^2\right) \overset{!}{=} \min_{\underline{W}} \qquad (1)$$

is solved if

$$E\left(x_0^* \underline{X} - \underline{XX}^* \underline{W}\right) := \underline{R} - \underline{\underline{M}}\,\underline{W} = \underline{0} \qquad (2)$$

(by the projection theorem in Hilbert spaces)
There are in general two ways of solving (2):

- direct methods
- iteration methods

The direct methods lead for example to the SMI-technique, to the Kalman filter (in form of a sequential estimator), to the Gram-Schmidt or Lattice filter, or to a combination of the Householder and Cholesky-algorithm /4,5/.

---

*Matrices are designated by double-underlined, vectors by single-underlined letters

The iteration methods lead to the gradient, to the conjugate gradient or to the Single Step methods. In general the SSM-technique is a gradient technique using all calculated coefficients

$$W_{m+1}(l) = W_m(l) + \gamma \Big\{ R(l) - \sum_{i=1}^{l-1} M(l,i)\; W_{m+1}(i) - \sum_{i=l}^{n} M(l,i)\; W_m(i) \tag{3}$$

Since the covariance matrix $\underline{\underline{M}}$ and the correlation vector $\underline{R}$ are unknown, we estimate them by the observed data.

$$\underline{\underline{M}}_m = (1/m) \sum_{i=1}^{m} \underline{X}_i \cdot \underline{X}_i^*$$

$$\underline{R}_m = (1/m) \sum_{i=1}^{m} x_{o,i}^*\; \underline{X}_i \tag{4}$$

In the context of this, we obtain a stochastic approximation method, called the SSM-Algorithm.

$$W_{m+1}(l) = W_m(l) + \gamma \cdot \Big\{ R_m(l) - \sum_{i=1}^{l-1} M_m(l,i)\; W_{m+1}(i) - \sum_{i=l}^{n} M_m(l,i)\; W_m(i) \Big\} \tag{5}$$

Next we show the consistence property of this estimate of the optimal filter.

CONVERGENCE PROPERTIES

First we devide the covariance matrix $\underline{\underline{M}}$ in two matrices $\underline{\underline{M}}^u$, $\underline{\underline{M}}^o$.

$$\underline{\underline{M}} = \begin{bmatrix} M(1,1) & M(1,2) & \dots & M(1,n) \\ \cdot & & & \cdot \\ \cdot & & & \cdot \\ \cdot & & & \cdot \\ \cdot & & & \\ M(n,1) & M(n,2) & \dots & M(n,n) \end{bmatrix}$$

$$= \begin{bmatrix} 0 & 0 & \dots & 0 \\ M(2,1) & 0 & & \cdot \\ \cdot & & \cdot & \cdot \\ \cdot & & \cdot & \cdot \\ \cdot & & \cdot & \cdot \\ M(n,1) & \dots & M(n,n-1) & 0 \end{bmatrix} + \begin{bmatrix} M(1,1) & & \dots & M(1,n) \\ 0 & M(2,2) & & \cdot \\ \cdot & \cdot & \cdot & \cdot \\ \cdot & \cdot & \cdot & \cdot \\ \cdot & \cdot & \cdot & \cdot \\ 0 & 0 & \dots\; 0 & M(n,n) \end{bmatrix}$$

$$:= \underline{\underline{M}}^u + \underline{\underline{M}}^o \tag{6}$$

Using (2) this leads straightforward to:

$$\underline{W} = (\underline{\underline{I}} + \gamma \underline{\underline{M}}^u)^{-1} (\underline{\underline{I}} - \gamma \underline{\underline{M}}^o)\, \underline{W} + (\underline{\underline{I}} + \gamma \underline{\underline{M}}^u)^{-1}\, \underline{R}\, \gamma \tag{7}$$

Equation (5) may now be written:

$$\underline{W}_{m+1} = (\underline{\underline{I}} + \gamma \underline{\underline{M}}_m{}^u)^{-1} (\underline{\underline{I}} - \gamma \underline{\underline{M}}_m{}^o)\, \underline{W}_m + (\underline{\underline{I}} + \gamma \underline{\underline{M}}_m{}^u)^{-1}\, \underline{R}_m \gamma \tag{8}$$

With reference to (7) and (8), we obtain

$$\begin{aligned} \underline{W}_{m+1} - \underline{W} = {} & (\underline{\underline{I}} + \gamma \underline{\underline{M}}_m{}^u)^{-1} (\underline{\underline{I}} - \gamma \underline{\underline{M}}_m{}^o)\, (\underline{W}_m - \underline{W}) \\ & + \Big\{ (\underline{\underline{I}} + \gamma \underline{\underline{M}}_m{}^u)^{-1} (\underline{\underline{I}} - \gamma \underline{\underline{M}}_m{}^o) - (\underline{\underline{I}} + \gamma \underline{\underline{M}}^u)^{-1} \\ & \cdot (\underline{\underline{I}} - \gamma \underline{\underline{M}}^o) \Big\}\, \underline{W} \\ & + \gamma (\underline{\underline{I}} + \gamma \underline{\underline{M}}_m{}^u)^{-1} (\underline{R}_m - \underline{R}) \\ & + \gamma \Big\{ (\underline{\underline{I}} + \gamma \underline{\underline{M}}_m{}^u)^{-1} - (\underline{\underline{I}} + \gamma \underline{\underline{M}}^u)^{-1} \Big\}\, \underline{R} \end{aligned} \tag{9}$$

---

lub = least upper bound

Now we get the following inequality by using the triangle inequality and the definition of lub /6/:

$$\left(L1 = \sup_{m} \left\{ \mathrm{lub} \left\{ (\underline{\underline{I}} + \gamma \underline{\underline{M}}_m{}^u)^{-1} (\underline{\underline{I}} - \gamma \underline{\underline{M}}_m{}^o) \right\}\right\} \right. \qquad \text{a.e.}^{**}$$

$$\left. L2 = \sup_{m} \left\{ \mathrm{lub} \left\{ (\underline{\underline{I}} + \gamma \underline{\underline{M}}_m{}^u)^{-1} \right\}\right\} \right)$$

$$\begin{aligned} \| \underline{W}_{m+1} - \underline{W} \|_2 \leq\; & L1 \cdot \| \underline{W}_m - \underline{W} \|_2 + |\gamma| \; L2 \cdot \left\{ \| \underline{R}_m - \underline{R} \|_2 \right. \\ & + \mathrm{lub} \left\{ (\underline{\underline{I}} + \gamma \underline{\underline{M}}^u)^{-1} \right\} \left\{ E (\mathrm{lub}^2 \{ M_m{}^u - M^u \} \right\}^{1/2} \| \underline{R} \|_2 \, |\gamma| \left. \right\} \qquad (10) \\ & + \left\{ E \left\{ \mathrm{lub}^2 \left\{ (\underline{\underline{I}} + \gamma \underline{\underline{M}}_m{}^u)^{-1} \cdot (\underline{\underline{I}} - \gamma \underline{\underline{M}}_m{}^o) - (\underline{\underline{I}} + \gamma \underline{\underline{M}}^u)^{-1} \cdot \right.\right.\right. \\ & \left.\left.\left. (I - \gamma M^o) \right\}\right\}\right\}^{1/2} \| \underline{W} \|_2 \end{aligned}$$

It is known that the estimators (4) (methods of moments) have the following order of convergence

$$\begin{aligned} \| \underline{R}_m - \underline{R} \|_2 &= O(1/\sqrt{m}) \\ \| \underline{\underline{M}}_m - \underline{\underline{M}} \|_2 &= O(1/\sqrt{m}) \end{aligned} \qquad (11)$$

Choosing an appropriate γ, it is now possible to show

$$\| \underline{W}_{m+1} - \underline{W} \|_2 = C/\sqrt{m} + L\,1 \cdot \| \underline{W}_m - \underline{W} \|_2 \qquad (12)$$

Analogous to the proof of convergence of the SMG-algorithm /7/ it follows for

$$L\,1 < 1$$

$$\| W_{m+1} - W \|_2 = O(\log(m)/\sqrt{m}) \qquad (13)$$

Using the Tschebyscheff inequality, we obtain the assertion.

Remark: (1) By a simple proof it is possible to show, that

$$\gamma_{l,m} = 1/M_m(l,l) \qquad (14)$$

is a convergent choice. (compare /8/, p. 225)

$\gamma_{l,m}$ is dependent of l and m. In this case γ has to be replaced by a diagonal-matrix $\underline{\underline{D}}_m$ throughout the proof.

(2) Using (14) in (5) we get the well known Gauss-Seidel method.

(3) In the m'th estimate of $\underline{W}$, we choose $\underline{\underline{M}}_m$, $\underline{R}_m$ for $\underline{\underline{M}}$, $\underline{R}$.

COMPARISON OF THE ALGORITHMS

A computer simulation of the SSM algorithm in a radar application shows the superiority of the processing scheme with respect to the convergence rate compared to the Widrow algorithm. A stationary case has been considered (fig. 2). For the SSM method we choose γ as in (14). The SMI method is simulated as a sequential filter. The Widrow LMS algorithm has a step size of $(1/10 \ldots 1/20 * 1/\lambda_{max}{}^*)$ in order to avoid intolerable fluctuation noise. Non-stationarity of the interference environment has been taken into account by a moving average (moving window) or Wiener extrapolation. (see for example (14))
In order to compare the numerical load of the various algorithms, we look to the number of complex multiplications per iteration

Algorithm	Number of complex multiplications
SMI (direct inversion)	$(n^3 + 5n^2 + n)/2$
SMI (sequential filter)	$2n^2 + 4n + 1$
SSM-algorithm	$(3n^2 + 5n)/2$
LMS-Algorithm	$2n + 1$

---

* λ_{max} maximum eigenvalue
** a.e. = almost everywhere

CONCLUSIONS

There are various mathematical methods to solve the Wiener filter equation, among them the discussed SSM algorithm. The SSM method has some advantages in terms of convergence rate and numerical load. It has been shown that the modified Gauss-Seidel method is a consistent estimator of the optimal filter. We then have proved that the filter coefficients converge by an order better than $0\ (\log(m)/\sqrt{m})$. Compared to the Widrow algorithm the convergence rate of the SSM algorithm is improved and may be comparable to the convergence rate of the direct methods. This result is achieved at the expense of a modest increase in complexity. One of the advantages of the SSM method is its numerical stability especially in the case of large antenna arrays.

LITERATUR

/1/ G. Ungerboeck
Theory of speed of convergence in adaptive equaliser,
IBM Journal Research and Development,
pp 546 - 555, 16/1972

/2/ L.E. Brennan, J.D. Mallett, I.S. Reed
Rapid Convergence in Adaptive Arrays,
IEEE Trans. Aerosp. El. Syst., Vol. AES-10, No. 6,
pp 853 - 863, Nov. 1974

/3/ R. Klemm
Adaptive pre-whitening filter
AGARD CP-103 1972

/4/ J. Worms
Rekursive Algorithmen fur adaptive Gruppenantennen
basierend auf beliebigen linearen Schatzverfahren,
Forschungsbericht 5-84 FHP, Wbg.-Werthhoven, April 1984

/5/ J. Worms
Ein Vergleich von Algorithmen zur adaptiven Storunterdruckung
(mit Gruppenantennen),
Forschungsbericht (to appear), FHP, Wbg.-Werthhoven

/6/ A. Householder
The Theory of Matrices in Numeric Analysis,
Dover Publications Inc., New York 1964

/7/ J. Worms, K. Krucker
On an improved gradient technique for adaptive array processing,
Radar Conf. 1985
(to appear)

/8/ J.N. Franklin
Matrix Theory,
Prentice-Hall Inc., Englewood Cliffs,
New Jersey, 1968

/9/ B. Widrow, L.J. Griffiths, E. Mantey
Adaptive Antenna Systems,
IEEE Proc., Vol. 55, No. 12, pp 2143 - 2159,
Dec. 1967

AD-A173 978 MULTIFUNCTION RADAR FOR AIRBORNE APPLICATIONS(U) 2/3
ADVISORY GROUP FOR AEROSPACE RESEARCH AND DEVELOPMENT
NEUILLY-SUR-SEINE (FRANCE) M H CARPENTIER ET AL.
UNCLASSIFIED JUL 86 AGARD-CP-381 F/G 17/9 NL

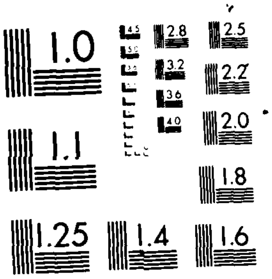

MICROCOPY RESOLUTION TEST CHART
NATIONAL BUREAU OF STANDARDS 1963-A

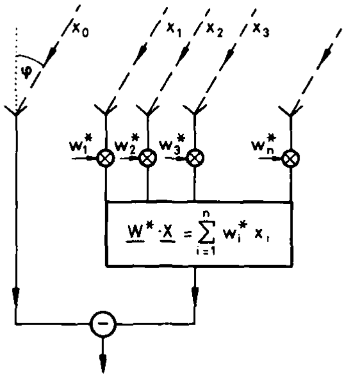

Figure 1: Structure of the Spatial Filter
(Sidelobe Canceller)

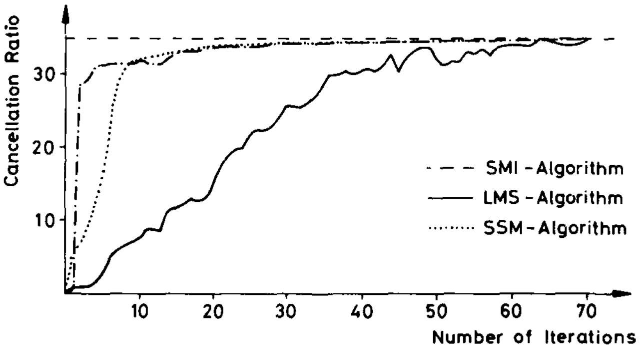

Figure 2:

Conditions: Partially adaptive array
with 3 degrees of freedom
2 Interference Directions (20°, 45°)
Receiver Noise: -40 dB related to Interference Power

DISCUSSION

J.Dorey

You have to make the whole calculation for each look direction?

Author's Reply

We considered only stationary targets. For non-stationary targets you can use the Wiener-extrapolation or by moving average.

OPTIMISATION DU FACTEUR DE FORME EN EMISSION HFR

par

Ph. LEBIENVENU
THOMSON-CSF
Division Equipements Avioniques
173, Avenue Pierre Brossolette
92120 MONTROUGE
FRANCE

RESUME

En émission à haute fréquence de récurrence, donc à faible facteur de forme, les éclipses et l'échantillonnage conduisent à des pertes importantes sur le signal. L'objet de cette communication est de présenter des méthodes d'évaluation de ces pertes, à partir de courbes de probabilité de détection en fonction de la distance et d'utiliser ces méthodes pour rechercher, sous certaines contraintes de puissance émise et de charges de calcul, l'optimum à adopter pour le facteur de forme.

1 - INTRODUCTION

La forme d'onde HFR (haute fréquence de répétition), du fait du faible facteur de forme (2 à 20) conduit à des pertes d'information importantes en raison des éclipses. De plus, la discrétisation du signal (échantillonnage) conduit, elle aussi, à des pertes supplémentaires. On présentera ici différentes méthodes pour évaluer la probabilité de détection en tenant compte du facteur de forme et du nombre d'échantillons pris dans la récurrence. Ces méthodes permettent de déterminer l'optimum sur le facteur de forme en tenant compte des contraintes de puissance d'émission (moyenne ou crête) et des charges de calcul liées au nombre d'échantillons utilisés dans la récurrence.

2 - PRESENTATION DES MODES HFR

2.1. Définition (figure 1)

T_E : durée d'impulsion émise

T_R : période de répétition

F_R : fréquence de répétition $= \frac{1}{T_R}$

T : période d'échantillonnage

T_B : temps d'occultation

Celui-ci est le temps de commutation du récepteur avant et après émission. Le temps d'occultation total sur une récurrence est $2 \times T_B = 400$ ns.

On considèrera ici deux fréquences de récurrence $F_R = 100$ KHz et $F_R = 200$ KHz.
Le facteur de forme est $F = \frac{T_R}{T_E}$.

2.2. Filtrage de l'impulsion reçue

On considère un filtre adapté à une durée ΔT, c'est-à-dire dont la fonction de transfert est la conjuguée de la transformée de Fourier d'une impulsion rectangulaire de durée ΔT. La réponse d'un tel filtre à des impulsions rectangulaires de durée T_E et d'amplitude 1 est présentée sur la figure 2.

Par la suite, on considèrera un filtre constamment adapté à la période d'échantillonnage T, le filtre étant réadapté artificiellement à la durée d'émission T_E, après échantillonnage du signal reçu filtré, par recombinaison en sommes glissantes de N échantillons successifs, de façon à avoir $T_E = N.T$ (figure 3).

2.3. Puissance de bruit

Si b est la densité spectrale de bruit, la puissance de bruit pour un échantillon élémentaire (avant recombinaison) est $P_B = b.\Delta T = b.T$. Le filtre étant optimal et adapté à T, les bruits sont décorrélés d'un échantillon élémentaire à l'autre, donc dans le cas d'une sommation de N échantillons successifs, la puissance de bruit est $P_B = N.b.T$.

De plus, on suppose l'entrée du filtre mise à la masse en même temps que le récepteur est fermé (soit sur une récurrence pendant $T_E + 2\ T_B$). Le filtre n'intégrant alors plus de bruit pendant les éclipses, la puissance de bruit pour les échantillons voisins des bords de la récurrence est plus faible.

2.5. Puissance de signal

Si To est l'instant d'arrivée de l'impulsion reçue (de durée T_E) dans la récurrence, le signal utile est fonction de To. En effet :

- si $To \leq T_B$: le signal est complètement occulté,
- si $T_B < To \leq T_E + T_B$: une partie seulement du signal est hors éclipse. Le signal utile a donc une durée $To + T_E - (T_E + T_B) = To - T_B$,
- si $T_E + T_B < To \leq T_R - T_B - T_E$: le signal est entièrement reçu. Le signal utile dure T_E,
- si $T_R - T_B - T_E < To \leq T_R - T_B$: le signal utile dure $T_R - T_B - To$,
- si $T_R - T_B < To \leq T_R$: le signal est complètement occulté.

La puissance de signal reçue, dépendant de la durée du signal utile, est donc fonction de To, instant d'arrivée de l'écho reçu dans la récurrence.

3 - PRESENTATION DES RESULTATS

Les résultats des différentes méthodes décrites ci-dessous seront présentés sous forme de courbe : Pd = f(D) avec Pd = probabilité de détection
D = distance cible.

On prend comme référence le cas d'une cible telle que avec un filtrage adapté à l'émission, si on échantillonne au maximum en sortie du filtre et si la cible est en dehors des éclipses, on ait une probabilité de détection de 50 % pour D = 100 km. On considèrera par la suite des cibles stationnaires. Ceci fixe donc le rapport signal à bruit SBo de référence donnant Pd = 0,5 et correspondant à 100 km.

Le rapport signal à bruit d'une cible située à la distance D se déduit de SBo par $SB = SBo \frac{Do^4}{D^4}$.

La figure 4 représente la courbe Pd = f(D) de référence (cible stationnaire perpétuellement hors éclipses et hors pertes d'échantillonnage). On peut dire également que cette référence correspond au cas d'un radar CW, à condition que l'antenne de réception soit différente de celle d'émission.

4 - METHODE 1

Cette méthode consiste à faire varier la distance de la cible avec un pas de quantification petit devant l'ambiguïté distance ($AD = \frac{cT_R}{2}$ avec c : vitesse de la lumière). Ainsi, l'instant d'arrivée de l'écho varie lentement dans la récurrence et les phénomènes d'éclipse et d'échantillonnage sont visibles.

On suppose pour cette méthode l'échantillonnage adapté à l'émission, soit $T = T_E$. En fonction de To, instant d'arrivée de l'écho ($To = \frac{2D}{c}$), on peut positionner l'écho dans la récurrence (figure 5). Du fait que $T = T_E$, il n'y a au plus que deux échantillons contenant du signal. Pour chacun d'eux, on connait l'atténuation à apporter au rapport $\frac{S}{B}$ ($= SBo \frac{Do^4}{D^4}$). Cette atténuation tient compte de la position de To dans la récurrence (éclipse) et de l'échantillonnage par rapport à la sortie du filtre. On peut donc calculer les probabilités de détection Pd_1 et Pd_2 pour chacun des 2 échos. Du fait que la cible est stationnaire et que $T = T_E$, les deux probabilités sont indépendantes. On peut donc dire $Pd = 1 - (1 - Pd_1)(1 - Pd_2)$.

Si Pdo = f(D) est la courbe de référence (échantillonnage au maximum et hors éclipse), la probabilité Pd varie donc entre 0 et Pdo en fonction de la distance.

Pd = o quand l'écho est en éclipse totale

Pd < Pdo quand l'écho est en éclipse partielle

Pd = Pdo quand To est tel que l'échantillonnage ait lieu au maximum

Pd < Pdo sinon.

La figure 6 présente Pd = f(D), D variant de 100,5 km à 101,25 km (Pdo voisin 0,5) avec comme hypothèse :

F_R = 200 KHz (T_R = 5 µs, AD = 750 m)

T_E = 1 µs (F = 5)

T_B = 0,25 µs

T = 1 µs.

Les différents temps et instants d'échantillonnage y sont représentés.

La figure 7 présente Pd = f(D) dans les mêmes conditions, D variant de 50 à 150 km. On y constate les fluctuations importantes dues au fait que Pd varie entre 0 et Pdo.

Cette méthode, représentant la vraie probabilité de détection en fonction des éclipses et de l'échantillonnage, est inexploitable simplement du fait des fluctuations importantes.

De plus, cette méthode n'est valable que dans le cas d'une cible stationnaire et d'un filtrage et échantillonnage adaptés à 1 émission, de façon à avoir l'indépendance des probabilités de détection des différents échantillons (qui ne serait plus assurée en cas de sommations glissantes d'échantillons successifs).

5 - METHODE 2

Pour une distance D donnée, le calcul de la probabilité de détection est identique à celui de la méthode 1 : $Pd = 1 - (1 - Pd_1)(1 - Pd_2)$.

Mais on effectue ici, pour chaque distance D, le calcul pour plusieurs fréquences de récurrence voisines de quelques pourcent de la fréquence de récurrence moyenne et on effectue la moyenne des Pd obtenues. Une méthode équivalente consiste à n'avoir qu'une seule F_R mais à faire varier aléatoirement la distance sur une récurrence autour de la distance D et à effectuer une moyenne des Pd obtenues. Les deux méthodes donnent des résultats équivalents.

Les fluctuations importantes de la méthode 1 sont ainsi moyennées et on obtient une courbe Pd = f(D) d'autant plus lisse qu'on a pris plus de F_R ou plus de points dans la récurrence. La figure 8 présente Pd = f(D), D variant de 10 à 150 km dans les mêmes conditions que précédemment, calculée avec une moyenne sur 200 points par récurrence pour chaque distance.

On constate que la courbe ne tend pas vers 1 quand D tend vers 0. En effet, en raison des temps d'occultation T_B, la probabilité maximale de détection est la probabilité pour que l'instant de réception To soit supérieur à T_B et inférieur à $T_R - T_B$, soit :

$$Pdmax. = 1 - \frac{2T_B}{T_R}$$

En l'occurence : $T_B = 0{,}25\ \mu s$: $Pdmax. = 0{,}9$

$T_R = 5\ \mu s$

Cette méthode permet de travailler avec un pas de quantification plus élevé pour la distance que pour la méthode 1. Elle permet surtout d'obtenir une courbe moyenne de probabilité de détection directement utilisable.

Les limitations de cette méthode sont les mêmes que pour la précédente, à savoir :

- cible stationnaire,
- filtrage et échantillonnage adaptés à l'émission.

6 - METHODE 3

Celle-ci consiste à calculer une probabilité de détection moyenne sur une ambiguïté distance AD. Le domaine distance pour lequel on veut la courbe Pd = f(D) est découpé en ambiguïtés. Pour une ambiguïté de rang K donné, on fait varier la distance de la cible de K.AD à (K + 1).AD avec un pas suffisamment fin.

L'écho reçu est échantillonné : on a ainsi des amplitudes Ai de signal ($0 \leq Ai \leq 1$), dépendantes de l'instant de réception et de sa position par rapport à l'échantillonnage. Dans le cas où $T_E = N.T$, chaque échantillon avant sommation a donc un rapport $\frac{S}{B}$ valant $SBo\ \frac{Do^4}{D^4}\ \frac{Ai^2}{N}$ (D : distance centrale de l'ambiguïté). Connaissant B, on a donc la puissance Xi^2 de chaque échantillon. On peut donc effectuer les sommations glissantes de N échantillons. Chaque échantillon résultant a comme puissance de signal $PS = (\sum_{i=1}^{N} Xi)^2$. L'échantillon résultant tient bien compte des corrélations des échantillons élémentaires dont il est la somme.

De plus, on connait pour chaque échantillon résultant la puissance de bruit P_B ($P_B \leq N.B$), fonction de la position de l'échantillon dans la récurrence.

Cette puissance permet en outre de déterminer le seuil de détection connaissant la probabilité de fausse alarme. Il est en effet possible dans la pratique de mettre des seuils différents selon la position de l'instant d'échantillonnage dans la récurrence.

On peut donc générer un signal complexe Z de puissance P_S par rapport à P_B. Ce signal est généré avec deux gaussiennes de moyenne et d'écart type fonctions d'une part de P_S et P_B, d'autre part de l'hypothèse de cible stationnaire ou fluctuante. Z^2 est ensuite comparé au seuil de détection. En cas de non détection, on passe à l'échantillon suivant et on recommence. En cas de détection, on peut passer à une autre position de l'écho dans la récurrence. Il ne reste plus qu'à calculer la moyenne des détections obtenues sur la récurrence, donnant ainsi Pd fonction de D.

La figure 9 montre un exemple de courbes calculées par cette méthode et par la méthode 2 dans les mêmes conditions que précédemment. Les deux courbes sont tout à fait semblables.

La figure 10 représente la courbe Pd = f(D) dans le cas : F_R = 200 KHz

T_E = 1 µs

T = 0,5 µs.

On effectue dans ce cas des sommations 2 à 2 d'échantillons. L'avantage de cette méthode par rapport aux autres est, d'une part, de permettre le suréchantillonnage car elle ne suppose pas l'indépendance d'échantillons consécutifs, et d'autre part, de permettre, pour la même raison, le calcul dans le cas d'une cible fluctuante.

7 - METHODE 4

Cette méthode est purement analytique. Elle consiste à évaluer les pertes que les éclipses et l'échantillonnage apportent sur le rapport signal à bruit.

Pour cela, on suppose un écho de rapport $(\frac{S}{B})_0$ donné et on fait varier son instant de réception To de 0 à T_R. Pour chaque valeur de To, on calcule de la même façon que précédemment le rapport $\frac{P_S}{P_B}$ pour chaque échantillon (après sommation éventuelle) et on ne conserve que le maximum. Puis on effectue la moyenne, sur le nombre de position de To, de ces maxima de $\frac{P_S}{P_B}$, soit $(\frac{S}{B})_1$.

Le rapport L = $(\frac{S}{B})_1$ / $(\frac{S}{B})_0$ caractérise les pertes sur le rapport signal à bruit initial, dues aux éclipses et à l'échantillonnage.

Pour obtenir la courbe Pd = f(D), on calcule pour chaque valeur de D le rapport :

$$\frac{S}{B} = \frac{SBo}{L} \frac{Do^4}{D^4} \text{ puis la Pd associée.}$$

C'est la courbe Pd_1 représentée sur la figure 11. Cette méthode ne prend pas en compte le fait que Pdmax. = $1 - \frac{2.T_B}{T_R}$ -

Ainsi pour introduire cette influence des occultations, on considère des pertes L calculées comme précédemment *mais en supposant* $T_B = 0$. On multiplie ensuite la Pd obtenue avec ces pertes par $1 - \frac{2.T_B}{T_R}$ - . Ceci donne la courbe Pd_2 de la figure 11. La figure 12 compare la courbe obtenue avec cette méthode avec celle obtenue par la méthode 3 dans les conditions suivantes : F_R = 200 KHz

T_E = 1 µs

T = 0,5 µs.

Les différences sont faibles. L'intérêt de cette méthode est sa rapidité. Une fois le calcul des pertes effectué (pour une seule récurrence), la courbe est immédiate. Cette méthode permet d'estimer rapidement la distance donnant une Pd donnée (0,5 par exemple), pour ensuite effectuer la méthode 3 autour de cette distance pour avoir des résultats exacts.

8 - OPTIMISATION DU FACTEUR DE FORME A PUISSANCE MOYENNE EMISE CONSTANTE

Si F est le facteur de forme et Pc la puissance crête émise, la puissance moyenne émise est :

$$Pm = \frac{Pc}{F}$$

On se place ici à Pm constante, donc Pc varie avec F.

La puissance moyenne d'une cible est donc indépendante de la variation de F ainsi que la courbe de référence Pdo = f(D). Rappelons que celle-ci correspond au cas d'une cible perpétuellement hors éclipse et hors pertes d'échantillonnage et que Pdo = 0,5 pour Do = 100 km, ce qui fixe Pm.

Avec la méthode 4, pour estimer la distance à Pd = 0,5 et la méthode 3 pour affiner les résultats autour de cette distance, on va calculer les variations de la portée à Pd = 0,5 en fonction du facteur de forme, ceci en gardant une période d'echantillonnage constante. Quand F varie, T_E varie. Le nombre d'échantillons successifs à sommer pour réadapter le filtre varie donc également.

La période d'échantillonnage étant constante, la charge de calcul pour les traitements en aval reste donc la même quelque soit le facteur de forme (mis à part les sommations d'échantillons consécutifs qui représentent cependant très peu de calculs).

Pour un échantillonnage donné et une période de récurrence donnée, on calcule donc pour chaque valeur de F la distance D donnant Pd = 0,5 . Les résultats sont exprimés sous forme de perte par rapport à la référence Do, soit L = 40 log $(\frac{D}{Do})$.

La figure 13 représente cette perte L en fonction de F pour F_R = 200 KHz et pour des périodes d'échantillonnage différentes : T = 250 ns (courbe 1)
T = 500 ns (courbe 2)
T = 1000 ns (courbe 3).

La figure 14 représente les mêmes courbes pour F_R = 100 KHz.

On constate que le minimum de pertes est obtenu autour du facteur de forme 5 (entre 4 et 6). Ces pertes tendent vers $-\infty$ (en dB) quand F tend vers 1 : on se rapproche alors des radars CW où il n'y a plus de réception possible par la même antenne.

Quand F augmente, les pertes augmentent également : si il y a moins d'éclipses, l'écho étant moins long, l'influence de l'échantillonnage devient importante. Celle-ci diminue quand on augmente la cadence de l'échantillonnage (courbe 1). Si on l'augmente beaucoup, les pertes diminuent quand le facteur de forme augmente et l'optimum tend à disparaître : on a alors intérêt à prendre un facteur de forme élevé.

9 - OPTIMISATION DU FACTEUR DE FORME A PUISSANCE CRETE EMISE CONSTANTE

Si Pc est constante, Pm varie avec F. La courbe Pdo = f(D) de référence va donc dépendre de F, le maximum de portée étant atteint pour F = 1 (radar CW). La figure 15 représente diverses courbes (hors éclipse et hors pertes d'échantillonnage) pour différents facteurs de forme.

La portée de référence restant 100 km, on peut déduire les courbes précédentes (à Pm constante), les courbes à Pc constante en ajoutant aux pertes déjà calculées des pertes supplémentaires égales à $10 \log (\frac{1}{F})$. La figure 16 représente ces pertes pour :

F_R = 200 KHz et T = 250 ns (courbe 1)
T = 500 ns (courbe 2)
T = 1000 ns (courbe 3).

La figure 17 représente ces mêmes courbes pour F_R = 100 KHz. On constate que le minimum de pertes est obtenu pour un facteur de forme voisin de 2. Quand F est faible, la puissance moyenne est élevée mais les éclipses sont fréquentes. Quand F est élevé, les éclipses sont moins gênantes mais la puissance moyenne est plus faible.

10 - CONCLUSION

On a présenté ici 4 méthodes pour estimer la probabilité de détection. Si les deux premières sont restrictives quant aux conditions d'utilisation (cible stationnaire, filtrage et échantillonnage adaptés à l'émission), les deux dernières ne le sont pas. De plus, la quatrième est très rapide.

Ces méthodes permettent d'obtenir facilement des portées de détection pour des radars HFR, en estimant des pertes par rapport à un radar CW qui aurait la même puissance et ceci pour différentes charges de calcul.

Ces méthodes permettent également de déterminer, pour une puissance moyenne donnée et un échantillonnage donné, l'optimum du facteur de forme (qui éventuellement n'existe pas si la cadence d'échantillonnage est très élevée).

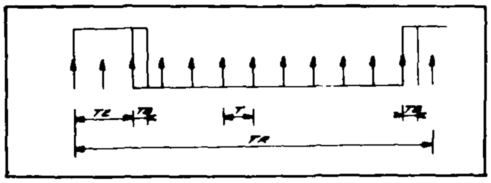

Fig. 1

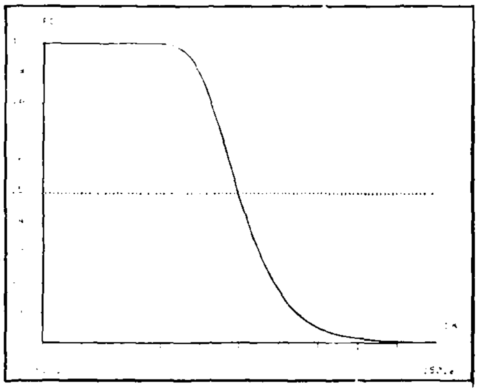

Fig. 4

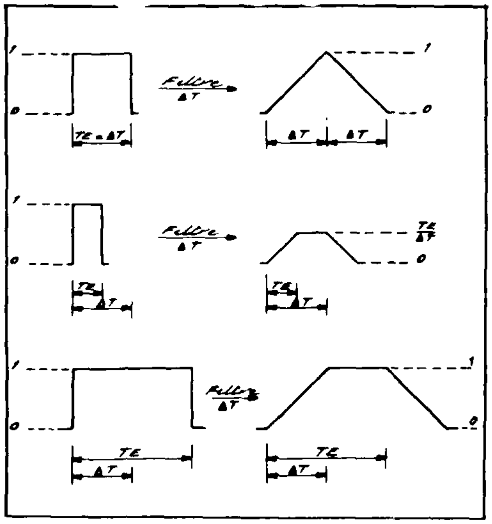

Fig. 2

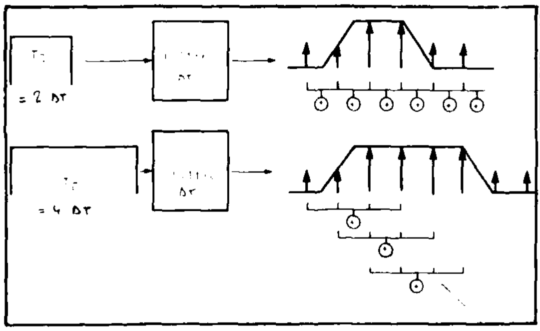

Fig. 3

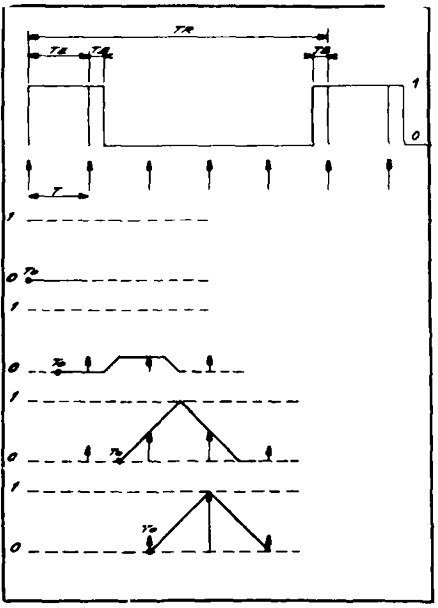

Fig. 5

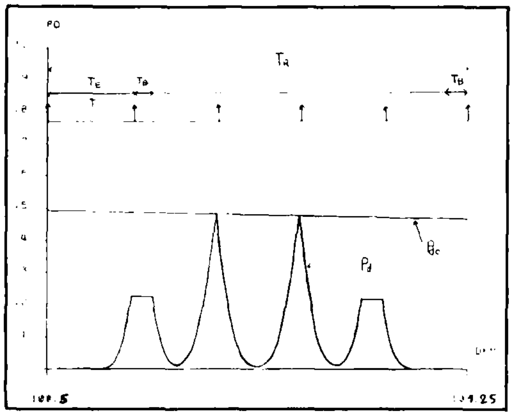

Fig. 6

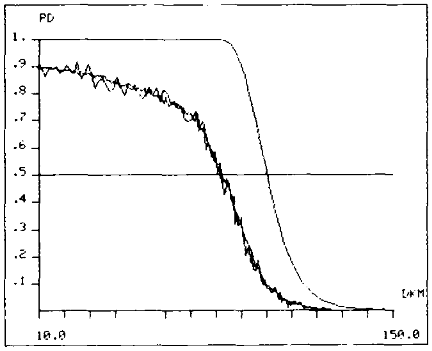

Fig. 9

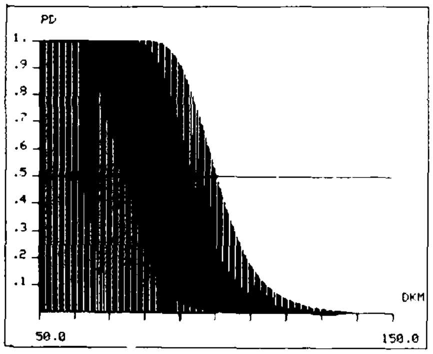

Fig. 7

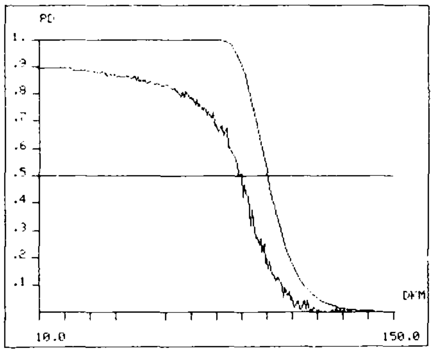

Fig. 10

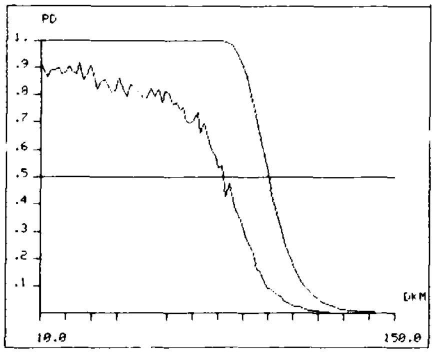

Fig. 8

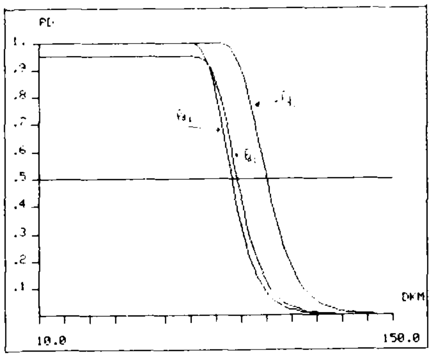

Fig. 11

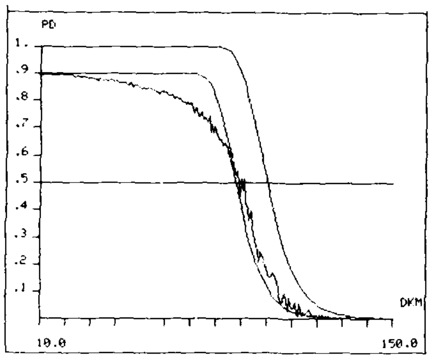

Fig. 12

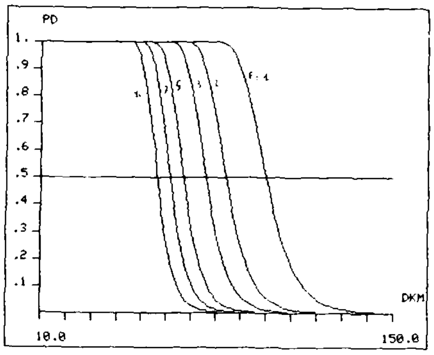

Fig. 15

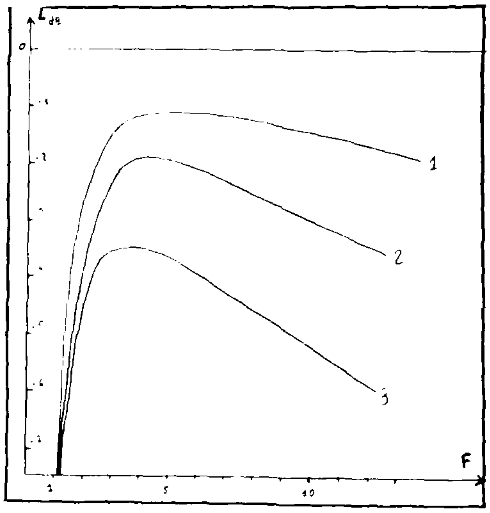

Fig. 13

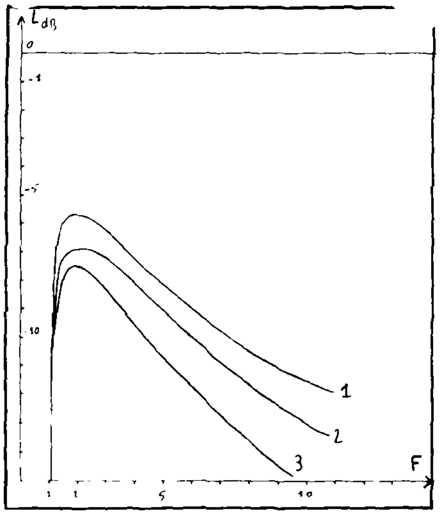

Fig. 16

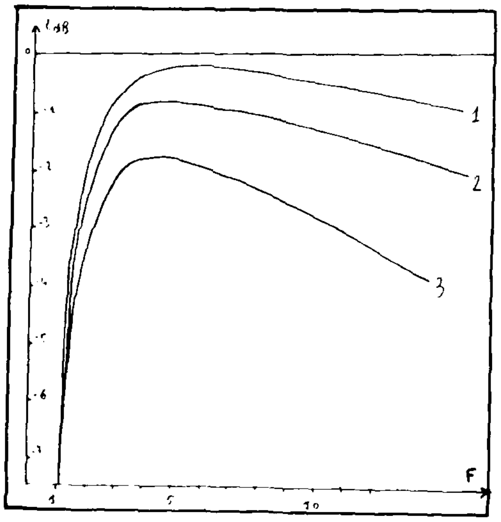

Fig. 14

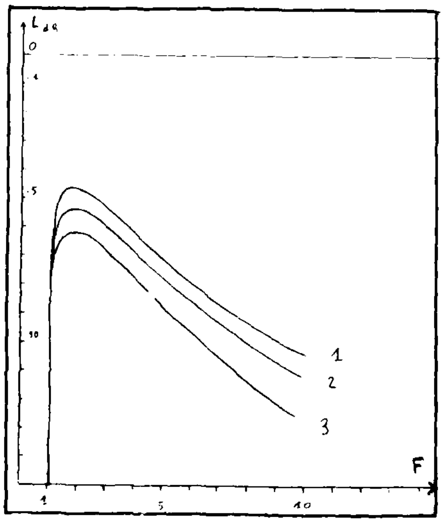

Fig. 17

DISCUSSION

A.Pratesi

Which fluctuation case did you assume for the target? Probably the model adopted was that of a non-fluctuating target otherwise the performance would have been much worse.

Author's Reply

Yes, we assumed an ideal, non-fluctuating target in order to simplify the analysis of the statistical process.

A GENERAL SOLUTION FOR THE SYNTHESIS OF BINARY SEQUENCES WITH DESIRED CORRELATION SEQUENCE

Robert J. Polge
Department of Electrical and Computer Engineering
The University of Alabama in Huntsville
Huntsville, Alabama 35899, USA

SUMMARY

Binary sequences are of considerable interest in many applications. In particular, the performance of a radar depends on the ambiguity function. For the case of binary phase modulation, the zero-doppler performance of a pulse radar is a function of the discrete autocorrelation of the corresponding binary sequence. Alternately, a binary sequence can be expressed as a sequence of runs where the length of a run is equal to the number of contiguous bits of same sign. Given a run pattern the discrete autocorrelation can be computed easily and more rapidly than with the standard technique. The inverse problem, which is the synthesis of a run pattern given the desired discrete autocorrelation sequence, is much more difficult.

This paper develops a set of sequential relations which relate the desired autocorrelation sequence to properties of the run pattern. For example, the autocorrelation at lag 1 defines the number of runs for a sequence of specified length. The autocorrelation at lag 2 now determines the number of runs of length 1. More generally the autocorrelation at lag (k+1) establishes a relation between consecutive runs with sum exactly equal to k. Judicious use of these relations greatly facilitates the computer synthesis of binary sequences. While the method is quite general, emphasis is on tracking applications where it is desired to minimize the sidelobes as far as possible.

1.0 Introduction

Binary sequences (elements +1 or -1) are of considerable interest. In radar, one is frequently interested in pulse compression, which involves the transmission of a long coded pulse and the processing of the received echo to obtain a relatively narrow pulse. In particular, the performance of a radar depends on the ambiguity function. The desired goal is to achieve high range resolution, as in a narrow pulse, and good doppler resolution and high average power, as in a wide pulse. In the case of binary phase modulation, the zero-doppler performance is determined by the discrete autocorrelation of the corresponding binary sequence.

A new and efficient technique to compute the discrete autocorrelation of a binary sequence in terms of run structure was presented in [1], where a run is defined as the number of contiguous bits of the same sign. The inverse problem is the synthesis of binary sequences with specified correlation. It was illustrated by the synthesis of binary sequences of length 17 such that the absolute value of the sidelobes of the correlation sequence is not greater than 1 up to lag 7.

This paper develops new relations and an efficient strategy which makes possible the synthesis of binary sequences of much greater lengths. Assume for example a length of 128 bits. A brute force approach (using only symmetry) would require the computation of 2^{126} correlation sequences which is clearly impossible. In the proposed technique each element of the desired correlation sequence determines necessary structural run relations which eliminate most of the binary sequences. This is done sequentially starting with lag 1 and continuing with lag 2, then lag 3, and so on. For example, in a tracking application one may want minimum sidelobes as far as possible. Very rapidly, the combined relations define a very narrow class of sequences and the synthesis becomes practical.

The paper is organized as follows:
(1) the run correlation technique developed in [1] is reviewed,
(2) the structural relations necessary for synthesis are derived,
(3) a method to define the allowable set of tails for a specified correlation sequence is presented,
(4) the procedure for the general synthesis of binary sequences using a digital computer is discussed,
(5) the last section contains conclusions and recommendations.

2.0 Run Correlation Technique

First, let us consider a general finite sequence of length N, defined as (a_i, i=0, 1,...,N-1), where the a(i) are arbitrary real numbers. We define the autocorrelation function c(k) as follows:

$$c(0) = N$$

$$c(k) = \sum_{i=0}^{N-1-|k|} a(i)\,a(i-|k|), \quad |k| = 1,2,\ldots,N-1 \tag{1}$$

$$c(k) = 0 \qquad |k| \geq N.$$

Let us now consider a rectangular waveform x(t), defined as a sequence of N contiguous pulses of duration T and height a(0), a(1), ..., a(N-1). Thus

$$x(t) = \sum_{i=0}^{N-1} a(i)\,\mathrm{rect}_T(t-(i+0.5)T), \tag{2}$$

where $\mathrm{rect}_T(t)$ is a unit rectangular pulse of height 1 and width T, centered at the origin.

It can easily be shown that the autocorrelation of this waveform is

$$\phi_{xx}(\tau) = \sum_{k=-(N-1)}^{N-1} T\, c(k)\Delta_{2T}(\tau - kT) \tag{3}$$

where the c(k) are given in (1) and $\Delta_{2T}(t)$ is a triangular pulse of height 1 and width 2T, centered at the origin. Note that for $\tau = jT$.

$$\begin{aligned} \phi_{xx}(jT) &= T\, c(j) \quad \text{for } |j| < N \\ &= 0 \qquad\qquad\quad |j| \geq N \end{aligned} \tag{4}$$

and the remaining values of $\phi_{xx}(\tau)$ are obtained simply by drawing straight lines between these points. For convenience, we assume in the sequel that T = 1 as a simple choice of time scale.

Let us now specialize to consider only binary sequences; that is a(i) takes only values ± 1. For a binary sequence, it is convenient to introduce the concept of run length, the number of consecutive pulses of the same sign. For example, consider the sequence

$$[a(i),\ i=0,10] = [1,-1,1,1,1,-1,-1,-1,1,1,-1] \tag{5}$$

with autocorrelation function

$$[c(k),k=-10,10] = [-1,2,-1,-2,1,2,1,-4,-3,0,11,0,-3,-4,1,2,1,-2,-1,2,-1]. \tag{6}$$

In terms of run lengths, this sequence could be identified as

$$[r(i),i=1,6] = [1,1,3,3,2,1], \tag{7}$$

where we can assume, without loss of generality, that the sequence starts with +1.

The rectangular waveform x(t) is still given by (2) where $|a(i)| = 1$. Alternatively x(t) can be viewed as a sum of step functions, where a new step function is introduced to effect the changes of sign in x(t). Thus our example can be written as

$$x(t) = u(t) + 2 \sum_{i=1}^{5} (-1)^i\, u(t-\rho_i) + u(t-10), \tag{8}$$

where u(t) is the unit step and $\rho_i = \sum_{j=1}^{i} r_j$, with $\rho_0 = 0$. Assuming that the sequence starts with a +1, the general formula is

$$x(t) = u(t) + 2 \sum_{i=1}^{R-1} (-1)^i\, u(t-\rho_i) + (-1)^R\, u(t-N), \tag{9}$$

where N and R are, respectively, the length and number of runs and $N = \sum_{i=1}^{R} r_i$.

The autocorrelation is

$$\phi_{xx}(t) = x(-t) * x(t), \tag{10}$$

where $x(-t) = -u(t) + 2 \sum_{i=1}^{R-1} (-1)^{i+1}\, u(t+\rho_i) + (-1)^{R+1} u(t+N)$ and * stands for convolution. Using

$$u(t-a) * u(t-b) = u_1(t-(a+b)), \tag{11}$$

where $u_1(t) = t$ for $t > 0$ and zero elsewhere (the unit ramp), it follows that

$$\phi_{xx}(t) = \sum_{i=0}^{R} \sum_{j=0}^{R} (-d_i d_j)\, u_1(t-\rho_i + \rho_j), \tag{12}$$

where $d_0 = 1$, $d_R = (-1)^R$, $d_i = (-1)^i\, 2$ for $i = 1,\dots,R-1$.

Each step of x(t) and of x(-t) is described by a pair of integers: coefficient and delay. Similarly, each ramp in $\phi_{xx}(t)$ is described by a pair of integers: coefficient and delay. Therefore the correlation can be performed using a tabular arrangement, where the horizontal and vertical entries are, respectively, the pairs defining x(t) and x(-t). The elements of the table, which are obtained using (11), define all the ramps which combine to form $\phi_{xx}(t)$. This is illustrated in Table 1 for an arbitrary six-run sequence. Pairs with the same delay must be collected by adding the coefficients algebraically to find the net coefficient for the ramp starting at that delay.

Starting with the most negative delay, -N, one can work forward to the greatest positive delay, N, to obtain the entire autocorrelation function. Let us take our original example, defined in terms of run lengths, $[r_1 = 1,6] = [1,1,3,3,2,1]$. Using these numerical values in Table 1 and gathering terms, one obtains

$$\phi_{xx}(T) = -u_1(t+11) + 4u_1(t+10) - 6u_1(t+9) + 2u_1(t+8) + 4u_1(t+7) - 2u_1(t+6) - 2u_1(t+5) - 4u_1(t+4) + 6u_1(t+3) + 2u_1(t+2)$$

$$+8u_1(t+1)-22u_1(t)+8u_1(t-1)+2u_1(t-2)+6u_1(t-3)-4u_1(t-4)-2u_1(t-5)-2u_1(t-6)+4u_1(t-7)+2u_1(t-8)-6u_1(t-9)$$

$$+4u_1(t-10)-u_1(t-11) \qquad (13)$$

To evaluate $\phi_{xx}(j)$ replace each term such as $u_1(j+k)$ by $j+k$ if $j > -k$ and by zero otherwise, and accumulate. Alternately, one can use an iterative procedure as follows:

Let ϕ_k = autocorrelation at lag k (change in slope)

ρ_k = slope of ramp originating at lag k

s_k = net slope of ramp leaving at lag k.

Then

$$s_k = s_{k-1} + \rho_k$$

$$\phi_{k+1} = \phi_k + s_k \quad \text{for } k = -N, N-1 \qquad (14)$$

with initial conditions

$$s_{-N-1} = \phi_{-N} = 0$$

and the ρ_k are read from the table ($\rho_{-N} = (-1)^{R+1}$). Since the autocorrelation is symmetric it needs to be computed only for positive lags using (14) for k = 0, N-1 with initial conditions

$$s_{-1} = 2R-1,\ \rho_0 = -4R+2,\ \phi_0 = N.$$

Thus in our example

$$[\phi_i, i=0,10] = [11,0,-3,-4,1,2,1,-2,-1,2,-1]$$

$$[\rho_i, i=0,10] = [-22,8,2,6,-4,-2,-2,4,2,-6,4] \qquad (15)$$

$$[s_i, i=0,10] = [-11,-3,-1,5,1,-1,-3,1,3,-3,1].$$

x(t) x(-t)	1 0	-2 r_1	2 r_1+r_2	-2 $r_1+r_2+r_3$	2 $r_1+r_2+r_3+r_4$	-2 $r_1+r_2+r_3+r_4+r_5$	1 N
-1 0	-1 0	2 r_1	-2 r_1+r_2	2 $r_1+r_2+r_3$	-2 $r_1+r_2+r_3+r_4$	2 $r_1+r_2+r_3+r_4+r_5$	-1 N
2 $-r_1$	2 $-r_1$	-4 0	4 r_2	-4 r_2+r_3	4 $r_2+r_3+r_4$	-4 $r_2+r_3+r_4+r_5$	2 $r_2+r_3+r_4+r_5+r_6$
-2 $-r_1-r_2$	-2 $-r_1-r_2$	4 $-r_2$	-4 0	4 r_3	-4 r_3+r_4	4 $r_3+r_4+r_5$	-2 $r_3+r_4+r_5+r_6$
2 $-r_1-r_2-r_3$	2 $-r_1-r_2-r_3$	-4 $-r_2-r_3$	4 $-r_3$	-4 0	4 r_4	-4 r_4+r_5	2 $r_4+r_5+r_6$
-2 $-r_1-r_2-r_3-r_4$	-2 $-r_1-r_2-r_3-r_4$	4 $-r_2-r_3-r_4$	-4 $-r_3-r_4$	4 $-r_4$	-4 0	4 r_5	-2 r_5+r_6
2 $-r_1-r_2-r_3-r_4-r_5$	2 $-r_1-r_2-r_3-r_4-r_5$	-4 $-r_2-r_3-r_4-r_5$	4 $-r_3-r_4-r_5$	-4 $-r_4-r_5$	4 $-r_5$	-4 0	2 r_6
-1 -N	-1 -N	2 $-r_2-r_3-r_4-r_5-r_6$	-2 $-r_3-r_4-r_5-r_6$	2 $-r_4-r_5-r_6$	-2 $-r_5-r_6$	2 $-r_6$	-1 0

Table 1: TABULAR ARRANGEMENT FOR CORRELATION CALCULATION

Table 1 is a square array of dimension M = R+1 with interesting structural properties. It is skew symmetric, with each entry above the principal diagonal having a corresponding entry of opposite sign below the principal diagonal. The magnitude of the coefficients of the corner entries is 1; the magnitude of the other coefficients along the edges of the table is 2; the magnitude of all other coefficients is 4. The principal diagonal contains all the ramps starting at lag zero, resulting in a change of slope $\rho_0 = -4R+2$ and a net slope forward $s_0 = -2R+1$. By symmetry, since $\phi_0 = N$, it follows that $\phi_1 = N-2R+1$. Note that ϕ_1, the autocorrelation at lag 1, depends only on sequence length and number of runs. In particular, for any sequence with N odd and $R=(N+1)/2$, the autocorrelation at lag 1 will be 0. Also, the change in slope at delay 1 is

$$\rho_1 = 4n_1 - 2t_1 \tag{16}$$

where n_1 is the total number of runs of length 1 and t_1 is the number of such runs occurring at the end of the sequence. Because of the symmetry, all the remaining information is contained in the elements above the principal diagonal, and the element in the upper right corner is always N.

The lag values along the first diagonal above the principal diagonal are list of runs, i.e., r_1, r_2, ..., r_R. The coefficients of the end terms on this diagonal are 2; the coefficients of the remaining terms are 4. The lag values along the next diagonal *are sums of consecutive runs taken 2 at a time. All coefficients* on this diagonal are negative, with the end coefficients being -2 and the other coefficients -4. A similar pattern can be seen on the other diagonals. To facilitate both visualization and computation, it is convenient to present a revised tableau, as shown in Table 2.

This tableau gives just the delays of the ramp pairs. The first column contains the delays of the first diagonal above the principal diagonal; the second column contains the delays of the next diagonal; *and so on. The coefficients* to be associated with each delay can be determined by a simple rule. All the coefficients associated with any given column have the same sign, and the signs alternate from column to solumn, starting with a plus for the first column. In each column the magnitude of the coefficients for the first and last delay is 2; the magnitude of the remaining coefficients is 4.

The table is computed in a straightforward manner, one row after the other. At the same time the set of slope changes $[\rho_i]$ are computed; that is, when the element of the table is equal to i, then ρ_i is incremented by the appropriate signed weight. Thus the elements of the table are used immediately and need not be stored. The number of additions in the table is (R-1)(R-2)/2 plus R(R-1)/2 additions for accumulating the ρ values. Following (14), we need 2 additions to compute s_k, and ϕ_{k+1} from s_{k-1} and ϕ_k, using ρ_k, for a total of 2(R-1) additions. Thus the computation of $[\phi_i]$ requires $(R-1)^2$ additions. As a general rule, $R \approx N/2$; hence, using the table, one requires approximately $(N-2)^2/4$ additions and no multiplications.

The direct calculation of the autocorrelation function requires N(N-1)/2 multiplications and (N-1)(N-2)/2 additions. Even if we assume that the multiplications can be performed as exclusive or's at the same cost as an addition, the proposed technique should be *four times faster than the direct method.*

3.0 Structural Relations

It is easy to eliminate s_k in (14) and to express ϕ_k in terms of s_0 and ρ_k:

$$\phi_1 = \phi_0 + s_0$$

$$\phi_2 = \phi_0 + 2s_0 + \rho_1 \tag{17}$$

$$\cdots\cdots\cdots\cdots$$

$$\phi_k = \phi_0 + ks_0 + (k-1)\rho_1 + (k-2)\rho_2 + \ldots + \rho_{k-1}$$

where $\phi_0 = N$ and $s_0 = -2R+1$.

Observe a binary sequence, from left to right, through a moving window of width m. For each position compute the sum of the m runs in the window and tabulate. Let s_{km} be the number of times that the sum of m runs is exactly equal to k, within a complete window scan. Let t_{km} be the number of times that the sum of m runs is exactly equal to k for the two ending positions of the window; t_{km} can take only one of three values: 0, 1 and 2. It can be shown that the incremental slope ρ_k is a function of s_{km} and t_{km} where m ranges from 1 to k:

$R_1(+)$	$R_2(-)$	$R_3(+)$	$R_4(-)$	$R_5(+)$
r_1	r_1+r_2	$r_1+r_2+r_3$	$r_1+r_2+r_3+r_4$	$r_1+r_2+r_3+r_4+r_5$
r_2	r_2+r_3	$r_2+r_3+r_4$	$r_2+r_3+r_4+r_5$	$r_2+r_3+r_4+r_5+r_6$
r_3	r_3+r_4	$r_3+r_4+r_5$	$r_3+r_4+r_5+r_6$	
r_4	r_4+r_5	$r_4+r_5+r_6$		
r_5	r_5+r_6			
r_6				

Table 2: Revised Tableau

$$\rho_1 = 4s_{11} - 2t_{11}$$

$$\rho_2 = 4s_{21} - 2t_{21} - 4s_{22} + 2t_{22} \qquad (18)$$

$$\rho_3 = 4s_{31} - 2t_{31} + 4s_{33} - 2t_{33} - 4s_{32} + 2t_{32}$$

and so on. For a more compact notation, let ω_k be the number of times that the sum of runs is equal to k for windows with odd width and let η_k be the number of times the sum of runs is equal to k for window with even width. Let also ω_k' and η_k' be the number of times that the sum of runs is equal to k for ending windows with odd or even width, respectively. Then, the relations for ρ_k become

$$\rho_1 = 4\omega_1 - 2\omega_1'$$

$$\rho_k = 4(\omega_k - \eta_k) - 2(\omega_k' - \eta_k') \text{ for } k = 2,3,\ldots \qquad (19)$$

The specific run patterns are denoted by a second index which is defined by ordering the patterns as increasing integers. For example,

$$\omega_4 = \omega_{41} + \omega_{42} + \omega_{43} + \omega_{44} = \#(4) + \#(112) + \#(121) + \#(211)$$

$$\eta_4 = \eta_{41} + \eta_{42} + \eta_{43} + \eta_{44} = \#(13) + \#(22) + \#(31) + \#(1111) \qquad (20)$$

$$\omega_5 = \omega_{51} + \omega_{52} + \omega_{53} + \omega_{54} + \omega_{55} + \omega_{56} + \omega_{57} + \omega_{58} = \#(5) + \#(113) + \#(122) + \#(131) + \#(212)$$
$$+ \#(221) + \#(311) + \#(11111)$$

$$\eta_5 = \eta_{51} + \eta_{52} + \eta_{53} + \eta_{54} + \eta_{55} + \eta_{56} + \eta_{57} + \eta_{58} = \#(14) + \#(23) + \#(32) + \#(41) + \#(1112)+\#(1121)$$
$$+ \#(1211) + \#(2111).$$

Sometimes one may want to count together a pattern and its symmetric, this is indicated by underlining the pattern index. For example

$$\eta_{5\underline{1}} = \eta_{51} + \eta_{54} = \#(14) + \#(4i)$$

$$\omega_{5\underline{2}} = \omega_{52} + \omega_{57} = \#(113) + \#(311) \qquad (21)$$

We have shown how the sequence of incremental slopes $[\rho_k]$ relate to the sequence structure in (18). The sequences $[s_k]$ and $[\rho_k]$ can be computed from the desired correlation sequence $[\phi_k]$ using (14):

$$s_k = \phi_{k+1} - \phi_k \qquad (22)$$

$$\rho_k = s_k - s_{k-1} = \phi_{k+1} - 2\phi_k + \phi_{k-1}$$

Together (19) and (22) establish a connection between the desired correlation sequence and the required run structure.

As an illustration, assume that a tracking application requires

$$[\phi_k,\ k=0,\ N-1] = [N,0,-1,0,-1,0,-1, \text{ as far as possible}]. \qquad (23)$$

From (22) one obtains

$$[s_k,\ k=0,\ N-1] = [-N,-1,1,-1,1,-1 \text{ as far as possible}]$$

$$[\rho_k,\ k=0,\ N-1] = [-2N,\ N-1,\ 2,-2,2,-2 \text{ as far as possible}] \qquad (24)$$

Since $s_o = -2R + 1 = -N$, it follows that N is odd and that it can be written as $N = 4j + 1$ or $N = 4j + 3$. Consider the case $N = 4j + 3$, then $R = 2(j+1)$ and $\phi(N-1) = -1$. The number of runs of length 1 is determined from

$$\rho_1 = N-1 = 4\omega_1 - 2\omega_1' \qquad (25)$$

which becomes

$$2j + 1 = 2\omega_1 - \omega_1'. \qquad (26)$$

The solution of (26) is $\omega_1' = 1$ which means that the sequence starts with a run of length 1 and that the number of runs of length 1 is $n_1 = \omega_1 = j + 1$. The remaining relations can be written as

$$\rho_k = 2(-1)^k = 4\omega_k - 2\omega_k' - 4\eta_k + 2\eta_k'$$

$$\text{or} \quad (-1)^k = 2\omega_k - \omega_k' - 2\eta_k + \eta_k' \text{ for } k=2,3\ldots \qquad (27)$$

Relation (27) establishes constraints on the sequence structure. It also shows that the sequence endings (tails) must satisfy

$$\omega_k' + \eta_k' = 1 \text{ for } k = 2,3,\ldots \qquad (28)$$

4.0 Set of Allowable Tails

Continuing the example defined by relations (24) through (28) let us determine the set of allowable tails. Assume that we want to satisfy (24) for the first m steps, i.e. through ϕ_{m+1}. Relation (28) means that for each k, where k=1 to m, the runs in the tails will add exactly to k exactly one time. The set of allowed tails can be defined sequentially. From (26), the sequence is of the form

$$1 \ldots \overline{2} \tag{29}$$

where $\overline{2}$ denotes a run of length 2 or more. Now, to satisfy (28) for k=2, one has two choices

$$11 \ldots \overline{3} \quad \text{or} \quad 1\overline{2} \ldots 2 \tag{30}$$

To satisfy (28) for k=3 one must expand each of the two choices

$$\begin{aligned} 11 \ldots \overline{3} &\rightarrow 111 \ldots \overline{4} \quad \text{or} \quad 11\overline{2} \ldots 3 \\ 1\overline{2} \ldots 2 &\rightarrow 12 \ldots \overline{2}2 \quad \text{or} \quad 1\overline{3} \ldots 12 \end{aligned} \tag{31}$$

Continuing this procedure through m = 5, i.e. ϕ_6, one obtains 16 sets of allowable tails

$$\begin{aligned} &11111 \ldots \overline{6},\ 1111\overline{2} \ldots 5,\ 1112 \ldots \overline{2}4,\ 111\overline{3} \ldots 14 \\ &1121 \ldots \overline{3}3,\ 112\overline{2} \ldots 23,\ 113 \ldots \overline{2}13,\ 11\overline{4} \ldots 113 \\ &1211 \ldots \overline{4}2,\ 121\overline{2} \ldots 32,\ 122 \ldots \overline{2}22,\ 12\overline{3} \ldots 122 \\ &131 \ldots \overline{3}12,\ 13\overline{2} \ldots 212,\ 14 \ldots \overline{2}112,\ 1\overline{5} \ldots 1112. \end{aligned} \tag{32}$$

5.0 Procedure for Synthesis

We want to find binary sequences of a given length which will match a specified correlation pattern for as many lags as possible.

An optimum procedure is presented to define the class of binary sequences which satisfy a specified correlation pattern up to lag 6. While the technique could be extended beyond lag 6, this may not be necessary. Indeed in order to satisfy the correlation pattern up to lag 6 one eliminates most of the binary sequences and the acceptable class of sequences has very few degrees of freedom left. Thus an intelligent computer search becomes feasible even if it is not optimum.

To determine the class of sequences which satisfy the desired correlation pattern up to lag 6, the steps are as follows: (1) Select N and compute the number of runs R from ϕ_1, (2) Compute the sequence of incremental slopes $[\rho_k,\ k=0,5]$ from the specified correlation sequence $[\phi_k,\ k=0,6]$ using (22), (3) Determine the set of allowable tails as explained in Section 4.0 and incorporate this information in $[\rho_k]$ to obtain $[\rho_k^*]$ where the end effects have been removed, (4) Define the class of sequences which satisfy all the structural constraints implicitly contained in the relations ρ_1^*, ρ_2^*, ρ_3^*, ρ_4^*, and ρ_5^*. This is the most difficult part of the synthesis, (5) Translate the set of constraints obtained above into a list of acceptable sequences.

To illustrate the procedure let $N = 4j+3 = 31$ and assume a correlation sequence as in (23). Then the number of runs is

$$R = \frac{N+1}{2} = 2(j+1) = 16. \tag{33}$$

From (24)

$$[\rho_k,\ k=0,5] = [-62,30,2,-2,2,-2]. \tag{34}$$

Among the sets of tails listed in (32) select one, say

$$1121 \ldots \overline{3}3. \tag{35}$$

The sequences ω_k' and η_k' are easily computed for the selected set of tails

$$\begin{aligned} [\omega_k',\ k=1,5] &= [1,0,1,1,0] \\ [\eta_k',\ k=1,5] &= [0,1,0,0,1]. \end{aligned} \tag{36}$$

Write ω_k and η_k as

$$\begin{aligned} \omega_k &= \omega_k^* + \Delta\omega_k \\ \eta_k &= \eta_k^* + \Delta\eta_k \end{aligned} \tag{37}$$

where $\Delta\omega_k$ and $\Delta\eta_k$ are the contributions from the tails. One reads

$$\begin{aligned} [\Delta\omega_k,\ k=1,5] &= [3,1,1,2,0] \\ [\Delta\eta_k,\ k=1,5] &= [0,1,2,0,1] \end{aligned} \tag{38}$$

where $\overline{3}$ is not yet usable.

Compute the sequences $[\rho_k^*]$ by plugging $[\omega_k']$, $[\eta_k']$, $[\Delta\omega_k]$, $[\Delta\eta_k]$ into the sequences $[\rho_k]$ given by (25) and (27) and solve. One obtains 5 relations

$$\begin{aligned} &\omega_1^* = 5 \\ &\omega_2^* = \eta_2^* \\ &\omega_3^* = \eta_3^* + 1 \\ &\omega_4^* + 1 = \eta_4^* \\ &\omega_5^* = \eta_5^* \ . \end{aligned} \tag{39}$$

Denote as frame the part of the sequence which needs to be specified,

$$1 \ \ldots \ \bar{3}. \tag{40}$$

From there on the discussion will refer to the frame unless indicated otherwise. Equation (39-1) defines n_1^* the additional runs of length 1

$$\omega_1^* = n_1^* = 5. \tag{41}$$

It follows that the number of runs of length 1 is $n_1 = 6$, that the number of runs of length $\bar{2}$ (2 or more) is $n_{\bar{2}} = 6$, and that these $n_{\bar{2}}$ runs span $N_{\bar{2}} = 18$ bits. Let n_2 be the number of runs of length 2. The first set of bounds for n_2 is $\xi(n_2) = (0,5)$.

Define p_1 as the number of packs of 1, where a pack consists of consecutive identical runs. Based on n_1, $n_{\bar{2}}$, and the structure of the frame, the first set of bounds for p_1 is $\xi\ (p_1) = (1,6)$. Equation (39-2) establishes a relation between n_2 and p_1

$$\begin{aligned} & n_2 = n_{11} = n_1 - p_1 \\ \text{or} \quad & n_2 + p_1 = n_1 = 6. \end{aligned} \tag{42}$$

After combining the bounds of n_2 and p_1, one obtains the final set of bounds for p_1

$$\xi(p_1) = (1,6). \tag{43}$$

In other words there are 6 choices for (p_1, n_2). Let the packs of 1 be partitioned into packs made of a single run and packs made of multiple runs

$$p_1 = \sigma_1 + \rho_{1\bar{2}} \ . \tag{44}$$

The first set of bounds for σ_1, $\xi\ (\sigma_1)$, is easily obtained given n_1 and p_1. From n_1, p_1 and σ_1 one can compute the first set of bounds on ω_{32}, $\xi\ (\omega_{32})$, using

$$\omega_{32} = \#(111) = n_1 - 2p_1 + \sigma_1. \tag{45}$$

Similarly one can compute the bounds for $\omega_{31} = \#(3)$, $\xi\ (\omega_{31})$, given $N_{\bar{2}}$, n_2 and $n_{\bar{3}}$. These results are listed in Table 3 for our example.

p_1	n_2	$n_{\bar{3}}$	$\xi\ (\omega_{31})$	$\xi\ (\omega_{32})$
1	5	1	0, 0	4, 4
2	4	2	0, 1	2, 3
3	3	3	0, 2	0, 2
4	2	4	2, 3	0, 1
5	1	5	4, 4	0, 0
6	0	6	6, 6	0, 0

Table 3: Constraints Through ρ_2 or ϕ_3

The number of runs of length k and the number of packs of runs of length k have been denoted as n_k and p_k, respectively. Let r_k and π_k be used, respectively, as symbols for a run of length k and a pack of runs of length k. We define as a level k block an interlaced sequence made of packs π_k and $\pi_{\overline{k+1}}$, where $\pi_{\overline{k+1}}$ is the symbol for a pack of runs of length k+1 or more. Let l and m, denote respectively, the number of packs π_k and the number of packs $\pi_{\overline{k+1}}$ in the block. As a concise representation a level k block will be written

$$\beta(k, l, m, i) \tag{46}$$

where $i = 1$ or 2 depending whether the block starts with π_k or $\pi_{\overline{k+1}}$. At this stage, the frame can be represented as a level 1 block

$$\beta(1,\ p_1,\ p_1,\ 1). \tag{47}$$

the last element of this block is the right edge of the frame and it will be denoted as Tie.

Tie is a $\pi_{\bar{2}}$ which is made up of one or more $r_{\bar{2}}$ (including the visible $\bar{3}$). Our next step is to specify Tie as a level 2 block,

$$\text{Tie} = \beta(2, l, m, i).$$

One needs to distinguish 4 cases:

$$\begin{aligned} \text{Tie}\ (1) &= \beta(2,0,1,2) \\ \text{Tie}\ (2) &= \beta(2,1,1,1) \\ \text{Tie}\ (3) &= \beta(2,j,j+1,2) \\ \text{Tie}\ (4) &= \beta(2,j+1,j+1,1) \end{aligned} \qquad (48)$$

where $j=\bar{1}$ (one or more). Table 4 expands on Table 3 by specifying the choice of Tie for each p_1. Denote as Window the remainder of Frame minus Tie, then $\hat{w}_k$ denotes the maximum number of runs r_k available for use in the window. Obviously $\hat{w}_2$ and $\hat{w}_{\bar{3}}$ will restrict the selection of level 2 blocks within the window. Also the choice of Tie is restricted by ρ_1, n_2 and $n_{\bar{3}}$ given in Table 3. The last column of Table 4 gives the first set of bounds for η_3 in the frame, $\xi\ (\eta_3)$.

p_1	Tie (k)	$\hat{w}_2$	$\hat{w}_{\bar{3}}$	$\xi\ (\eta_3)$	$\xi\ (\lambda_3)$
1	2	0	0	0,0	empty
2	1	4	1	1,2	2,3
2	2	3	1	1,3	2,4
2	3	3	0	2,2	3,3
2	4	2	0	3,3	4,4
3	1	3	2	1,4	2,4
3	2	2	2	1,5	2,4
3	3	2	1	2,4	3,4
3	4	1	1	3,3	4,4
4	1	2	3	1,4	2,4
4	2	1	3	1,3	2,4
4	3	1	2	2,2	3,3
5	1	1	4	1,2	empty
5	2	0	4	1,1	empty
6	1	0	5	0,0	empty

Table 4: Constraints Through ρ_2 Including Tie

For each allowed choice of p_1 and Tie(k) the bounds on ω_{31}, ω_{32}, and η_3 are specified in Tables 3 and 4. We are now ready to solve (39.3). It can be written as

$$\omega_{31} + \omega_{32} = \eta_3 + 1 = \lambda_3 \qquad (49)$$

where λ_3 is the intermediate solution. The bounds on λ_3, which are obtained by merging all bounds in (49), are also listed as $\xi(\lambda_3)$ in Table 4. Altogether there are only 23 distinct combinations of p_1, Tie(k), and λ_3. By completing the solution for each of the above combinations, one defines CLASS-4 sequences, i.e., sequences which satisfy the specified correlation sequence up to ϕ_4.

As an illustration, Table 5 lists all the necessary and sufficient structural constraints for the members of CLASS-4 generated by two combinations: $(p_1, k, \lambda_3) = (3, 3, 3)$ and $(3, 3, 4)$. Consider for example the member of CLASS-4 defined by the first row. In FRAME, the runs of length 1 are organized as 3 packs, two of which are single. Tie is completely defined in terms of packs

$$\text{Tie}(3) = \beta(2,1,2,2) = r_{\bar{3}}\, r_2\, r_{\bar{3}}. \qquad (50)$$

Window contains $\beta(2,1,0,1) = \Pi_2$ and $\beta(2,0,1,2) = \Pi_{\bar{3}}$. In the third row $\beta(2,1,1,x)$ means $\Pi_2\, \Pi_{\bar{3}}$ or $\Pi_{\bar{3}}\, \Pi_2$.

p_1	Tie(k)	λ_3	ω_{31}	ω_{32}	η_3	σ_1	$\beta(2,1,0,1)$	$\beta(2,0,1,2)$	$\beta(2,1,1,X)$
3	3	3	1	2	2	2	1	1	0
3	3	3	2	1	2	1	1	1	0
3	3	4	2	2	3	2	1	0	1

Table 5: Structural Constraints for CLASS-4 Sequences

Now we want to follow up on each member of CLASS-4 to see if it can generate one or more members of CLASS-5, a class of sequences which matches the specified correlation up to ϕ_5. Consider the sequence of packs Π_1 and ignore for the time being *the interlacing blocks* β. *This* sequence consists of p_1 packs of runs of length 1 which are divided into $\sigma_1 = p_{11}$ singles and $p_{1\bar{1}}$ multiples; the symbols are Π_{11} and $\Pi_{1\bar{1}}$, respectively. Group the consecutive Π_{11} and the consecutive $\Pi_{1\bar{1}}$ into Bunches with symbols Γ_{11} and $\Gamma_{1\bar{1}}$, respectively. Let γ_{11} and $\gamma_{1\bar{1}}$ be respectively the number of Γ_{11} and $\Gamma_{1\bar{1}}$ in the Frame. The sequence of packs Π_1 can be viewed as one Cluster of Bunches

$$C(1, \gamma_{11}, \gamma_{1\bar{1}}, X) \tag{51}$$

where X is 1 if the Γ_1 sequence starts with a Bunch made of Π_{11} and *2 otherwise. One can view the Cluster* as defining Holes which will contain the elements β. There are four kinds of Holes: (1) H_{11} between two Π_{11}, (2) $H_{1\bar{1}}$ between Π_{11} and $\Pi_{1\bar{1}}$, (3) $H_{\bar{1}1}$ between $\Pi_{1\bar{1}}$ and Π_{11}, and (4) $H_{\bar{1}\bar{1}}$ between $\Pi_{1\bar{1}}$ and $\Pi_{1\bar{1}}$. At this stage, we do not need to distinguish between $H_{1\bar{1}}$ and $H_{\bar{1}1}$ and we use the symbol $H_{\underline{1\bar{1}}} = H_{1\bar{1}}$ or $H_{\bar{1}1}$. Let h_{11} and $h_{1\bar{1}}$ and $h_{\bar{1}\bar{1}}$ denote the number of such holes. *It is easy to show that* $h_{11} = p_{11} - \gamma_{11}$, $h_{\bar{1}\bar{1}} = p_{1\bar{1}} - \gamma_{1\bar{1}}$, and $h_{\underline{1\bar{1}}} = \gamma_{11} + \gamma_{1\bar{1}} - 1$. As an illustration, consider the first row of Table 5 which defines a member of CLASS-4. *For this case there are* 3 possible Cluster patterns and for each pattern one can easily find $\xi(\omega_{4\underline{2}})$ the bounds for $\omega_{4\underline{2}}$, assuming various assignments of the β blocks in the Holes:

$$\begin{aligned} C(1,1,1,1) &= \Gamma_{11}\Gamma_{1\bar{1}},\ \xi(\omega_{4\underline{2}}) = (0,1) \\ C(1,2,1,1) &= \Gamma_{11}\Gamma_{1\bar{1}}\Gamma_{11},\ \xi(\omega_{4\underline{2}}) = (1,1) \\ C(1,1,1,2) &= \Gamma_{1\bar{1}}\Gamma_{11},\ \xi(\omega_{4\underline{2}}) = (0,1). \end{aligned} \tag{52}$$

The limits on other elements of ω_4 are easily obtained: $\xi(\omega_{41}) = (1,1)$, $\xi(\omega_{43}) = (0,1)$. Similarly the bounds on η_4 are $\xi(\eta_{4\underline{1}}) = (0,2)$, $\xi(\eta_{42}) = (1,1)$, *and* $\xi(\eta_{44}) = (1,1)$. *One is ready to solve* (39-4)

$$\omega_{41} + \omega_{4\underline{2}} + \omega_{43} + 1 = \eta_{4\underline{1}} + \eta_{42} + \eta_{44} = \lambda_4. \tag{53}$$

The bounds on λ_4 are obtained by merging all the bounds: $\xi(\lambda_4) = (3,4)$. The four solutions for the first cluster pattern are

$$(\lambda_4, \omega_{41}, \omega_{4\underline{2}}, \omega_{43}, \eta_{4\underline{1}}, \eta_{42}, \eta_{44}) = (2,1,0,0,0,1,1) \text{ or } (3,1,0,1,1,1,1) \text{ or } (3,1,1,0,1,1,1) \text{ or } (4,1,1,1,2,1,1) \tag{54}$$

Together with the third row of Table 4, the first row of Table 5, and (52), these solutions define the structure of members of CLASS-5.

The next step would be to consider each member of CLASS-5, to partition it, and to check for possible generation of members of CLASS-6. We have developed algorithms *for this purpose*, but discussing them would require too much space.

6.0 Conclusions and Recommendations

We have presented a powerful technique for the generation of binary sequences *with specified* correlation sequence. It was shown that for a binary sequence of length 31 there are only 16 sets of tails allowed, and that for each choice of tails there are only *about 200 members* of CLASS-5 sequences which match the specified correlation through ϕ_5. We are in the process of developing a computer program which will synthesize binary *sequences of length* up to 128 which match a specified correlation pattern as far as possible. It is expected that new sequences will be discovered which will significantly improve the performance of many radar or communication systems. Future plans include the synthesis of cyclic binary sequences.

7.0 Reference

POLGE, *R.* J. *and Stern, H.* E., "A New Technique for the Design of Binary Sequences with Specified Correlation,"pp. 164 - 169, IEEE SOUTHEASTCON 81, Huntsville, Alabama.

BASIC MONOSTATIC POLARIMETRIC BROADBAND TARGET SCATTERING ANALYSIS REQUIRED FOR HIGH RESOLUTION POLARIMETRIC RADAR TARGET DOWNRANGE/CROSSRANGE IMAGING OF AIRBORNE SCATTERERS

by

Bing-Yuen Foo, Sujeet K. Chaudhuri* and Wolfgang-M. Boerner
Communications Laboratory
Department of Electrical Engineering & Computer Science
University of Illinois at Chicago, P.O. Box 4348 (m/c 154)
Chicago, IL 60680 U.S.A.

*Department of Electrical Engineering
University of Waterloo
Waterloo, Ontario N2L 3G1 Canada

SUMMARY

It has been well known that high frequency radar interrogation may (will) disclose fine geometrical as well as indepth material decomposition of radar targets, whereas low frequency interception may (will) only recover such coarse information as target size and target volume. At low frequencies, a target behaves as if it were a point source; within the resonance frequency regime it may disclose its natural frequency structure; and at high frequencies (PO/GO) its geometrical fine structures. Any target descriptor which is intended to describe the geometry becomes somewhat loose in its validity at low and resonant frequencies. For a target descriptor to describe fine geometrical structure, it has to be defined on a high frequency basis.

In the phenomenological wideband polarimetric approach of the polarimetric radar target description first introduced by Kennaugh [2,11] and further extended by Huynen [7], the proper specification of frequency range of validity has not been pointed out. In both treatments little care was given to this fact, which resulted in an haphazard early rejection of these important high resolution polarimetric radar target imaging theories because the resulting algorithms were incorrectly applied to the total spectral region.

In view of these unsubstantiated claims of the "Complete Uselessness of High Resolution Polarimetric Radar Imagery", here, the main objective is to show, based on rigorous electromagnetic vector scattering theory, that the Kennaugh, and particularly the Huynen polarimetric target descriptors, at high frequencies, can be closely related to specular geometry (in particular, specular curvature).

For the purpose of verifying our approach the perfectly conducting ellipsoid is considered versus similar spherical target shapes. Numerical verification with measured scattering data for these shapes is shown, and application of the Kennaugh and Huynen target characteristic descriptors in downrange target discrimination, imaging and identification is suggested or demonstrated.

LIST OF FIGURES

I. INTRODUCTION

Huynen's target descriptors [7] have been successfully applied to polarimetric radar target discrimination [12]. For instance, by comparing descriptors of different targets (at fixed aspect angles) at a fixed frequency, depiction of target shapes can be conceived; by comparing downrange values of the descriptors of a fixed target, a 'tune' of downrange description can be obtained, and any abrupt change of the tune directly indicates target characteristics or singularities. However, all these descriptions are rather qualitative and some mental gymnastics may be necessitated to figure out target shapes. One alternative is to build up an enormous target shape and signature library, in which correspondence between signature and shape is to be matched. Yet the problems of uniqueness and exhaustive search may render this logistic approach practically futile. What is proposed and initiated here is an imaging algorithm by which Kennaugh [9] and Huynen's theories are applied and extended to reconstruct the specular shape of a target. As suggested by Chaudhuri [4] and Borden [3], the theories of differential geometry have already hinted a reconstruction scheme. The solution to this so-called Christoffel-Hurwitz problem requires input of intrinsic invariant geometrical parameters such as curvatures. Since curvatures do not depend on frequency, whereas Huynen's descriptors do, Huynen's descriptors cannot, in general, be applied to retrieve curvatures or any other invariant geometrical parameters. Recently, Chaudhuri, Foo and Boerner

[5,6] have investigated the frequency dependence of Huynen's descriptors in the high frequency regime, and they demonstrated that the high frequency Huynen's descriptors behave in such a way that its asymptotic values are directly related to specular electrical curvatures.

To have an overall view of the relation between the high frequency descriptors and specular geometry, the Kennaugh-Cosgriff's [10] physical optics approach, which links the backscattered impulse response and target geometry, is introduced in the next section. Since physical optics suffer from polarization-independence, Bennett's first order correction [1] to physical optics is adopted. Bennett et al. [1] simplified their space-time integral equation approach and found that first order correction is proportional to curvature difference. By taking the Fourier transform of the corrected impulse response, Foo, Chaudhuri and Boerner [6] obtained the high frequency dependence of the monostatic relative phase scattering matrix elements in terms of curvatures, polarization, frequency and an aspect-dependent geometrical function, as described in Section III. In Section IV, Huynen's algebraic approach [8] is followed to obtain the elements of the Mueller matrix in terms of the elements of the scattering matrix. Hence, the Huynen's descriptors, based on the Mueller matrix elements, can be related to the specular curvatures and target orientation, as shown in Section V. Numerical results are presented in Section VI. Some applications of Huynen's descriptors are discussed in Section VII. Conclusions and recommendations are in Section VIII.

II. *FIRST ORDER CORRECTION TO PHYSICAL OPTICS SCATTTERING*

For a perfectly conducting target, the far scattered field $\vec{H}_s$ can be expressed in terms of current induced on the target surface due to incidence field [1]

$$r\vec{H}_s(\vec{r},t) = \frac{1}{4\pi}\int\int \{ \frac{\partial}{\partial\tau}\vec{J}(\vec{r}',\tau) \times \hat{a}_r \, ds' \qquad (1)$$

where $\vec{J}$ denotes the induced surface current density, $\vec{r}$ and $\vec{r}'$ denote position vectors to the observation point and integration point, respectively, $\hat{a}_r$ denotes the unit vector of $\vec{r}$ and τ is the retarded time.

A space-time integral equation derived by Bennett [1] enables $\vec{J}$ to be written as a sum of physical optics currents $\vec{J}_{po}$ and contribution of retarded currents $\vec{J}_\varepsilon$, where

$$\vec{J}_{po} = 2\hat{a}_n \times \vec{H}_i \qquad (2)$$

and

$$\vec{J}\varepsilon = \{\hat{a}_u J_u - \hat{a}_v J_v\} \frac{K_u - K_v}{4} \varepsilon_0 \qquad (3)$$

$\hat{a}_n$ denotes the outward normal vector, $\hat{a}_u$ and $\hat{a}_v$ denote unit vectors along the principal directions with curvatures K_u and K_v, J_u and J_v are the components of $\vec{J}$ along $\hat{a}_u$ and $\hat{a}_v$, respectively. Equation (3) is a first order approximation derived [1] from integrating over a *small specular patch of radius* ε_0. *Discussion here is restricted to the illuminated side of a smooth, conducting, asymmetric convex target.* By assuming physical optics currents for J_u and J_v in Eq. (3) and then substituting Eqs. (2) and (3) into Eq. (1), the total impulse response *far scattered field* $\vec{H}_s$ *due to both* $\vec{J}_{po}$ and $\vec{J}_\varepsilon$ can be obtained [6,1]

$$r\,\vec{H}_s(\vec{r},t) = \frac{1}{2\pi}\frac{\partial^2}{\partial t^2} A(t)\,\hat{a}_{H_i} + \frac{K_u - K_v}{4\pi}\frac{\partial A(t)}{\partial t}\{(\hat{a}_{H_i} \bullet \hat{a}_u)\hat{a}_u - (\hat{a}_{H_i} \bullet \hat{a}_v)\hat{a}_v\} \qquad (4)$$

where $\hat{a}_{H_i}$ is the unit vector along the incident field $\vec{H}_i$ (Figure 1), and A(t) is the silhouette area of the target as delineated by the wavefront moving at half the speed of light.

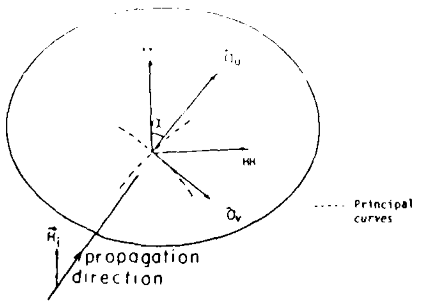

Figure 1: Specular Coorindate System

The first term in Eq. (4) gives the Kennaugh-Cosgriff formula [10], which is polarization-independent. The second term gives the first order polarization correction and takes the functional form of the first derivative of the area function A(t) and is proportional to the principal curvature difference $(K_u - K_v)$. The polarization correction to the Physical Optics approximation is essential, if the high frequency scattering matrix elements containing polarization information are to be related to target geometry.

III. SCATTERING MATRIX IN TERMS OF CURVATURE DIFFERENCE

Taking the Fourier transform of Eq. (4), expressions for the scattering matrix components can be obtained [6]

$$S_{11} = \frac{1}{2\pi}(jk)^2 A(k) - (jk)\,A(k)\,\frac{K_u - K_v}{4\pi}\cos 2\alpha \tag{5}$$

$$S_{11} = \frac{1}{2\pi}(jk)^2 A(k) + (jk)\,A(k)\,\frac{K_u - K_v}{4\pi}\cos 2\alpha \tag{6}$$

$$S_{21} = (jk)\,A(k)\,\frac{K_u - K_v}{4\pi}\sin 2\alpha = S_{12} \tag{7}$$

where A(k) is the Fourier transform of A(t), k is the wave number, and α is the polarization angle (Figure 1).

Note that from Eqs. (5-7), a phase-curvature relationship [6] can be arrived at:

$$\frac{K_u - K_v}{2} = -\frac{k}{\cos 2\alpha}\tan\frac{\Phi_{22} - \Phi_{11}}{2} \tag{8}$$

A special case of Eq. (8) in which $\alpha = 0$ or $\pi/2$ occurs when the incident linear polarization coincides with one of the principal directions at the specular point, implying that there is no depolarization of the energy in the backscattered direction.

The recovery of curvature difference in Eq. (8) is not practical since it requires accurate measurements of relative phase, yet the extension of Eq. (8) to the bistatic/dielectric case and the relative phase difference $(\Phi_{22} - \Phi_{11})$ have become important in remote sensing.

To apply Eqs. (5-7) to Huynen's descriptors, which are based on Mueller's matrix, the relation between the scattering matrix elements and the Mueller matrix elements must be investigated.

IV. THE SCATTERING MATRIX AND THE MUELLER MATRIX

The scattering matrix [S] can be defined by the incident $[E^i]$ and the scattered $[E^s]$ fields:

$$[E^s] = [S][E^i]$$

where

$$[S] = \begin{bmatrix} S_{VV} & S_{VH} \\ S_{HV} & S_{HH} \end{bmatrix} \tag{9}$$

The matrix [S] contains two co-polarized elements and two cross-polarized elements. In the monostatic backscattering case, $S_{VH} = S_{HV}$ by reciprocity of the propagation in an isotropic medium. The subscripts V and H denote a pair of orthogonal polarization bases (e.g. H ≙ horizontal, V ≙ vertical). Properties of the relative phase scattering matrix [S] were investigated in the pioneering studies of Kennaugh [11] used and further interpreted by Huynen [7], as summarized in Boerner [2].

The voltage induced at the receiving antenna is given by:

$$V^r = [S][E^i]\bullet[E^r] \tag{10}$$

in which $[E^r]$ is the polarization vector of the receiving antenna. The power received is given by:

$$P^r = [M]g[E^i]\bullet h[E^r] \tag{11}$$

in which $g[E^i]$ and $h[E^r]$ are the Stokes vectors of $[E^i]$ and $[E^r]$ respectively, and [M] denotes the 4x4 Mueller matrix. The elements of [M] and [S] are related through Huynen's algebraic approach [8], in which [S] is represented by algebraic variables $\underline{a}$, $\underline{b}$ and $\underline{c}$, as follows:

$$[S] = \begin{bmatrix} \underline{a}+\underline{b} & \underline{c} \\ \underline{c} & \underline{a}-\underline{b} \end{bmatrix} \tag{12}$$

In [8], [M] is given as:

$$[M] = \begin{bmatrix} A_o+B_o & F & C_\psi & H_\psi \\ F & -A_o+B_o & G_\psi & D_\psi \\ C_\psi & G_\psi & A_o+B_\psi & E_\psi \\ H_\psi & D_\psi & E_\psi & A_o-B_\psi \end{bmatrix}$$

where

$$A_o = \frac{1}{2}|\underline{a}|^2$$

$$B_o = \frac{1}{2}(|\underline{b}|^2 + |\underline{c}|^2)$$

$$B_\psi = \frac{1}{2}(|\underline{b}|^2 - |\underline{c}|^2) \tag{13}$$

$$C_\psi + jD_\psi = \underline{a}^*\underline{b}$$

$$E_\psi + jF = \underline{b}\ \underline{c}^*$$

$$H_\psi + jG_\psi = \underline{a}\ \underline{c}^*$$

*(with * denoting conjugation)*

and now using Eqs.(9), (12) and (13) for the purely coherent case, the Huynen descriptors are expressed in terms of the elements of [S] as follows [8]:

$$A_o = 1/8(|S_{VV}|^2 + |S_{HH}|^2 +2|S_{VV}||S_{HH}|\cos\phi_B) \tag{14a}$$

$$B_o = 1/8(|S_{VV}|^2 + |S_{HH}|^2 -2|S_{VV}||S_{HH}|\cos\phi_B) + \tfrac{1}{2}|S_{HV}|^2 \tag{14b}$$

$$B_\psi = 1/8(|S_{VV}|2 + |S_{HH}|^2 -2|S_{VV}||S_{HH}|\cos\phi_B) - \tfrac{1}{2}|S_{HV}|^2 \tag{14c}$$

$$C_\psi = 1/4(|S_{VV}|^2 - |S_{HH}|^2) \tag{14d}$$

$$D_\psi = 1/2(|S_{VV}||S_{HH}|\sin\phi_B) \tag{14e}$$

$$E_\psi + jF = 1/2(|S_{VV}|-|S_{HH}|e^{-j\phi_B})|S_{HV}|e^{j\phi_A} \tag{14f}$$

$$H_\psi + jG_\psi = 1/2(|S_{VV}| + |S_{HH}|e^{-j\phi_B})|S_{HV}|e^{j\phi_A} \tag{14g}$$

where $\phi_A=\phi_{VV}-\phi_{VH}$ and $\phi_B=\phi_{VV}-\phi_{HH}$, the ϕ's being the corresponding relative phases of the elements of [S].

In Huynen [7], the sum A_o+B_o is considered as a rough measure of half the total power in the wave returned from the target. A_o is associated with regular, smooth, spherical types of surface scattering, which contributes to specular returns such as from a sphere. B_o may be considered as a measure of all the target's non-symmetric, irregular, rough-edged, non-spherical depolarizing components of scattering. C_ψ is related to oblongity and F to helicity.

If the specular region is smooth and convex, and if the incident field is along one of the principal directions, then the cross-component $|S_{HV}| = 0$ [6], and

$$\begin{aligned} B_o &= B_\psi \\ E_\psi = F = G_\psi &= H_\psi = 0 \end{aligned} \tag{15}$$

In particular, in the simple case of a sphere, B_o and B_ψ vanish because of symmetry. In contrast, for an ellipsoid-like target, a non-zero value for B_o is expected. Thus B_o may serve to discriminate between spherical and ellipsoidal targets.

V. INTERPRETATION OF HUYNEN'S DESCRIPTORS IN TERMS OF SPECULAR CURVATURES

By substituting Eqs. (5-7) in Eq. (14), the Mueller matrix descriptors can be written as [5]:

$$A_o = \frac{1}{8}\frac{k^4}{\pi^2}|A(k)|^2 \tag{16}$$

$$B_0 = \frac{1}{8}\frac{k^4}{\pi^2}|A(k)|^2\left(\frac{K_u-K_v}{2k}\right)^2 \qquad (17)$$

$$B_\psi = \frac{1}{8}\frac{k^4}{\pi^2}|A(k)|^2\left(\frac{K_u-K_v}{2k}\right)^2 \cos 4\alpha \qquad (18)$$

$$D_\psi = \frac{-k^4}{4\pi^2}|A(k)|^2\left(\frac{K_u-K_v}{2k}\right)\cos 2\alpha \qquad (19)$$

$$E_\psi = \frac{-k^4}{8\pi^2}|A(k)|^2\left(\frac{K_u-K_v}{2k}\right)^2\sin 4\alpha \qquad (20)$$

$$G_\psi = \frac{k^4}{4\pi^2}|A(k)|^2\left(\frac{K_u-K_v}{2k}\right)\sin 2\alpha \qquad (21)$$

$$C_\psi,\ F,\ H_\psi \rightarrow 0 \text{ with increasing frequency} \qquad (22)$$

It is now obvious here that B_0 is a measure of non-spherical symmetry, and hence serves to differentiate between spherical and non-spherical target shapes. The orientation invariance of B_0 as shown by Eq. (17) enhances its practicality.

The high frequency assumption (equivalent to the specular region contributions only) is already implied in this interpretation of the Huynen descriptors, as Eqs. (5-7) are derived on the assumptions of leading edge (high frequency) conditions.

It can be observed that Eqs. (14a to 14g) do not explicitly show the frequency dependence of the descriptors, whereas Eqs. (16-21) do. Morever, in [4] it has been shown that A(k) takes the functional form of $\frac{1}{k^2}$ in the case of ellipsoids for large values of k. Consequently, all the descriptors except A_0 eventually tend to zero with increasing frequency. This is not surprising as the target then virtually looks like a flat plate, (specular "patch"), and there is no polarization dependence in the optical region. It is conjectured that these arguments can be extended to any target with smooth, convex specular sections.

The target orientation explicitly appears in the form of the polarization angle α. A_0 and B_0, which are related to total power, are orientation invariant. Other orientation invariances, namely, $B_\psi^2 + E_\psi^2$ and $D_\psi^2 + G_\psi^2$, are also separately satisfied as required in [7]. It is important to note that target orientation with respect to polarization basis directions can be recovered practically and accurately by taking the ratios B_ψ/B_0 and E_ψ/B_0

$$\cos 4\alpha = B_\psi/B_0\ , \text{ or} \qquad (23)$$

$$\sin 4\alpha = E_\psi/B_0 \qquad (24)$$

A smooth convex scatterer can be roughly modeled as a combination of two scattering centers, one at the specular region, which gives rise to the specular return, and the other being the creeping waves which circumnavigate and return energy characteristic of their paths. At low resonance frequencies, the contributions of both the specular return and the creeping wave return are comparable and interfere with each other. This interference masks correlation between fine geometry and Huynen's descriptors. The correlation between the specular geometry or orientation and the Huynen's descriptors at very high frequencies is expected to be good. This is because at high frequencies, it is known that the creeping waves decay and the specular return dominates the backscattered signal. In order to extract the specular geometry information, it is thus suggested that the specular contribution and the creeping wave contribution in the total backscattered signal be separated. A method for such separation will be discussed next, and will be applied to the bandlimited measured data. Based on the separated specular data, which are approximately equivalent to high frequency data, Huynen's descriptors will be computed, and the results will be compared with the theoretical predictions of Eqs. (16-22).

VI. SEPARATION OF THE SPECULAR RETURN AND NUMERICAL RESULTS [5]

The purpose is to decompose the measured scattering matrix, which is in the frequency domain, by time-gating, into the specular component and the creeping wave components. For the simple canonical shapes of the sphere and the ellipsoid, complete scattering matrix data are available from the Electro-Science Laboratories at the Ohio State University (ESL-OSU) [13]. In general, the data consist of amplitudes and phases, from 1 to 12 GHz, in steps of 10 MHz, with different aspect angles.

The range of the spectrum of a "first derivative Gaussian" pulse (functional dependence: gte^{-gt^2}) is made to coincide with that of the measured data, by adjusting the narrow pulse width. By multiplying the pulse spectrum with the measured complex spectrum and inverse Fourier transforming the product, the specular return and the creeping wave return are distinctly separated in the time domain, provided that the first derivative Gaussian (FDG) pulse is sufficiently narrow relative to the target size. Either returns can thus be time-gated, Fourier-transformed, and finally divided by the spectrum of the FDG pulse to form new elements of the separated [S]. Obviously for very broadband measurements, the FDG pulse is very narrow relative to the target size, and hence the creeping wave has a large delay with respect to the specular return, so that the time-gating process becomes trivial. In practice, measurements can be bandlimited, and the target can be small, and partial overlapping may occur for the creeping wave and specular returns in the time domain. Yet by locating the transition point in the overlapping region through the approximate knowledge of the "space width" of the interrogating pulse (~ pulse width × free space propagation velocity) and the creeping wave path length, reasonably good results have been obtained by this technique. Figure 2 corresponds to the former case (very broadband data), in which ka ranges from 0.8 to 9.6 (1 to 12 GHz), where a is the smallest semi-axis of the ellipsoidal target; the semi-axes are 6": 3": 1.5". Nose-on aspect and vertical polarization data were taken in this case.

The separated co-polarized specular contribution is depicted in Figure 3. Due to the nature of the deconvolution involved in the signal processing, the end portions are not accurate. However, other than the end frequencies, the whole range shows that the amplitudes are steady in general. The reason is that with the creeping wave removed, the target behaves as if it were the specular portion, which resembles a small flat plate. Therefore, there is less frequency dependence at low frequencies than if the data were not processed. Thus the separation technique enables equivalent high frequency information to be approximated from low frequency bandlimited measurements.

The other component of [S], due to creeping wave contributions only, is shown in Figure 4. Once again, the end portions are not accurate, but the whole range, in general, is in accordance with the fact that the creeping waves decay as the frequency increases. Figure 5 shows that the two components add up to the original measured scattering matrix [S] for the case of horizontal polarization. At high frequencies, the measured [S] approaches the specular [S]. Obviously, if the Huynen descriptors are computed with measured [S] at low frequencies, the fluctuations in contrast to the steady, flat-plate behavior at high frequencies will not lead to an observable correlation with the target specular geometry.

VII. APPLICATION OF SPECULAR [S] [5]

(i) Comparison between the experimentally processed and theoretically calculated target-descriptors

The target-descriptor Mueller matrix elements, normalized with respect to A_0, are computed from the specular [S] using the expressions given in Eq. (14). For instance, B_0/A_0 values are compared with the corresponding theoretical values calculated using Eqs. (16) to (22) and are shown in Fig. 6(i). The scattering geometry used for these data involves broadside plane wave incidence on a conducting ellipsoid of semi-axes 6":3":1.5", with the polarization angle $\alpha=30°$. The agreement between the theoretical and experimental results in Fig. 6(i) is good and acceptable. It is emphasized here that the theoretical values are derived from high frequency assumptions, thus as the frequency increases the difference between the theoretical and experimental results decreases.

(ii) A_0 as a measure of specular size

Since A_0 is approximately related to the vector, i.e., involving two orthogonal polarizations, specular return, larger values of A_0 are associated with larger sizes of the specular region. This is verified by comparing A_0 of a sphere of diameter 1.5" and A_0 of an ellipsoid of the semi-axes $\frac{1.5"}{2}$: $\frac{1.5"}{4}$: $\frac{1.5"}{8}$ for nose-on incidence (Figure 7).

(iii) B_0/A_0 as a measure of electric specular curvature difference

From Eqs. (16 and 17),

$$\frac{B_0}{A_0} = \left(\frac{K_u - K_v}{2k}\right)^2 \tag{25}$$

The normalization of B_0 with respect to A_0 is introduced to remove the factor A(k). At any rate, B_0 or B_0/A_0 should be zero for a sphere, and should deviate from zero for ellipsoidal targets. In Figure 6(ii), the values of B_0/A_0 are plotted for the ellipsoid of 6": 3": 1.5", with nose-on incidence.

The specular curvature difference $K_u - K_v$, in this case, is 78.74 per meter as computed from Minkowski's support functions [4]. In Fig. 6(ii), the theoretical values predicted by Eq. (25) is also compared with the measured values, showing good agreement at high frequencies. At low frequencies, Eq. (25), based on the high frequency leading edge assumption, does not hold, and thus causes discrepancies. Again, at the high frequency end, the deconvolution process introduces inaccuracy of B_0/A_0 computed from the specular [S].

The B_0/A_0 curve for the case of broadside incidence (α = 30°) on the above ellipsoid has been given in Fig. 6(i). There the agreement between the theoretical predictions and the processed measurement data is excellent. This clearly indicates that the correction term added to the physical optics in Eq. (4) holds more accurately for smaller curvature difference at the specular point (for Fig. 6(i), $K_u - K_v$ = 49.21 per meter).

(iv) Orientation recovery from B_ψ/B_o or E_ψ/B_o

In some of the measurement data described so far, the incident field is along one of the principal directions of the ellipsoid. Under such circumstances the cross-polarized element of [S] is zero provided the target is sufficiently smooth so that finite principal curves exist at the specular point. On the other hand, if the incident field is not along one of the principal directions, then the cross-polarized elements are non-zero, and the orientation can be recovered using Eq. (23) or Eq. (24). In Fig. 8, both values of computed from Eqs. (23) and (24) are shown separately, and match the value of the polarization angle set up in the ESL-OSU measurement arrangement. The conditions in which measurements were made are the same as those of Fig. 6(i).

VIII. CONCLUSIONS

The target descriptors are related to specular geometrical information such as specular size, curvature difference and orientation. Although the discussion in this paper is restricted to smooth, convex objects, the proposed time-gating technique can be applied to a certain class of objects with one or more specular regions which may include edges, or wedges, etc. Each specular region serves as a scattering center to interfere with others, but the response of each center, time-gated out of the total time-domain return, should provide Mueller matrix target descriptors characteristic of its geometry. Thus objects of complex shapes may be studied through modeling and decomposition into simpler scattering centers; and separately for each scattering center, the target characteristic polarimetric operators must be analyzed for the object classification and identification algorithms.

The creeping wave component, which can be isolated by the separation technique described, should deserve more investigation in the future as it certainly contains information about the geometry within the shadow region. This multifrequency inverse scattering approach requires a broadband measurement. Not only broadband measurements are required, but also the phases in the scattering matrix must be coherent and as accurate as possible to enable curvature differences to be determined correctly. In contrast, the orientation angle has been quite accurately determined with the existing ESL-OSU data. By knowing the curvature difference sufficiently accurately, the target profile can be reconstructed through the application of differential geometry [3].

IX. REFERENCES

[1] C.L. Bennett, et al., Space Time Integral Equation Approach to the Large Body Scattering Problems, Sperry Research Center, Sudbury, MA., May 1973, Final Report on Contract #F30602-71-C-0162, AD763794.

[2] W-M. Boerner, et al., Editors, Proceedings of NATO Advanced Research Workshop on Inverse Methods in Electromagnetic Imaging, Vols. 1 & 2, NATO ASI Series C: *Mathematical & Physical Sciences*, Vol. 143, published by D. Reidel Publ. Co., Dordrecht, Holland, 1985 (see pp. 1-32, 33-42 and 609-628).

[3] B. Borden, Application of the Christoffel-Hurwitz Inversion Identity to Electromagnetic Imaging, Proceedings of NATO Advanced Research Workshop on Inverse Methods in Electromagnetic Imaging (eds. W-M. Boerner et al.), Vols. 1 & 2, NATO ASI Series C: Mathematical & Physical Sciences, Vol. 143, published by D. Reidel Publ. Co., Dordrecht, Holland, 1985, pp. 251-259. (Also see IEEE Trans. on Ant. & Prop., Vol. AP-32, June 1984, pp. 651-654.)

[4] S.K. Chaudhuri, Utilization of Polarization-Depolarization Characteristics in Electromagnetic Inverse Scattering, Ph.D. thesis, University of Manitoba, Canada, 1977.

[5] S.K. Chaudhuri, B-Y. Foo, W-M. Boerner, A Validation Analysis of Huynen's Target-Descriptor Interpretations of the Mueller Matrix Elements in Polarimetric Radar Returns Using Kennaugh's Physical Optics Impulse Formulation, to appear in IEEE Trans. on Ant. & Prop., 1985.

[6] B-Y. Foo, S.K. Chaudhuri and W-M. Boerner, A High Frequency Inverse Scattering Model to Recover the Specular Point Curvature from Polarimetric Scattering Matrix Data", IEEE Trans. on Ant. & Prop., Vol. AP-32, No. 11, November 1984, pp. 1174-1178.

[7] J.R. Huynen, Phenomenological Theory of Radar Targets, Ph.D. Disseration, Technical University, Delft, The Netherlands, 1970.

[8] J.R. Huynen, *Polarization Discrimination with Applications to Target* Classification and Identification, Final Report, Boeing Aerospace Corporation, Kent Space Research Center, Contract No. CH 6891, 1983.

[9] E.M. *Kennaugh, D.L. Moffatt, Transient Current Density Waveforms on a Perfectly* Conducting Sphere, Proceedings of NATO Advanced Research Workshop on Inverse Methods in Electromagnetic Imaging (eds. W-M. Boerner et al.), Vols. 1 & 2, NATO ASI Series C: Mathematical & Physical Sciences, Vol. 143, published by D. Reidel Publ. Co., Dordrecht, Holland, 1985, pp. 1-31.

[10] E.M. Kennaugh and R.L. Cosgriff, The Use of Impulse Response in Electromagnetic Scattering Problems, IRE National Convention Record, Part I, 1958.

[11] E.M. Kennaugh, Research *Studies on the Polarization Properties of Radar Targets*, ElectroScience Laboratory, Department of Electrical Engineering, The Ohio State University, Commemorative Volumes I and II (condensed collection of selected research reports from original 4 volume works of Kennaugh). July 1984.

[12] A.C. Manson and W-M. Boerner, Interpretation of High Resolution Polarimetric Radar Target Downrange Signatures Using Kennaugh's and Huynen's Target Characteristic Operator Theories, Proceedings of NATO Advanced Research Workshop on Inverse Methods in Electromagnetic Imaging (eds. W-M. Boerner et al.), Vols. 1 & 2, NATO ASI Series C: Mathematical & Physical Sciences, Vol. 143, published by D. Reidel Publ. Co., Dordrecht, Holland, 1985, pp. 695.720.

[13] E.K. Walton and J.D. Young, The Ohio State University Compact Range Cross-Section Measurement Range, IEEE Trans. on Ant. & Prop., November 1984.

X. ACKNOWLEDGMENTS

The research reported in this study would not have been possible without the pioneering contributions of the late Professor Edward M. Kennaugh, Professor Emeritus, The Ohio State University, and of Dr. J. Richard Huynen, whose many constructive comments are gratefully acknowledged. This research was supported parts by the Office of Naval Research under Contract Nos. US ONR N00014-80-C-0773 and US ONR N00014-80-C-00708; Naval Air Systems Command under Contract No. US ONR N00019-81-C-0352; Naval Air Development Center under contract No. N62269-83-C-0317; the Army Research Office under contract No. US ARMY DAAG 29-80-K0027; and under the NATO-IMOR Contract No. SA.5.2.03B(189)84.

The interest shown by our contract sponsors, Dr. Richard G. Brandt, ONR, Pasadena Branch; Dr. Günter Winkler, NWC, China Lake, CA.; and by Dr. James W. Mink, ARO, Research Triangle Park, N.C., is recalled with pleasure. Thanks to their support we were able to obtain, with the collaboration of Dr. Jonathan Young and Prof. David L. Moffatt, the superb measurement data collected on the OSU-ESL, Columbus, OH. near-field/far-field measurement range under the capable supervision of Dr. Eric Walton, whose many comments contributed to our data interpretation.

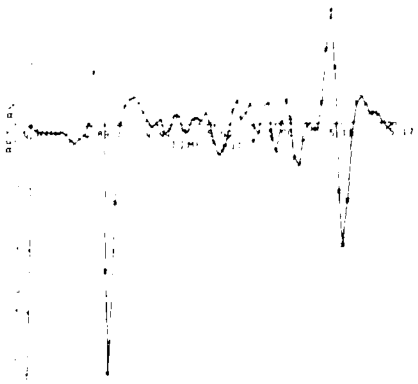

Figure 2: Return due to relatively narrow [illegible] pulse

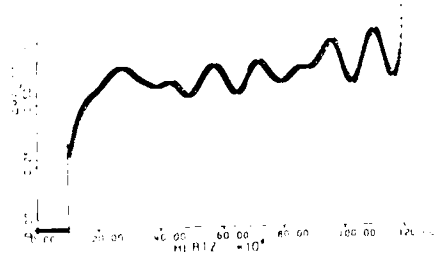

Figure 3: Specular $|S_{VV}|$ obtained from Figure 2

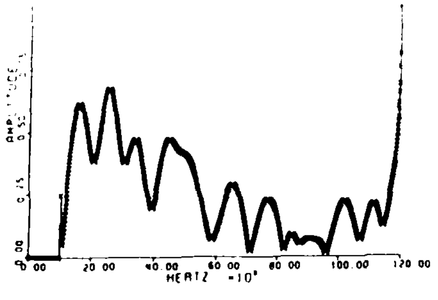

Figure 4: Creeping wave component of $|S_{VV}|$ obtained from Figure 2

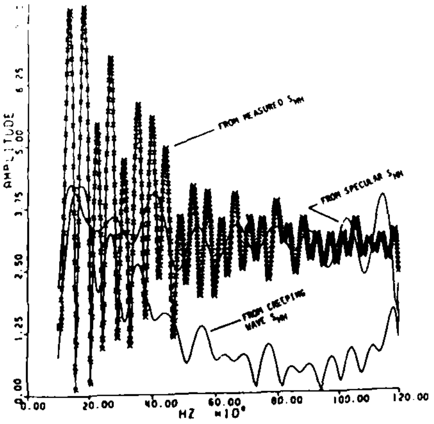

Figure 5: Decomposition of S_{HH} into specular S_{HH} and creeping wave component (nose-on incidence)

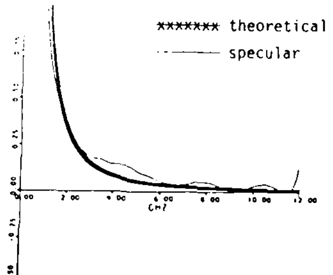

Figure 6(i): B_o/A_o (broadside incidence)

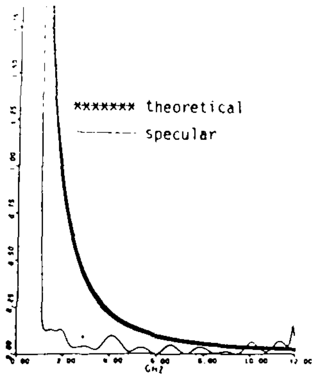

Figure 6(ii): B_o/A_o (nose-on incidence)

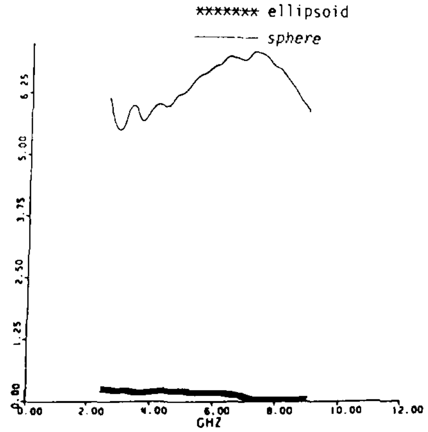

Figure 7: Comparision of A_o

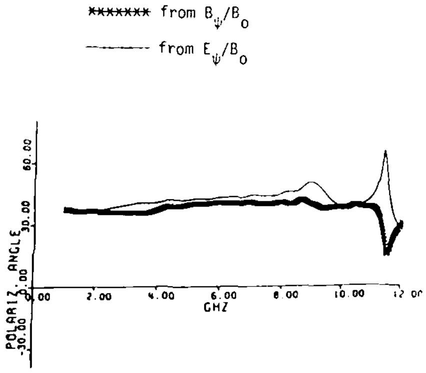

Figure 8: Determination of orientation angle from measured data

DISCUSSION

Y.Brault

In your paper you mention the influence of R.F. frequency upon the disclosing of the geometrical structure of the target. You even talked about the resonant frequency for a specific target.

(1) Can you comment on the R.F. frequencies which will be best matched to the size of a specific target to achieve the best recognition?

(2) Do you feel that a frequency scanning will be required when multiple targets of different size will be encountered?

Author's Reply

Please, refer to paper by Mr L.A.Cram, NATO-ARW-IMEI-1983/Proceedings and also to papers by Dag T.Gjessing, Torleif Orhang and André J.Poelman, "Target imaging".

(1) Radar targets of finite closed, but arbitrarily complicated structure (e.g. helicopter) all possess eigen resonances which are *independent* of aspect and polarization (SEM/TEF-methods). See Gjessing's books/papers.

(2) Yes, absolutely! Best ranges for current aircraft sizes 8 to 18 GHz/20—24 GHz/38—46 GHz/60—63 GHz/92—98 GHz. In each "spectral window" are different target problems, target size/shape exhaust plume properties, detection of detailed substructures. See papers by Lend/Gjessing.

(3) Important for target in clutter detection "unproved and more logical clutter description".

MULTI-(BI)-STATIC HIGH FREQUENCY (PO/GO) RADAR TARGET IMAGING OF AIRBORNE SCATTERERS

by
Sujeet K. Chaudhuri
Department of Electrical Engineering
University of Waterloo
Waterloo, Ontario N2L 3G1 Canada

and

Wolfgang-M. Boerner
Communications Laboratory
Department of Electrical Engineering & Computer Science
University of Illinois at Chicago, P.O. Box 4348 (m/c 154)
Chicago, IL 60680 U.S.A.

SUMMARY

Electromagnetic scattering at distances remote from a complex-shaped object, at high frequencies (Physical Optics/Geometric Optics), is dominated by certain specular components which are highly bistatic aspect and multifrequency dependent. The locations of these specular points on the complex object are known as the scattering centers. Generation of these scattering centers is dependent on the local geometry and local material in-depth decomposition of the object with respect to the aspect directions of the transmitter and receiver locations (monostatic as well as bistatic cases). The knowledge of the locations and the local geometries plus underlying material decomposition of these scattering centers can be useful in developing air-target discrimination/identification algorithms. Based upon this existing available basic multistatic scattering formulation, which is highly polarization-dependent, a basic vector inverse scattering model can be developed to recover these scattering centers from poly-(bi)-static polarimetric (bistatic scattering matrix) signatures which then may be used to formulate target classification, imaging and identification algorithms.

The approach adopted in this investigation is based on the solution (direct problem: analysis) to the general poly-(bi)-static high frequency isolated scattering center recovery problem. Once this direct model solution (analysis) is established and verified with the analytically model-generated and measured model test data, it is used as a building block toward the following more complicated inverse problems (synthesis) for the following realistic situations:

Analysis: A.1 (Direct Problem)	Multiple distributed scattering centers: no interaction between the centers using multi-(bi)-static and monostatic scattering matrix input data.
Analysis: A.2	Multiple distributed scattering centers: one or more interactions between the scattering centers (bi/di-hedrals, cones, flat plates, dipoles, left/right helices, semi-spherical/cone nose and afts, wings and fins, etc. of an air target); poly-(bi)-static and monostatic input data.
Synthesis: B.1 (Inverse Problem)	Scattering center recovery with aspect/frequency restricted measurements for more economic/realistic implementation (limited bi/mono-static aspect angles, narrow bandwidth, CW multi-(bi)-static angle data, etc.) for the development of classification/imaging/identification algorithms.
Synthesis: B.2	Shape/surface material decomposition pattern recognition algorithms based on the knowledge of the recovered distribution of 3-dimensional distributed scattering centers on a complex shaped target.

1 INTRODUCTION

Electromagnetic scattering from a complex object, at high frequencies (physical optics, geometric optics), is dominated by certain specular components. The locations of these specular points on the complex object are known as the scattering centers. Generation of these scattering centers is dependent on the geometry of the object with respect to the aspect directions of the transmitter and the receiver (general bistatic case). The knowledge of the locations and the local geometries of these scattering centers can be useful in developing discrimination/identification algorithms. Therefore, a basic inverse scattering model to recover these scattering centers from polystatic polarimetric signatures of the target is investigated here.

This work deals with the development of a solution to the general polystatic high-frequency isolated scattering center recovery problem. Once this model solution is established it can be used as a building block towards the following more complicated and more realistic situations.

2 PARAMETERS OF A SCATTERING CENTER

For the electromagnetic scattering analysis, the isolated scattering center is modeled as a conducting rectangular flat plate. This tangent plane approximation to the specular region has been used successfully in sea surface scattering models (Barrick and Peake, 1968; Kwoh and Lake, 1983).

The geometry of a scattering center with respect to a given coordinate system is shown in Fig. 1. In this figure $\hat{n}$ denotes the unit normal to the scattering center. The vector location of the scattering center with respect to the fixed reference coordinate system is given by $\underline{d}$. The vector sides $\underline{s}_1(=s_1\hat{a}_{s_1})$ and $\underline{s}_2(=s_2\hat{a}_{s_2})$ determine the local geometry of the scattering center, and they point in the directions of the principal curves of the scattering target at that specular point. The magnitudes of $\underline{s}_1$ and $\underline{s}_2$ are indicative of the radii of the curvature of these principal curves. Determination of $\hat{n}$, $\underline{s}_1$, $\underline{s}_2$, $\underline{d}$ from the multistatic polarimetric scattering matrix (with plane wave incidence) data in the context of the present work is known as the "scattering center recovery" problem.

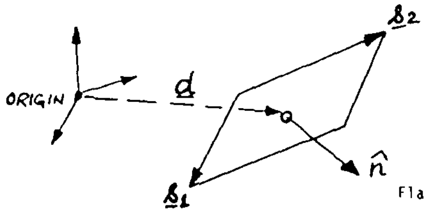

Flate Plate Model of the Scattering Center

Fig. 1: Scattering Center Geometry

3 COORDINATE SYSTEM FOR BISTATIC POLARIMETRIC SCATTERING DATA

There is a certain ambiguity associated with the measurement of the scattering matrix by a bistatic radar system. In the monostatic case, the transmit-receive antenna polarizations are defined in the same system of coordinates. The bistatic configuration implies physical separation of the transmit and receive antennas, therefore, requiring two separate coordinate systems to define the antenna polarizations. In such a case, the idea of common transmit-receive antenna polarization has no physical meaning, and must, therefore, be given an artificial definition, based on the scattering matrix [S]. By choosing a fixed global spehrical coordinate scheme, the transmitter and the receiver polarization basis vectors can be defined consistently. At each location the orthogonal polarization basis is given by the spherical unit vectors $\hat{a}_\theta$, and $\hat{a}_\phi$, at that point. Thus the transmitter polarization is

$$\underline{h}_i = h_{\theta_i} \hat{a}_{\theta_i} + h_{\phi_i} \hat{a}_{\phi_i},$$

and the receiver polarization is

$$\underline{h}_r = h_{\theta_r} \hat{a}_{\theta_r} + h_{\phi_r} \hat{a}_{\phi_r}.$$

Now the bistatic scattering matrix [S], is defined as:

$$[\underline{h}_r] = [S][\underline{h}_i] \Rightarrow \begin{bmatrix} h_{\theta_r} \\ h_{\phi_r} \end{bmatrix} = \begin{bmatrix} S_{\theta\theta} & S_{\theta\phi} \\ S_{\phi\theta} & S_{\phi\phi} \end{bmatrix} \begin{bmatrix} h_{\theta_i} \\ h_{\phi_i} \end{bmatrix}$$

The elements of the bistatic scattering matrix (BSM) above are complex and, in general, the matrix is not symmetric, i.e., $S_{\phi\theta} \neq S_{\theta\phi}$ (Davidovitz and Boerner, 1983; Davidovitz, 1983). Thus a total of eight parameters are required to give the complete bistatic scattering matrix (seven, if only the relative phases are of interest).

Two other conventional choices of the coordinate systems for BSM measurements have been used by Peake and Oliver (1971) and Heath (1983), respectively. The system used by Peake and Oliver is shown in Fig. 2. There, the two orthogonal polarization states are specified by (i) the horizontal components $\underline{p}_i^h$, $\underline{p}_s^h$ in x-y plane perpendicular to $\underline{k}_i$ and $\underline{k}_s$, respectively; and (ii) the vertical components $\underline{p}_i^v = \underline{p}_i^h \times \underline{k}_i$ and $\underline{p}_s^v = \underline{p}_s^h \times \underline{k}_s$. From this description it is clear that ($\underline{p}_i^h$, $\underline{p}_i^v$; $\underline{p}_s^h$, $\underline{p}_s^v$) are the same vectors as ($\hat{a}_{\phi_i}$, $\hat{a}_{\theta_i}$; $\hat{a}_{\phi_r}$, $\hat{a}_{\theta_r}$) introduced in the previous paragraph. Therefore, the coordinate system proposed here is essentially the same as the one used by Peake and Oliver (1971).

The coordinate system used by Heath (1983) defines the vertical polarizations as the direction normal to the plane formed by $\underline{k}_i$ and $\underline{k}_s$, i.e., $\underline{p}_i^v$ and $\underline{p}_s^v$ are same directions, and the horizontal polarization is in the plane of $\underline{k}_i$, $\underline{k}_s$ and normal to $\underline{p}_i^v$ and $\underline{k}_i$, $\underline{p}_s^v$ and $\underline{k}_s$, respectively. This system is useful only for the bistatic cases; for polystatic cases, since the planes defined by $\underline{k}_i$ and $\underline{k}_s$ corresponding to different receiver directions will generally be different, one cannot define a consistent polarization basis for the whole problem. Thus, for the present application, this coordinate system is <u>not</u> recommended.

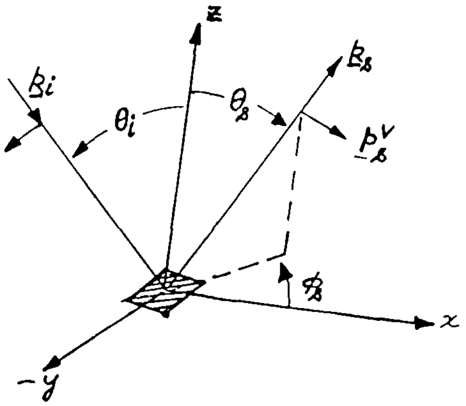

Fig. 2: Bistatic Scattering Matrix Coordinate System

4 DERIVATION OF THE BISTATIC SCATTERING MATRIX (BSM)

To obtain the BSM of the geometry in Fig. 1, first the physical optics approximation is used to obtain the induced current on the flat plate. This is done for a given direction of incidence with the transmitter polarization in a_{θ_i} (or a_{ϕ_i}) direction. Next, these induced surface currents are used in the scattered far-field integral to obtain the vector scattered field at the receiver location. Finally, this vector scattered field is decomposed to construct the elements of the BSM. These analytical expressions are in terms of the scattering center geometry parameters n, $\underline{s}_1$, s_2, and $\underline{d}$. Therefore, these relations can be useful in inverse scattering applications.

From electromagnetic theory, the induced surface current, $\underline{J}_i$, on the conducting flat plate model of the scattering center is given by

$$\underline{J}_s = 2\hat{n}\times\underline{H}_i - \left(\hat{n} \times \int_{s'} \underline{J}'_s \times \nabla G ds'\right) \tag{1}$$

where $\underline{H}_i$ is the incident magnetic field, S' is the surface of the scatterer except the observation point, $\underline{r}$ and $\underline{r}'$ are the position vectors to the observation point and the integration points, respectively, G is the appropriate Green's function, and $\underline{J}'_s$ represents the surface current at the integration patch ds'. The first term on the right hand side of Eq. (1) is the physical optics term and the second term represents the interaction between the currents at the various points of the scatterer. In the physical optics (high frequency) formulation, the interaction term is assumed to be small, and only the first term is retained for obtaining $\underline{J}_s$.

The contribution to the radiation fields from the electric surface current, $\underline{J}_s$, is found by evaluating the magnetic vector potential

$$\underline{A} = \frac{e^{-jkr}}{4\pi r} \int\int_s \underline{J}_s (\underline{r}')e^{jk\hat{r}\cdot\underline{r}'} ds', \tag{2}$$

where, as shown in Fig. 3, S denotes the surface of the scatterer, and k = $2\pi/\lambda$, λ-wavelength of the operating frequency; this means $\underline{k}_i=k\hat{k}_i$, and $\underline{k}_s=k\hat{k}_s$. The far-zone scattered electric field is found from the components of

$$\underline{E}_s = -j\omega\mu\underline{A}. \tag{3}$$

For a general formulation of the scattering problem one should also consider the electric vector potential $\underline{F}$, which is associated with the magnetic current density. In the present case, however, F=0, since the magnetic current density on a perfect electric conductor is zero (tangential electric field boundary condition).

Using physical optics formulation ($\underline{J}_s=2\hat{n}\times\underline{H}_i$) one can now write

$$\underline{A} = \frac{e^{-jkr}}{2\pi r}\hat{n} \times \int_s \underline{H}_i e^{jk\hat{r}\cdot\underline{r}'} ds' = \frac{e^{-jkr}}{2\pi r}\hat{n} \times \underline{Q} \qquad (4)$$

where, $\underline{Q} = \int_s \underline{H}_i e^{jk\hat{r}\cdot\underline{r}'} ds'$ (5)

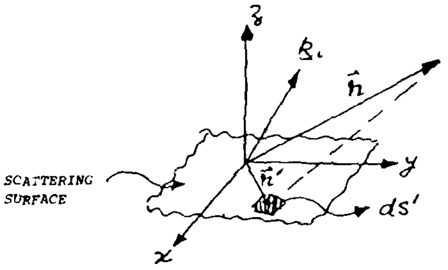

Fig. 3: Geometry for Calculating Vector Potential

If the components of $\underline{Q}$ in $\hat{a}_{s1}$ and $\hat{a}_{s2}$ directions are written as Q_{s1} and Q_{s2}, respectively, then using Eqs. (3) and (4), the far scattered field is written as

$$\underline{E}_s = jk\eta \frac{e^{-jkr}}{2\pi r} [Q_{s2}\hat{a}_{s1} - Q_{s1}\hat{a}_{s2}], \qquad (6)$$

where η is the characteristic impedance of the propagation medium. In deriving Eq. (6) use has been made of the fact that $\hat{a}_{s1}$, $\hat{a}_{s2}$, $\hat{n}$ form an orthogonal unit vector basis (unitary matrix).

ELEMENTS OF THE BSM

In the global fixed spherical coordinate system of this work, a general polarization of the electric field associated with an incident plane wave is represented by

$$\underline{E}_i = \eta(E_{\theta_i}\hat{a}_{\theta_i} + E_{\phi_i}\hat{a}_{\phi_i}) \qquad (7)$$

In order to calculate the elements of the BSM one considers two special cases of Eq. (7). In one case, $E_{\theta_i} = 0$, which yields the $S_{\phi\theta}$ and $S_{\phi\phi}$ elements of the BSM. To obtain the remaining two elements ($S_{\theta\phi}$ and $S_{\theta\theta}$) of the BSM, one considers $E_{\phi_i} = 0$. The detailed calculations are as follows:

(a) $$E_{\theta_i} = 0,\ E_{\phi_i} = \eta \Rightarrow \underline{E}_{\phi_i} = \eta\hat{a}_{\phi_i} [e^{-jk|\underline{r}_i-\underline{d}|+jk\hat{k}_i\cdot\underline{r}'}]$$

Using the plane wave equations, the corresponding magnetic field is given by

$$\underline{H}_\theta = \hat{a}_\theta [e^{-jk|\underline{r}_i-\underline{d}|+jk\hat{k}_i\cdot\underline{r}'}] \qquad (8)$$

With Eq. (8) describing the incident magnetic field on the scattering geometry of Fig. 1, the integral in Eq. (5) is used to obtain the corresponding components of the $\underline{Q}$ vector in the directions $\hat{a}_{s1}$ and $\hat{a}_{s2}$. These are

$$Q^\phi_{s1} = H^\theta_{s1} s_1 s_2 \operatorname{sinc}\left[\left(\frac{\underline{k}_s+\underline{k}_i}{2}\right)\cdot\underline{s}_1\right] \operatorname{sinc}\left[\left(\frac{\underline{k}_s+\underline{k}_i}{2}\right)\cdot\underline{s}_2\right], \qquad (9a)$$

$$Q^\phi_{s2} = H^\theta_{s2} s_1 s_2 \operatorname{sinc}\left[\left(\frac{\underline{k}_s+\underline{k}_i}{2}\right)\cdot\underline{s}_1\right] \operatorname{sinc}\left[\left(\frac{\underline{k}_s+\underline{k}_i}{2}\right)\cdot\underline{s}_2\right], \qquad (9b)$$

where $H^\theta_{s1} = \underline{H}_{\theta_i} \cdot \hat{a}_{s1}$, and $H^\theta_{s2} = \underline{H}_{\theta_i} \cdot \hat{a}_{s2}$.

Now, by using Eqs. (6) and (9) one obtains the normalized (w.r.t. $jk\eta e^{-jkr}/2\pi r$) co- and cross-polarized signals at the bistatic receiver site as follows:

$$E^s_{\phi\theta} = S_{\phi\theta} = \underline{E}_{s\phi}\cdot\hat{a}_{\theta_r} = Q^\phi_{s2}(\hat{a}_{s_1}\cdot\hat{a}_{\theta_r}) - Q^\phi_{s1}(\hat{a}_{s2}\cdot\hat{a}_{\theta_r}) \qquad (10a)$$

$$E^s_{\phi\phi} = S_{\phi\phi} = \underline{E}_{s\phi}\cdot\hat{a}_{\phi_r} = Q^{\phi}_{s2}(\hat{a}_{s_1}\cdot\hat{a}_{\phi_r}) - Q^{\phi}_{s1}(\hat{a}_{s2}\cdot\hat{a}_{\phi_r}) \tag{10b}$$

(b) *For the remaining elements of the BSM,* consider $E_{\phi i}=0$, $E_{\theta i} = \eta$. This will yield, for the plane wave incidence:

$$\underline{H}_{\phi_i} = \hat{a}_{\phi_i}\, [e^{-jk|\underline{r}_i - \underline{d}| + jk\hat{k}_i\cdot\underline{r}'}]$$

Using the same method as used for ϕ-polarization incidence, one gets:

$$Q^{\theta}_{s1} = H^{\phi}_{s1}s_1s_2\mathrm{sinc}\left[\left(\frac{\underline{k}_s+\underline{k}_i}{2}\right)\cdot\underline{s}_1\right]\mathrm{sinc}\left[\left(\frac{\underline{k}_s+\underline{k}_i}{2}\right)\cdot\underline{s}_2\right], \tag{11a}$$

$$Q^{\theta}_{s2} = H^{\phi}_{s2}s_1s_2\mathrm{sinc}\left[\left(\frac{\underline{k}_s+\underline{k}_i}{2}\right)\cdot\underline{s}_1\right]\mathrm{sinc}\left[\left(\frac{\underline{k}_s+\underline{k}_i}{2}\right)\cdot\underline{s}_2\right], \tag{11b}$$

where $H^{\phi}_{s1} = \underline{H}_{\phi_i}\cdot\hat{a}_{s1}$, and $H^{\phi}_{s2} = H_{\phi_i}\cdot\hat{a}_{s2}$.

Now the corresponding co- and cross-polarized components at the receiver are

$$E^s_{\theta\phi} = Q^{\theta}_{s2}(\hat{a}_{s1}\cdot\hat{a}_{\phi_r}) - Q^{\theta}_{s1}(\hat{a}_{s2}\cdot\hat{a}_{\phi_r}) \tag{12a}$$

$$E^s_{\theta\theta} = Q^{\theta}_{s2}(\hat{a}_{s1}\cdot\hat{a}_{\theta_r}) - Q^{\theta}_{s1}(\hat{a}_{s2}\cdot\hat{a}_{\theta_r}) \tag{12b}$$

Using Eqs. (10) and (12) the complete BSM is given as

$$[S] = \begin{bmatrix} S_{\theta\theta} & S_{\phi\theta} \\ S_{\theta\phi} & S_{\phi\phi} \end{bmatrix} = \begin{bmatrix} E^s_{\theta\theta} & E^s_{\phi\theta} \\ E^s_{\phi\theta} & E^s_{\phi\phi} \end{bmatrix}$$

$$= \begin{bmatrix} \{Q^{\theta}_{s2}(\hat{a}_{s1}\cdot\hat{a}_{\theta_r}) - Q^{\theta}_{s1}(\hat{a}_{s2}\cdot\hat{a}_{\theta_r})\} & \{Q^{\phi}_{s2}(\hat{a}_{s1}\cdot\hat{a}_{\theta_r}) - Q^{\phi}_{s1}(\hat{a}_{s2}\cdot\hat{a}_{\theta_r})\} \\ \{Q^{\theta}_{s2}(\hat{a}^{s1}\cdot\hat{a}_{\phi_r}) - Q^{\theta}_{s1}(\hat{a}_{s2}\cdot\hat{a}_{\phi_r})\} & \{Q^{\phi}_{s2}(\hat{a}_{s1}\cdot\hat{a}_{\phi_r}) - Q^{\phi}_{s1}(\hat{a}_{s2}\cdot\hat{a}_{\phi_r})\} \end{bmatrix} \tag{13}$$

Substituting for Q_{s1} and Q_{s2} from Eqs. (9) and (11), and making use of the vector relationships between $\hat{a}_{s1}$, $\hat{a}_{s2}$, and $\hat{n}$, the final form of the BSM of a flat rectangular conducting plate is given by

$$[S] = E_{0s}\begin{bmatrix} (\underline{H}_{\phi_i}\times\hat{a}_{\theta_r})\cdot\hat{n} & (\underline{H}_{\theta_i}\times\hat{a}_{\theta_r})\cdot\hat{n} \\ (\underline{H}_{\phi_i}\times\hat{a}_{\phi_r})\cdot\hat{n} & (\underline{H}_{\theta_i}\times\hat{a}_{\phi_r})\cdot\hat{n} \end{bmatrix} \tag{14}$$

with $E_{0s} = s_1s_2\ \mathrm{sinc}\left[\left(\frac{\underline{k}_s+\underline{k}_i}{2}\right)\cdot\underline{s}_1\right]\ \mathrm{sinc}\left[\left(\frac{\underline{k}_s+\underline{k}_i}{2}\right)\cdot\underline{s}_2\right]$. (15)

The form of the BSM in Eq. (14) is an interesting one from the imaging or recovery point of view, *since all the elements of the matrix are independent of frequency and* involves only one of the unknowns $(\hat{n})$. Thus this form of the BSM will be exploited in the next section to recover the surface normal to the scattering center. It must be noted, however, that the radar measurables are the complex numbers $S_{\theta\theta}$, $S_{\theta\phi}$, $S_{\phi\theta}$, and $S_{\phi\phi}$, hence E_{0s} in (14) is not known from the measurement and it has to be determined by *calculations before $\hat{n}$ can be obtained.*

5 RECOVERY OF THE SURFACE NORMAL $\hat{n}(n_1, n_2, n_3)$.

Vector algebraic expansion of the elements of the BSM in (14) results into the folowing four equations:

$$S_{\theta\theta} = E_{0s}[n_1\sin\theta_s\cos\phi_i + n_2\sin\theta_s\sin\phi_i + n_3\cos\theta_s\cos(\phi_s-\phi_1)] \tag{16}$$

$$S_{\theta\phi} = E_{0s}[n_3\sin(\phi_i - \phi_s)] \tag{17}$$

$$\begin{aligned} S_{\phi\theta} = E_{0s}[&n_1(\sin\theta_s\cos\theta_i\sin\phi_i - \cos\theta_s\sin\theta_i\sin\phi_s) \\ &+ n_2(\cos\theta_s\cos\phi_s\sin\theta_i - \sin\theta_s\cos\theta_i\cos\phi_i) \\ &+ n_3\cos\theta_s\cos\theta_i\sin(\phi_i - \phi_s)] \end{aligned} \tag{18}$$

$$S_{\phi\phi} = -E_{0s}[n_1\cos\phi_s\sin\theta_i + n_2\sin\phi_s\sin\theta_i + n_3\cos\theta_i\cos(\phi_s - \phi_i)] \tag{19}$$

Here (θ_i, ϕ_i), (θ_s, ϕ_s) are the spherical coordinate representations of the $\hat{k}_i$ and $\hat{k}_s$, respectively. From Eq. (17) one gets

$$n_3 = \left(\frac{1}{E_{0s}}\right) \frac{S_{\theta\phi}}{\sin(\phi_i - \phi_s)} \tag{20}$$

Using Eqs. (16) and (17), and Eqs. (19) and (17), the following two equations are obtained

$$n_1\sin\phi_i + n_2\cos\phi_i = R_5/E_{0s} \tag{21}$$

$$n_1\cos\phi_s + n_2\sin\phi_s = -R_6/E_{0s} \tag{22}$$

$$\text{with } R_5 = \frac{S_{\theta\theta} - S_{\theta\phi}\cos\theta_s\cot(\phi_i - \phi_s)}{\sin\theta_s} \tag{22}$$

$$\text{and } R_6 = \frac{S_{\phi\phi} + S_{\theta\phi}\cos\theta_i\cot(\phi_i - \phi_s)}{\sin\theta_i}$$

Solving Eqs. (20), (21), and (22) for $\hat{n}$, one gets

$$n_1 = \frac{1}{E_{0s}} \cdot \frac{R_5\cos\phi_s + R_6\sin\phi_i}{\cos(\phi_i + \phi_s)} \tag{23a}$$

$$n_2 = -\frac{1}{E_{0s}} \cdot \frac{R_6\cos\phi_i + R_5\sin\phi_s}{\cos(\phi_i + \phi_s)} \tag{23b}$$

$$n_3 = \frac{1}{E_{0s}} \cdot \frac{S_{\theta\phi}}{\sin(\phi_i - \phi_r)} \tag{23c}$$

By inspecting Eqs. (20) to (23), it is clear that the solution given in Eq. (23) is valid with the conditions,

$$\phi_i \neq \phi_s \text{ , and}$$

$$\theta_i, \theta_s \neq 0 \text{ or } \pi \text{ .}$$

The first of the two conditions rules out the use of the monostatic scattering matrix (MSM) as a special case of the BSM in obtaining the solution in Eq. (23). The second condition is expected because, θ_i, $\theta_s = 0$, or π represent a radar site at the poles (north or south, respectively) of the fixed spherical coordinate system. At these two points $\hat{a}_\theta$ and $\hat{a}_\phi$ directions are not defined uniquely, and consequently the mathematical representation of the system breaks down.

In the solution given in Eq. (23) the factor E_{0s}, as noted earlier, is still unknown from the radar measurables, $S_{\theta\theta}$, $S_{\theta\phi}$, $S_{\phi\theta}$, and $S_{\phi\phi}$. To determine E_{0s}, the expressions in Eq. (23) are substituted into the condition

$$|\hat{n}| = 1, \text{ i.e., } n_1^2 + n_2^2 + n_3^2 = 1.$$

This gives

$$E_{0s} = \pm\left[\left\{\frac{R_5^2 + R_6^2 + 2R_5R_6\sin(\phi_i + \phi_s)}{\cos^2(\phi_i + \phi_s)}\right\} + \frac{S_{\theta\phi}^2}{\sin^2(\phi_i - \phi_s)}\right]^{1/2} \tag{24}$$

The ± sign of E_{0s} from Eq. (24), substituted into Eq. (23) will simply result in two anti-parallel solutions $\pm\hat{n}$, which is inconsequential. If it is essential, then the proper sign of E_{0s} in Eq. (24) can be decided by using the condition

$$\hat{n} \cdot \hat{k}_i < 0 \text{ .}$$

It is interesting to note that if one attempts to use the MSM for the recovery of $\hat{n}$ by substituting $\hat{k}_i = k_s$ (i.e., $\theta_i = \theta_s$, $\phi_i = \phi_s$) into Eqs. (16) to (19) one obtains:

$$S_{\theta\theta} = -S_{\phi\phi} \; ; \; S_{\theta\phi} = S_{\phi\theta} = 0 \quad (\text{when } \theta_i=\theta_s,\ \phi_i=\phi_s)$$

Obviously, now these elements of the scattering matrix cannot be used for the recovery of $\hat{n}$. This, in the opinion of the authors, is a clear demonstration of the usefulness of the BSM in the target recovery problems.

Another interesting situation is the special case of the BSM where $\phi_i=\phi_s=\phi$, but $\theta_i \neq \theta_s$. This means that the transmitter and the receiver are placed along a polar great circle of the spherical coordinate system (therefore it can be referred to as the vertical stacking). For this configuration, from Eqs. (17) and (18), we find that $S_{\theta\phi}=0$, but $S_{\phi\theta} \neq 0$. This is expected, since now $\hat{a}_{\phi_i} = \hat{a}_{\phi_s}$, and $\hat{a}_{\theta_i} \neq \hat{a}_{\theta_s}$, which means half the polarization basis is like that for MSM and the other half follows the general definition given for BSM in Fig. 2.

For the vertically stacked configuration, the nonzero elements of BSM in Eqs. (16), (18), and (19) reduce to the following ($S_{\theta\phi}=0$):

$$S_{\theta\theta} = E_{0s}[n_1 \sin\theta_s \cos\phi + n_2 \sin\theta_s \sin\phi + n_3 \cos\theta_s] \tag{25}$$

$$S_{\theta\phi} = E_{0s}[n_1 \sin(\theta_s-\theta_i)\sin\phi - n_2 \sin(\theta_s-\theta_i)\cos\phi] \tag{26}$$

$$S_{\phi\phi} = -E_{0s}[n_1 \sin\theta_i \cos\phi + n_2 \sin\phi \sin\theta_i + n_3 \cos\theta_i] \tag{27}$$

Solving Eqs. (25), (26), (27) for $\hat{n} = (n_1, n_2, n_3)$ one gets:

$$n_1 = \frac{1}{E_{0s}} \cdot \frac{S_{\theta\theta}\cos\theta_i \cos\phi + S_{\phi\theta}\sin\phi + S\phi\phi \cos\theta_s \cos\phi}{\cos(\theta_s-\theta_i)} \tag{28a}$$

$$n_2 = \frac{1}{E_{0s}} \cdot \frac{S_{\theta\theta}\cos\theta_i \sin\phi - S_{\phi\theta}\cos\phi + S_{\phi\phi}\cos\theta_s \sin\phi}{\cos(\theta_s-\theta_i)} \tag{28b}$$

$$n_3 = \frac{1}{E_{0s}} \cdot \frac{S_{\theta\theta}\sin\theta_i + S_{\phi\phi}\sin\theta_s}{\cos(\theta_s-\theta_i)} \tag{28c}$$

Once again, before the solution in Eq. (28) can be useful E_{0s} has to be known. Applying $|\hat{n}| = 1$ condition on Eq. (28), the expression for E_{0s} is obtained as

$$E_{0s} = \pm \frac{[(S^2_{\theta\theta} + S^2_{\phi\theta} + S^2_{\phi\phi}) + 2(S_{\theta\theta}S_{\phi\phi}\cos(\theta_s-\theta_i))]^{1/2}}{\cos(\theta_s-\theta_i)} \tag{29}$$

6 RECOVERY OF THE SCATTERING CENTER SURFACE GEOMETRY ($\underline{s}_1$ and $\underline{s}_2$)

In the BSM representation of Eq. (14) it is seen that the information regarding $\underline{s}_1$ and $\underline{s}_2$ is contained only in the common factor E_{0s}. The dependence of E_{0s} on $\underline{s}_1$ and $\underline{s}_2$ is complicated due to the multivalued nature of the sinc function. Furthermore, only a partial information regarding $\underline{s}_1$ and $\underline{s}_2$ (namely their components in the $\frac{\underline{k}_s+\underline{k}_i}{2}$ direction, and their scalar magnitude) is contained in the factor E_{0s}. Therefore, a straight-forward recovery of the surface geometry from a single BSM (i.e. single frequency, single receiver) is not expected. Hence, in the following, this problem is approached from two viewpoints; one with the multifrequency BSM input data, and the other with the multistatic (multi-receiver) single frequency input data. It is pointed out here that the partial information about $\underline{s}_1$ and $\underline{s}_2$ in E_{0s}, in conjunction with the knowledge of $\hat{n}$ (from Section 5) and the orthogonal relationship between $\hat{a}_{s1}$, $\hat{a}_{s2}$, $\hat{n}$ was found to be sufficient to construct $\underline{s}_1$ and $\underline{s}_2$ uniquely.

(a) Multifrequency BSM approach

Once $\hat{n}$ is known, E_{0s} for the bistatic matrix at three harmonically related frequencies can be manipulated to extract information about $\underline{s}_1$ and $\underline{s}_2$.

Consider three frequencies corresponding to which the wave number k is given by $0.5k_0$, k_0, and $2k_0$, respectively. By using the method of Section 5, E_{0s} at each of these frequencies can be calculated from the measured BSM. These calculated values can in turn be related to $\underline{s}_1$ and $\underline{s}_2$ by using Eq. (15), i.e.,

$$s_1 s_2 \mathrm{sinc}(\psi_1/2)\mathrm{sinc}(\psi_2/2) = E_{0s}|_{0.5ko} \qquad (30a)$$

$$s_1 s_2 \mathrm{sinc}(\psi_1)\mathrm{sinc}(\psi_2) = E_{0s}|_{ko} \qquad (30b)$$

$$s_1 s_2 \mathrm{sinc}(2\psi_1)\mathrm{sinC}(2\psi_2) = E_{0s}|_{2ko} \qquad (30c)$$

$$\text{where } \psi_1 = \left(\frac{\underline{k}_{so} + \underline{k}_{io}}{2}\right) \cdot s_1 , \quad \psi_2 = \left(\frac{\underline{k}_{so} + \underline{k}_{io}}{2}\right) \cdot s_2 . \qquad (30d)$$

Using Eqs. (30a) and (30b), one gets

$$\cos(\psi_1/2)\cos(\psi_2/2) = \frac{E_{0s}|_{ko}}{E_{0s}|_{0.5ko}} = C_1 \qquad (31a)$$

similarly, combination of Eqs. (30b) and (30c) yields

$$\cos(\psi_1)\cos(\psi_2) = \frac{E_{0s}|_{2ko}}{E_{0s}|_{ko}} = C_2 \qquad (31b)$$

By manipulating the non-linear system of Eqs. in (31) one can solve for ψ_1 and ψ_2. These solutions are

$$\cos\frac{\psi_2}{2} = \pm\left[\left(\frac{1-C_1}{2}\right)^{1/2}\left\{\left(\frac{1}{2} + R\right) \pm \left(\frac{1}{4} + R\right)^{1/2}\right\}\right. , \qquad (32a)$$

$$\cos\frac{\psi_1}{2} = \frac{C_1}{\cos(\psi_2/2)} , \qquad (32b)$$

where $R = 2C_2^2/(1-C_1)$, and $C_1 \neq 1$, $C_1, C_2 < 1$.

By analyzing Eq. (31) one notes that when $C_1 = 1$, C_2 must be equal to 1, and

$$\psi_1, \psi_2 \rightarrow 0, \quad \text{or } 2n\pi , \quad n = 1, 2, \ldots .$$

Since all four solutions of Eq. (32a) are real, we must select the appropriate one before $\underline{s}_1$ and $\underline{s}_2$ can be constructed from the knowledge on $\hat{n}$, ψ_1, and ψ_2. The following observations are made regarding the selection procedure:

- The outside ± sign in Eq. (32a) will give a pair of solutions which will differ by $n\pi$, where n is odd;
- The inside ± sign will give two solutions; one will be in the region $0 < \psi_2/2 < \pi/2$ (+ solution), and the other one will be in the region $\pi/2 < \psi_2/2 < \pi$ (- solution).

By using these observations in conjunction with the expressions in Eq. (30) for E_{0s}, unwanted solutions of Eq. (32) can be identified.

(b) *Multiangle BSM approach*

From the practical point of view, the requirement of three harmonically related frequencies may not be desirable. Thus it is thought that the recovery of $\underline{s}_1$ and $\underline{s}_2$ using a single frequency, multiangle BSM should also be attempted.

The main problem in this approach is that it may not be possible to generate a system of equations similar to Eq. (30) from the original expression in Eq. (15). Consider three receiver sites identified by the reception direction, $\underline{k}_{s1}$, $\underline{k}_{s2}$, and $\underline{k}_{s3}$, respectively. Now, the arguments of the sinc functions in Eq. (15) becomes,

$$\left(\frac{\underline{k}_i + \underline{k}_{sj}}{2}\right) \cdot \underline{s}_1 , \quad \text{and } \left(\frac{\underline{k}_i + \underline{k}_{sj}}{2}\right) \cdot \underline{s}_2 ; \quad j = 1, 2, 3.$$

Unless these arguments for different values of j are harmonically related, one will generate six unknowns instead of two as in the Eq. (30). Consequently, the solution procedure presented earlier in this section cannot be applied.

One possible way to solve the multiangle problem is to control the transmit directions (say $\underline{k}_{im}$) and the receive directions ($\underline{k}_{sj}$) such that for various combinations of m and j the vector $(\underline{k}_{im} + k_{sj})/2$ yields

$$(\underline{k}_{io} + \underline{k}_{so})/2 , \quad (\underline{k}_{io} + \underline{k}_{so}), \quad 2(\underline{k}_{io} + \underline{k}_{so}), \quad \ldots, \qquad (33)$$

where $\underline{k}_{io}$, and $\underline{k}_{so}$, as used in the earlier multifrequency case, represent some reference directions. To elaborate on this method, consider

$$\underline{k}_i = k_{ix}\hat{a}_x + k_{iy}\hat{a}_y + k_{iz}\hat{a}_z ,$$

$$\underline{k}_s = k\underline{s}_x\hat{a}_x + k_{sy}\hat{a}_y + k_{sz}\hat{a}_z ,$$

$$\underline{s}_1 = s_{1x}\hat{a}_x + s_{1y}\hat{a}_y + s_{1z}\hat{a}_z ,$$

where $\hat{a}_x$, $\hat{a}_y$, $\hat{a}_z$ represent unit vectors in x,y,z directions in the global spherical coordinate system. The argument of the first sinc function in Eq. (15) can now be written

$$\left(\frac{\underline{k}_i + \underline{k}_s}{2}\right)\cdot\underline{s}_1 = s_{1x}\left(\frac{k_{ix} + k_{sx}}{2}\right) + s_{1y}\left(\frac{k_{iy} + k_{sy}}{2}\right) + s_{1z}\left(\frac{k_{iz} + k_{sz}}{2}\right) . \tag{34}$$

In Eq. (34) it should be possible to manipulate the values of (k_{sx}, k_{sy}, k_{sz}) to meet the requirements specified in Eq. (33).

Another adhoc, but straight-forward aproach to the multiangle problem, is to generate E_{0s} for a number of arbitrarily located receivers (the minimum number is expected to be 3) and then apply these to a suitable computer generated data fit to match the theoretical behavior of E_{0s} given in Eq. (15). This can be accomplished by using a non-linear optimization routine, with $\underline{s}_1$ and $\underline{s}_2$ as the optimization variables. This computer aided approach can be initiated only when some suitable, theoretically and experimentally generated numerical multistatic scattering matrix data is made available.

To construct $\underline{s}_1$ and $\underline{s}_2$ with the knowledge of ψ_1, ψ_2, and $\hat{n}$, one needs to consider the local geometry of the scattering center. This is shown in Fig. 4.

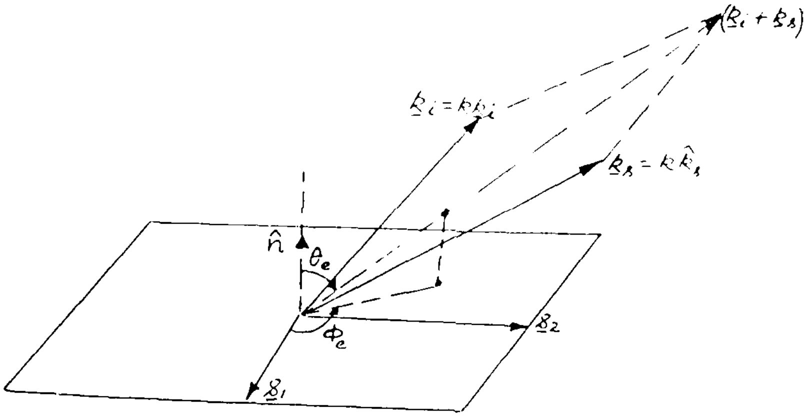

Fig. 4: Local Geometry of the Scattering Center

Using this scattering geometry, one can write

$$\cos\theta_e = \pi - (\underline{k}_{io} + \underline{k}_{so}) \cdot \hat{n} \tag{35}$$

Next, from the geometrical interpretation of ψ_1, and ψ_2 (i.e., projection of $\underline{s}_1$ and $\underline{s}_2$ onto the vector $\frac{\underline{k}_{io}+\underline{k}_{so}}{2}$, respectively) one can obtain

$$\psi_1\psi_2 = \frac{s_1 s_2}{4} \cos\Phi_e \sin\Phi_e (\cos^2\theta_e$$

or

$$\sin 2\Phi_e = \frac{8\psi_1\psi_2}{(s_1 s_2)\cos^2\theta_e} . \tag{36}$$

Using the expression for $E_{0s}\Big|_{k_0}$ in Eq. (30b), with the knowledge of ψ_1 and ψ_2, one can calculate the value of $s_1 s_2$ (area of the rectangular scattering center). Once $s_1 s_2$ is known θ_e and Φ_e can be calculated from Eqs. (35) and (36), respectively. With (θ_e, Φ_e) and ψ_1, ψ_2, from the Fig. 4, $\underline{s}_1$ and $\underline{s}_2$ is determined completely.

7 RECOVERY OF THE LOCATION VECTOR ($\underline{d}$)

The information about the location vector $\underline{d}$ is contained in the phase factor of the BSM and MSM. In going from Eq. (6) to Eq. (14) these phase terms were suppressed, since they were absorbed in the normalization factors. The normalization factors for the BSM (denoted by N_B) and the MSM (donated by N_M) are as follows:

$$N_B = jk\eta \, \frac{e^{-jk[|\underline{r}_s-\underline{d}| + |\underline{r}_i-\underline{d}|]}}{2\pi|\underline{r}_s-\underline{d}|} \tag{37a}$$

$$N_M = jk\eta \, \frac{e^{-jk[2|\underline{r}_i-\underline{d}|]}}{2\pi|\underline{r}_i-\underline{d}|} \tag{37b}$$

The relationship between $\underline{r}_s$, $\underline{r}$, and $\underline{d}$ is shown in Fig. 5. It is to be noted that since the location of the radar sites with respect to the fixed global spherical coordinate system is known, the vectors $\underline{R}_i$ and $\underline{R}_s$ are known, and the only unknown in the normalization factors of Eq. (37) is $\underline{d}$.

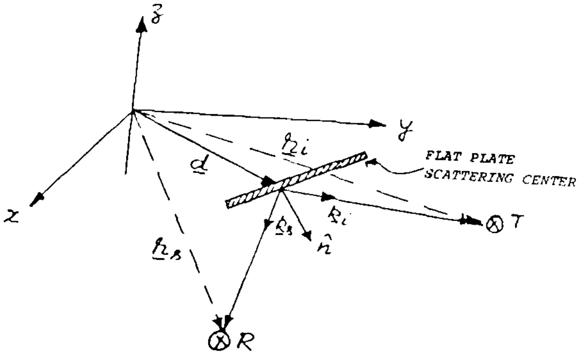

Fig. 5: Geometry for the Recovery of the Location Vector ($\underline{d}$).

Because of the multiple valued nature of the angular function measurements (i.e., $0<\theta<2\pi$, and $\theta+2n\pi$ both will be measured as θ on CW systems), the phase of N_M in Eq. (37b) cannot be used directly to obtain $\underline{d}$. To illustrate this point, consider ϕ_{M1} to be the measured phase of the MSM elements with the fixed origin as the phase reference. Then using Eq. (37b) one can write

$$2k|\underline{r}_i-\underline{d}| = \phi_{M1} + 2\pi\ell,$$

where ℓ is an integer number which is unknown. If the operating frequency is f_1, with corresponding wavelength λ_1, then

$$|\underline{r}_i-\underline{d}| = \left(\frac{\phi_{M1}}{2\pi} + \ell\right)\frac{\lambda_1}{2} \tag{38}$$

In order to determine the unknown integer ℓ, consider a second frequency f_2 which is very close to the frequency f_1 (say a few megahertz in a GHz range). Corresponding to this frequency the wavelength is λ_2, and the measured phase is ϕ_{M2}; now from Eq. (37b)

$$2|\underline{r}_i-\underline{d}| \cdot \frac{2\pi}{\lambda_2} = \phi_{M2} + 2\pi m; \text{ m-integer.}$$

Substituting for $|\underline{r}_i-\underline{d}|$ from Eq. (38), one gets

$$(\phi_{M1} + 2\pi\ell)\frac{\lambda_1}{\lambda_2} = 2\pi m + \phi_{M2}$$

or

$$m = \ell\,\frac{\lambda_1}{\lambda_2} = \frac{\phi_{M1} - \phi_{M2}}{2\pi} \tag{39}$$

The solution of Eq. (39), subjected to the restriction that the solutions m and ℓ must be integers, provide some interesting conclusions. First, there will be an infinite set of solutions [(m_i, ℓ_i), i = 1, 2....]. Second, the separation between the solution sets (m_i, ℓ_i) will depend on the "rational fraction" corresponding to (λ_1/λ_2). It can be shown that if λ_1 and λ_2 are two real numbers very close to each other, then the separation between solution sets (m_i, ℓ_i) will be large. Consequently, the multiple values of $|\underline{r}_i-\underline{d}|$ obtained from Eq. (38) corresponding to the multiple values of $\ell(\ell_i;\ i = 1,2....)$ will be spaced far apart. The knowledge of the approximate distance to the target space from the MSM radar site in conjunction with the above large solution separation will be useful in rejecting the unwanted solutions of Eq. (39).

Once $|\underline{r}_i - \underline{d}|$ is known, using the geometry of Fig. 5 one can determine the location of the tip of the vector $\underline{d}$, since the transmission direction $\hat{k}_i$ is known.

8 CONCLUSIONS

A high frequency bistatic/multistatic scattering matrix model for an isolated scattering center of a complex target has been developed. The elements of the resulting BSM in Eq. (14) has been analyzed to recover the following parameters:

- The BSM at a single frequency is sufficient to obtain $\hat{n}=(n_1,n_2,n_3)$ in terms of $S_{\theta\theta}$, $S_{\phi\phi}$, $S_{\phi\theta}$.
- An analytical solution for $\underline{s}_1$ and $\underline{s}_2$ has been obtained by recovering the expression E_{0s} given in Eq. (15) at three related frequencies, namely $0.5k_0$, k_0 and $2k_0$. It has been suggested that in a realistic experimental situation the above data requirement is not very economical. Therefore, an alternate method using a multi-receiver (i.e. multi-angle or multistatic) instead of the multi-frequency concept, has been proposed.
- Analyzing the phase of the normalization factor of the MSM in Eq. (37) simultaneously at two frequencies (which can be accommodated i a very narrow bandwidth), the vector location ($\underline{d}$) of the scattering center with respect to the origin of the fixed coordinate system can be recovered. From the target identification point of view, this is deemed to be a very important parameter of recovery.

It is possible to extend the isolated scattering center model of this paper to two and three scattering center models. This will require simultaneous processing of multistatic (minimum 3 and 4 receivers, respectively) data. Thus, a judicious combination of multi-frequency and multistatic scattering matrix data should be the focus of future polystatic radar target imaging investigations.

9. REFERENCES

D.E. Barrick and W.H. Peake, "A Review of Scattering from Surfaces with Different Roughness Scales", Radio Science, Vol. 3, August 1968, pp. 865-868.

M. Davidovitz, "Analysis of Certain Characteristic Properties of the Bistatic, Asymmetric Scattering Matrix", M.Sc. Thesis, University of Illinois at Chicago, Communications Lab., April 1983, Report No. EMID-CL-1983-04-15-03.

M. Davidovitz and W-M. Boerner, "Reduction of Bistatic Scattering Matrix Measurements for Inversely Symmetric Radar Targets", IEEE Trans. on Ant. & Prop., Vol. AP-31, No. 2, pp. 237-242, March 1983.

G.E. Heath, "Bistatic Scattering Reflection Asymmetry, Polarization Reversal Asymmetry, and Polarization Reversal Reflection Symmetry", IEEE Trans. Antennas & Propagation, Vol. AP-29, No. 3, May 1981, pp. 429-434.

D.S.W. Kwoh and B.M. Lake, "The Nature of Microwave Backscattering from Water Waves", AGARD Conference on Propagation Factors Affecting Remote Sensing by Radio Waves, AGARD Conf. Proceedings, No. 345, pp. 23-1 to 23-16.

W.H. Peake and T.L. Oliver, "The Response of Terrestrial Surfaces at Microwave Frequencies", ElectroScience Lab., The Ohio State University, May 1971, Report No. AFAL-TR-70-301, AD884106.

10. ACKNOWLEDGMENTS

This research was supported in parts by the Office of Naval Research under Contract No. US ONR N00014-80-C-0773; under NATO-IMOR Grant No. SA.5.2.03B(189)84; under General Dynamics Order No. 614972; and under Westinghouse Order No. 86EJ-HA-3069.

We would like to acknowledge the continued interest shown in our research by Dr. Richard G. Brandt, Office of Naval Research; Dr. Otto Kessler, Naval Air Development Center; Dr. James W. Mink, Army Research Office; Dr. Hans-Peter Schmid, General Dynamics, Pomona Division; and Mr. Norman Powell, Westinghouse Electric Corporation.

DISCUSSION

Y.Brault

How do you foresee the practical applications on your theories in the near future to achieve the automatic target recognition?

Author's Reply

Please refer to NATO-ARW-IMEI-1983/Proceedings, where about 50 of 72 papers deal directly with the NON-COOPERATIVE *target recognition problem from match* sign proc metrolog design and devices point of view. Especially, carefully study the working group reports (7 total) on specifics of this subject matter.

What was shown to this date: Mathem. signal processing methods developed, were checked positively against measurement data. Result: still not sufficient but highly (processing-dependent) promising.

Basic direct inverse scattering theories must be rapidly advanced simultaneously with signal processing techniques *(advancing rather well in* US/Europe, Pacific Orient, and Russia).

Metrology (Scattering Matrix) for various low RC and other targets embedded in free space clutter multiset operations must be advanced (requires substantial increases in funding and construction of testbed modular experimental radar systems covering continuously 06 to 200/300 GHz: EMI approach).

More emphasis on "clutter" description (hydrometeoric/ground-terrain sea, coastal battlefield etc) and ground paths assessment (talk to Mme Dr Thuy le Toon: World Expert Superieur).

Signal processing/transceiver device technology using acousto-electro-opt. device need to be rapidly advanced (coming along most impressively).

More interaction on national level between Academic Industry, Governm. Nat. Lab.

More specialists workshops on NATO-level.

More funding/more equipment and facilities required.

Prioritization reassessment of National Electronic Programs on Ecole Superieure level.

DISPOSITIF D'ANALYSE DE CIBLES PAR DISCRIMINATION FINE EN DISTANCE

par

R.Ambos
THOMSON-CSF
178 Bld Gabriel Péri
92240 Malakoff
France

RESUME

L'analyse fine de cibles en fonction de la distance nécessite l'émission d'un spectre à large bande instantanée, ainsi, pour une résolution de 50 cm, 300 MHz sont nécessaires.

Pour réaliser un dispositif d'analyse fonctionnant en compression d'impulsion modulée linéairement en fréquence, il est nécessaire de réaliser des lignes dispersives à très fort BT, coder et traiter des impulsions comprimées très brèves.

Le principe proposé consiste à contourner ces deux difficultés de la façon suivante:

- réaliser le fort BT nécessaire à l'émission par l'utilisation de lignes dispersives existantes suivie d'un traitement analogique spécifique.

CONSIDERATIONS IN UTILIZING IR SIGNATURES

by

Mr Wayne H.Tanaka
Naval Weapons Center
China Lake, CA 93555
USA

ABSTRACT

This presentation will discuss on a tutorial basis the relationships of RF and IR systems, characteristics of both active and passive IR sensor data, applications of laser radar sensors, and show signature data to illustrate these topics. The paper will begin by showing the radar equation and how it is used by both the RF and laser radar communities. This includes a carrier-to-noise budget analysis performed for both technologies for a proposed altimeter development. This leads to considering the basic features an active and passive IR sensor can exploit from a target. Issues of background rejection will be raised. A general discussion of the types of uses the DoD is considering for laser radars will then follow. These include altimetry, Doppler Navigation, obstacle avoidance for avionics, and remote sensing lidar.

Examples of signatures to be included are Forward-Looking-Infra-Red (FLIR) data of ships taken under Navy Target Signatures Program (TSP) auspices, Active CO_2 laser radar signatures of ships, again taken under TSP auspices, within the last two years, and laser radar signatures of tanks and vehicles taken in support of the Navy's Hybrid Target Acquisition System (HYTAS) program (recently merged with the Army's Infra-Red Surveillance, Targeting and Acquisition Radar for Tank Location and Engagement (IR-STARTLE) program) taken this spring.

The stress for this presentation will be the applicability of laser radar signatures to aid in target acquisition, detection, and classification.

"The mixture of different semiconductor technologies in Radar modules and its impact on cooling problems and reliability"

Prof. Dr. Erik Langer, Siemens A.G., Bereich Bauelemente, D-8000 Munich 80

Summary:

The T/R-modules of Active Phased Array Radars contain electronic circuits made by very different materials and technologies. The power dissipation of the dense packed modules produces much heat in the array which has only moderate cooling conditions. In consequence, the electronic devices must operate at ambient temperatures up to 90°C. Despite careful optimizing the heat paths, junction temperatures can rise up to 160°C. Hence also failure mechanisms with high activation energies (e.g. 1.85 eV) are relevant, even they can be normally neglected for reliability estimations.
By optimizing the individual devices one can expect with "soft degradation" that the mean repair interval (MRI) of the array will be about 1 ... 3 years accumulated service times. That is better than for other portions of the equipment.
The degradation of electrical performance at high temperatures is limiting only the transmission power and the receiver noise figure.
By application of an Arrhenius graph and modification of the "bath tube" curve, one can derive first reliability figures from stress tests with small numbers of samples in an early state of development.
The reliability and packaging problems can be solved, so that T/R-modules can meet the requirements of active PAR.

1. Introduction

Active Phased Array Multi Function Radars (subsequent abbreviated as "PAR") contain a great number of very dense packed Transmit/Receive modules. The package density is determinded by the wavelength of the microwave transmission signal and must be optimised with respect to the beam focusing and sidelobe levels. In case of an X-Band PAR the cross section of the modules is restricted to about 15 x 18 mm^2 (fig. 1). To realise all the functional devices for transmitting and receiving with the required control functions, nearly each advanced electronic components technology must be used.

In details there are (Table 1):

Function	Technology
Transmitter power amp.	GaAs-hybrid (Thin-film)
T/R-power switch	Si-hybrid (Thin-film)
Small signal and LNA	GaAs-monolithic-IC
Digit. controlled MW-phase shifter	GaAs- and MOS-IC
Digit. controlled MW-attennator	GaAs- and MOS-IC
Small signal T/R-switch	GaAs-monolithic-IC
Digit. control & monitor circuits	MOS- and bipol. Si-IC

Table 1

In addition there are also needed discrete active devices as GaAs-FET, PIN- and Zener-diodes, Schottky-diodes and bipolar- and MOS-transistors. All the active devices must be integrated on chip carriers in thin-film technique. The chip carriers have to be bonded on metallic base plates to allow a suitable mounting in the module case. Because of the very small space inside the modules there are not only packaging problems but also some critical temperature problems with respect to the very restricted cooling conditions of the array (see in fig. 1 the limited cross sections of cooling channels).

Considering the heat problems we have to examine the power consumption of the particular functional devices and their thermal resistance, because the operating temperature of the semiconductor junctions respectively FET-channels is the most important parameter for the reliability of the modules.

2. Power consumption and thermal balance

The power consumption and dissipation is mainly depending on the required transmission power and in consequence on the operational performance of the PAR. The power dissipation of the power amp. is direct proportional to the duty cycle. But note, one must distinguish between the DC-duty cycle (DC-DC) and the RF-duty cycle. The DC-DC must be longer than the RF-DC to ensure a sufficient thermal stability of the amps before transmitting. Hence the DC-DC is important; in addition, the maximum dissipation occures with activated power amp. and without RF-input. This can happen in specific operational situations (e.g. during tests) or when the RF-input fails. Under these conditions, the power amp. can dissipate more than 80 % of the total DC-power consumption of the module, as it is shown in table 2 for two examples with 1 W resp. 3 W RF-power and 30 % DC-DC:

Device	Mean power consumption (Watt)			
	Transmit mode		Receive mode	
Transm. power amp.	2.5	6.75	-	
T/R-power switch	0.03	0.2	0.04	0.12
Small signal and LNA	0.25		0.5	
Phase shifter	0.03		0.07	
Microwave attenuator	0.03		0.07	
Small signal T/R-switch	0.02		0.04	
Contr. & monitor circuits	0.05		0.10	
total	2.91	7.33	0.82	0.9

Table 2

In summa the mean power dissipation can vary according to the RF-power between ca. 3.75 ... 8.25 W. This power produces adequate heat and must be transfered through a chain of thermal resistances to the surface of the module case, where will be an heat exchange with the cooling air. With respect to cooling efforts and noise creation the cooling air velocity must remain below 1 m per second, that means the external surface of the modules will have a temperature in the range of 60°... 85°C, according to the particular surface area to the cooling air entrance.

To minimize the thermal resistance of the module case, we prefer to use a material with high thermal (and electrical) conductivity. But there are also other points to take into account, e.g. the thermal expansion, weight, corrosion and good performance for specific mechanical treatments. At least it is also required the ability for electron-beam or Laser welding, because the module case has to be hermetic sealed after assembling the electronics. With regard to restricted space, the majority of active elements has to be used as naked chips, hence the hermetic sealing can not be dispensed with.

In screening the available materials for the module case, there are copper, aluminium and their alloys (s.Table 3):

	Cu	Brass	Al	AlMgSi	
Heat conductivity	3.8... 4.0	0.8... 1.3	2.17	1.7... 2.1	W/cmK
Lin.therm.expans.coeff.	17(25°)34(200°C)	18.4	23.6	22 ... 23	ppm/K
Specif. weight	8.9	8.4... 8.7	2.7	2.7	g/cm^3
Electr. conductivity	58	~ 20	36	26 ... 32	S/cm

Table 3

Comparing these materials it is clear, we have to make a compromise in choosing a light weight material as aluminium or its derivates.

So far the material and the geometrical configuration of the module case is fixed, one must calculate the local thermal resistance of the case in the area of the inside mounted electronic circuit. This is a hard job with respect to the radiator fins of the case. In general it can be stated, that the local thermal resistance of the case can be reduced to about 0.5 ... 0.8 K/W.

Considering the thermal resistance of the electronic circuits up to the junctions or channels of the active elements, we have to take into account the heat paths of the semiconductor chips, the chip carrier, the base plate and - very important - the air gaps od solder layers between the particular parts (s. fig. 2).

With respect to thermal conductivity and good matched thermal expansion to GaAs and Silicon, the most favorable substrat material is Beryllium oxide. But because of price and the toxic mashining waste, in the majority aluminium oxide ceramic is prefered for the chip carriers, despite its ca. nine times worse thermal conductivity.

A serious problem is the selection of a proper material for the base plates of the hybrid devices and chip carriers. Because the ceramic substrates are too brittle to be fixed direct in the module case, one needs metallic base plates with good matched thermal expansion to the ceramic substrates and excellent thernal conductivity. These requirements are very contrary. The common used Kovar has the optimal thermal expansions, but is here to be excluded because of the very poor thermal conductivity. A permissible compromise is the application of Copper-Kovar-laminates for the base plates.

Using all these optimizing instruments carefully, we can only achieve a junction temperatures fo the semiconductors approx. 30°... 70°C above the internal case temperature. That means $T_J \approx 100^\circ \ldots 160^\circ C$, a temperature range with accelerated failure mechanisms and its impact on reliability.

3. Reliability of the T/R-module electronics

The manifold of components and technologies exhibits also a great diversity of failure mechanisms. Excluding the mechanical failures, the majority of troubles are temperature sensitive processes with activation energies in the scope of 0.2 ... 2.0 e.V., in extremum even more.

The activation energies for specific failures are mostly different for silicon and GaAs-devices.

The acceleration of failure mechanism is consistent with the specific activation energy E_{ai}. By transforming the Arrhenius equation (1) one gets for the acceleration factor from temperature T_1 to T_2 ($T_1 < T_2$):

Eq. (1)
$$F_i(T_1/T_2) = \exp\left\{\frac{E_{ai}}{k}\left(\frac{1}{T_1} - \frac{1}{T_2}\right)\right\}$$

with T_1, T_2 ... junction or channle temp. (K)

k ... Boltzmann const. (8.65×10^{-5} eV/K)

Because F_i is exponentially increasing with E_{ai}, failure mechanisms with great activation energy are for the high temperature operations in T/R-modules important, though they may be neglected at normal conditions.

Example:

In a collective at temperature T_1 is a fraciton n_1 of pieces with the failure rate $\lambda_1(T_1)$ for small E_a and the rest of pieces $n_2 = 1 - n_1$ has the failure rate $\lambda_2(T_1)$ for high E_a; then the expected failure rate is

Eq. (2)
$$\lambda(T_1) = n_1 \cdot \lambda_1(T_1) + n_2 \lambda_2(T_1) \approx n_1 \cdot \lambda_1(T_1).$$

By increasing the operating temperature to T_2, then we get

Eq. (3)
$$\lambda(T_2) = n_1 \cdot F_1(T_1/T_2) \cdot \lambda_1(T_1) + n_2 \cdot F_2(T_1/T_2) \cdot \lambda_2(T_1).$$

That means, if the acceleration factor is very high (as partly in the case of T/R-module operation conditions $F_2(100/150) \approx 750$) the term $F_2 \times \lambda_2$ can become significant, also when λ_2 is much smaller than λ_1.

While for silicon components very much experience and statistic data are available, in case of GaAs the situation is not so satisfactory. But with respect to the much higher band gap of GaAs compared with Silicon, we can assume that GaAs-devices can operate at higher junction temperatures than silicon semiconductors.

In particular, there are the following failure mechanisms:

3.1 MOS-LSI:
This technology, used for the control and monitor functions in the T/R-modules has failure mechanisms with activation energies E_a analogous to tabele 4:

Table 4

The distribution for these failure sources depends on the specific IC, but in the average there are e.g. for Micro-processors ca. 63 % of failures with small activation energies, ca. 15 % with medium and ca. 22 % with high activation energies (2). This distribution is roughly valid also for the MOS-part and likewise for the bipolar part of the module electronics.

By rigorous fully dynamic Burn-in procedures, a considerable part of the failures with small activation energy can be eliminated, so that a more suitable distribution remains. The reduction of failures with small activation energy is important, because these failure sources are extremely relevant for the reliability.

Because of the permitted operation temperature of silicon IC, this part of the module electronics should be arranged at the best cooled places in the module case.

3.2 GaAs-power FETs:
Also for these components not only one failure mechanism is to be considered. Clearly, chips with "via holes" have other problems than sheet grounded device or "flip-chip" mounted FETs. But two failure mechanisms are dominant at GaAs-power FETs, it is electromigration and contact degradation (3), (4).

Already years ago it was experienced that gold metallization is superior to aluminium, therefore we must only consider NiGeAu-systems for the drain and source contacts and TiWAu-systems for the Schottky gates. Because in the fabrication of power devices a rigorous inspection of the crystal quality and careful burn-in is usual and in contrast to MOS devices GaAs-MESFET have no gate oxide, electromigration of the gate metal at high channel temperatures and contact degradation are significant for the life time of these semiconductors. For this failure mechanism the activation energy is about 1.85 resp. 1.15 eV, that is much higher than for Si-power devices (0.6 ... 0.7 eV).

The high activation energy promises on the one hand a long mean life time (MTF), but also a high degree of temperature sensitivity for MTF and the failure rate. Because the power amps are the most heat producing elements in the T/R-module, one must calculate with channel temperatures of 130° ... 160°C; hence we must take here into account the maximal acceleration factors for the failure rates.

Usually MTF-figures are published for CW-operation, but in T/R-modules there is normally pulsed operation. For the MTF is the pulsed operation profitable, because only during the DC-DC the FETs are on supply voltage, and only in these periods the relevant electro-chemical processes occur. During the pulse intervals are the much slower diffusion processes in action, likewise as at temperature storage. Therefore the accumulated active operating time is relevant for the MTF, that means for an Duty-factor ν (corresponding) for the DC-DC):

Eq. (4)
$$MTF\ (\nu) \approx \frac{MTF\ (CW)}{\nu}$$

In this way, the effective life time is up to twenty times longer than data sheet figures expell.

3.3 GaAs-IC:
GaAs-IC for T/R-modules are in majority linear circuits. Though these devices have little power dissipation, they will be heated by the adjacent power devices. Therefore the channel temperatues of the FETs are about 100° ... 130°C. In praxi the active elements of the monolithic ICs occupy only a portion of the chip (5), but because of the poor thermal conductivity of GaAs, the heat can not distributed in the entire chip volume. Hence the active elements produce local hot areas on the chip. For the active elements of these ICs we can expect similiar failure mechanisms as for GaAs-power devices, but with less acceleration. Equivalent conditions are also valid for the hybrid circuits with discrete semiconductors.

4. Soft degradation of the array

Despite of the very good reliability figures of electronic circuits (MTBF $> 10^6$ h) we must consider the life time of the complex T/R-modules. Because of the great number of modules in a PAR, the equipment will not fail, when one or few modules fail, at the condition that defective parts are approximately uniform distributed in the array. If than a distinct percentage of modules may fail, we speak of "soft degradation". This percentage and the failure rate λ_M of the modules determine the mean repair interval (MRI) of the PAR (fig. 3).
The graph shows the MRI-figures for continuous operation. At intermittendt service, the MRI will be adequate longer.

If we can e.g. tolerate that 5 % of the modules fail in a periode of 1 ... 3 years, then a module failure rate λ_M may be in the scope of about 2 ... 6 x $10^{-6}h^{-1}$.
The module failure rate is additive composed of the individual failure rates λ_i of the different devices and some other failure sources (mounting faults etc.), what we will neglect in a first estimation:

Eq. (5) $\lambda_M \approx \lambda_{power} + \lambda_{small\ sign} + \lambda_{T/R\text{-}switch} + \lambda_{phasesh.} + \lambda_{control}$

All failure rates out of them are not experienced today on great number of tests, but supposed there are in detail errors of a factor two or three, the specific MTBF of the array may expected to be much longer than other portions of the equipment perform. That means, minimizing the T/R-module failure rate is not decisive for the military availability, but for the repair costs.

5. Electrical performance

High operating temperatures influence also the performance of the electronic circuits. Most important are:

- Loss of gain and increase of noise figure of LNA
- Loss of gain and output power of power amps
- Isolation loss of T/R-switches
- Increasing insertion loss (and phase errors) of phase shifters

The observed degradation of gain and noise figure is essentially caused by the decreasing electron mobility with rising temperatures. In a temperature interval from 20°C to 90°C a degradation of gain per stage of 0.4 dB and an 0.2 dB increasing of noise (see fig. 4 and 5) must be expected.

Regarding also the insertion loss of the T/R-switch the resulting noise figure of the receiver will be about 4.5 ... 5 dB.

In the same way the power amps are influenced. Considering the fact, that the individual power amp has a driver amp and some preamps, it can happen that the gain variation for the significant internal temperature range (20° ... 90°C) will be about 1.5 ... 2 dB. This variation of output power can not be tolerated. Therefore the gain of the transmission path must be controlled.

The degradation of the phase shifters depends strongly on the circuit concept. For "Switched-line" phase shifters, the influence of temperature is very low (0.1 dB increasing loss, no notable phase error), but for "Vector modulator" phase shifters the phase error can become considerable.

Loaded-line phase shifter are also not severily temperature sensitive regarding the phase characteristic, but somewhat mor influenced than switched-line phase shifters considering the insertion loss (up to 1 dB in the temp. intervall 20° ... 90°C).

The degradation of the power T/R-switch is important, because it means loss of isolation to the receiving path of the module during the RF-duty cycle. To prevent an unsufficient isolation one must design some redundancy, which enhances the power consumption expecially in case of PIN-diode switches.

6. Evaluation of reliability data

As noted in section 4 not for all specific circuits of T/R-modules experienced failure rates or MTBF-figures are available. Especially in case of the power devices, subsequent modifications to improve the reliability are expensive and very time consuming. In summary however the reliability must be included a priori in the design and be proven in a pilot production.

To get reliability data of new products, stress tests at high temperatures are conventional. Based on the Arrhenius graphs (1) extrapolations of the reliability at the specific operation temperature can be made. But these extrapolated life times are expected values of the median life (MTF) and not of the mean time before failure (MTBF) during a substantial period before "wearout".

If we modify the well known "bath tube" curve, the two siginificant periods in the life span of a device after burn-in can be plotted as shown in fig. 6. Each of the three curves is related to a specific operation temperature. The first two (marked with T_1 and T_2) are stress tests results, but the third on is an extrapolation for the desired operation temperature T_x. By means of an Arrhenius graph the figures MTF_1, MTF_2 and MTF_x could be derived but not the significant τ_x, which marks the end of useful life and is a corner-stone for the evaluation of the MTBF.

In persuance of that idea, one must make two stress tests; the first with a small number of devices only to find MTF_1. The second one with a moderate number of samples (30 ... 35 pieces) to ascertain the moment of increasing failure rate around τ_2 and then the MTF_2-figure. If we have these data, it is easy to calculate the end of the useful time τ_x at the desired temperature by extrapolation of MTF_x with an Arrhenius graph and then insert it in the formula

Eq. (6)
$$\tau_x = \tau_2 \cdot \frac{MTF_x}{MTF_2} \quad (h)$$

For the sum of failures at <u>constant</u> rate up to a certain point of time τ, the following relation is valid

Eq. (7)
$$\Sigma f_i = N_O \{1 - \exp(-\tau\cdot\lambda)\}$$

with N_O = number of samples at the begin of the test (after burn-in) and λ= failure rate during τ.

If in the second test up to τ_2 n samples were defect (Σf_i=n) then there exists a good chance that at the temperature T_x up to the moment τ_x also n pieces will fail (fig.6). In praxi $\tau_x \cdot \lambda_x \ll 1$ is applicable, so that with formula (4)

Eq. (8)
$$\lambda_x \approx \frac{n}{\tau_x \cdot N_O} \{h^{-1}\}$$

and

Eq. (9)
$$MTBF_x \approx \frac{\tau_x \cdot N_O}{n} \{h\}.$$

Of course, with such approximations definite reliability figures are not available, but one can save money and time in avoiding wrong designs or not suitable technological processes before the mass production starts. This is extremely important for T/R-modules, because active PAR are military equipments with very big quantities of microwave circuits, so that production lines must have capacities comparable to the entertainment industry.

7. Conclusions

Power consumption is the limiting parameter of active PAR. The higher the frequency range the smaller the transmission power, however the progress in the efficiency of power devices opens a very promising future for them.

The packaging and reliability problems can be managed with high sophisticated design and technology so that the T/R-modules will meet expected performance and practical military requirements.

8. References

{1} Pool, W., Walshak, L.:
"A five-year quest to prove MW power transistor reliability"
Microwave & RF, July 1984, pp. 71 - 80.

{2} Wurnik, F., Pelloth, W.:
"Zuverlässigkeit von integrierten Schaltungen"
NTZ 37/1984, H. 11, S. 710 - 716.

{3} Cohen, E.D., Macpherson A.C., Christou, A.:
"Reliability of power GaAsFETs-Au gates and Au-Al linked gates"
IEEE Trans. on Microw. Theory and Techn.
Vol. MTT-29, No 7, 1981.

{4} Immorlica A.A.Jr.:
"Get a handle on power GaAs FETs"
Microwaves & RF, Feb. 1984, pp. 79 - 87.

{5} Pettenpaul, E.; Langer, E.; Huber, J.; Mampe, H.; Zimmermann, W.:
"Discrete GaAs Microwave Devices for Satellite TV Converter Front Ends"
Siemens-Forschungs- und Entw.Ber., Bd. 13/1984, Nr. 4, S. 163 - 170

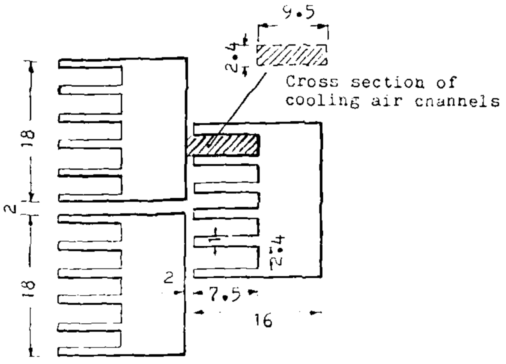

Fig. 1: Arrangement of T/R-modules in an array

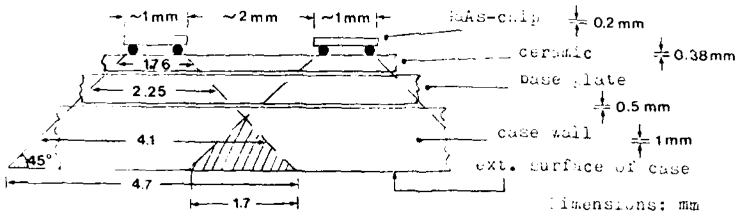

Fig. 2: Heat distribution paths from FET-chip to the module surface

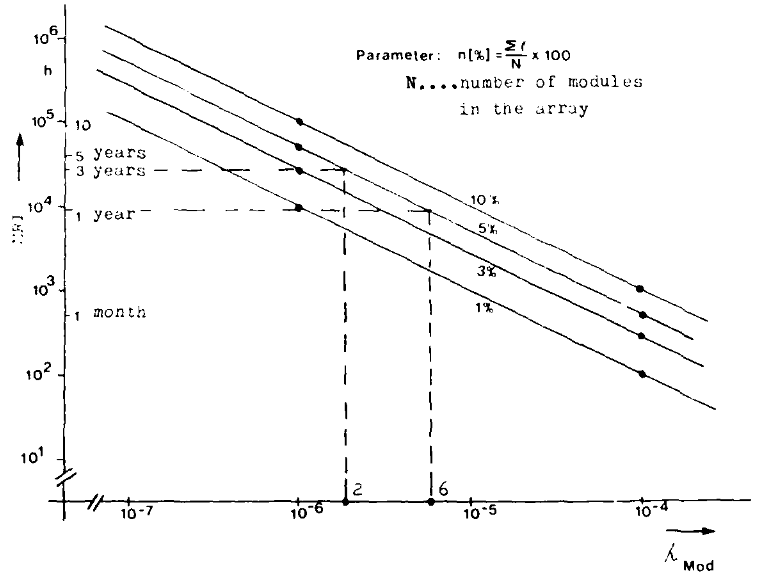

Fig. 3: Mean Repair Interval (MRI) vs module failure rate

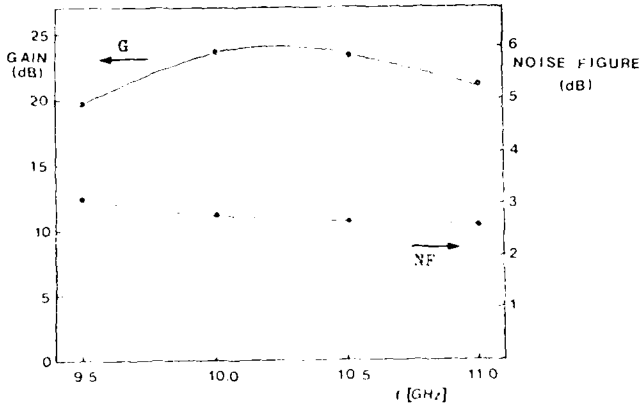

Fig. 4: Typical Gain and Noise Figure of monolithic 2-stage GaAs-LNA

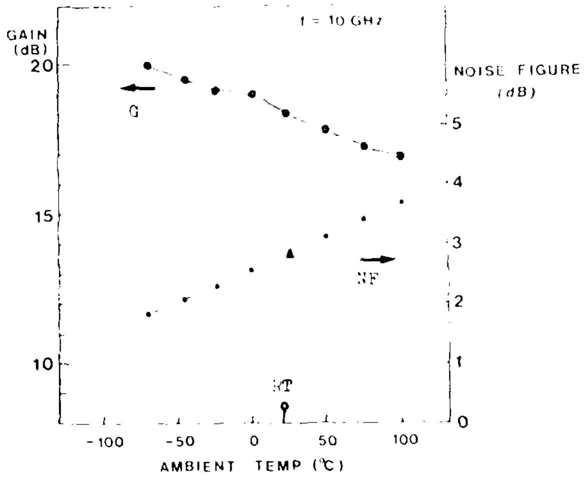

Fig. 5: Gain and Noise Figure of monolithic GaAs-LNA vs temperature

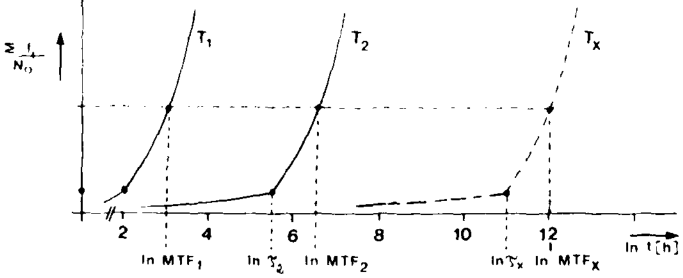

Fig. 6: Accumulation of failures vs logarithm of time

MMIC T/R MODULES FOR THE NEXT GENERATION AIRBORNE SURVEILLANCE PLATFORMS (U)

By: Edward J. Jones, Michael O. Little, Thomas A. McEwen,
R. Hunter Chilton, and Joseph P. Polniaszek

Rome Air Development Center/OCTP
Griffiss AFB, NY 13441-5700

Abstract

(U) Technology for a lightweight low cost transmit/receive (T/R) module for the next generation airborne surveillance phased array radar is described in this paper. The T/R module in an active phased array radar is a primary system cost driver; therefore, a low cost module had to be developed in order to make future phased arrays affordable. Monolithic Microwave Integrated Circuit (MMIC) technology is the technology being developed to fill the above requirement. MMIC technology is an approach wherein all the active and passive elements of the circuit and their required interconnections are formed on a single semiconductor material; e.g., gallium arsenide. MMIC technology appears to be ideal because of the inherent low cost involved with production of integrated circuits. The low production cost is due to the lack of manual handling and assembly, improved reliability, improved reproducibility, small size and weight, circuit design flexibility, and broadband performance.

1.0 Introduction (U)

(U) The requirement for lightweight, low cost transmit/receive modules for the next generation airborne surveillance platform was identified approximately five years ago. At that time, a system study pointed to the need for a large aperture phased array radar conformally fitted to the skin of an aircraft. This requires individual transmit/receive (T/R) modules at each radiating element. This requirement for T/R modules, coupled with other projected needs in ground-based tactical radars and space-based radars, provided the impetus to initiate a T/R module development program.

(U) A second study was conducted to summarize the needs of the various radar concepts that were under discussion. The study showed that there was a great deal of commonality between all of the active phased array concepts in terms of what is required for transmit/receive modules. With the exception of peak power and frequency, the modules were functionally identical. That is, they all require a multibit phase shifter, a low noise amplifier, and a low to medium power amplifier. Therefore, it was assumed that the same technology base could be used. In addition, all the concepts require a collocated controller for beam steering. The study also showed that for any of the system concepts the number of modules required is extremely large. Therefore, it was obvious that to meet the weight requirements and cost constraints, the modules needed to be extremely lightweight and very low cost.

(U) Monolithic Microwave Integrated Circuit (MMIC) technology is the technology being developed to meet the above requirement and is described in section 2. The advantages of using MMIC T/R module technology over the current methods of generating RF power is described in section 3. This paper also summarizes the future application of MMIC technology.

2.0 MMIC Technology and T/R Modules (U)

(U) Monolithic Microwave Integrated Circuit (MMIC) technology is an approach wherein all of the active and passive elements of the circuit and its required interconnections are formed on a single semiconductor material; e.g., gallium arsenide (GaAs), as shown in Figure #1. MMIC technology appears to be ideal to fulfill the above T/R module requirement because of the inherent low cost, improved reliability and reproducibility, small size and weight, circuit design flexibility, and broadband performance.

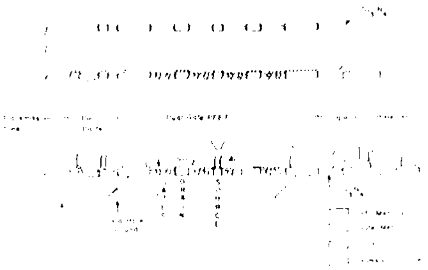

Figure #1 (U) MMIC Circuit on Gallium Arsenide

(U) Low cost, improved reliability, and reproducibility are derived from two areas: 1) inherent low cost involved with production of integrated circuits due to the lack of manual handling and assembly and 2) lack of a large number of wire bonds. Wire bonds have always been a serious problem in reliability and reproducibility for any microwave circuit. Furthermore, wire bonding is very labor intensive and, therefore, a significant cost factor in any microwave circuit. The elimination of a large number of wire bonds also eliminates undesired parasitics which limit broadband performance of conventional circuits.

(U) Small size and weight is an intrinsic property of the MMIC approach. Circuit integration is on a chip level, ranging from the lowest degree of complexity such as an oscillator, mixer, or amplifier, to a next higher functional block level; for example, a receiver front end or a phase shifter. A still higher level of circuit complexity, for example, a transmit/receive module, can be integrated onto a single chip. Large numbers of MMIC circuits are processed on a single 3 inch wafer, and large numbers of wafers are batch processed simultaneously. Cost is determined in part by the cost of wafer fabrication and circuit yield; the higher the circuit count per wafer and the higher the circuit yield, the lower the circuit cost.

(U) A T/R module, as shown in Figure #2, is composed of four basic functional blocks; i.e., a power amplifier, a low noise amplifier, a multibit phase shifter and a controller. By properly varying the relative amplitudes and phase of each T/R module in an array, it is possible to steer the direction of the radiated beam, and control the sidelobes of the antenna. Examples of MMICs developed to date for T/R modules are given below, and are by no means a complete set covering all frequency ranges and applications. The monolithic circuits shown are all at S-Band and because of the functional complexity of the chips, lumped-element circuit components have been used to minimize the size of the chips. This is required to maximize yield and minimize cost.

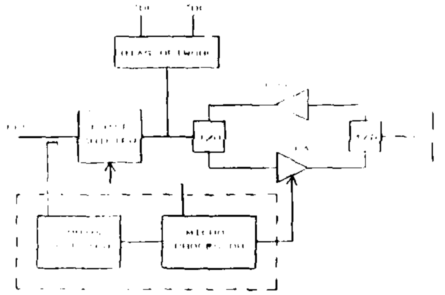

Figure #2 (U) Block Diagram of T/R Module

(U) A phase shifter circuit consisting of four cascaded bit sections with phase shifts of 22.5, 45, 90, and 180 degrees is shown in Figure #3. The switching action is provided by 14 GaAs MESFET passive switch devices with one micron gate lengths and a total of 13.2mm of gate periphery. The only DC bias required is the gate control voltages with a total current of less than 50 microamps for the chip, which is due to gate leakage only. The two low order bits, the 22.5 and 45 degree sections, are lumped-element loaded lines with switched reactive loading to produce the phase shift steps. The two high order bits, the 90 and 180 degree sections, use the FET device to switch between high-pass or low-pass lumped-element sections which provide either a phase lead or lag for the phase shifting action. The fabricated chip size is 3.5mm by 2.8mm.

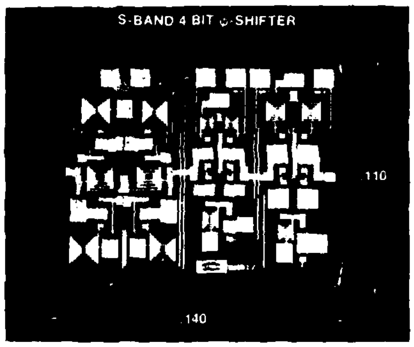

Figure #3 (U) MMIC Phase Shifter

(U) A medium power amplifier consisting of a three-stage amplifier integrated with the T/R switches and bias networks on the chip is shown in Figure #4. The FET devices have gate lengths of two microns with a total gate periphery of 4.1mm. The matching circuits use lumped-element spiral inductors and metal-insulator-metal (MIM) capacitors and incorporate the T/R switching networks at the input and output of the amplifier, all on a chip that is 3.7mm by 3.2mm. This chip has about 20dB of gain across a 10% bandwidth, with about 0.5 watts of output power.

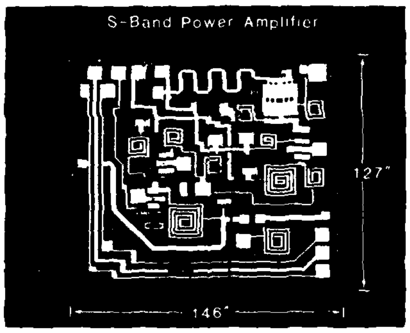

Figure #4 (U) MMIC Medium Power Amplifier

(U) A low noise amplifier, shown in Figure #5, consists of a three-stage amplifier with T/R switches like the power amplifier. This chip uses FET devices with gate lengths of one micron with a total gate periphery of 3.6mm. The T/R switches are similarly integrated into the lumped-element matching circuits on a chip that is 4.1mm by 2.5mm. This circuit has about 22dB of gain across a 30% bandwidth with a noise figure of about 4dB.

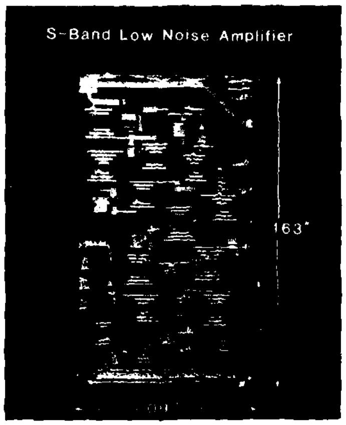

Figure #5 (U) MMIC Low Noise Amplifier

(U) A higher power amplifier chip, as shown in Figure #6, can be added to the medium power amplifier chip to increase module output power. This chip has a power FET with two micron gate lengths and total periphery of 12mm. The matching circuitry on the chip uses lumped-element MIM capacitors and inductors which, because of the low impedances, are short transmission lines. The circuit is fabricated on a chip that is 2.8mm by 3.2mm and has about 7dB of gain at power output of 5 watts.

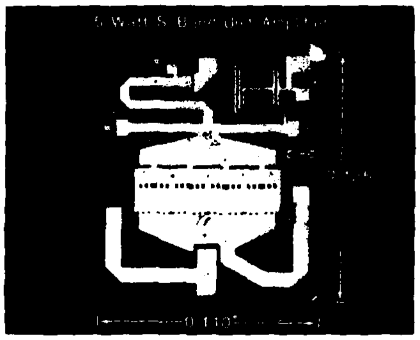

Figure #6 (U) MMIC Power Amplifier

(U) These chips have been assembled into medium-power and high-power T/R modules. The transmit mode microwave performance for the prototype high-power module is shown in Figure #7 at 1dB gain compression. The receive mode performance is shown in Figure #8.

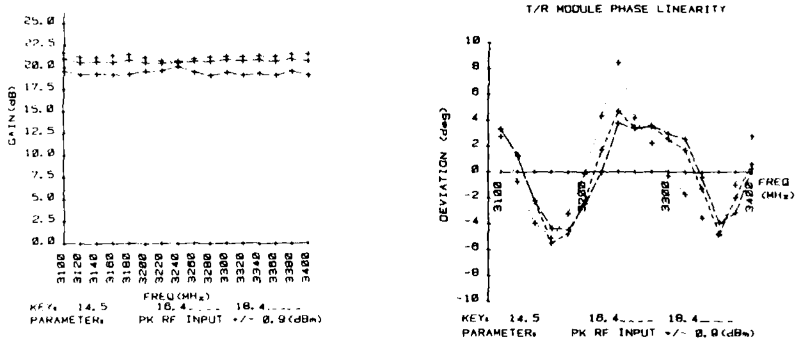

Figure #7 (U) Module Performance In Transmit Mode

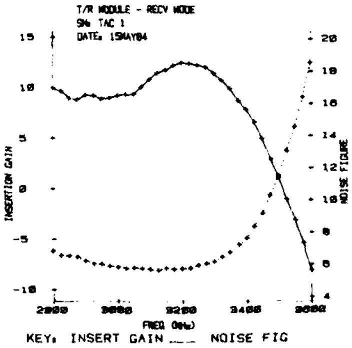

Figure #8 (U) Module Performance In Receive Mode

3.0 MMIC Impact On Surveillance Platforms (U)

(U) The current airborne surveillance system (E3A) employs two parallel RF amplification chains driving a corporate fed passive phased array which has a radiant to prime power efficiency of about 10%. The RF signal (RF excitation) from the STALO is amplified through each chain which consists of three stages of amplification: a predriver, a driver, and a high-power amplifier. A traveling wave tube (TWT) is used for the driver stage and a klystron tube is used for the high-power amplifier. The prime power distribution system provides both DC and 3-phase high voltage, which of course is all derived from aircraft power. The system's low efficiency is primarily due to three areas: 1) high RF power losses in the beam forming network of the corporate feed, 2) high RF power loss in the combining network of the two amplification chains, and 3) the power required for the transmitter environmental controls and cooling system within the corporate feed network.

(U) In comparison, an active phased array employing MMIC T/R modules conformally fitted to the skin of an aircraft has a radiant to prime power efficiency of about 20%. This means that for a given radiated power the active phased array uses less prime power. This translates to a lower rate of fuel consumption for the same mission, which allows more time on station for the surveillance platform.

(U) Further, overall system performance can be improved by using an active phased array. By having the T/R module very close to the antenna the detection ability of the system will increase by several dBs. This is due to the module's high gain low noise amplifier being introduced into the front-end of the receiver chain, well before the high loss incurred in the beam forming network. This translates into detection of smaller targets and/or increasing radar range. Another performance advantage that an active phased array has over the current system is the ability to electronically steer the radiated beam, thus, giving the operator the ability to look longer in the high threat areas; obvious advantages.

(U) Another obvious advantage that conformally fitted MMIC T/R module approach has over the current radome technique is less overall drag on the aircraft. This also translates to a lower rate of fuel consumption for a given mission.

4.0 Conclusions And Future Application (U)

(U) RADC has developed the first 1 through 4 GHz lumped element MMIC circuits for radar T/R modules. These circuits are now starting to find their way into other microwave systems as well; e.g., Global Positioning System (GPS), Direct Broadcast Satellite (DBS), and microwave instrumentation. However, significant work still needs to be accomplished before these MMIC chips are placed into an operational system. To date, the MMIC world has concerned itself primarily with the technical aspects of producing the chips; i.e., designing for microwave performance. However, the item that will determine the future of MMICs is total cost of a finished unit. Total cost of a finished unit can be broken down into four major areas: 1) chip design, 2) fabrication, 3) assembly (i.e., packaging), and 4) testing in all phases of fabrication. The total time to produce a MMIC unit needs to be shortened also. At present, it takes somewhere between 6-7 months to design and fabricate a given chip; this needs to be reduced to 1-2 months to be cost effective. At the present time, about 2/3 of the total cost of a unit is in assembly and testing throughout the fabrication to final testing stage. This is a common problem for any microwave circuit and requires significant effort to reduce this cost driver. Another area that requires a great deal of work is in the reproducibility of MMIC circuits from wafer to wafer and from lot to lot. Two areas that are just now beginning to be addressed are: 1) reliability of MMICs, and 2) radiation effects on the performance of these circuits. These are two very important areas that need to be addressed before MMIC circuits are placed in space. In conclusion, it is obvious that MMICs are starting to become available for system use, but a lot of effort still needs to be accomplished before they are as common as a transistor.

(U) It is apparent that MMIC technology will have a profound impact on airborne surveillance systems in the future. This impact will be from an economical point of view by making active phased arrays less costly, increasing their efficiency, and by increasing system performance and flexibility due to the electronically steered beam.

References (U)

1. R. H. Chilton, "MMIC Module For SBR (U)", Ninth DARPA Strategic Space Symposium, Monterey, CA, October 1983, SECRET.

2. I. R. Selin, J. P. Sasonoff and D. N. Jessen, "S-Band Radar Transceiver Module With Monolithic GaAs Circuits (U)", Tenth DARPA Strategic Space Symposium, Monterey, CA, October 1984, UNCLASSIFIED.

DISCUSSION

Y.Brault

When do you foresee the implementation of active phased array antennas on the airborne fire control radar operating at X-band?

Author's Reply

People at Wright Patterson AFB are working on similar modules for S-band. It depends, however, on the development of appropriate technologies and is, therefore, difficult to predict.

K.Solbach

(1) What is really holding back the introduction of active T/R module arrays?

(2) What is the module price objective?

Author's Reply

(1) High cost for hybrid T/R-modules.

(2) We are looking for a $100 module; the price has to drop at least below $500.

Blinston

Is your figure of 20% efficiency a prediction or an achievement?

Author's Reply

Achieved.

L.Daouphars

How do you cope with EMP in a system when the RF elements are exposed to the energy without benefit of waveguide cut-off as in conventional systems?

Author's Reply

We are working on the problem.

R.G.Cuthbert

In modules where several active devices are employed do you need to carry out manual trimming or do you accept mismatches? If it is the latter case, what kind of yield do you achieve of an acceptably matched module which includes several active elements?

Author's Reply

Mismatch between circuits has been very low. Yield has been between 20–40% on most chips.

LOW-COST, MONOLITHIC BEAMFORMING COMPONENTS FOR RADAR

Paul H. Carr, Scott W. Mitchell and Richard T. Webster
Electromagnetic Sciences Division
Rome Air Development Center
Hanscom AFB, MA, 01731, USA

ABSTRACT

Planar, monolithic technology offers the possibility of lowering the cost of beamforming components, which contribute significantly to the high price of phased array radars. The most immediate opportunity for planar technology could be to replace the costly ferrite phase shifters in current use. PIN diode phase shifters have the advantage of faster switching times (sub-microsecond) than ferrites and the disadvantage of slightly higher insertion loss, which is due to the fact that microstrip is inherently more lossy than waveguide. Low cost PIN phasers can be fabricated by monolilthic technology or automated, robotic hybrid thick-film techniques.

Monolithic phase shifters on GaAs have typical losses of 6 dB and power handling capabilities under a watt. This eliminates them from consideration as replacements for ferrite phasers in the corporate fed arrays considered above. New research results on reducing this insertion loss will be presented. The insertion loss is not critical if the phase shifter is followed by an efficient power amplifier. The French have reported on MISFET amplifiers on InP with 33% power added efficiency and a power output at 9 GHz of 4W/mm gate width, which is more that twice that of the best GaAs MESFET. These MISFETs unfortunately had unstable silicon dioxide gate insulators, and researach is continuing in the U.S. to improve this.

Monolithic technology is especially attractive at mm-wave frequencies, due to the smaller component size and the minimization of parasitics. Results on 44 GHz phase shifters will be presented.

Electronically variable time delay rather than phase shift is required for low-sidelobe phased arrays having wide instantaneous bandwidth. Monolithic SAW tapped delay lines on GaAs will be described for use at center frequencies under 1 GHz. Above 1 GHz, magnetostatic wave devices are capable of continuous variable time delay over a 40 nsec range.

ANTENNE A BALAYAGE ELECTRONIQUE AEROPORTEE POUR AVION D'ARME DES ANNEES 90

par

C.Chekroun
S.E.R.
Avenue de l'Atlantique
91942, Les Ulis
France

RESUME

Une antenne à Balayage Electronique 7 Bits a ete mise au point dans nos laboratoires.

Les possibilités de couverture angulaire importante (cone 70°), les performances radioélectriques (diffus inférieurs à − 15 dBi) et la bande de frequence de cette antenne, permettent de l'envisager pour le radar multifonction air-air des années 90.

On décrira dans une première étape l'antenne et on en donnera quelques résultats en bande X.

EHF MULTIFUNCTION PHASED ARRAY ANTENNA

Klaus Solbach
AEG-Telefunken
Radio & Radar Systems Group
Box 1730, D-7900 Ulm
Fed. Rep. Germany

Abstract

It is our conviction that now it has become possible to produce full-scale phased array antennas for modern fighter aircraft using conventional microwave integrated circuit (MIC) techniques at a price compatible with the budget for the envisioned application. Mainly to achieve the goal of realistic price level for the antenna several options have been chosen in the design of our demonstration EHF Multifunction-Phased Array Antenna: Both, the radiating elements and the phase-shifter circuits are realized on microstrip substrate material in order to allow photolithographic batch fabrication. Self-encapsulated beam-lead PIN-diodes are employed as the electronic switch elements to avoid expensive hermetic encapsulation of the semiconductors or complete circuits.

A space-feed using a horn-radiator to illuminate the array from the front-side is found to be the simplest and most inexpensive feed. The phased array antenna thus operates as a reflect-array, the antenna elements employed in a dual role for the collection of energy from the feed-horn and for the re-radiation of the phase-shifted waves (in transmit-mode).

The antenna is divided into modules containing the radiator/phase-shifter plate plus drive- and BITE-circuitry at the back. Both drive- and BITE-components use "gate-array" integrated circuits especially designed for the purpose. Several bus-systems are used to supply bias and logical data flows to the modules.

The beam-steering unit utilizes several signal processors and high-speed discrete adder circuits to combine the pointing, frequency and beam-shape information from the radar system computer with the stored phase-shift codes for the array elements. Since space, weight and power consumption are prime considerations only the most advanced technology is used in the design of both the microwave and the digital/drive circuitry:
The PIN-Diodes are driven with quite low forward currents, the logical circuitry contains custom-made high-speed CMOS-IC's and the BITE circuit can be switched off to consume power only if a test cycle is started.

BASIC CHARACTERISTICS OF FM-CW RADAR SYSTEMS

By

Ir. L.P. Ligthart, ir. L.R. Nieuwkerk, ir. J.S. van Sinttruyen
Delft University of Technology
Dept. of Electrical Engineering
P.O. Box 5031
2600 GA DELFT
The Netherlands

1. INTRODUCTION

Due to rapid technological progress in real-time signal processing, FM-CW radar systems are expected to become a more serious competitor to pulse radar systems.

This paper deals with basic radar principles such as modulating waveforms and ambiguity functions characteristics. Advantages and disadvantages of FM-CW radar systems are compared to pulse radar systems.

The inherent signal processing used in FM-CW radar systems allows a flexible choice of system parameters. In this context aspects like sensitivity, range and velocity resolution are discussed.

It is elucidated that the use of digital processors for signal processing (frequency determination, filtering, etc.) offers the possibility to exchange dedicated hardware solutions with software implementations.

Attention is paid to equipment like the antennas, diplexer, transmitter and receiver, and to isolation problems between transmitter and receiver.

Results of an experimental FM-CW research radar are shown. In addition, the future prospects of FM-CW radar, with the aerial and solid-state r.f. head-end integrated, are indicated.

2. AMBIGUITIES IN PULSE- AND FM-CW RADAR

When determining target range and target range rate by means of simultaneous measurements an inevitable ambiguity exists, dependent on the characteristics of the transmitted signal u(t). By selecting waveform parameters f.i. in favour of good range precision performance a fine is paid in either range rate precision or self generated clutter or both. This ambiguity is mostly described by the ambiguity function $\chi(\tau,\omega)$:

$$\chi(\tau,\omega) = \int_{-\infty}^{\infty} u(t)u^*(t+\tau)e^{-j\omega t}dt \quad \text{where:}$$

τ - delay time ($\tau = 0$ is the time the target return arrives)
ω - Doppler frequency (target range rate)
$*$ - complex conjugate

It is noted that $\chi(\tau,\omega)$ represents the output of an optimal matched filter receiver.

In this paragraph some examples of ambiguity functions will be shown for different transmitted waveforms having a rectangular envelope in common. Attention will be paid to conventional pulse signals as an extreme, via chirp signals to FM-CW signals as another extreme. In the examples shown delay time, Doppler frequency and repetition time are normalized with respect to the width d of the rectangular envelope:

τ_n normalized delay time - τ/d
ω_n normalized Doppler frequency - $\omega d/2$
T_n normalized repetition time - T/d (T repetition time)

```
Time-frequency product        -    0.
Normalized repetition time -    1.
# of pulse repetitions        -   1
Constant Doppler frequency -    0.
```

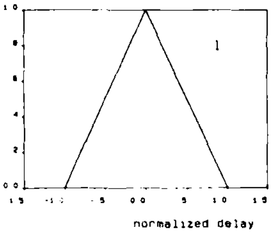

```
Time-frequency product        -    0.
Normalized repetition time -    1.
# of pulse repetitions        -   1
Constant delay                -    0.
```

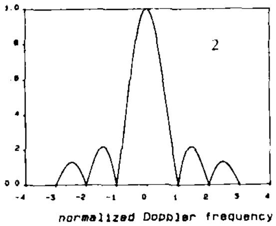

```
Time-frequency product        -   100.
Normalized repetition time -     1.
# of pulse repetitions        -    1
Constant Doppler frequency -     0
```

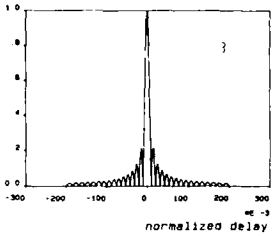

```
Time-frequency product        -   100.
Normalized repetition time -     1.
# of pulse repetitions        -    1
Constant delay                -     0.
```

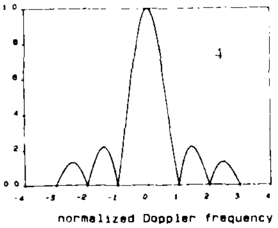

```
Time-frequency product        -   100.
Normalized repetition time -     1.
# of pulse repetitions        -    1
Constant delay                -        .005
```

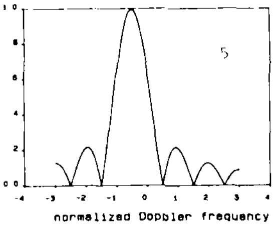

```
Time-frequency product        -   100.
Normalized repetition time -     1.
# of pulse repetitions        -    1
Constant delay                -        .01
```

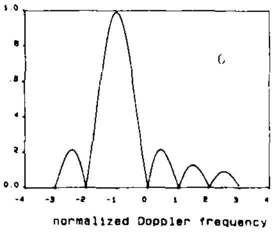

```
Time-frequency product        -   100.
Normalized repetition time -     2.
# of pulse repetitions        -    1
Constant Doppler frequency -     0.
```

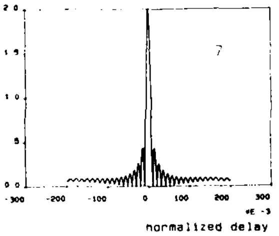

```
Time-frequency product        -   100.
Normalized repetition time -     2.
# of pulse repetitions        -    1
Constant delay                -     0.
```

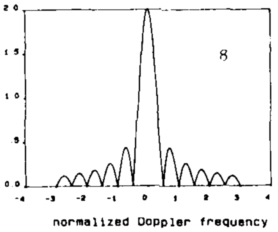

```
Time-frequency product        -   100.
Normalized repetition time -     2.
# of pulse repetitions        -    1
Constant delay                -        .005
```

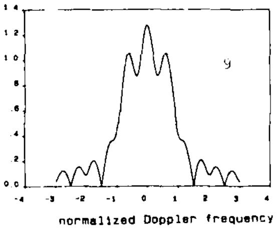

```
Time-frequency product        -   100.
Normalized repetition time -     2.
# of pulse repetitions        -    1
Constant delay                -        .01
```

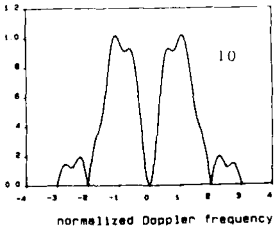

```
Time-frequency product        -    0.
Normalized repetition time -    10.
# of pulse repetitions        -   16
Constant Doppler frequency -     0.
```

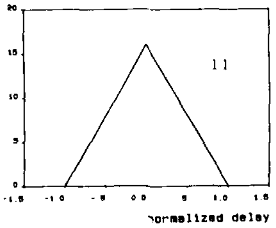

```
Time-frequency product        -    0.
Normalized repetition time -    10.
# of pulse repetitions        -   16
Constant Doppler frequency -     0
```

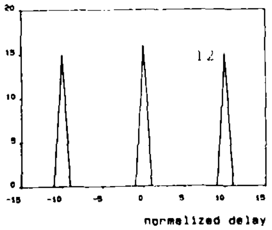

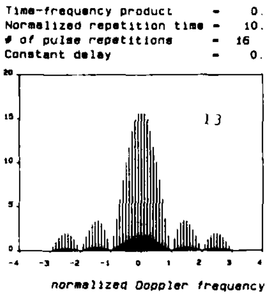

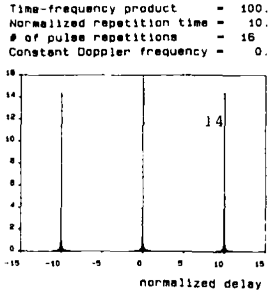

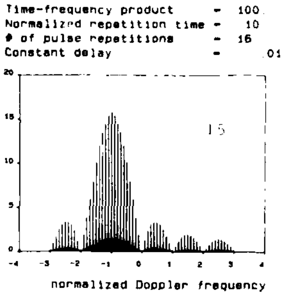

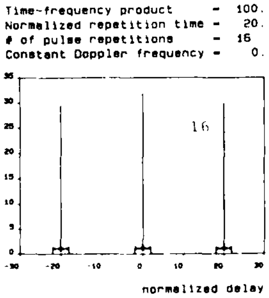

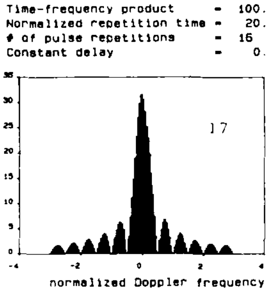

Figures 1 thru 10 show ambiguity functions for basic nonrepetitive waveforms whereas figures 11 thru 17 show the effects of waveform repetition. Figures 1 and 2 show $\chi(\tau_n,0)$, i.e. the absolute value of the autocorrelation function, and an orthogonal cut $\chi(0,\omega_n)$ for a "no-chirp" pulse. The triangular form of $\chi(\tau_n,0)$ directly results from the correlation process of a rectangular pulse with width 1. If the pulse width d is shortened the non-normalized $\chi(\tau,0)$, describing the uncertainty in range measurement, is "compressed", improving range measurement precision, as $\chi(0,\omega)$ is widened resulting in impaired range rate measurement precision. In adding linear frequency modulation the ambiguity function $\chi(\tau,\omega)$ is changed to a sheared version $\chi(\tau,\omega+2p\tau)$ with 2 pd being the time-bandwidth product (100 in the examples) In figure 3 showing $\chi(\tau_n,0)$ over the sub-interval (-0.2,0.2) it is shown that range measurement precision is increased (due to the increase in spectral width) at the expense of the introduction of a vast number of sidelobes. Range rate measurement precision for various range delays (figures 4 thru 6) is almost not changed relative to the "no-chirp" case. In comparing figures 4 thru 6 it is noted that the shape of the ambiguity function is nearly independent of range delay, the only effect being a shift in the ambiguity function position. This range delay-Doppler coupling is caused by the shearing effect for large time-frequency products. Figures 7 thru 10 show similar results for a triangular frequency modulated pulse. The pulse width is doubled relative to previous examples as the pulse consists of a superposition of two modulated pulses with an up and down sweep respectively, resulting in improved range rate measurement precision (fig. 8). Hence $\chi(\tau_n,\omega_n)$ consists of two sheared contributions, resulting from each individual pulse, and cross terms. The latter cross ambiguity functions build a pedestal (fig. 7) for the former sheared ambiguity functions. Figures 8 thru 10 show that range delay-Doppler coupling no longer exists in the triangular case (as a consequence of the double shearing) and a delay parameter dependent shape of the ambiguity function results. Figure 10 clearly shows separate contributions of the sheared functions, figure 9 interaction and figure 8 coincidence as the value of the range delay parameter is diminished.

As the transmitted pulse is repeated in a coherent way the following effects in relation to measurement precision occur. In the range delay domain the original ambiguity function (figure 11 for a "no-chirp" pulse) is repeated at integral multiples of the repetition time (figure 12) thus giving rise to "second time round" ambiguities which occur when the repetition time is chosen smaller than radar range delay. Moreover as a result of repetition a

$\sin[(N-k)\omega_n T_n]/\sin(\omega_n T_n)$ where N- number of repetitions
k- integer $0 \leq k < N$

weighting occurs in the Doppler domain related to "blind" range rate of targets (figure 13). A a consequence of the coherency the main lobe of the ambiguity function narrows and its amplitude becomes greater (pre-detection matched filter integration) both linearly dependent on the number of pulse repetitions. Figures 14, 15 show similar effects for a linear frequency modulated chirp radar and figures 16, 17 for the case of triangular frequency modulation, the pedestal being particularly clear in figure 16.

In choosing the repetition time equal to the pulse width the ambiguity function for a FM-CW radar is obtained. The number of pulse repetitions (sweeps) can be directly related to FFT requirements for Doppler data processing (§ 4.2). Figures 18 thru 20 show ambiguity functions for a "sawtooth" FM-CW radar system whereas figures 21 and 22 give similar functions for a triangular FMCW radar system.

Time-frequency product = 100.
Normalized repetition time = 1.
# of pulse repetitions = 16
Constant Doppler frequency = 0.

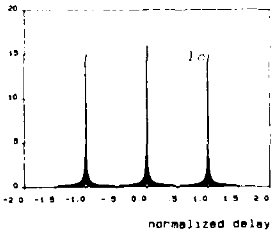

18

Time-frequency product = 100.
Normalized repetition time = 1.
# of pulse repetitions = 16
Constant delay = 0.

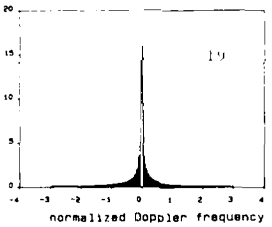

19

Time-frequency product = 100.
Normalized repetition time = 1.
# of pulse repetitions = 16
Constant delay = .01

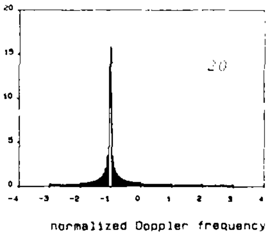

20

Time-frequency product = 100.
Normalized repetition time = 2
# of pulse repetitions = 16
Constant Doppler frequency = 0

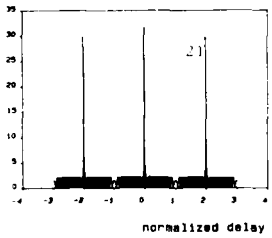

21

Time-frequency product = 100.
Normalized repetition time = 2.
# of pulse repetitions = 16
Constant delay = 0.

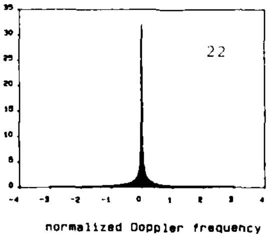

22

3. COMPARISON BETWEEN FM-CW AND PULSE RADAR SYSTEMS

3.1 Principles of operation and assumptions

In figure 23 the fundamental principles of FM-CW and pulse radar are shown. The following assumptions have been made:

FM-CW radar - There is a linear frequency sweep
- no amplitude modulation
Pulse radar - There is no chirp

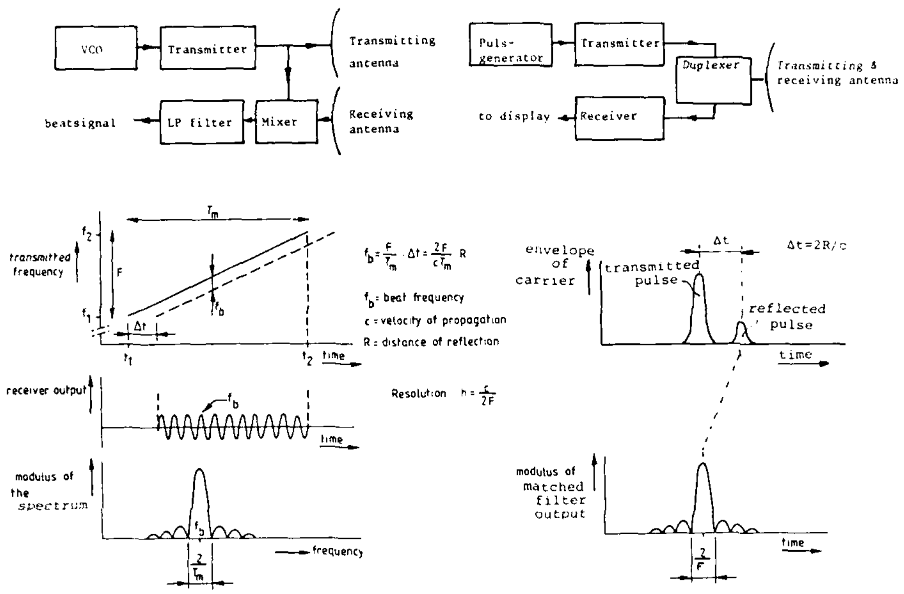

Figure 23 Principles of FM-CW and Pulse radar

3.2 Differences, similarities, advantages and disadvantages of both radar principles

- Transmitter

Due to the continuous wave feature of FM-CW the mean transmitted power equals the peak transmitted power, while with the pulse radar the peak power is dependent on the average power, pulse length and pulse repetition frequency. FM-CW radar allows therefore to have a low voltage power supply and a compact transmitter unit, furthermore the rf component of the transmitter can be integrated with the antenna feeder system, hence true solid state FM-CW radar is feasible.

The frequency generating source of FM-CW radar has to be highly linear with low FM-noise and low amplitude modulation in order to produce the required range and velocity resolution. With pulse radar strict requirements are needed for low frequency jitter to obtain the accurate Doppler data.

- Receiver

An inherent characteristic of the FM-CW receiver unit is the matched filter. To obtain a matched filter receiver in a pulse Doppler radar is far more complicated. When using a zero - if mixer a loss of 3 dB in signal / noise ratio occurs, a price to pay in this case for simplicity. As the FM source in the FM-CW radar is used also as a local oscillator the transmitter and receiver can be easily integrated. CW radarsystems have the disadvantage of high isolation between transmitter and receiver in order to prevent saturation of the receiver, on the other hand low minimum range is obtainable.

- Antennae

In order to obtain the already mentioned high isolation between transmitter and receiver special attention has to be paid to the design of the antennae. One solution uses separate antennae for transmitting and receiving. Gain requirements result in larger antennae constructions for the FM-CW radar case relative to pulse radar.

- Signal processing equipment

Frequency establishment in FM-CW radar is part of the matched filter receiver and has to be performed before even range data is obtained. This can be done by fast digital computers or dedicated hardware using fast fourier transforms. Having powerful signal processors additional tasks can be easily performed at the same time, such as Doppler processing, calculation of power spectra, logarithms, averaging etc. Exercises with data obtained from the radar can be processed in order to suppress clutter, to update calibration and to enhance picture quality.

The spread spectrum characteristic of the FM-modulated signal must be emphasised which is not the case with a simple pulse radar. In addition security can be obtained by applying further frequency agility in the center frequency.

3.3 Comparison between a conventional pulse Doppler radar and a competitive FM-CW radar

In the table below the parameters of a FM-CW radar and a pulse Doppler radar with nearly equal performance are listed.

	Pulse radar		FM-CW radar
Central frequency		9 GHz	
Range resolution		100 m	
rf bandwidth		1,5 MHz	
maximum unambiguous range		35 km	
average transmitted power	50 W		1 W
peak transmitted power	50 kW		1 W
pulse/sweep repetition frequency		1500 Hz	
minimum RCS at maximum range	50 m^2		10 m^2
antenna gain		33,5 dB	
isolation transmitter-receiver	-		50 dB
minimum range	2 km		0,2 km
maximum unambiguous Doppler velocity		240 km/hr	

The differences between a conventional pulse radar and a FM-CW radar demonstrate the advantages of FM-CW radar with the exception of the isolation requirement and consequences. It is assumed that pulseradar is well-known and therefore in the next table some examples of a FM-CW radar are given with different system parameters.

Example	1		2	
parameter				
frequency excursion	2	MHz	12	MHz
sweep time	0,6	ms	0,6	ms
sample frequency	1,365	MHz	8,192	MHz
# of points FFT	1024		6144	
max. unambiguous velocity	40	km/hr	240	km/hr
minimum RCS	10	m^2	10	m^2

A typical set up of a FM-CW radar configuration is shown in figure 24.

To get the required radar performance extensive signal processing is necessary, for this eason an array processor and a video display processor connected to a host computer are needed.

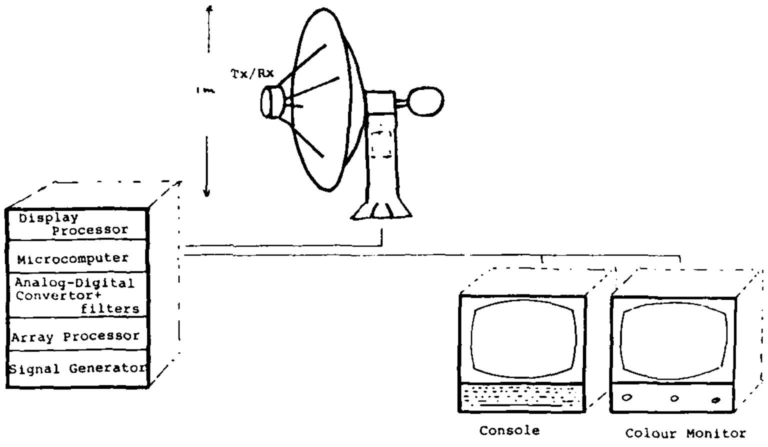

Figure 24 Typical set up of a possible FM-CW radar configuration

4. FM-CW signal processing

4.1 Basic signal processing requirements

To carry out signal processing of the received FM-CW radar data we start with the radar equation for separate transmitting and receiving antennae. The averaged received power becomes:

$$\overline{P_r} = \frac{P_t G_t G_r \lambda^2}{(4\pi)^3 R^4} \sigma ,$$

where P_t and P_r are transmitted and received power, G_t and G_r are gains in the specific directions to the radar target, R is radar target distance and σ the radarcrosssection of the target to be measured. In case the two beams of the separate antennae are not fully coincident the radar equation has to be modified. This takes place close to the radarsite and is depending on the mutual spacing between the two antennae. As a rule of thumb it can be said that for radar distances larger than A^2/λ the radar equation can be considered to be similar with the equation for the monostatic case, where A is the maximum size of the combination of the two antennae.

The target is characterised by its geometry which determines the radar crosssection, its distance and velocity. The radarcrosssection can be described by its amplitude, frequency, phase, velocity spectrum and polarization properties. A quantitative analysis can be done only by a multiparameter radar with sensitive calibration.

To do so different types of radar signal processing have to be performed like processing for:
- calibration
- range
- Doppler
- polarization
- clutter suppression
- picture enhancement

4.2 Possible signal processing approach

The processing for calibration of the radar can be distinquished into absolute calibration by means of standard reflectors with known radarcrosssection. At Delft a rotating planar reflector is used for this purpose. The known reflectivity pattern of the rotating reflector allows the suppression of unwanted reflections from its surroundings. Relative calibration can be obtained by using a delayline which creates an artificial target. Real-time monitoring indicates changes in the system parameters except for the antennae, environment and atmosphere. This can be done in an interleaved mode with normal radar operation.

A second relative calibration makes use of the wide band thermal noise of the preamplifier of the receiver and can therefore be seen as a relalative calibration receiver. To get range and Doppler information the different techniques have been reported [1]. For range only information a fast fourier transform is applied to a single sweep and for range- and Doppler information fast fourier transforms are applied to consecutive sweeps. Beside the fast fourier transform other methods based on parameter estimation like ARMA and Pisarenko methods have been published, but have not been performed up till now due to impredictable side effects.

Polarization processing requires the availability of polarizers in the antenna structure. Separate transmitting and receiving antennae allow separate polarizers to measure the full polarization matrix continuously with one receiver only under the condition that measurements for different polarizations can be done within the decorrelation time of the target. This feature enables differentiation on a polarization basis between different targets c.q. unwanted reflections (clutter).

Real-time polarization processing necessitates a fast processor, due to the limited decorrelation time and the derivation of the six polarization coefficients that characterize the target.

For clutter syppression use can be made of the correlation of succeeding measurements of the radarcrosssection or the already mentioned polarization properties.

The availability of computer equipment needed to perform the processing functions can at the same time be used to execute programs for picture enhancement. Algorithms like time filtering, spatial filtering, windowing, averaging, noise- and clutter suppression can be set up.

5. FM-CW HARDWARE

5.1 Microwave hardware

To produce pencilbeams parabolic reflector antennae are in use. When two antennae have to be used large dimensions are the consequence. The pattern requirements are similar to those of pulse radar antennae. Long line effects have to be omitted as well as possible to avoid amplitude modulation over the used frequency band. Matching circuitry is needed at the ends of long microwave transmission lines. These types of problems can be avoided by full integration of transmitter and receiver in one aerial under the condition that sufficient isolation between transmitter and receiver can be obtained to prevent saturation of the receiver.

Solid state frequency generating sources with good phase noise performance, solid state power amplifiers and solid state low-noise amplifiers are available. When special attention is paid to the if circuitry 3 dB lower thermic noise figure can be obtained in comparison with the simple zero if receiver.

5.2 Intermediate frequency hardware

Introducing an intermediate frequency much larger than the frequency excursion the if circuitry can be used for relative calibration but also to analyse non-linearities in the sweep, amplitude modulation and parasitic noise. By using a coaxial cable as delay line whereby the delayed signal is fed into the receiver an artificial target is generated for this analysis.

The choice of using an intermediate frequency is inspired by the gain in signal to noise ratio and also by the availability of stable frequency generating sources at lower frequencies and of other signal processing hardware like steerable amplifiers, attenuators, couplers etc.

5.3 Low frequency hardware

Depending on the maximum frequency in the beatsignal the low frequency hardware has to be adjusted. We distinguish the gain envelope of the zero if amplifier in the receiver to correct for spatial extension of the radar waves, the filters to avoid aliasing, the sample frequency for the analog to digital convertor, the number of bits in the adc to get the wanted dynamic range and the computer hardware. A special role has to be fulfilled by the timing generator which takes care of all the needed signals in the radar to obtain coherency.

To visualize the processed data a quasi real time quick look monitoring is essential. The beatsignals that include all received data can be collected on an analog instrumentation recorder for further use.

6. RESULTS WITH THE DELFT ATMOSPHERIC RESEARCH RADAR

In this paragraph we show some results of clutter maps, Doppler velocity spectra of rain and polarization properties of a single target. The measurements have been carried out with DARR described in literature [2].

DARR has a transmitting antenna with a diameter of 4.28 m and a receiving antenna with a diameter of 2.12 m. The transmitted power during the measurements shown is 1 Watt. The sweep time was chosen to be 2.5 ms so that the maximum unambiguous Doppler velocity becomes 9m/s. Other relevant radar parameters selected are given in the figures. The first radar pictures (figure 25) show the cluttermap in the surroundings of Delft with elevation angles 0° and $4,13^{\circ}$ and at different maximum range. The strong reflections from nearby clutter are reduced by processing taking into account the R^4 law of discrete targets. To visualize the large dynamic range we use a colour scale instead of a grey scale. Every displayed sector consists of averaging 16 consecutive power spectra to improve clutter to noise ratio. At an elevation of 0° and a maximum range of 15 km we see the reflection from discrete targets with a displayed dynamic range of 30 dB. The lowest reflectivity value can be chosen. The transmitted power was ¼10^{-3} Watt. For an elevation of 4.13° and a maximum range of 15 km it is seen from the figure the influence of the side lobes of the antennae resulting in circular arcs. The dynamic range has been reduced to 20 dB while the transmitted power is increased to 1 Watt. For 0° elevation and a maximum range

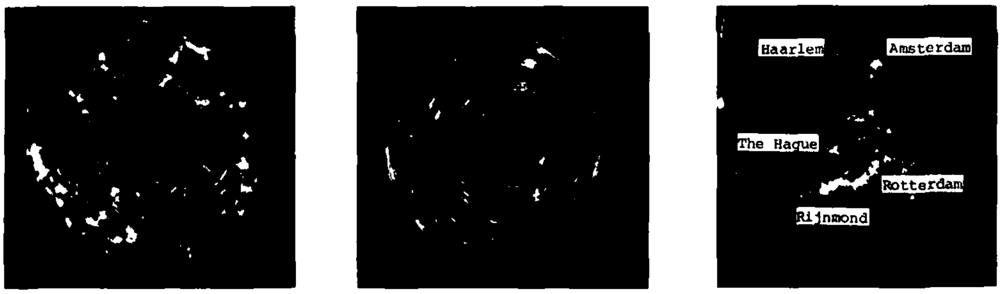

a) Elevation 0°, Range 15 km b) Elevation 4.13°, Range 15 km c) Elevation 0°, Range 75 km

Figure 25 Clutter maps of the surroundings of Delft of 75 km figure 25 C is obtained ($P_t = 10^{-2}$ Watt). The cities Amsterdam and Haarlem, the coast and Rijnmond can be distinguished.

As a result of high resolution Doppler measurements we show figure 26, which is computed from reflectivity data obtained with the radar looking to zenith. Because the sweep time is less than the decorrelation time of rain, rain reflectivity cannot be considered as clutter and therefore raindrop fall velocity spectra can be measured. The processed data consist of reflectivity as function of height, the mean Doppler velocity, the Doppler spectrum width and the skewness in the Doppler spectra. Results of this can be used to determine the rain drop-size distribution.

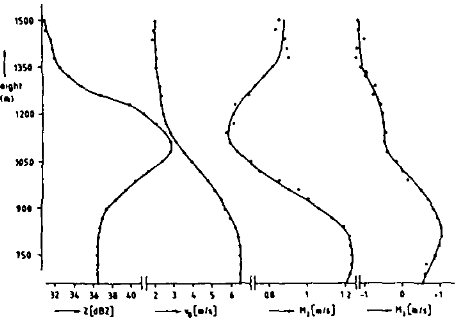

Figure 26 Spectral moments of rain measured with DARR. P_t=1 Watt, h = 30 m [1]

When two polarizers are used in DARR both steered sinusoidally but in opposite sense over angles ±45° we have situations that the transmitted and received polarizations are the same and there exist situations that the polarizations differ 90°. In figure 27 the polarization dependency of a tower some 1100 m away is given as a function of the difference in polarization angle.

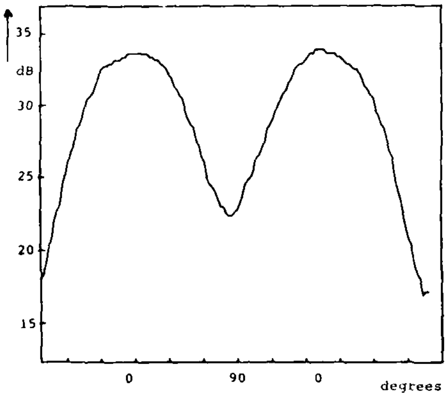

Figure 27 Received power as function of polarization angle difference

CONCLUSION

In this paper attention has been paid to coherent FM-CW radar system parameters, their similarities and differences with coherent pulse radars. On the basis of matched filter analysis we show two dimensional ambiguity functions in range and in Doppler domain for a pulse radar, a pulse radar with FM chirp during the pulse and the FM-CW radar. We illustrate that the coherent pulse radar and the FM-CW radar are at both ends of the generalized concept of a pulse radar with FM-chirp. Most simple pulse radar systems are not of the matched filter type while inherently to the FM-CW radar principles the FM-CW radar receiver can be considered in this way. This means that in this circumstance the FM-CW radar can be advantageous as far as transmitted power, minimum range and sensitivity is concerned. A disadvantage can be the required isolation between transmitter and receiver. Different from pulse radar systems is the signal processing of the radar data coming from a FM-CW radar. This is caused by the fact that range and Doppler processing has to be done in the frequency domain. Additional processing for calibration, windowing, polarimetry, clutter suppression and picture enhancement is discussed based on experiences obtained with the Delft Atmospheric Research Radar (DARR). Real time signal processing in this radar is a research item in itself and requires real time radar system management as well to keep the radar parameters under computer control. The advantage of this approach is the flexibility in the FM-CW radar as is shown by different experiments in which the radar has been reconfigurated by software only.

The hardware needed to build FM-CW radar systems allows the thought that solid state powerful radar systems can become reality. Results with DARR show its capabilities concerning high range resolution, Doppler processing, cluttermaps and polarimetry.

REFERENCES

1. L.P. Ligthart, L.R. Nieuwkerk, J.S. van Sinttruyen:"FM-CW Doppler Radar Signal Processing for Precipitation Measurements". Proc. of the 22nd Conference on Radar Meteorology, Zürich, Switzerland, september 1984, pp. 538 - 543
2. L.P. Ligthart, L.R. Nieuwkerk: "FM-CW Delft Atmospheric Research Radar", Proc. IEE, Vol 127, Pt.F, No 6, December 1980, pp. 421 - 426

VISUALISATION RADAR
CONVERSION DE BALAYAGE : DÉFAUTS ET TECHNIQUES D'AMÉLIORATION

PAR
JEAN-CLAUDE BARON
THOMSON-CSF / DIVISION A.V.S.
178 BD GABRIEL PÉRI - 92240 MALAKOFF - FRANCE

RESUME

Les informations vidéo-radar en sortie des circuits de traitement sont naturellement en coordonnées polaires. La présentation de ces informations sur un écran nécessite un stockage préalable dans une mémoire dîte "mémoire de la carte radar" ou "mémoire d'image".

Dans de nombreux cas, une organisation de la mémoire d'image en coordonnées cartésiennes est intéressante car elle permet :

- d'effectuer facilement certains traitements radar,
- de compenser les mouvements du porteur (en translation),
- d'être d'accès direct pour une présentation de l'image en mode télévision.

La conversion de balayage, qui permet d'inscrire la vidéo-radar présente en coordonnées polaires, dans la mémoire, architecturée en coordonnées cartésiennes, peut engendrer des defauts dont les plus évidents sont :

- la perte d'informations radar pour des distances proches,
- une image avec des zones noires pour les distances les plus grandes.

Les techniques qui permettent de supprimer ou de compenser ces défauts sont basées sur :

- une harmonisation entre les paramètres radar et ceux de la mémoire d'image,
- des techniques de traitement au niveau des points mémoire ou au niveau des pixels de l'image,
- des techniques de remplissage par interpolation.

1 - INTRODUCTION

Les dispositifs de présentation des informations radar, réalisés avec des tubes rémanents ou des tubes à mémoire sont progressivement remplacés par des sytèmes de visualisation présentant l'information sur des tubes cathodiques classiques noirs et blancs ou couleurs.

L'utilisation de ces tubes nécessite l'utilisation de circuits électroniques pour la mise en forme et la memorisation des informations.

La qualité des images obtenues dépend des choix effectués au niveau de l'architecture des circuits électroniques et au niveau du mode de balayage de l'écran. Ces choix sont d'autant plus critiques que l'image correspond à une carte radar très dense, telle que, par exemple, une carte du sol dans le cas d'un radar aéroporté.

Dans de nombreuses applications, pour des raisons qui ne sont pas données dans le présent exposé, le balayage de l'écran est effectué en mode "télévision". Le signal radar en sortie des circuits de traitement est délivré sous forme "polaire". La conversion de balayage, qui permet de transformer les coordonnées polaires du radar en coordonnées cartésiennes de la télévision, est effectuée par les circuits électroniques dit "de conversion de balayage et de mémorisation". Cette conversion de balayage engendre des défauts qui nuisent à la qualité de l'image et qui peuvent dégrader les performances du radar.

Le but du présent exposé est de situer les paramètres de la conversion de balayage, de mettre en évidence les défauts qui en découlent et de proposer des techniques qui permettent de les supprimer ou de les compenser.

2 - ARCHITECTURE GENERALE DES CIRCUITS DE CONVERSION DE BALAYAGE (planche N° 1)

Les circuits de conversion de balayage sont architecturés autour d'une mémoire principale qui permet de stocker une carte radar complète. La carte radar est l'ensemble des informations reçues par le radar pendant un cycle du balayage de l'antenne.

Les circuits d'écriture effectuent l'inscription du signal vidéo-radar dans la mémoire principale. Le calcul des adresses des points à inscrire dans la mémoire constitue la conversion de balayage proprement dite (planche N° 2).

Les circuits de lecture délivrent un signal vidéo-composite compatible avec le balayage télévision de l'écran ; le contenu de la mémoire est lu à cadence suffisante pour assurer une présentation sans scintillation (50 ou 60 Hz ou plus).

3 - CHOIX DES CARACTERISTIQUES DES CIRCUITS DE CONVERSION DE BALAYAGE

Les caractéristiques des circuits seront évaluées dans un cas bien précis d'application. L'adaptation des résultats à d'autres cas pourra être effectué le plus souvent par simple transposition.

Le radar est un radar aéroporté qui observe le sol vers l'avant :

- le mode de fonctionnement est la cartographie,

- le secteur balayé par le faisceau couvre un domaine qui a été limité à plus ou moins 60 degrés,

- le signal vidéo est délivré, après traitement, sous forme échantillonnée, récurrence par récurrence. Le rang de l'échantillon dans la récurrence donne la distance,

- la position angulaire du faisceau (gisement) est fournie par le calculateur du radar par l'intermédiaire d'un bus.

Le module écran est du type moniteur de télévision :

- il peut être noir et blanc ou couleur/shadow-mask,

- ses dimensions sont relativement faibles pour permettre son intégration dans une planche de bord,

- un balayage de 512 lignes de 512 points (pixels) est suffisant pour effectuer une couverture homogène de l'écran,

- la résolution propre de l'écran est moins bonne que celle qui correspond à une ligne ou à un point de la ligne ; cette résolution n'est donc pas dégradée par le choix du nombre de lignes et de points par ligne.

3.1. Choix de la capacité de la mémoire

La résolution de la mémoire ne doit pas être inférieure à celle de l'écran. Il en résulte que la capacité minimale de cette mémoire doit être de 512 x 512 points.

Le nombre de bits par points dépend du type d'application. Ces bits contrôlent la luminance et la chrominance des pixels du tube :

- en monochrome le nombre de bits peut être compris entre 3 et 8 (souvent 4 bits),

- en couleur, 3 ou 4 bits peuvent être affectés à la chrominance et 3 à 8 pour la luminance.

La capacité de la mémoire de 512 x 512 points peut être augmentée pour mettre en oeuvre dans de bonnes conditions des fonctions telles que :

- agrandissement d'une partie de l'image pour mieux visualiser certains détails (zoom),

- décentrement pour découvrir une zone située en dehors de l'écran,

- rémanence,

- etc.

Dans tous les cas, la capacité de la mémoire est dimentionnée pour que, après mise en oeuvre de la fonction agrandissement ou décentrement etc, la partie de la mémoire correspondant à ce qui est présenté sur l'écran ait une capacité de 512 x 512 points.

3.2. Paramètres des circuits d'écriture

Les circuits d'écriture reçoivent le signal vidéo radar sous forme échantillonnée récurrence par récurrence.

Les paramètres à prendre en compte sont :

- le nombre N d'échantillons pour la distance D à présenter sur l'écran,

- l'écart angulaire $\Delta\theta$ entre deux récurrences successives,

- la précision et le bruit sur la valeur de la direction θ des récurrences,

- la précision des calculs de la transformation de coordonnées.

Les principaux défauts qui apparaissent à l'écriture sont :

- la perte d'information qui se produit lorsque plusieurs échantillons sont inscrits dans la même cellule mémoire. Sans traitement particulier, seule la dernière information inscrite est conservée. Plusieurs types de traitements sont possibles parmi lesquels la conservation du "plus grand" ou la conservation de la moyenne. Ces traitements sont dits "traitement points",

- les points mémoires non adressés ; sans traitement particulier, ces points restent vides et donnent des pixels noirs ou gardent le contenu inscrit au balayage précédent.

L'analyse géométrique de l'opération d'écriture montre que :

- le nombre d'échantillons en distance doit être au moins égal au nombre N de points mémoires sur un rayon, soit :

$$N > 512$$

- l'écart angulaire maximal doit permettre d'inscrire deux points mémoires consécutifs en limite d'écran soit, un écart $\Delta\theta$ de :

$$1/512 \approx 2 \text{ milliradians} \approx 0{,}1 \text{ degré}$$

Ces valeurs de N et de $\Delta\theta$ seront prises comme référence dans la suite de l'exposé.

3.3. Circuits de lecture

Les circuits de lecture délivrent le signal vidéo composite dans un format compatible avec les standards de télévision.

La lecture de l'ensemble de la mémoire est effectuée à la même cadence que celle du renouvellement de l'image sur l'écran. Cette cadence peut être du 25 ou du 30 Hz comme dans la télévision grand public mais, pour supprimer les phénomènes de scintillation, il est préférable de monter à 50 ou 60 Hz.

En principe, la lecture n'introduit pas de défauts mais, l'ensemble, composé des circuits de lecture et de l'écran TV peut engendrer des défauts d'aspect si la bande passante des circuits n'est pas suffisante. Les figures 1, 2 et 3 de la planche N° 3 montrent que le niveau de luminance voulu n'est atteint de manière satisfaisante pour un point isolé que si la bande passante est 2 à 3 fois supérieure à la cadence de répétition des points.

Des circuits de traitement peuvent être associés aux circuits de lecture pour atténuer les conséquences des défauts créés par la conversion de balayage. Ces traitements sont de type filtrage ou filtrage spacial ; des exemples de ces traitements sont donnés dans la suite de l'exposé.

4 - MISE EN EVIDENCE DES DEFAUTS

Les caractéristiques qui sont prises en compte pour juger de la qualité de la carte radar sur l'écran sont les suivantes :

- taux de remplissage après un balayage,

- qualité de la restitution des formes,

- absence de perte d'informations,

- qualité visuelle de l'image.

Les images représentées sur les planches suivantes permettent de mettre en évidence les défauts.

Planche N° 4 : image mettant en évidence le taux de remplissage après un balayage. Les points noirs qui apparaissent sont ceux qui n'ont pas été adressés par la transformation de coordonnées.

Planche N° 5 : signal vidéo radar dont les échantillons sont alternativement à "1" ou à "0". Si la restitution était bonne, l'image devrait être composée de cercles concentriques.

Planche N° 6 : signal vidéo dont les échantillons sont alternativement deux "1" suivis de deux "0". Les cercles plus épais et plus espacés que sur la planche N° 5 sont représentés convenablement (les points manquants ne sont pas très visibles).

Planche N° 7 figure 1 : signal vidéo dont les échantillons sont alternativement un "1" suivi de quinze 0. L'analyse fine montre des cercles "troués" vers les grandes distances et vers 45 degrés.

Planche N° 8 figure 1 : signal vidéo composé alternativement de deux récurrences à "1" suivies de deux récurrences à "0".

Planche N° 9 figure 1 : une recurrence à "1" et quinze récurrences à "0".

Pour ces deux dernières planches, la restitution des formes est loin d'être satisfaisante.

5 - INFLUENCE DES PARAMETRES, TECHNIQUES D'AMELIORATION

5.1. Influence du traitement point

Lorsqu'un même point mémoire est adresse plusieurs fois, sans traitement particulier, seul le dernier échantillon inscrit est conservé et donc, les autres echantillons sont perdus. Les traitements qui peuvent être appliques au niveau du point mémoire pour éviter cet inconvénient sont :

- conserver l'échantillon ayant la plus grande amplitude,

- effectuer la moyenne des échantillons.

L'utilisation de l'un ou l'autre de ces "traitements point" depend de la nature du signal. Dans ce qui suit, seule l'influence du traitement "le plus grand" est analyse.

Le traitement point est sans action sur le taux de remplissage, mais, son effet est fondamental pour un radar car, il permet de ne pas perdre les echantillons de plus fortes amplitudes. Les effets du traitement "le plus grand" sont également tres nets sur la qualité de la restitution des formes ; cet effet est mis en evidence sur les figures 2 des planches 7, 8 et 9 qui sont à comparer aux figures 1 des mêmes planches.

5.2. Influence du nombre N d'échantillons en distance

Les courbes de la planche N° 10 donnent le pourcentage de points non adressés par rapport au nombre total de points dans la mémoire :

- dans le cas de référence, avec un écart angulaire de 0,1 degré entre récurrences (courbe N° 4), le taux de remplissage est bon pour N = 512 et devient 100 % à partir de 700 points,

- pour un écart angulaire de 0,05 degré, 512 points sont suffisants (courbe N° 5),

- pour des écarts angulaires plus grands que 0,1 degré (courbes N° 1, 2 et 3) il n'est pas possible d'obtenir un taux de remplissage de 100 % quel que soit le nombre N d'échantillons.

Les courbes de la planche N° 11 indiquent la répartition des points non atteints en fonction de la direction de pointage θ pour différentes valeurs de N. La zone la plus mauvaise est située à 45 degrés (par suite de la symétrie de l'image, autour de 0, seule la partie droite est analysée, avec extension du domaine balayé jusqu'à 90°).

Le nombre d'échantillons réels dont dispose le radar en sortie du traitement doit être adapté au nombre d'échantillons nécessaires pour obtenir une bonne image, l'adaptation peut se faire :

- si le nombre est a priori trop petit : en suréchantillonnant ou en répétant plusieurs fois une même information,

- si le nombre est trop grand : soit effectuer l'adaptation directement dans les circuits d'écriture grâce au traitement "le plus grand", soit effectuer un regroupement préalable.

Le meilleur procédé pour obtenir une bonne carte radar est d'adapter la résolution radar et la résolution de l'écran. Il ne sert à rien dans un mode donné d'avoir une résolution radar très supérieure à celle de l'écran. L'analyse des courbes des planches 10 et 11 montrent que :

- un nombre d'échantillons en distance égale au nombre de points mémoire donne déjà des résultats satisfaisants,

- augmenter le nombre de points radar par un suréchantillonnage dans un rapport entre 1 et 1,4 améliore sensiblement ces mêmes résultats,

- au-delà d'un rapport 1,4 le suréchantillonnage n'apport plus rien.

5.3. Influence de l'écart angulaire $\Delta\theta$

Le taux (en %) de points non inscrits en fonction de l'écart angulaire est donné sur les courbes de la planche 12. Les différentes courbes correspondent à différentes valeurs du nombre N d'échantillons. Ces courbes confirment que pour $N < 512$ (courbes 1, 2,3) quel que soit $\Delta\theta$, la quantité de points non inscrits n'est pas tolérable.

La courbe 4 qui correspond au cas de référence avec $N = 512$ montre que les performances s'améliorent quasi linéairement entre l'écart de référence de 0,1 degré et l'angle moitié ; diminuer l'écart au-delà de cet angle de 0,05 degré n'apporte plus d'amélioration sensible.

Les courbes de la planche 13 montrent que, pour une surface élémentaire donnée, à une distance donnée, le plus grand nombre de points non inscrits est situé dans la direction à 45 degrés (voir remarque § 5.2. planche 11).

La résolution angulaire du radar est constante ; pour les radars connus cette résolution, quasi constante en fonction de la distance, est située, en ordre de grandeur, entre 0,1 degré et quelques degrés. La résolution angulaire vue au niveau de l'écran est directement proportionnelle à la distance ; cette résolution tient à des *critères objectifs mais également* à des critères visuels plus subjectifs. Dans les meilleures conditions, c'est-à-dire avec $N > 700$ points et $\Delta\theta < 0,05$ degrés, la résolution peut être estimée à :

- 0,12 degré pour les distances les plus grandes (planche 14, couples de rayon au pas de 2 degrés avec un espace entre rayons de 0,12 degré),

- 0,25 degré (en moyenne) à mi-distance (planche 15 : couples de rayons au pas de 2 degrés avec un espace entre rayons de 0,25 degré),

- 1 degré au 2/10 de la distance maximale.

La position angulaire du faisceau, prise en compte pour les calculs de transformation de coordonnées, est :

- donnée sous forme numérique donc est quantifiée,

- issue de mesure et de calculs donc est affectée d'un bruit.

La quantification et le bruit doivent être pris en compte pour l'évaluation de l'écart angulaire maximal. Par exemple, si la position angulaire θ est donnée en 14 bits avec une précision de ± 1/2 LSB, un écart angulaire théorique $\Delta\theta$ de 0,088 degré (4 LSB) sera en fait équivalent, vis-à-vis de la qualité de l'image à un écart de 0,1 degré.

6 - AMELIORATION DE LA QUALITE DE L'IMAGE PAR FILTRAGE

La quantification de l'image en lignes et en points, au niveau de l'écran proprement dit et au niveau des circuits de mémorisation, donne une image dont la texture est nécessairement granuleuse. Cet effet est plus ou moins visible suivant la manière dont est effectuée la conversion de balayage et également suivant la nature de l'image. L'effet de granulation est assez sensible sur les surfaces à faible gradient de variation de luminosité et, les effets de la quantification sont très marqués sur les contours à formes géométriques (lignes droites, cercle, etc.).

Un des procédés les plus efficaces pour réduire ces effets consiste à effectuer un filtrage spatial de l'image. Les figures des planches 14 et 15 donnent des exemples de l'effet de tels filtrages. Le filtre utilisé effectue une convolution spatiale "3 x 3" de type passe bas.

7 - CONCLUSION

Les écrans de visualisation de type télévison étant imposés dans de nombreux systèmes, il est nécessaire d'effectuer une conversion pour adapter le balayage en rotation (polaire) du radar au balayage en translation (cartésien) de l'écran. Cette conversion qui, dans le principe, ne peut être effectuée sans dégradation de la qualité de l'image peut cependant donner des résultats très satisfaisants si les circuits électroniques qui effectuent l'adaptation sont convenablement paramétrés. Les principales conditions à respecter pour obtenir de bons résultats sont :

- de dimensionner la mémoire de la carte radar de manière à utiliser au mieux les performances de l'écran soit :

  . un nombre de lignes mémoire égale au nombre de lignes du balayage,

  . un nombre de points par lignes supérieur au nombre de points par lignes sur l'écran (entre 1 et 1,4),

  . que la capacité mémoire définie ci-dessus ne concerne que la partie présentée sur l'écran, indépendamment des mémoires nécessaires pour effectuer des zoom ou des décentrements,

- d'adapter les signaux video radar avant de les transférer dans la mémoire de telle manière que :

. le nombre d'echantillons en distance soit au moins égal au nombre de points memoires correspondant à la même distance ; le cas optimal étant le rapport 1,4,

. l'écart angulaire entre deux récurrences successives soit supérieur à l'angle permettant de passer d'un point à la plus grande distance au point suivant à la même distance. Des ameliorations réelles sont constatées jusqu'à un rapport 2.

- d'effectuer un traitement au niveau du point mémoire. Ce "traitement point" permet de ne pas perdre des informations indispensables pour la détection radar et importantes pour la restitution des formes. Les traitements les plus simples consistent à garder le plus grand échantillon ou à effectuer la moyenne, des échantillons vidéo inscrits dans le même point mémoire.

Enfin, une amélioration sensible de la qualité visuelle peut être apportée par un filtrage spatial passe bas de la carte contenue dans la memoire, avant de la présenter sur l'écran.

Dans un avenir proche, la généralisation des ecrans à haute resolution associés à des memoires de grande capacité permettra d'éliminer les conséquences des derniers défauts résiduels dus à la conversion de balayage.

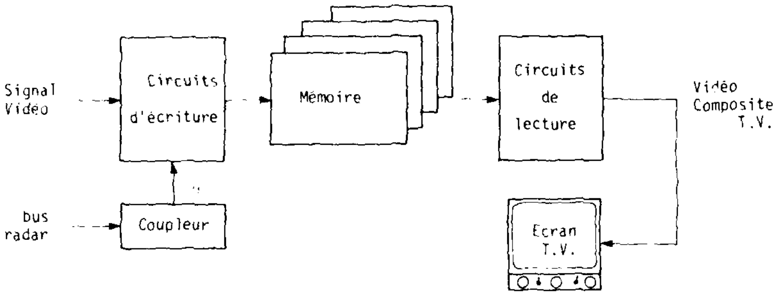

Planche 1

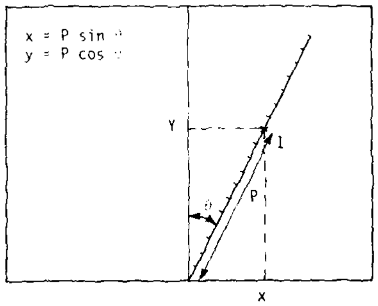

Planche 2

Point isolé

Points accolés

Figure 1 : bande passante insuffisante

Point isolé

Points accolés

Figure 2 : bande passante juste suffisante (bande adaptée)

Point isolé

Points accolés

Figure 3 : bande passante optimale

Pour une certaine ambiance lumineuse extérieure, la partie hachurée représente la luminance effective des points.

Planche 3

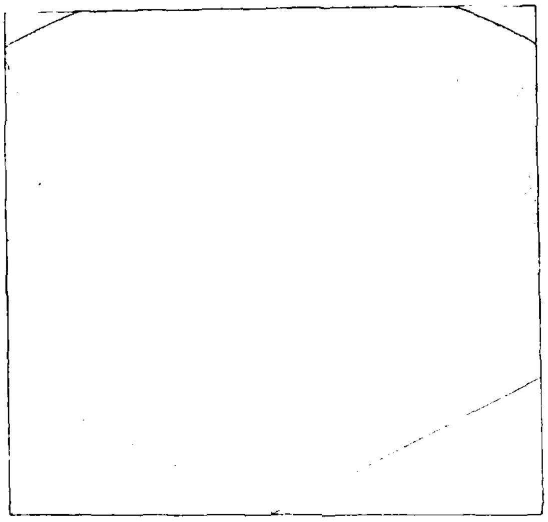

Planche 4

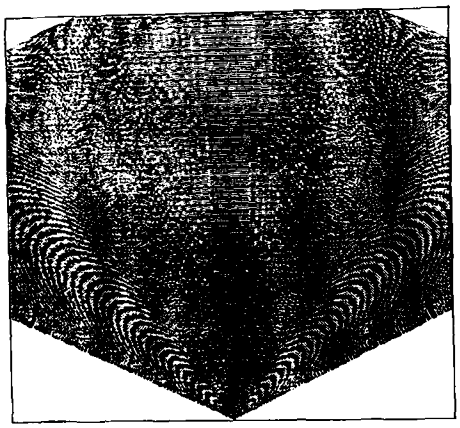

Planche 5

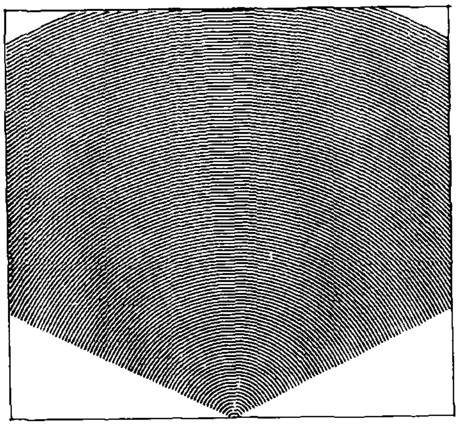

Planche 6

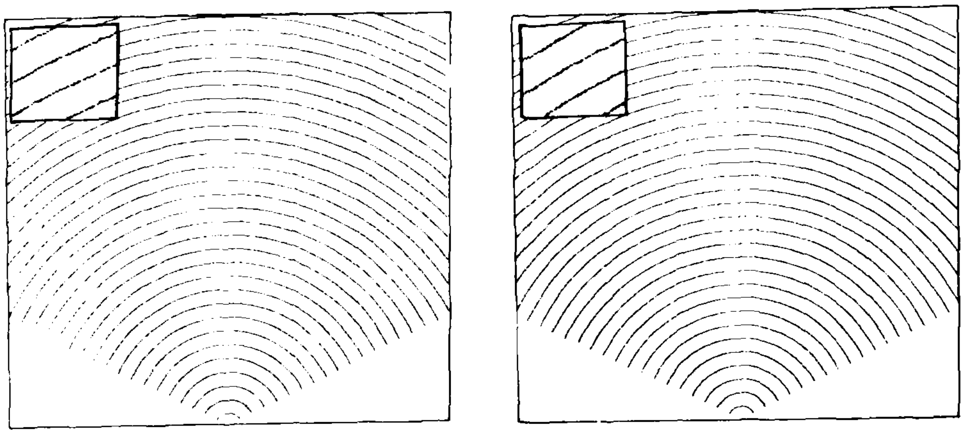

Figure 1

Figure 2

Planche 7

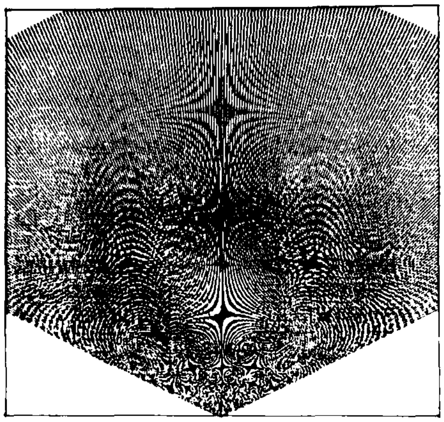

Figure 1

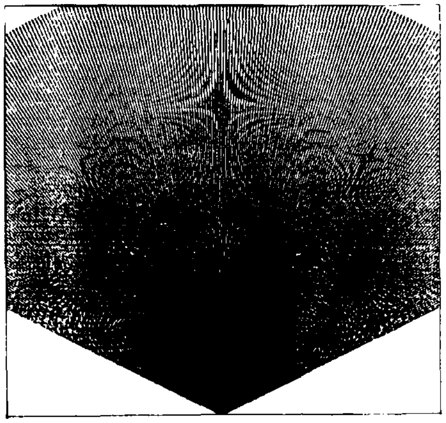

Figure 2

Planche 8

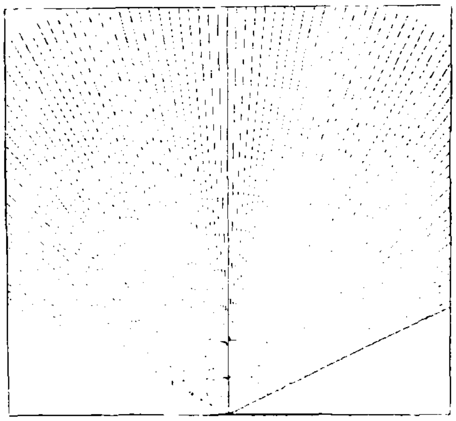

Figure I

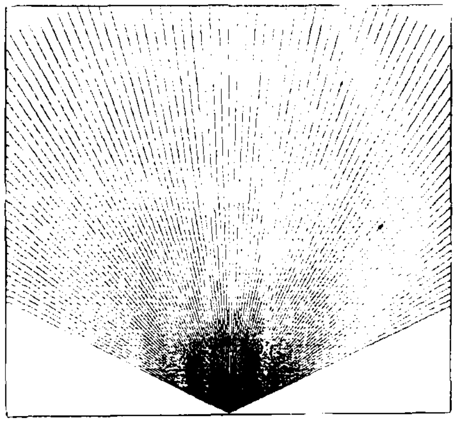

Fiqure 2

Planche 9

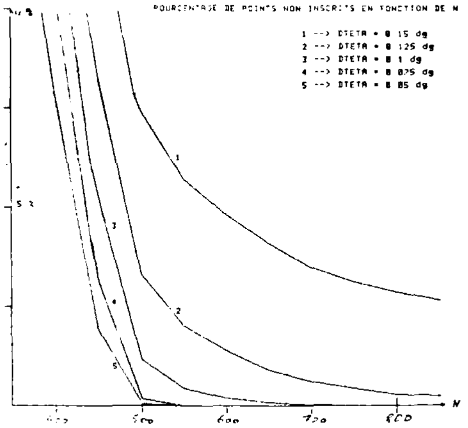

Planche 10

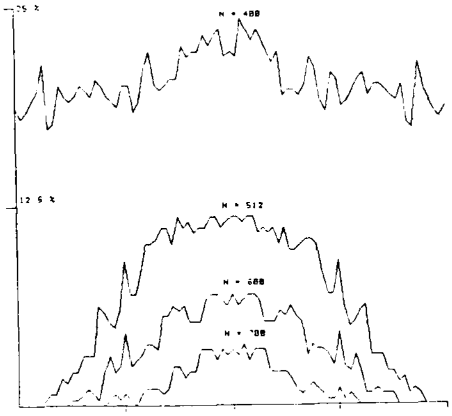

Planche 11

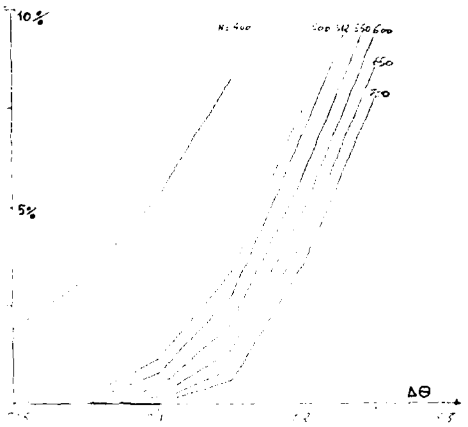

Planche 12

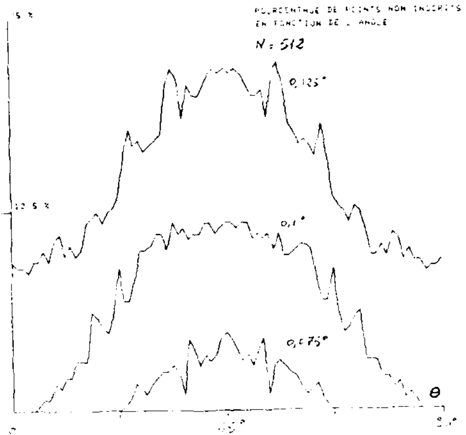

Planche 13

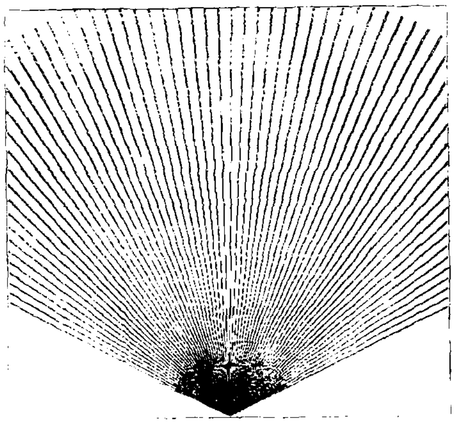

Planche 14

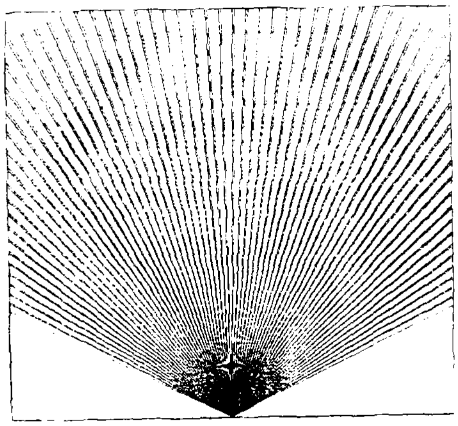

Planche 15

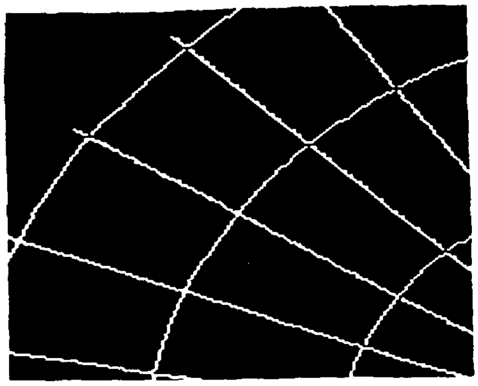

sans filtrage

Planche 16

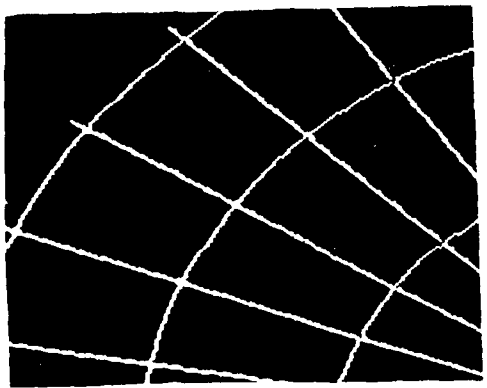

avec filtrage

Planche 17

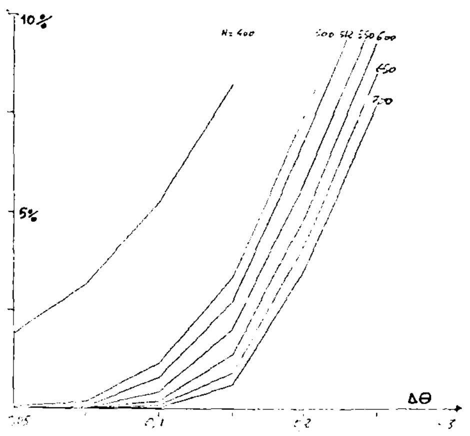

Planche 12

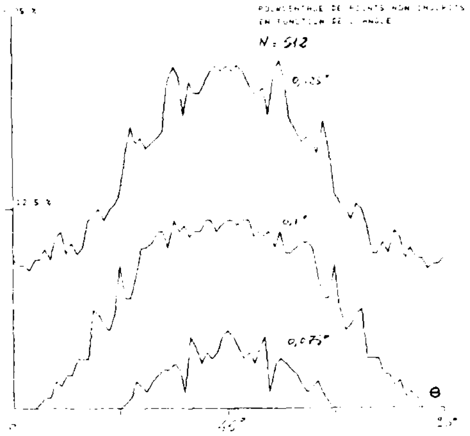

Planche 13

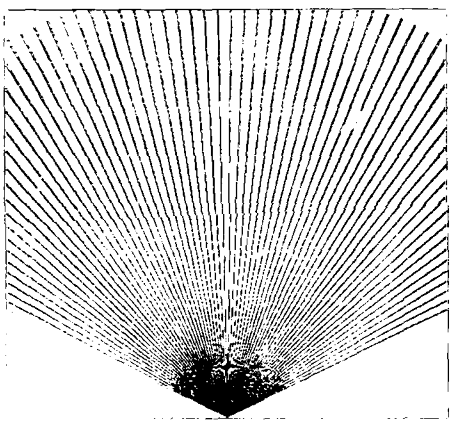

Planche 14

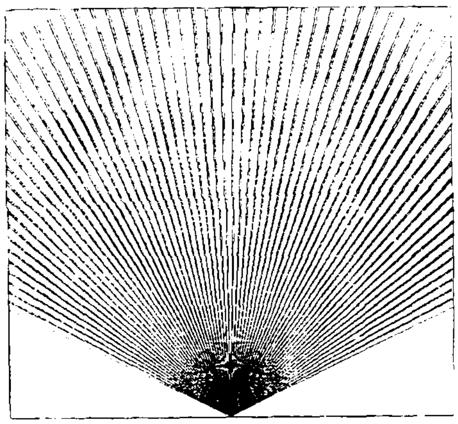

Planche 15

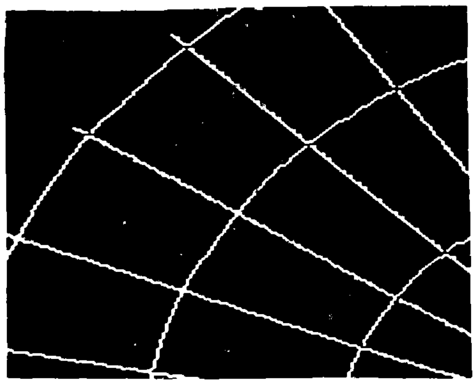

sans filtrage

Planche 16

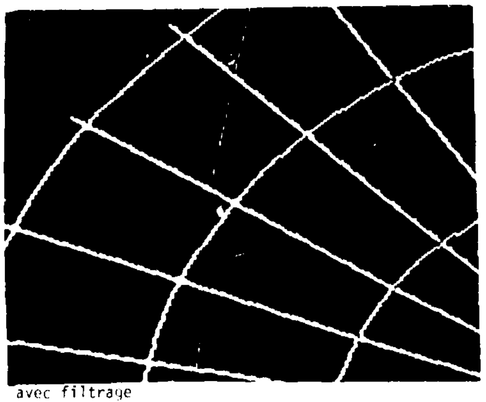

avec filtrage

Planche 17

POSTINTÉGRATION D'IMAGES RADAR

PAR
DANIEL GARNIER
THOMSON-CSF / DIVISION A.V.S.
178 BD GABRIEL PÉRI - 92240 MALAKOFF - FRANCE

RESUME

L'intégration de cartes radar, obtenues avec des radars aéroportés à antenne synthétique, améliore la qualité des dites cartes par augmentation du contraste des échos réels par rapport au bruit de fond.

L'amélioration porte plus particulièrement sur le bruit dit "granulation" ou "speckle", caractéristique des radars cohérents.

L'intégration de cartes radar représentant une même scène, obtenues au cours de balayages successifs, donc sous des angles et à des distances différents, nécessite une compensation précise des mouvements du porteur. Cette compensation est analysée dans le cas d'un stockage des échos dans une mémoire architecturée en XY et dans le cas d'une architecture en ρ-θ.

Deux types de filtres sont examinés :

- filtre de type RC,
- filtre moyenne glissante.

Différents résultats expérimentaux sont présentés pour chacun des procédés en analysant les avantages et les inconvénients.

DUAL FREQUENCY MM-WAVE RADAR FOR ANTITANK HELICOPTER

by

F.X.Jehle and H.Meinel
AEG-Telefunken
Sedanstr. 10
7900 Ulm
Federal Republic of Germany

ABSTRACT

All over the world, helicopters are gaining increasing significance for air close support, airborne landing, tank unit interdiction and both helicopter and tank engagement missions.

The mission phases can be broken down as follows:

- cruise flight
- nose-on-earth (NOE) and contour flight
- weapon delivery.

To support these mission phases, sensors are required for

- obstacle warning
- navigation
- moving and fixed target indication for weapon designation.

The majority of the present systems use optical and infrared sensors; some of them apply laser systems. These sensor systems are subject to considerable limitations with respect to their capability of penetrating bad weather zones, fog, and battlefield environment (dust, smoke, man-made fog etc.). This paper presents the design concept of a dual-frequency radar operating in the millimetre wave range; it avoids these drawbacks and complements the existing sensors.

It consists of a 60 GHz radar subsystem for obstacle warning including the detection of wires up to a range of approximately 500 m; due to the selection of a frequency in the absorption line of oxygen resulting in a high atmospheric attenuation (16 dB/km), the susceptibility to interception and thus also to interference (ECM) can be maintained at a very low level

A 50 GHz radar subsystem (attenuation as low as 0.3 dB/km) with its range of approximately 5 km against targets of interest is used for navigation, fixed and moving target indication as well as weapon designation.

Due to the combination of the two subsystems (50/60 GHz), high-value components (antenna, scanner, receiver assemblies, control and indicator units) can be used jointly for both subsystems, so that the special features of each subsystem become available at reasonable expenses.

SIMULATION OF MULTISTATIC AND BACKSCATTERING CROSS SECTIONS FOR AIRBORNE RADAR

Albert W. Biggs
Department of Electrical and Computer Engineering
The University of Alabama in Huntsville
Huntsville, Alabama 35899, USA

SUMMARY

In order to determine susceptibilities of airborne radar to Electronic Counter Measures and Electronic Counter-Counter Measures simulations of multistatic and backscattering cross sections were developed as digital modules in the form of algorithms. Cross section algorithms are described for prolate (cigar shape) and oblate (disk shape) spheroids. Backscattering cross section algorithms are also described for different categories of terrain.

Backscattering cross section computer programs are also written for terrain categorized as vegetation, sea ice, glacial ice, geological (rocks, sand, hills, etc.), oceans, man-made structures, and water bodies.

PROGRAM SIGTERRA is a file for backscattering cross section modules of terrain (TERRA) such as vegetation (AGCROP), oceans (OCEAN), Arctic sea ice (SEAICE), glacial snow (GLASNO), geological structures (GEOL), man-made structures (MANMAD), or water bodies (WATER). AGCROP describes agricultural crops, trees or forests, prairies or grassland, and shrubs or bush cover. OCEAN has the SLAR or SAR looking downwind, upwind, and crosswind at the ocean surface. SEAICE looks at winter ice and old or polar ice. GLASNO is divided into glacial ice and snow or snowfields. GEOL has bare soil, sand, lava beds, hills, mountains, valleys, rocks or boulders, permafrost, and clay. MANMAD includes buildings, houses, roads, railroad tracks, airfields and hangars, telephone and power lines, barges, trucks, trains, and automobiles. WATER has lakes, rivers, canals, and swamps.

PROGRAM SIGAIR is a similar file for airborne (AIR) targets such as prolate (PROLATE) and oblate (OBLATE) spheroids.

1.0 INTRODUCTION AND OBJECTIVES

The effects of Electronic Counter Measures (ECM) and Electronic Counter-Counter Measures (ECCM) on modern radar systems are very difficult to evaluate analytically. These difficulties increase with the continuously changing ECM environment. Current airborne radar systems have been designed primarily with basic system performance as the major objective. Operation of these systems in ECM environments has not received a corresponding level of evaluation. Furthermore, modern radar complexity has grown with, and in some areas, paced the growth of technology. When this growth is combined with the neglect of ECM, the result is a relatively unknown radar system performance in an ECM environment.

During the last few years there has been an increased awareness of the Warsaw Pact ECM capability and the formidable threat it presents to the operation of our airborne radar systems. As a response to this threat, the Department of the Air Force is committing resources to determine various susceptibilities in its radar systems. A sequence of simulations and analyses will be made to identify these susceptibilities and areas for significant ECCM development.

As part of these simulations and analyses, digital models of bistatic and backscattering cross sections for terrain and airborne targets were developed. Bistatic and backscattering cross section computer programs are described for prolate (cigar shape) and oblate (disk shape) spheroids. Backscattering cross section computer programs are described for terrain categorized as vegetation, sea ice, glacial ice, geological (rocks, sand, hills, etc.), oceans, man-made structures, and water bodies.

The computer programs appear in the Appendix of this report. When referenced in the text, they will be written in CAPITAL LETTERS. Variables and parameters referenced in the text will be written in (CAPITAL LETTERS) within parentheses.

2.0 THE RADAR EQUATION

The fundamental relation between characteristics of radar systems, terrain and airborne targets, and received signals in the radar equation. In PROGRAM RADAREQ, the radar scattering cross section σ_b (SIGMA) in m^2, is suitable for bistatic and monostatic radar systems. In bistatic form, received power (PRE) in watts is

$$P_r = \frac{\sigma_b}{4\pi R_r^2 L_p(r)} \frac{1}{L_s} \frac{P_t G_t}{4\pi R_t^2 L_p(t)} \frac{G_r \lambda^2}{4\pi}$$

$$= P_t \frac{G_r G_t \lambda^2 \sigma_b}{(4\pi)^3 R_r^2 R_t^2 L_p(r) L_p(t) L_s} , \qquad (1)$$

where P_t is transmitted signal power (PTR) in watts, G_r and G_t are receiving and transmitting antenna gains (GRE, GTR), P_r and R_t are distances from the receiver and transmitter to the target (DISTR, DISTT) in m, λ is the signal wavelength (LAMDA) in m, and $L_p(r)$, $L_p(t)$, and L_s are propagation losses over receiver to target and transmitter to target paths, and system losses (LRE, LTR, LSYS).

In monostatic form, transmitter and receiver distances to the target are identical because their locations are the same, and the same antenna transmits and receives, so that

$$R_t = R_r = R,\ G_t = G_r = G, \tag{2}$$

and the received power becomes

$$P_r = P_t \frac{G^2 \lambda^2 \sigma}{(4\pi)^3 R^4 L_p(r) L_p(t) L_s}\ . \tag{3}$$

In bistatic form, the scattering cross section (SIGMAB) is calculated in PROGRAM BISPRULMP and PROGRAM BISTATIC for prolate (cigar shape) spheroid targets. The letters MP designate a main program without subroutines. In these programs, prolate pheroidal coordinates are used with foci (0, 0, ℓ), (0, 0, -ℓ) (L) and families of ellipses (when rotated about the major axis, a prolate spheroid is generated) of constant u(U). *The equation for a prolate spheroid, in spherical coordinates, U, T and φ, is*

$$\frac{x^2+y^2}{\ell^2(u^2-1)} + \frac{z^2}{\ell^2 u^2} = 1, \tag{4}$$

with 2ℓU equal to the sum of the focal radii at the point (x, y, z) on the surface of the spheroid.

A more familiar form for a prolate spheroid is

$$\frac{x^2+y^2}{b^2} + \frac{z^2}{a^2} = 1,\ a > b, \tag{5}$$

where a and b are the major and minor axes (MAJAX, MINAX). The scattering cross section (SIGMAB) in this form is found in PROGRAM BISPPABMP and PROGRAM BISPROAB.

A similar form for an oblate spheroid is found with

$$\frac{x^2+y^2}{b^2} + \frac{z^2}{a^2} = 1,\ b > a, \tag{6}$$

in PROGRAM BISOBLMP and PROGRAM BISOBLAB with major axes (MAJAX) in the x-y plane and minor axis (MINAX) along the Z-axis.

The backscattering cross sections (SIGMAB) are calculated in PROGRAM MONPROLMP and PROGRAM MONPROLAT for prolate spheroids and in PROGRAM MONOBLMP and MONOBLATE for oblate spheroids. The major and minor axes format is used in these programs.

In backscattering cross sections of terrain, the differential scattering coefficient σ^0 (SIGFTV) is developed in empirical forms in PROGRAM SIGTERRA. If a subsequent grant is received for additional research, this program will be "linked" with PROGRAM SIGMAVEG to provide a more detailed σ^0 description. Since σ^0 is the scattering cross section per unit area, it must be multiplied by the terrain area under surveillance in order to find the scattering cross section.

Not included are pulse widths, antenna patterns as functions of θ and φ, signal-to-noise ratios (SNR) in terms of kT_0B noise, receiver noise figures, pulse repetition rates, and time delays between pulses.

Also excluded are computer programs for propagation path losses, which are identical for monostatic radar and different for bistatic radar. Rain attenuation programs would include raindrop size distribution, rainfall rates, rain height, and slant path direction. Snowfall, hail, and fog (sand and dust in desert areas) attenuations would have similar parameters.

3.0 ANALYSIS OF THE BISTATIC CROSS SECTION OF A PROLATE SPHEROID

This section is an analysis of the bistatic radar cross section of a perfectly conducting prolate spheroid which is much larger than the wavelength of the incident signal. The geometrical theory of optics yields useful results except in the shadow region in and near the forward direction. In Eq. (1), the first part was arranged in a form to separate the bistatic cross section (SIGMAB), or an approximate value (SB) for the bistatic cross section. The power density, in Eq. (1), reaching the target is

$$U_t = P_t \frac{G_t}{4\pi R_t^2 L_p(t)}, \tag{7}$$

while the power density U_r at the receiver is

$$U_r = \frac{4\pi P_r L_s}{G_r \lambda^2} = \frac{\sigma_b}{4\pi R_r^2 L_p(r)} U_t, \tag{8}$$

with system loss L_s assumed to occur at the receiver. Equation (8) contains the bistatic cross section σ_b, *and rearranging results in*

$$\sigma_b = 4\pi R_r^2 L_p(r) \frac{U_r}{U_t}\ . \tag{9}$$

Figure 1 is the coordinate system which orients the prolate spheroid in space. The major axis of the spheroid is along the Z-axis. The ratio of major axis to minor axis is 3.0 in this example. The transmitter lies in the y-z plane which, because of the symmetry about the Z-axis, does not affect the calculations for the prolate spheroid or for subsequent calculations in oblate spheroid and backscattering cross section configurations.

Figure 2 is a geometric optics picture of an incident ray reflected from a curved surface on the spheroid. The incidence direction is given by the unit vector $\vec{k}$ with components k_1(K(1)), k_2(K(2)), k_3(K(3)), and the reflection direction is given by the unit vector $\vec{k}'$. Since the spheroid surface is convex, there is no interference between reflected rays from different reflection points on the surface. This divergence allows U_r to be described with $\vec{k}'$, and the decrease of reflected power density with distance r from each reflected point. At the receiving antenna location, r equals R_r(DIST). If negligible path loss is assumed, $L_r(r)$ is approximately unity. Reflected power density at the distance r is

$$U_r(r) = U_* \frac{\sigma_b}{4\pi r^2} = \frac{U_*}{F(r\vec{k}')}, \tag{10}$$

where $F(r\vec{k}')$ describes the spreading loss associated with reduction of power over a sphere of radius r surrounding the spheroid in the $\vec{k}'$ direction.

Each reflection point P(x, y, z) on the spheroidal surface defines a tangent plane. With the expression for the prolate spheroid in Eq. (5), the normal unit vector $\vec{N}$ at $\vec{P}$ is

$$\vec{N} = C\left(x, y, \frac{b^2}{a^2} z\right), \tag{11}$$

with the coordinates of P given by (P(1), P(2), P(3)) in PROGRAM BISPRABMP, and C equal to

$$C = \left[x^2 + y^2 + \left(\frac{b}{a}\right)^4 z^2\right]^{-\frac{1}{2}} \tag{12}$$

The coordinate system with P as the origin appears in Fig. 2. One axis is in the $\vec{N}$ direction. The second axis is in the direction of the unit vector $\vec{B}$,

$$\vec{B} = \frac{(+y, -x, 0)}{\left[x^2 + y^2\right]^{1/2}}, \tag{13}$$

and the third axis is in the direction of the unit vector $\vec{T}$,

$$\vec{T} = \vec{N} \times \vec{B}, \tag{14}$$

where $\vec{B}$ and $\vec{T}$ define a tangent plane at P. $\vec{B}$ was chosen because of symmetry about the Z-axis. It is tangent to any circle formed at Z = constant, and is normal to $\vec{N}$.

The incident and reflected waves have directions given by unit vectors $\vec{k}$ and $\vec{k}'$, with components of $\vec{k}$ equal to (K(1), K(2), K(3)), and located in a plane containing $\vec{N}$. They are related by

$$\vec{k}' = \vec{k} - 2\,(\vec{k} \bullet \vec{N})\vec{N}. \tag{15}$$

With the reflection direction from Eq. (15), the spreading loss function $F(r\vec{k}')$ is evaluated. Figure 3 illustrates assumptions for this evaluation. Power is reflected from the small rectangle in the B-T plane with sides $\lambda\vec{T}$ and $\gamma\vec{B}$. Scalars λ and γ are small increments in directions $\vec{T}$ and $\vec{B}$, respectively. Power reflected passes through the surface formed by the tips of the vectors $r\vec{k}_0$, $r\vec{k}_1$, $r\vec{k}_2$, and $r\vec{k}_3$. The surface formed by the tips of these vectors has sides $\vec{R}_1$ and $\vec{R}_2$,

$$\vec{R}_1 = \lambda\vec{T} + r\vec{k}_1' - r\vec{k}_0', \tag{16}$$

$$\vec{R}_2 = \gamma\vec{B} + r\vec{k}_2' - r\vec{k}_0'. \tag{17}$$

The vectors $\vec{R}_1$ and $\vec{R}_2$ are the sides of the rectangle at the tips of $r\vec{k}_i$ (i = 0 to 3), and $F(r\vec{k}_0')$ is

$$\vec{F}(r\vec{k}_0') = \lim_{\substack{\lambda \to 0 \\ \gamma \to 0}} \left| \frac{\vec{k}_0' \cdot \vec{R}_1 \times \vec{R}_2}{\vec{k}_0' \cdot \lambda\vec{T} \times \gamma\vec{B}} \right|. \tag{18}$$

Maclaurin's Series is used to find the first two terms of $\vec{k}_1'$ and $\vec{k}_2'$,

$$\vec{k}_1' = \vec{k}_0' + \lambda \frac{d\vec{k}_0'}{d\lambda}, \tag{19}$$

$$\vec{R}_2' = \vec{R}_0' + \gamma \frac{d\vec{R}_0'}{d\gamma} , \tag{20}$$

where

$$\frac{d\vec{R}_0'}{d\lambda} = \frac{d\vec{R}'}{d\lambda} + \lambda\vec{T}, \ \lambda \rightarrow 0, \tag{21}$$

$$\frac{d\vec{R}_0'}{d\gamma} = \frac{d\vec{R}'}{d\gamma} + \gamma\vec{B}, \ \gamma \rightarrow 0, \tag{22}$$

where the derivations are claculated in SUBROUTINE DERIVP. For the oblate spheroid calculations, SUBROUTINE DERIVO is used instead of DERIVP. With prolate spheroidal coordinates, SUBROUTINE DERIVL is used. The main programs are also different, but the remaining subroutines are the same for the above spheroids and for the backscattering cross sections for these spheroids.

With substitution of Eqs. (19) and (20) into Eqs. (16) and (17), $\vec{R}_1$ and $\vec{R}_2$ become

$$\vec{R}_1 = \lambda(\vec{T} + r \frac{d\vec{R}_0'}{d\lambda}), \quad \vec{R}_2 = \gamma(\vec{B} + r \frac{d\vec{R}_0'}{d\gamma}), \tag{23}$$

and with Eq. (23), $F(r\vec{k})$ is

$$F(r\vec{R}') = \left| \frac{\vec{R}_0' \cdot \left[-\vec{N} + r\left(\vec{T} \times \frac{d\vec{R}_0'}{d\gamma} + \frac{d\vec{R}_0'}{d\lambda} \times \vec{B} \right) + r^2 \left(\frac{d\vec{R}_0'}{d\lambda} \times \frac{d\vec{R}_0'}{d\gamma} \right) \right]}{\vec{R}_0' \cdot \vec{N}} \right| \tag{24}$$

Equation (24) is simplified by differentiating Eq. (15) with k constant,

$$\frac{d\vec{R}_0'}{d\lambda} = -2\left(\vec{R} \cdot \frac{\partial\vec{N}}{\partial\lambda}\right)\vec{N} - 2(\vec{R}\cdot\vec{N})\frac{d\vec{N}}{d\lambda} , \tag{25}$$

$$\frac{d\vec{R}_0'}{d\gamma} = -2\left(\vec{R} \cdot \frac{\partial\vec{N}}{\partial\gamma}\right)\vec{N} - 2(\vec{R}\cdot\vec{N})\frac{d\vec{N}}{d\gamma} , \tag{26}$$

and then with $\vec{N}$ expressed in terms of x, y, z, in Eq. (11),

$$\frac{d\vec{N}}{d\lambda} = C\left(T_x, T_y, \frac{b^2}{a^2}T_z\right) - C^2\left[xT_x, yT_y, z\left(\frac{b}{a}\right)^4 T_z\right]\vec{N}, \tag{27}$$

$$\frac{d\vec{N}}{d\gamma} = C\left(B_x, B_y, \frac{b^2}{a^2}B_z\right) - C^2\left[xB_x, yB_y, z\left(\frac{b}{a}\right)^4 B_z\right]\vec{N} . \tag{28}$$

Since σ_b has the form,

$$\sigma_b = \frac{4\pi r^2}{F(r\vec{R}')} , \tag{29}$$

and only r^2 terms are kept,

$$\sigma_b = \frac{4\pi\,|\vec{R}_0' \cdot \vec{N}|}{\left|\vec{R}_0' \cdot \frac{d\vec{R}_0'}{d\lambda} \times \frac{d\vec{R}_0'}{d\gamma}\right|} . \tag{30}$$

In PROGRAM BISPRABMP, the input parameters are MAJAX, MINAX, THETA, DIST, INCAY, and INCAZ. THETA is the angle of incidence of the incident field, and is measured from the positive Z-axis in the Y-Z plane in the direction of the positive Y-axis. MAJAX and MINAX are the major and minor axes in meters. DIST is the observation distance in meters. Coordinates of the observation distance (OBSPNT) are measured in angles α(ALPHA) and β(BETA). Angle α is in the Z-Y plane, and is measured from the positive Z-axis toward the positive Y-axis in increments of α (INCAZ). Angle β is in the X-Y plane, and is measured from the positive Y-axis in the direction of the positive X-axis in increments of β (INCAY). Conversions to spherical coordinates θ(THET) and ϕ(PHI) are made. The output includes ALPHA, BETA, THETA, PHI, SB, and SIGMAB.

4.0 BISTATIC CROSS SECTION FOR AN OBLATE SPHEROID

PROGRAM BISOBLAB and PROGRAM BISOBLAMP are similar to those programs for the prolate spheroid. Differences are in the major (MAJAX) axes. Input data are MAJAX, MINAX, DIST, THETA, INCAZ, and INCAY. Output data are ALPHA, BETA, THET, PHI, SB, and SIBMAB.

5.0 BACKSCATTERING CROSS SECTIONS OF PROLATE AND OBLATE SPHEROIDS

PROGRAM MONOBLATE and PROGRAM MONOBLMP are similar to programs for bistatic cross sections of oblate spheroids, but only one angle is considered because *the incident angle* (THETA) equals the backscattering angle (THETA). Input data are MAJAX, MINAX, DIST, and THETA. Output data are THETD, SIGMAB, and SB.

6.0 SUBROUTINES FOR BISTATIC AND BACKSCATTERING CROSS SECTIONS FOR SPHEROIDS

SUBROUTINE ADD (A,B,C) adds two vectors, $\vec{A}$ and $\vec{B}$, and the sum is a third vector $\vec{C}$. The vectors are expressed in terms of components along the x,y,z axes.

SUBROUTINE CONVRT (A,B,C,D) takes distance (A) and angles alpha (B) and beta (C), and converts these to the observation point (D) desired. In the backscattering model, we use SUBROUTINE CONVRT (A,B,C), where only distance (A) *and angle* alpha (B) *are* used to find the observation point (C). In this case, alpha equals theta.

SUBROUTINE CROSS (A,B,C) is the cross produce of one vector (A) and another vector (B), equal to a third vector (C), in terms of components of *each*.

SUBROUTINE DERIVL (P,T,U,DLN) yields the derivative of *the unit vector* N (DLN) *with respect to* λ in the T (T direction, or with respect to γ in the $\vec{B}$ (T) direction, at the point P (P) on the spheroid surface. Rolate spheroidal coordinate u (U) is indicated by L in DERIVL. When major *and minor* axes *are* introduced as input data, SUBROUTINE DERIVP (P, T, MAJAX, MINAX, DLN) and SUBROUTINE DERIVO (P, T, MAJAX, MINAX, DLN) are used for prolate and oblate spheroids.

REAL FUNCTION DOT, (A, B) finds the dot product of two vectors (A, B) in terms of their components. *The resulting scalar is* DOT.

SUBROUTINE *FINDKP* (*K*, N, *B*, *T*, KPRIME) imposes the $\vec{N}$, $\vec{B}$, $\vec{T}$ coordinate system on the spheroid at the reflection point. The vector $\vec{B}$ (B) is obtained from the vector $\vec{N}$ (N), which is an input datum. The cross product subroutine, *CROSS (N, B, T), finds the vector* $\vec{T}$ *(T). With k (K) as an* input datum, k (KPRIME) is calculated.

REAL FUNCTION MAG (A) is the magnitude of a vector (A) with three orthogonal components. The output datum is simply MAG.

SUBROUTINE NORM (A, B) is the vector $\vec{A}$ (A) divided by the magnitude of $\vec{A}$, yielding the *normalized* value (B).

IN SUBROUTINE SCLMLT (A, B, C), a vector (B) is multiplied by a scalar (A) to yield another vector (C).

SUBROUTINE *SUB* (A, B, *C*) is the vector difference (C) obtained when one vector (B) is subtracted from another vector (A).

7.0 BACKSCATTERING CROSS SECTIONS OF TERRAIN

PROGRAM SIGTERRA is a file for backscattering cross sections of *different* types of terrain (TERRA) such as vegetation (AGCROP), oceans (OCEAN), Arctic sea ice (SEAICE), glacial ice or snow (GLASNO), geological structures (GEOL), man-made structures (MANMAD), or water bodies (WATER).

Vegetation is divided into agricultural crops, tree cover or forest, prairie or grasslands, brushes, *and* shrubs, or flower cover. Oceans are divided into the radar looking downwind, upwind, and crosswind at the ocean surface. Sea ice is divided into winter ice (less than a year old) and old or polar ice (*more than a year* old). Glacial ice or snow is divided into glacial ice and snow or snowfields. Geological structure is divided into bare soil, sand, lava beds, hills, moutains, valleys, rocks or boulders, *permafrost, and clay. Man-made structures* include houses, buildings, roads and highways, airfields and runways, aircraft hangars and farm buildings, railroad tracks, telephone lines, power lines, boats, barges, ships, automobiles, trucks, buses, *and* trains. Water bodies include lakes, rivers, canals, irrigation ditches, marshes, and swampland.

PROGRAM SIGAIR is a *similar file for airborne* (AIR) targets, such as prolate (cigar shape) spheroids (PROLATE), oblate (disk shape) spheroids (OBLATE), and spheres (SPHERES).

PROGRAM SIGMAVEG receives input data in the form of frequency (FREQG) of the incident wave, type of terrain (VEGETA), angle of incidence of the incident wave (THETA), and actual values of the backscattering cross sections sigma. σ^0 (SIGV) for incremental values of angle of incidence (J) and increments of frequency (FREQIN (I)). A set of sigma versus theta curves are computed for each frequency such as 5, 10, 15, 20, 25, and 30 GHz. Theta increments are at 0, 5, 10, 15, 20, and 25 degrees. Interpolation formulas yield the value of sigma (SIGFTV) at the actual frequency (FREQG) and actual angle of incidence (J). Also, polarization (POLAR) is included in the form of HH, VV, HV, VH, RHC, and LHC.

8.0 RESULTS

Figures 4-7 show σ_b for various transmitter positions. The observation plane is the y,z plane. The prolate spheroid has major axis one unit long, and minor axis .33 units long. σ_b is in square units.

Figure 8 shows σ_b for a sphere of a radius one unit.

Figures 9-11 show σ_b in varying cases when the observation plane is not the y,z plane. (These are all for a prolate spheroid with major to minor axis ratio of 3:1). The observation plane in Figure 9 contains the z axis, but is at 45° with respect to the y axis. In Figure 10, the observation plane is the x,z plane. In Figure 11, the observation plane is the x,z plane, but rather than having the transmitter on the y axis as in Graphs 7 and 8, the transmitter is at 30° with respect to the z axis in the y,z plane.

Figure 12 shows σ_b when the major axis to minor axis ratio is changed from 3:1 to 10:1. In all other respects, this is the same as Figure 5.

The observation distance was equal to 1000 units in Figures 4-12.

It will be seen immediately that for a prolate spheroid with major axis, 1 unit, the maximum value of σ_b is ∞. Figures 4-7 show that this maximum value in the y-z plane is at 180° minus the transmitter angle which is exactly as expected in terms of reflections, and geometrical optics. It is also interesting to note that the patterns in Figures 4-7 are exactly the same except for being rotated in space.

Figures 7-10 show another aspect of this pattern in space. The pattern has maximum width in the plane containing the transmitter and z axis, and becomes increasingly narrow as we rotate the observation plane away from the y,z plane. It is to be noted that the value of σ_b as we approach the shadow becomes underterminate. In the x,y plane, $\sigma_b = \infty$ for all angles, while in the y,z plane, σ_b approaches .02702.

Figures 5 and 11 show the same behavior as Figures 7-10, except that the transmitter is now at an angle of 30° with respect to the z axis rather than being on the y axis. Again, the pattern approaches being infinitely thin, and is indeterminate as we approach the shadow.

Lastly, a comparison of Figures 5 and 12 shows the effect of increasing the major axis to minor axis ratio. If the prolate spheroid becomes narrower the maximum value remains ∞, but the pattern becomes much narrower.

9.0 REFERENCES

ANDREASEN, M. G., March 1965, "Scattering from Bodies of Revolution," IEEE Trans., Vol. AP-13, pp. 303-310.

BICKEL, S. H., January 1966, Polarization Extension of the Monostatic-Bistatic Equivalence Theorem, Mitre Corp. Report TM-4242.

BIGGS, A. W., 1969, "Volume Scattering from Sea Ice and Glacial Snow," Fall URSI Meeting, Austin, Texas, December 8-10.

BIGGS, A. W., 1977, "Sea Ice Thickness Measurements with Short Pulse Radar Systems," URSI Symposium on Propagation in Non-Ionized Media, LaBaule, France, April 28 - May 6.

BIGGS, A. W., 1983, "Radar and Infrared Remote Sensing of Terrain, Water Resources, Arctic Sea Ice, and Agriculture," EWPP/AGARD Symposium on Propagation Factors Affecting Remote Sensing by Radio Waves, Oberammergau, Germany, May 22-29.

BURKE, J. W., et al, October 1965, Ripple Tank Analogs of Electromagnetic Scattering by Metallic and Dielectric Cylinders, Electronic Defense Laboratory Tech. Memo EDL-M810.

CORRIHER, H. A., Jr., et al, August 1965, "A Bibliography of Articles on Radar Reflectivity and Related Subjects," Proc. IEEE, Vol. 53, pp. 1025-1064.

CRISPIN, J. W., Jr., et al, July 1959, A Theoretical Method for the Calculation of Radar Cross Sections of Aircraft and Missiles, University of Michigan Radiation Laboratory Report 2591-1-H.

EINARSSON, O., et al, February 1966, Studies in Radar Cross Sections. I: Diffraction and Scattering by Regular Bodies. IV: The Circular Cylinder, University of Michigan Radiation Laboratory Report 7133-3-T.

ERTEZA, A., et al, October 1966, "Bistatic Determination of Eta and Mu for a Smooto Convex Target," Proc. IEEE, Vol. 54, pp. 1473-1474.

KELL, R. E., March 1965, "On the Derivation of Bistatic RCS from Monostatic Measurements," Proc. IEEE, Vol. 53, pp. 983-988.

KLEINMAN, R. E., February 1965, Diffraction and Scattering by Regular Bodies, University of Michigan Radiation Laboratory Report 3648-1-F.

KODIS, R. C., August 1965, "Propagation and Scattering in Plasma," Proc. IEEE, Vol. 53, pp. 1016-1024.

LOGAN, N. A., December 1965, Numerical Investigation of Electromagnetic Scattering and Diffraction by Convex Objects, Lockheed Missile and Space Co. Final Report, Contract AF 19(628)-439[illegible].

MULLIN, C. R., et al, January 1965, "A Numerical Technique for the Determination of the Scattering Cross Sections of Infinite Cylinders of Arbitrary Geometric Cross Section," IEEE Trans., Vol. AP-13, pp. 141-149.

PEAKE, W. H., et al, 1971, The Response of Terrestrial Surfaces at Microwave Frequencies, Ohio State University Technical Report 2440-7, Columbus, Ohio.

SIEGEL, K. M., 1958, Bistatic Radars and Forward Scattering, National Conference Proc. of Aeronautical Engineers (Dayton, Ohio), pp. 286-290.

SEIGEL, K. M., May 12-14, 1958, Bistatic Radars and Forward Scattering, Proc. National Conference of Aero. Electronics, pp. 286-290.

SKOLNICK, M. I., March 1961, "An Analysis of Bistatic Radar," IRE Trans., Vol. ANE-8, pp. 17-28.

SKOLNICK, M. I., 1980, Introduction to Radar Systems, McGraw-Hill, pp. 553-560.

ULABY, F. T., et al, 1975, "Radar Response to Vegetation II: 8-18 GHz Band," IEEE Trans. Ant. Prop., AP-23, pp. 608-618.

ULABY, F. T., et al, 1976, "Corn Growth as Monitored by Radar," IEEE Trans. Ant. Prop., AP-24, pp. 819-828.

ULABY, F. T., et al, 1978, "Microwave Backscattering Dependence on Surface Roughness, Soil Moisture and Soil Texture, Part I: Bare Soil," IEEE Trans. Geosci. Electr., GE-16, pp. 286-295.

ULABY, F. T., et al, 1979, "Microwave Backscatter Dependence on Surface Roughness, Soil Moisture and Soil Texture, Part II: Vegetation-Covered Soil," IEEE Trans. Geosci. Electr., GE-17, pp. 33-40.

ULABY, F. T., 1980, "Vegetation Clutter Model," IEEE Trans. Ant. Prop., AP-28, pp. 538-545.

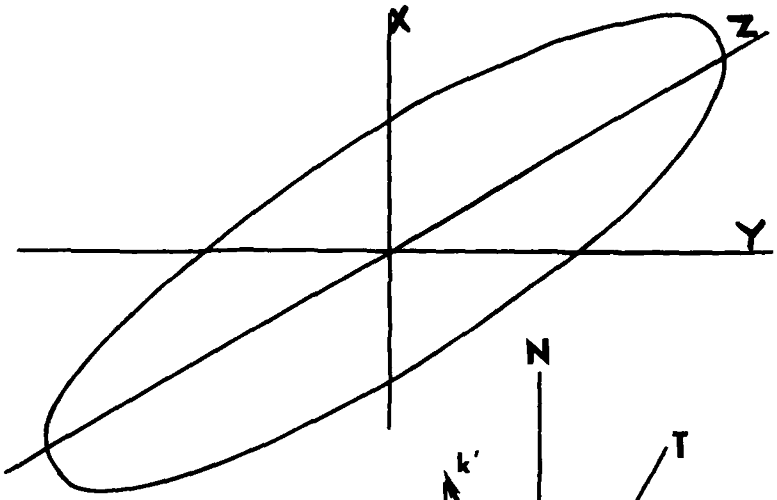

1. Coordinate system for the prolate spheroid.

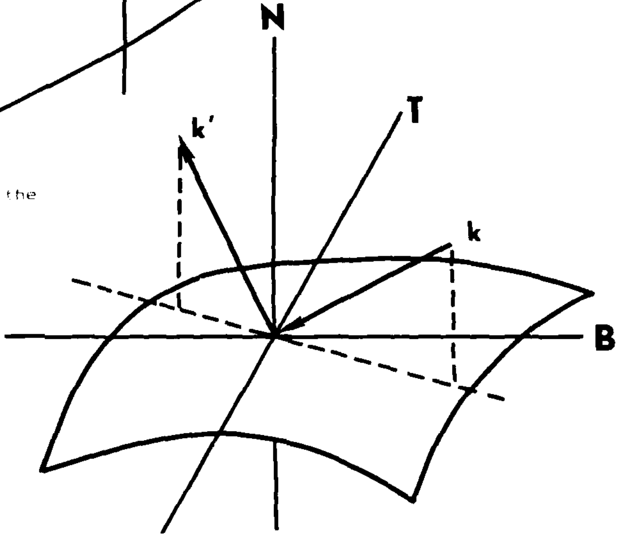

2. Geometric optics picture of waves incident on the spheroid.

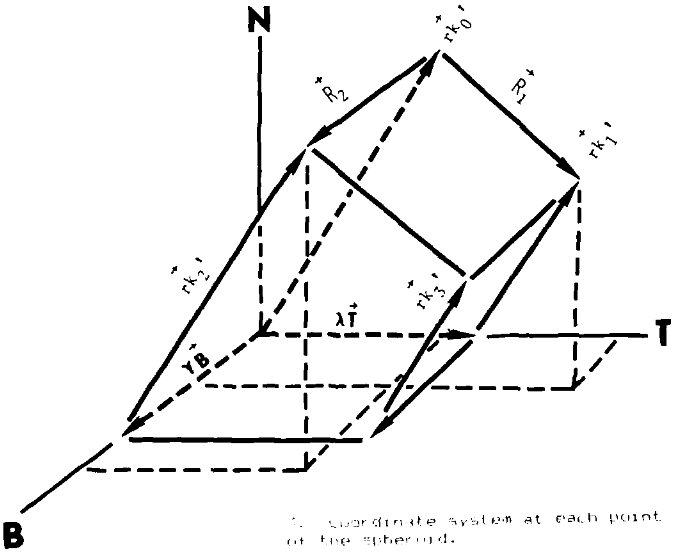

3. Coordinate system at each point of the spheroid.

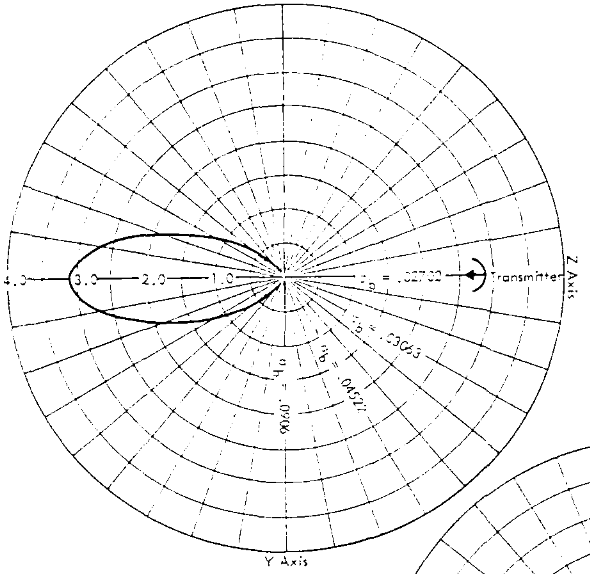

4. Transmitter on the Z axis with observation point on the YZ plane.

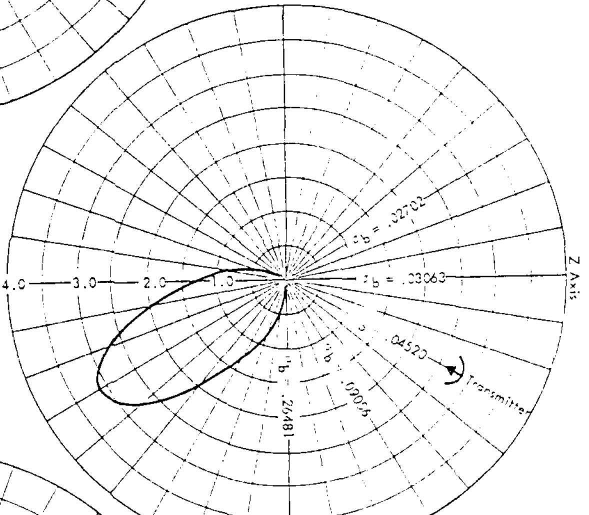

5. Transmitter on the YZ plane and 45 degrees from the Z axis, with observation point on the YZ plane.

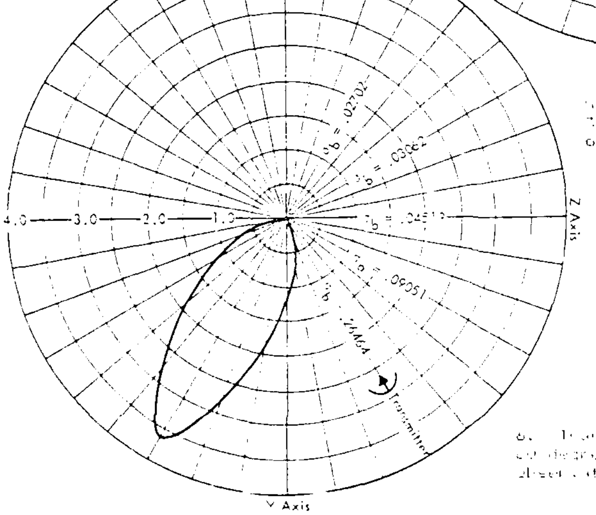

6. Transmitter on the YZ plane and 60 degrees from the Z axis, with observation point on the YZ plane.

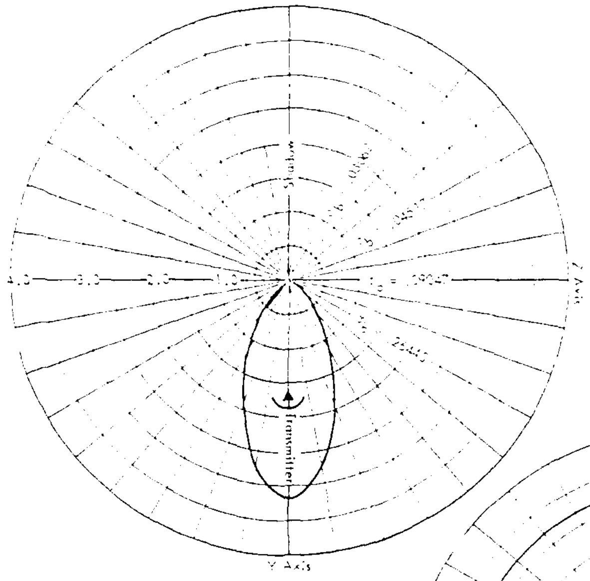

7. Transmitter on the Y axis, with observation point on the YZ plane.

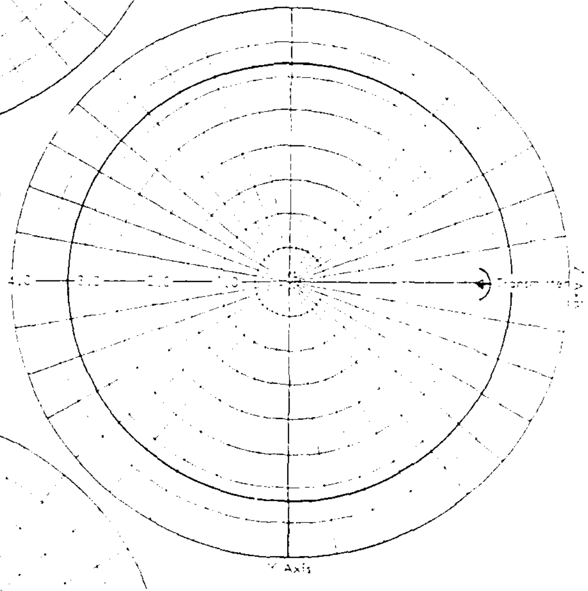

8. Bistatic cross section for a sphere with a radius one unit.

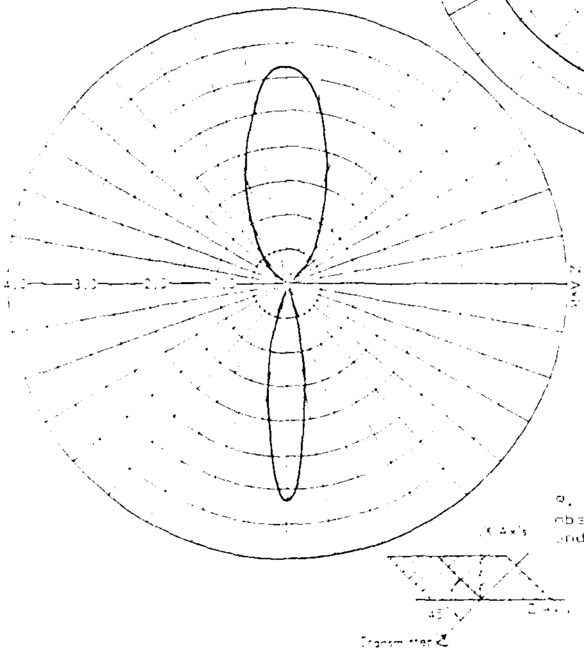

9. Transmitter on the Y axis, with observation point on the YZ plane and 45 degrees from the Y axis.

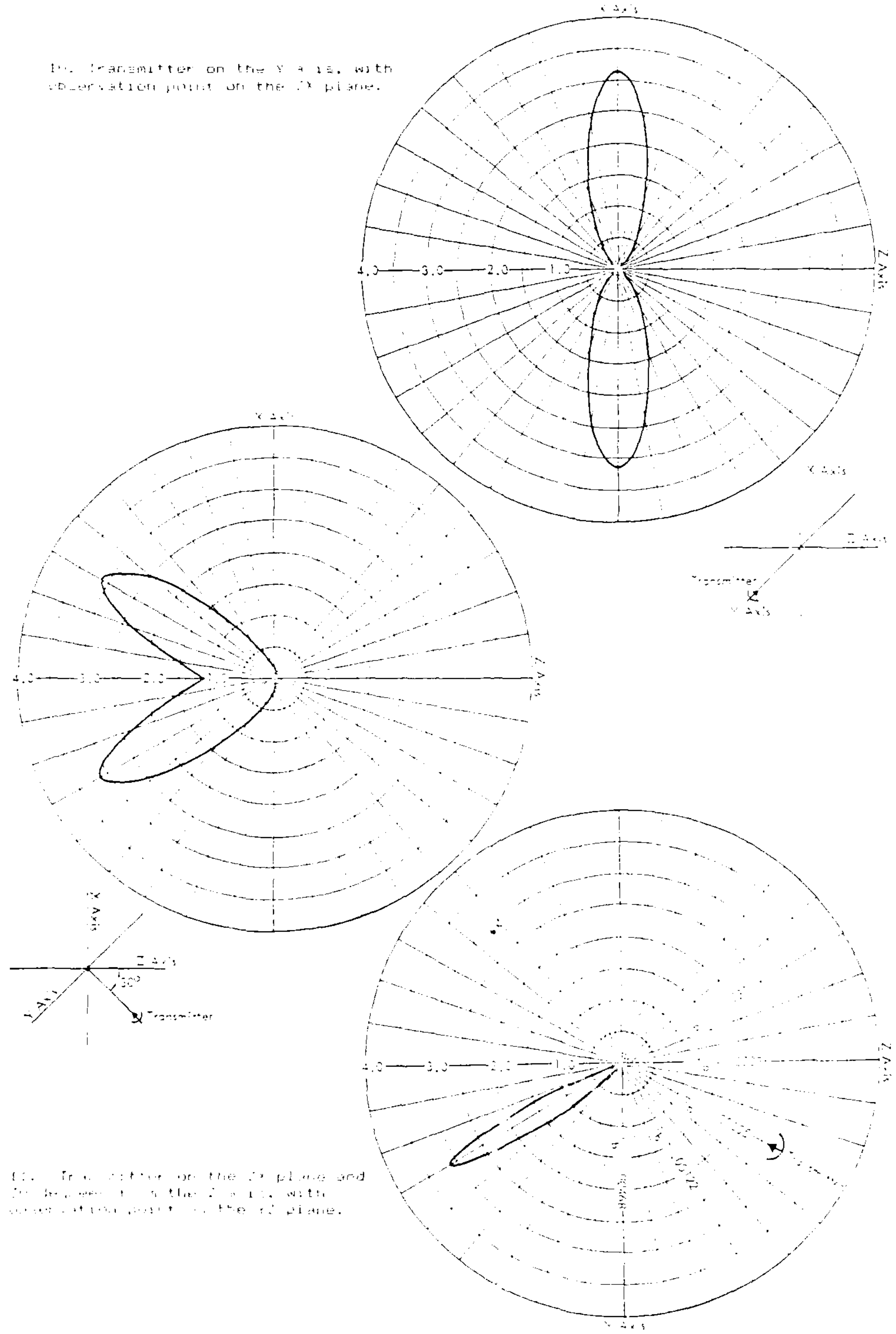

(b). Transmitter on the Y axis, with observation point on the ZX plane.

(c). Transmitter on the ZY plane and 30° between it and the Z axis, with observation point on the XZ plane.

AD-A173 978 MULTIFUNCTION RADAR FOR AIRBORNE APPLICATIONS(U) 3/3
ADVISORY GROUP FOR AEROSPACE RESEARCH AND DEVELOPMENT
NEUILLY-SUR-SEINE (FRANCE) M H CARPENTIER ET AL.
UNCLASSIFIED JUL 86 AGARD-CP-381 F/G 17/9 NL

END
DATE
FILMED
[illegible]

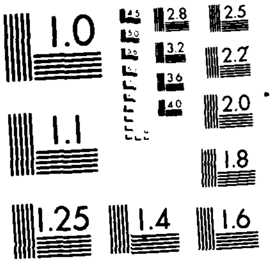

MICROCOPY RESOLUTION TEST CHART
NATIONAL BUREAU OF STANDARDS 1963-A

THE USE OF SIMULATED SYNTHETIC-APERTURE RADAR SIGNALS OF SHIPS IN THE DEVELOPMENT OF AN AUTOMATIC SHIP CLASSIFICATION SYSTEM

Malcolm R. Vant, Kam H. Wu
Government of Canada
Dept. of Communicatons
Communications Research Centre
P.O. Box 11490, Station H
Ottawa, Ontario
K2H 8S2

J.K.E. Tunaley
London Research and Development
1495 Geary Avenue
London, Ontario
N5X 1G6

SUMMARY

One of the major problems encountered in developing and testing any target classification scheme is the collection of an adequate data base for training and testing the classifier. This is particularly a problem if one must obtain radar information from a large number of viewing angles and over a large number of targets, some of which may be unfriendly.

This paper describes a method for obtaining this information by simulation. Synthetic-Aperture Radar signals such as would be obtained from either a moving or a stationary ship, are simulated and it is shown how such a facility can be used in the development of an automatic ship classification system. The images of stationary ships are used to train and test the classification system and the images of moving vessels are used to show how the classifier performance degrades if the motion is left uncorrected.

A readily available data base such as Jane's Book of Ships is used to compile 3-D outlines of the vessels of interest. These outlines, accurate down to the 1-m level, are used to decompose the ship's superstructure into a set of radar scatterers. The returns from the scatterers are then summed, taking into account the viewing angle of the radar. Using this technique, the radar scattering models for a complete library of ships can be formed, and the library used to develop and test various automatic classification schemes.

This paper will give examples of simulated SAR images of ships, and compare the real image of a particular ship to its simulated one. The limitations of the technique will be discussed, and the use of the data in testing an actual classification scheme will be briefly outlined.

REQUIREMENTS AND APPLICATIONS FOR RADAR SIMULATIONS - A STANDPOINT OF AN AIRFRAME COMPANY

Dr. Werner Kohl and Dr. Wolfgang Hetzner
Messerschmitt-Bölkow-Blohm GmbH
Postfach 80 11 60
D-8000 München 80
Federal Republic of Germany

SUMMARY

The paper gives an overview of requirements and applications for radar simulations performed by an airframe company.

The discussion covers offline computer models either as stand alone or implemented within air or sea combat simulations. The use for online models reach from interface simulations to rather complex models for manned aircraft simulations.

The paper presents realized examples of radar models for air or sea combat simulations, an experimental engineering tool which simulates a core avionic system, a 1 versus 1 advanced flight simulation with a pilot in the loop and a radar signal simulation implemented in a terrain following closed loop simulation at an avionic rig.

1. INTRODUCTION

Radar simulations performed by airframe companies are significantly different from simulations carried out by radar manufacturers. Radar companies primarily emphasize the detailed simulation of the radar itself whereas simulation work of airframe companies has to cover overall system aspects.

These simulations are in general related to one of the following categories.

- Comparison of radar systems under identical operational assumptions.
- Combat simulations to evaluate weapon system effectiveness in a combat scenario.
- Avionic simulations to optimize and evaluate system or subsystem performance.
- Advanced flight simulations with a pilot in the loop.
- Avionic rig operations with equipment simulation or stimulation.

Typical applications at MBB cover the air combat simulation with a program called SILKA and a naval simulation called MKRIEG. An Experimental System Engineering Tool (EXSET) is a set up used to evaluate and develop avionic system concepts. For the development and performance access of control-configured aircraft together with an integrated fire flight control system an advanced flight simulation is employed with a pilot in the loop. Terrain Following (TF) system tests have been carried out with the help of a TF-closed loop simulation.

Fig. 1 shows these applications and their relation to project phases.

2. REQUIREMENTS

Several functions of airborne radars are considered in this paper generally divided in air-to-air and air-to-ground modes, whereby radar mapping functions are excluded. According to the functions radar simulations are wide spread because of several different simulation objectives. Before we discuss some special applications of radar simulation it will be helpful to establish the requirements imposed on the radar system simulation.

2.1 GENERAL ASPECTS

The basic requirements of radar simulation arise from the main functions of radars which are detection and tracking.

Detection

Detection of a target of interest is the principal function of the radar. To simulate detection performance, the detection probability can be calculated as a function of radar parameters, engagement geometry, target attributes and interference. A firm decision of target detection can be derived by comparing the detection probability p with a random variable u, distributed uniformly between 0 and 1. A detection is defined if u is less or equal p.

Tracking

The radar can track manoeuvering targets, which have already been detected, along their trajectory by performing repeated measurements. To simulate track performance, the tracking range can be calculated as a function of radar parameters, engagement geometry, target attributes and interference. For modern radars single as well as multiple target tracking is available.

General aspects of performance simulation cover the achievable accuracy of radar measurements for both detection and tracking and the influence of interference on radar functions and accuracy.

Accuracy

System simulations often require modelling of measurement errors which may be calculated in detail or with certain error distributions around the error free measurement values.

Interference

The signals received from the targets are obscured by interference which might be hostile jammers or clutter portions from ground sea or weather. The influence of interfering signals is mainly determined by signal processing of the radar to be modelled. Therefore especially ECM vulnerability is difficult to simulate at a system level without appropriate inputs from the radar designer. Based on our experience this point is one of the problem areas of radar simulations.

Integration aspects are related to the interaction of the radar with the overall avionic system or to the operator. From a system point of view quite often requirements exist for test-set-ups to simulate the radar interfaces very accurately. Normally in this case the simulation of performance has minor importance.

Interface to the Avionic System

This interface is to be simulated if the radar equipment is substituted by a computer model in a test-set-up or an avionic rig.

Interface to the Operator

The interface to the radar operator is characterized by the radar display presentation, the moding of the radar and the handling by the operator which is most important for simulations with a pilot in the loop.

Signal Generation

Inserting signals entering the radar receiver means a simulation of the radar interface to the outside world. Since the radar is used as real equipment it is a very special radar simulation usually called radar stimulation. Depending on the objectives a RF or video stimulation can be applied.

There are several other requirements left, that are placed on radar simulations. The following one is of major importance.

Processing Time

The driving factor of radar simulation is speed, especially if there exists a real time requirement. Otherwise even for large offline simulations a radar model is invoked periodically and must deliver the desired results in a certain time slot. In any case speed affects costs.

The complexity of radar models is tied to a large extent to the simulation objective which determines the amount of detail which must be incorporated in the simulation. Since modern multimode radars become more and more sophisticated, simulation complexity grows rapidly. This in turn affects the effort necessary to establish, test and verify the models. Finally complex radar simulations usually require a number of detailed input data which must be provided by the radar designers.

2.2 RADAR MODEL CHARACTERISTICS

Offline radar models are used as stand alone computer simulation for radar comparisons. The output of these models is the single scan or cumulative probability of detection versus range. For the calculation the following aspects have to be considered.

- Radar parameters including details of signal processing.

- Target fluctuation and radar cross section.

- Atmospheric attenuation due to weather.

- Ground clutter depending on waveform and geometrical situation.

- Performance degradation due to jammers.

The most critical point for this kind of simulation is the need for a number of detailed radar data which are not easily available on modern radars. Therefore in many cases a first approximation is a parameter assessment which can be adjusted by comparing simulation results with those of the radar manufacturers.

Offline radar models more often are embedded in an overall air or sea combat simulation with quite a lot of radar platforms equipped with different radars like pulse or pulse doppler systems for airborne or shipborne applications and for missile seeker heads.

An air-to-air combat simulation deals with bombers and fighters which have to be appropriately modelled with respect to manoeuverability and tactics. Each platform has to be supplied with sensor models (e. g. radar, radar warning etc.) with weapon models which in turn contain sensor models and some sort of fire control algorithms.

In general the result of the simulation is a mass of detail information like times of missile launches, numbers of missiles fired, plots of the platform motion as well as missile trajectories, kill probabilities and exchange ratios.

Fig. 2 shows a typical SILKA plot. The solid lines mark the aircraft manoeuvres, the dashed lines are drawn for the missile trajectories with the dotted lines indicating the missile active phase.

Because of the above mentioned complexity of such simulations all models including radar have to be fairly coarse. The radar models for this kind of application shall be able to deliver detection ranges, track ranges, track accuracies and they should account for different radar modes, weather and jammer effects.

The decision of radar detection is derived from detection probability which is based on signal-to-interference ratio, taking into account receiver noise, weather and jammer influence and ground clutter which is most critical for pulse doppler radars. For this type of simulation it is too complicated to calculate clutter distributions in the range doppler domain. Instead it is possible to work with general approximations or look up tables which may be derived from the above mentioned stand alone radar simulation.

Online radar models normally substitute real radar equipment for test facilities like EXSET or avionic rigs. For these applications the main requirements are low processing time to allow real time simulations and an accurate modelling of the system interface. Detection, tracking and accuracy have to be modelled depending on the actual application which might cover the complete range of very coarse to very detailed simulation models. That applies also for the moding and handling aspects.

The most demanding radar models generally are required for an advanced flight simulation because they have to show a very realistic radar characteristic to the pilot. Therefore the radar simulation must contain a detailed moding and handling module, it has to show appropriate response times to the pilot and must be able to deliver representative display information. This requires e. g. details of antenna scan and a fairly detailed operational performance of detection, track and their associated accuracies.

Online signal simulations usually are neccessary to simulate real radar equipment integrated in test-set-ups or rigs. In general the requirements for signal simulation are tied to the radar system response which in turn is the result of signal and data processing. Depending on the actual application RF or video simulations can be used.

Online signal simulations will be performed for

- Performance investigation
- System validation
- Auto-TF clearance achievment
- Initial pilot training

The simulation categories are shown in table 1.

3. EXAMPLES FOR RADAR SIMULATIONS

In the following some typical examples for radar models used in weapon system simulation at MBB are presented. Requirements as pointed out in para. 2.1 are summarized in table 2 as they apply to the examples which will be discussed in the subsequent paragraphs.

3.1 RADAR MODELS FOR COMBAT SIMULATIONS

3.1.1 MKRIEG

The purpose of the operational model MKRIEG is the evaluation of weapon systems effectiveness within the scope of naval operations.

In the model different navy weapon systems are represented within assumed scenarios allowing naval operations like the concentration of naval forces in the presence of air threat and a subsequent sea combat in a time frame of several hours. Anti-ship weapons are also modelled in a way that the influence of different technical parameters can be investigated. Ship-to-ship and ship-to-air combat can be simulated simultaneously with a maximum of 48 participants.

The simulation is executed step by step in time based on a Monte Carlo method. A scenario can be set up and technical parameters can be fixed via inputs. The outputs of the model deliver the progress of the combat, a statistic of certain events like detections, missile launches, kills etc. and a graphical representation of the results as well.

In the model MKRIEG a pulse radar model of a search radar on ships against air and sea targets and a LPRF pulse radar model of an airborne radar against sea targets are implemented. Modelling is accomplished with the help of formulas and equations wherein the following quantities can be varied.

- Radar parameters
- Clutter depending on sea state and rain rate
- Atmospheric attenuation due to weather conditions
- Radar cross section of the target
- Jammer parameters

The radar model increases the efficiency of the overall simulation with respect to operational performance e. g. detection and accuracies. Fig. 3 shows a simplified program flow chart of the airborne radar model after the geometrical target detection in azimuth and elevation. During program initialization at the first call of the model, numerical values are introduced for the desired parameter and calculation is executed for

- the integrated pulses per scan
- the detection threshold
- the atmospheric attenuation
- the rain attenuation
- the maximum radar range.

To cope with an ECM environment, the received jamming power is calculated if the actual target range does not exceed the maximum detection range. For the detection calculation the power ratio of signal to interference S/I is determined. The interference power I comprises all unwanted power portions like noise, clutter, rain backscatter and jammers.

After having determined the signal to interference ratio S/I the detection probability is calculated, which is a function of S/I, the detection threshold and the number of the integrated pulses. From the probability of detection a firm decision for detection is derived using the statistical process pointed out in para. 2.1. In a further step the calculated values of range, angles and their derivatives are changed by error values. For these errors a normal distribution is assumed.

3.1.2 SILKA

SILKA is a deterministic m-versus-n air combat simulation. It consists of offensive weapon systems like bombers and escort fighters and air defence fighters. All weapon systems are represented by aircraft and weapon capabilities as well as avionic or sensor performance and counter measures. The number of blue interceptors is limited to four, the red attack formation may consist of up to 26 aircraft. Using preliminary simulations like CAP or GCI models input data for SILKA such as geometry, fuel- and armament status, altitude, speed and information status are produced.

For SILKA a time intervall of 1 second is used, but there exists the possibility to apply a seperate time step of .1 second for certain decisions. As it was mentioned earlier, the model is deterministic to decisions but stochastic with respect to detection and missile effectiveness. To get reliable statistical results it is necessary to perform about 30 - 50 simulations.

Both pulse and pulse doppler radars are modelled in SILKA at the level of signal to interference analysis. The pulse doppler radar originally represented in SILKA was a High PRF coherent radar. Some improvements with respect to Medium PRF modes have been implemented during the last years.

A Track-While-Scan mode was made available which can not be entered until the signal to interference ratio for a target has raised above a threshold corresponding to the Medium PRF noise and clutter level for the given circumstances.

For the pulse doppler radar the following modes of operation are available.

- Velocity Search
- Range-While-Search
- Track-While-Scan
- Single-Target-Track
- Silent

The normal mode of operation is to run the model in Velocity Search or Range-While-Search until the detection probability on a particular target rises above a threshold value at which the model shifts to a Track-While-Scan mode and attempts to establish track.

If a preset threshold of the cumulative probability of detection is crossed, a successful track is declared and track information is made available.

Fig. 4 shows the cumulative probability of detection increasing with combat time.

A single target track facility is also available and finally the radar can be flown in a silent condition being activated by tactical considerations for example receipt of a radar warning detection.

3.2 EXSET

EXSET stands for Experimental System Engineering Tool. The main task of EXSET is practical and realistic development and optimization of system concepts for the avionic/armament system of future fighter aircraft.

A block diagram of EXSET is shown in fig. 5. The set up consists of a simulation computer PDP 11/60 on which aircraft, sensor and target models are installed. A seperate computer which can be programmed in ADA is used as attack processor. All the display surfaces and the voice command and warning system are driven by a display management processor. An interface unit allows access to an multifunction keyboard and various analog or discrete signals. All the equipment listed above are interfaced to a MIL-1553B avionic bus. Based on this bus architecture EXSET has high flexibility to cope with additional equipment or changing test requirements. During the different phases of EXSET upgrades, computer models used will be replaced step by step by real avionic systems in order to limit the models to a minimum.

Embedded in the core avionic system of EXSET is a radar model fed from an appropriate target model. Several targets can be generated flying on preprogrammed courses or operator controlled by joysticks.

Since a multimode air-to-air pulse doppler radar has to be simulated, the following modes have to be implemented.

- Air Combat Mode (ACM) with three different scan patterns, autoacquisition and lock-on-reject facility.
- Range-While-Search (RWS) with selectable scan patterns, appropriate display information and target designation.
- Single-Target-Track (STT)
- Track-While-Scan (TWS) for up to 8 targets with target priority allocation.
- Raid-Assessment Mode (RAM).

Fig. 6 shows the context of the radar model for EXSET.

The target model which provides target data to the radar is part of the environment simulation. Radar information data are presented to the pilot on the displays. System control represents these functions of the avionic system which either controls the radar or processes radar data.

Fig. 7 is a graphic presentation of the highest level functional analysis of the radar model. The MIL-bus interface appears as data store for all radar inputs and outputs except target data.

Due to the fact that EXSET works on a real 1553B avionic Bus, the MIL-Bus interface has to be modelled very realisticly including radar status information, track status and track data. Therefore emphasis was given to the interface simulation at this early state of EXSET.

At present detection performance is of minor importance. Thus it is kept as simple as possible allowing targets to be detected and tracked within fixed ranges and within the scan limits. However a more sophisticated detection module can be easily implemented using the modified algorithms developed for the offline pulse doppler simulation and a realistic simulation of the antenna scan which has been developed for the manned simulation.

At a later stage error models have to be included to detoriarate the error free target data to check system performance with respect to error sensitivity.

3.3 ADVANCED FLIGHT SIMULATION

Advanced flight simulations with pilots in the loop became more and more realistic tools for pilot training without spending fuel, ammunition or missiles and service life of the airframe. For this kind of simulation there exists a large variety of applications for an airframe company.

At first the simulation can be used for the development and optimization of the man-machine interface. That includes the display, control and warning concept, the cockpit layout and the pilot vision evaluation of future aircraft.

At second the simulation is a very valuable tool to complement and extend operations research studies or offline air combat simulations. In that sense a flight simulation is used to evaluate weapon system effectiveness with respect to advanced aircraft layout, avionic or flight control concepts, e. g. control configured aircraft, fuselage aiming or integrated fire flight control system.

Finally a flight simulation allows pilot evaluation of flyability and acceptability under operational conditions and tactical analysis of high dynamic air-combat duel situations.

The advanced flight simulation facility at MBB up to now was equipped with a computer generated image system and a beam splitter which is presently replaced by a projection dome. Fig. 8 shows a simplified block diagram of the advanced flight simulation. All the simulation models including radar are installed on a HEP 1 computer.

The radar model is based on a modern state of the art pulse doppler fighter radar but only the air-to-air modes being modelled. A module serving for radar moding and handling has been established according to the controls concept of a future single seated fighter aircraft. At present a very comfortable antenna scan module is developed which allows the pilot to select various scan pattern and to adjust azimuth offset and tilt of the patterns within the gimbal limits. The output of the antenna module is used to decide on geometrical detection of the targets and to drive some basic display functions like azimuth symbol, elevation bar indication and target presentation.

For the range calculation a derivative of the simple SILKA algorithms is utilized up to now, which is planned to be replaced by a more sophisticated module in the near future.

Further upgrades are concerned with error models and the influence of an ECM environment.

3.4 TERRAIN FOLLOWING CLOSED LOOP SIMULATION

Starting development of a TF-system a pure digital simulation consisting of adequate modelled equipment is used to optimize the whole TF-loop.

For a more representative simulation a rig was built up to include the original aircraft hardware. For TF-simulations the following equipment of an overall "Integrated Avionic/ Armament Test Rig" have been used (Fig. 9):

- Terrain Following Radar (TFR)
- Radar Altimeter (RAD/ALT)
- E-Scope
- Central Computer
- Head Up Display (HUD)
- Autopilot

The test rig cockpit is identical to the aircraft layout to provide the possibility of a pilot in the loop. The TF loop has been closed via a simulation computer which contains the aircraft model, the engine, the undercarriage, the Command and Stability Augmentation System (CSAS) and the actuators as well as the sensors like Inertial Navigator (IN), Secondary Attitude and Heading Reference (SAHR), Air Data Computer (ADC) and the Doppler.

Because the TF-algorithms and a lot of monitors are executed in the radar processor, the real TF-radar was used instead of a simulation model. Thus the TF-radar has to be stimulated with none or only minor equipment modifications and of course with acceptable effort.

For the TF simulation an additional microprocessor is used for the real time computation of the distance between aircraft and terrain. For this purpose various types of terrain are stored in the processor. Using actual radar antenna look angle and attitude data the range will be computed and submitted to the TF-radar via a delay generator (Fig. 10). So in this case the radar simulation reduces to radar signal simulation.

In general the set-up was designed as a video-stimulation because of the high effort a RF-stimulation would require. Therefore the RF-sections of the radar are not used for this purpose. The choice of video rather than RF-stimulation is due to the fact that the test set up is treated from an overall system level rather than an equipment level. Another important system aspect - the radome influence on system performance - was explicitly excluded.

From the radar the following signals are supplied via a special designed interface:

- Momentary antenna look angle which is used by the microprocessor to calculate the range to the stored terrain.
- The Master Trigger signal actually derived from the transmit pulse, which is used as the trigger signal of the delay generator whose delay time is programmed from the microprocessor according to the range calculated.
- Test signals sent during the antenna reversal on top end of scan which must be supplied to the radar receiver to prevent a radar failure situation.

A comparison of simulation results and actual flight test data shown in Fig. 11 indicates a very good agreement which in turn means that the simulation satisfactory represents actual weapon system performance.

4. CONCLUSION

Modern multifunction radars have major influence on weapon system performance. To demonstrate weapon system effectiveness, simulations have to be performed with emphasis placed on system aspects. The requirements for simulations change with project phases. During later project phases, radar designers normally participate in simulation work carried out by airframe companies. However during competition in early project phases, radar manufacturers are well advised to support simulations which will reflect the operational benefit of their advanced multimode radar systems.

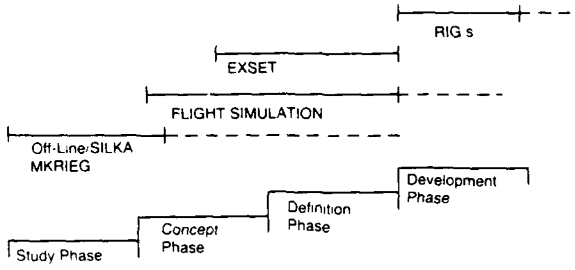

Fig. 1: Applications of radar simulations during project phases

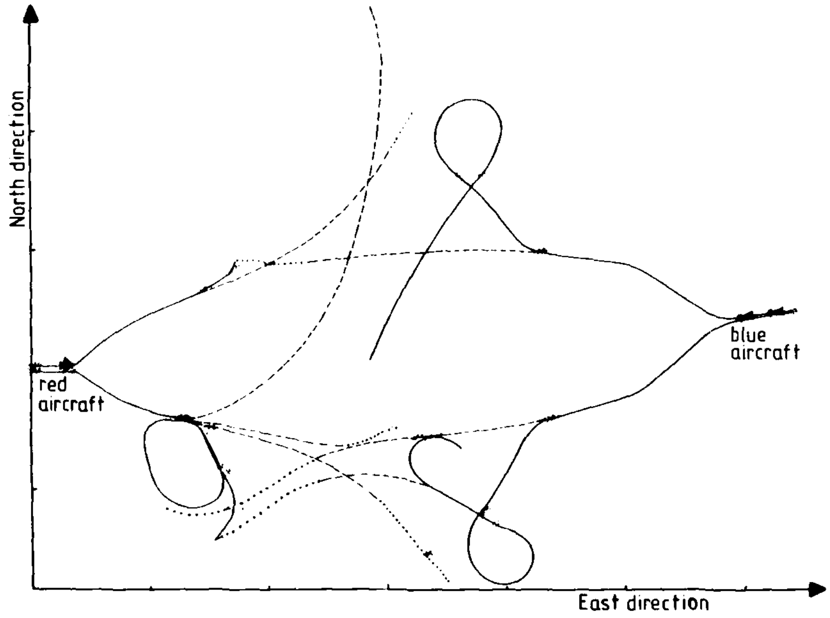

Fig. 2: Typical SILKA result

	Radar Sensor Simulation	Radar Signal Simulation
Off-Line Simulations	Pulse/pulse-doppler models Models for combat simulations • MKRIEG/SILKA	To be performed by radar designers
On-Line (Real time) Simulations	Equipment substitution for test facilities • EXSET • Avionic rig Manned Simulation	Equipment stimulation for ground test facilities • RF stimulation • Video stimulation TF Closed Loop

Table 1: Simulation categories

Requirements Simulation Model	Detection	Tracking	Accuracy	Influence of Interference	Interface Simulation	Handling	Signal Generation	Processing Time
MKRIEG	X		X	X				X
SILKA	X	X	X	X				X
EXSET	X	X	(X)		X	X		X
FLIGHT SIMUL.	X	X	X	X		X		X
TF Closed Loop				X			X	X

Table 2: Requirements of radar simulation applications

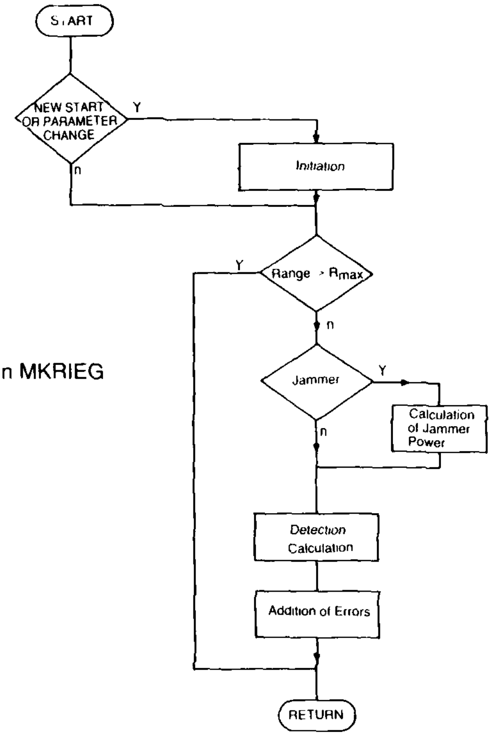

Fig. 3: Flow chart of the radar model in MKRIEG

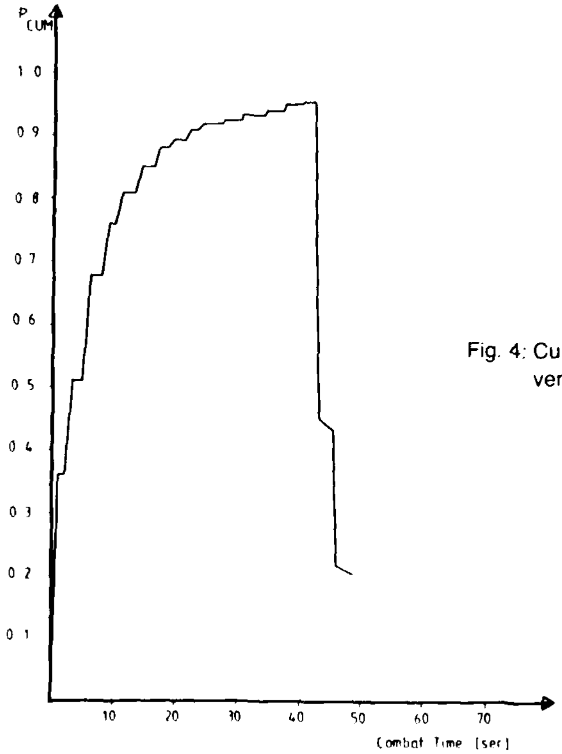

Fig. 4: Cumulative probability of detection P_{cum} versus SILKA combat time

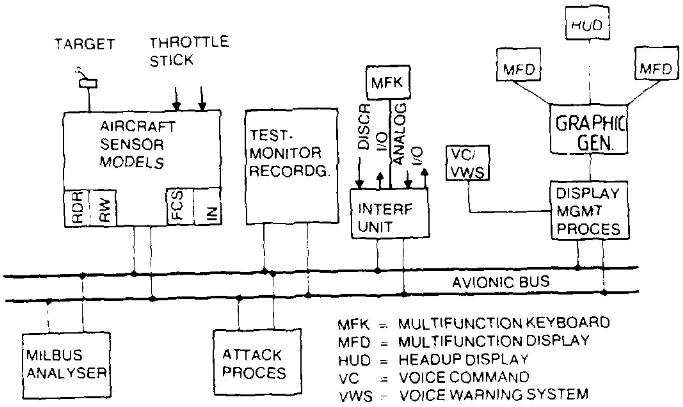

MFK = MULTIFUNCTION KEYBOARD
MFD = MULTIFUNCTION DISPLAY
HUD = HEADUP DISPLAY
VC = VOICE COMMAND
VWS = VOICE WARNING SYSTEM

Fig. 5: EXSET block diagram

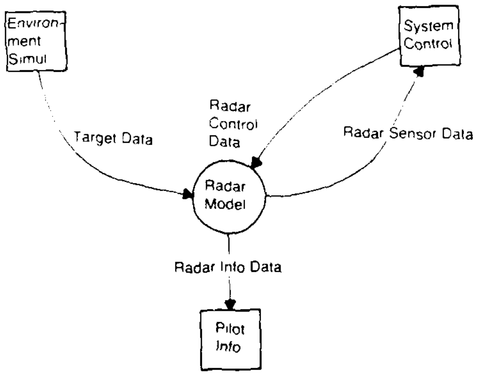

Fig. 6: Context of the radar model for EXSET

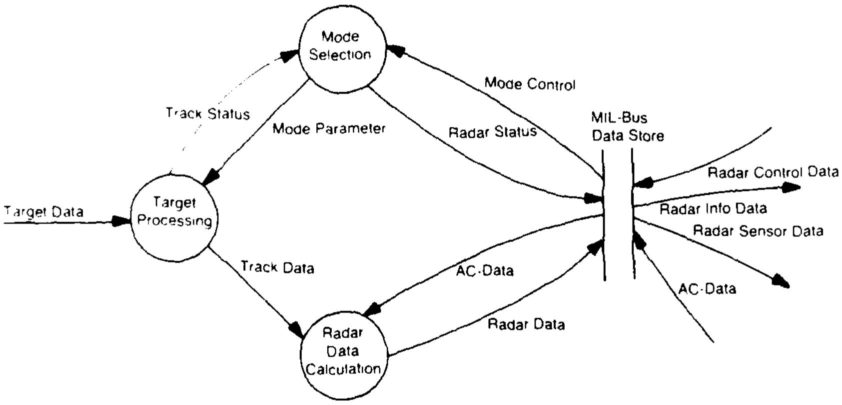

Fig. 7: Functional analysis of the EXSET radar model

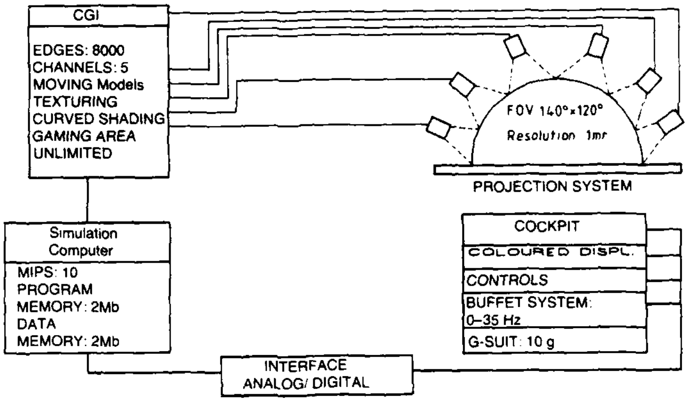

Fig. 8: Simplified block diagram of the advanced flight simulation

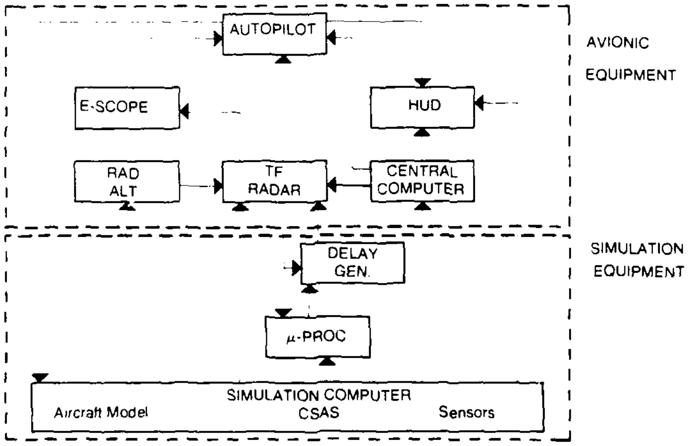

Fig. 9: Block diagram of the TF-closed loop simulation

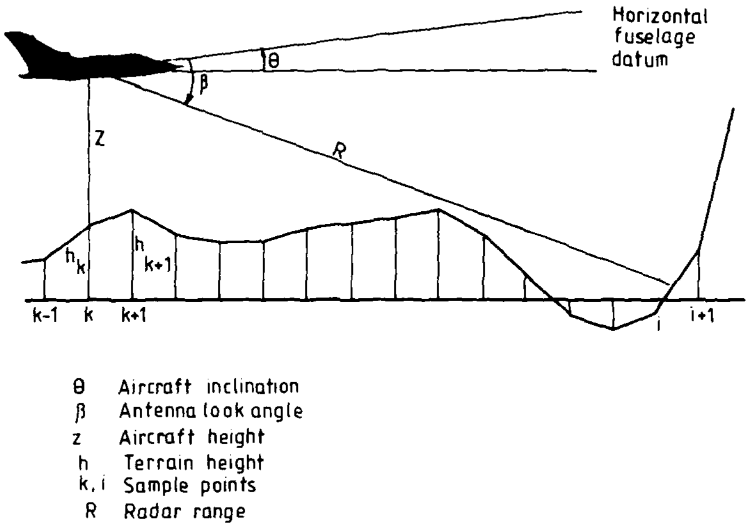

Fig. 10: Radar range calculation of TF-simulation

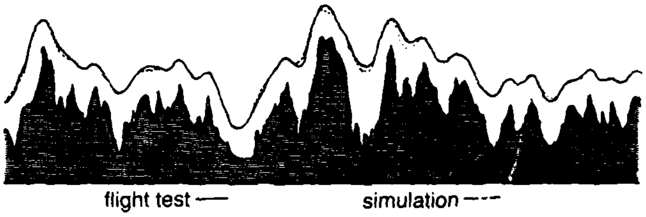

Fig. 11: Comparison flight test – TF-simulation

CRITERES POUR L'EVALUATION DES PERFORMANCES DE PORTEE EN INTERCEPTION AIR/AIR

par

P.Ramstein
THOMSON-CSF
165—173 Avenue P.Brossolette
92120 Montrouge
France

RESUME

Les performances de portée d'un radar sont en général données soit pour une probabilité de détection en un balayage égale à 50%, soit pour une probabilité de détection cumulée égale à 85% ou 90%, dépendant de la vitesse de rapprochement de la cible et de la durée d'un cycle de balayage. Ces valeurs n'offrent cependant qu'une information incomplète sur les performances opérationnelles en interception.

Une information plus complète peut être obtenue en considérant, pour une cible donnée, la probabilité d'accrochage, ou mieux, la probabilité d'accrochage définitif, c'est-à-dire non suivi d'un décrochage à grande ou moyenne distance.

La communication fait part d'une méthode rapide de calcul de ces probabilités, ce qui évite l'emploi de simulations statistiques. Cette méthode, fondée sur l'emploi des chaînes de Markov, prend en compte les logistique d'acquisition et de décrochage, ainsi que les probabilités de détection en un passage.

Des exemples sont présentés, montrant comment optimiser la vitesse de balayage et permettant de comparer des modes avec et sans agilité de fréquence d'émission. Enfin, une discussion est effectuée, visant à définir le critère d'évaluation le mieux adapté à une situation opérationnelle donnée.

REPORT DOCUMENTATION PAGE

1. Recipient's Reference	2. Originator's Reference	3. Further Reference	4. Security Classification of Document
	AGARD-CP-381	ISBN 92-835-0395-3	UNCLASSIFIED

5. Originator
Advisory Group for Aerospace Research and Development
North Atlantic Treaty Organization
7 rue Ancelle, 92200 Neuilly sur Seine, France

6. Title
MULTIFUNCTION RADAR FOR AIRBORNE APPLICATIONS

7. Presented at
the Avionics Panel 50th Symposium held in Toulouse, France,
14—18 October 1985.

8. Author(s)/Editor(s)	9. Date
Various	July 1986

10. Author's/Editor's Address	11. Pages
Various	232

12. Distribution Statement
This document is distributed in accordance with AGARD policies and regulations, which are outlined on the Outside Back Covers of all AGARD publications.

13. Keywords/Descriptors

Multifunction radar
Doppler
Beam steering
High resolution image (SAR)
VLSI
VHSIC
SAW

14. Abstract

Radar is still the most important sensor in military aircraft. A number of important features make radar superior to optical systems and other sensors:

- — long range performance
- — penetration of weather (fog, clouds),
- — range and doppler estimation,
- — flexibility due to electronic beam steering,
- — various signal processing routines,
- — high resolution imaging (SAR).

Different tasks such as target search, tracking and missile guidance can be fulfilled by radar. In a military aircraft, additional tasks such as terrain following and avoidance, mapping, doppler navigation and SAR imaging may be required. Since most of the output data is combined on a single on-board computer, the question of which radar functions should be integrated and at what level arises. Reducing size, weight, cost and power consumption are particular goals for commonality in airborne radar systems.

This symposium brought together specialists in the various fields of radar technology who discussed and presented the state-of-the-art in multifunction radar. New concepts for the design of future radar systems were emphasized.

AGARD Conference Proceedings No.381
Advisory Group for Aerospace Research and Development, NATO
MULTIFUNCTION RADAR FOR AIRBORNE APPLICATIONS
Published July 1986
232 pages

Radar is stilll the most important sensor in military aircraft. A number of important features make radar superior to optical systems and other sensors:

— long range performance,
— penetration of weather (fog, clouds),
— range and doppler estimation,
— flexibility due to electronic beam steering,
— various signal processing routines,
— high resolution imaging (SAR).

P.T.O

AGARD-CP-381

Multifunction radar
Doppler
Beam steering
High resolution imaging (SAR)
VSLI
VHSIC
SAW

AGARD Conference Proceedings No.381
Advisory Group for Aerospace Research and Development, NATO
MULTIFUNCTION RADAR FOR AIRBORNE APPLICATIONS
Published July 1986
232 pages

Radar is stilll the most important sensor in military aircraft. A number of important features make radar superior to optical systems and other sensors:

— long range performance,
— penetration of weather (fog, clouds),
— range and doppler estimation,
— flexibility due to electronic beam steering,
— various signal processing routines,
— high resolution imaging (SAR).

P.T.O

AGARD-CP-381

Multifunction radar
Doppler
Beam steering
High resolution imaging (SAR)
VSLI
VHSIC
SAW

AGARD Conference Proceedings No.381
Advisory Group for Aerospace Research and Development, NATO
MULTIFUNCTION RADAR FOR AIRBORNE APPLICATIONS
Published July 1986
232 pages

Radar is stilll the most important sensor in military aircraft. A number of important features make radar superior to optical systems and other sensors:

— long range performance,
— penetration of weather (fog, clouds),
— range and doppler estimation,
— flexibility due to electronic beam steering,
— various signal processing routines,
— high resolution imaging (SAR).

P.T.O

AGARD-CP-381

Multifunction radar
Doppler
Beam steering
High resolution imaging (SAR)
VSLI
VHSIC
SAW

AGARD Conference Proceedings No.381
Advisory Group for Aerospace Research and Development, NATO
MULTIFUNCTION RADAR FOR AIRBORNE APPLICATIONS
Published July 1986
232 pages

Radar is stilll the most important sensor in military aircraft. A number of important features make radar superior to optical systems and other sensors:

— long range performance,
— penetration of weather (fog, clouds),
— range and doppler estimation,
— flexibility due to electronic beam steering,
— various signal processing routines,
— high resolution imaging (SAR).

P.T.O

AGARD-CP-381

Multifunction radar
Doppler
Beam steering
High resolution imaging (SAR)
VSLI
VHSIC
SAW

Different tasks such as target search, tracking and missile guidance can be fulfilled by radar. In a military aircraft, additional tasks such as terrain following and avoidance, mapping, doppler navigation and SAR imaging may be required. Since most of the output data is combined on a single on-board computer, the question of which radar functions should be integrated and at what level arises. Reducing size, weight, cost and power consumption are particular goals for commonlality in airborne radar system.

This symposium brought together specialists in the various fields of radar technology who discussed and presented the state-of-the-art in multifunction radar. New concepts for the design of future radar systems were emphasized.

Papers presented at the Avionics Panel Symposium held in Toulouse, France 14–18 October 1985.

ISBN 92-835-0395-3

Different tasks such as target search, tracking and missile guidance can be fulfilled by radar. In a military aircraft, additional tasks such as terrain following and avoidance, mapping, doppler navigation and SAR imaging may be required. Since most of the output data is combined on a single on-board computer, the question of which radar functions should be integrated and at what level arises. Reducing size, weight, cost and power consumption are particular goals for commonlality in airborne radar system.

This symposium brought together specialists in the various fields of radar technology who discussed and presented the state-of-the-art in multifunction radar. New concepts for the design of future radar systems were emphasized.

Papers presented at the Avionics Panel Symposium held in Toulouse, France 14–18 October 1985.

ISBN 92-835-0395-3

Different tasks such as target search, tracking and missile guidance can be fulfilled by radar. In a military aircraft, additional tasks such as terrain following and avoidance, mapping, doppler navigation and SAR imaging may be required. Since most of the output data is combined on a single on-board computer, the question of which radar functions should be integrated and at what level arises. Reducing size, weight, cost and power consumption are particular goals for commonlality in airborne radar system.

This symposium brought together specialists in the various fields of radar technology who discussed and presented the state-of-the-art in multifunction radar. New concepts for the design of future radar systems were emphasized.

Papers presented at the Avionics Panel Symposium held in Toulouse, France 14–18 October 1985.

ISBN 92-835-0395-3

Different tasks such as target search, tracking and missile guidance can be fulfilled by radar. In a military aircraft, additional tasks such as terrain following and avoidance, mapping, doppler navigation and SAR imaging may be required. Since most of the output data is combined on a single on-board computer, the question of which radar functions should be integrated and at what level arises. Reducing size, weight, cost and power consumption are particular goals for commonlality in airborne radar system.

This symposium brought together specialists in the various fields of radar technology who discussed and presented the state-of-the-art in multifunction radar. New concepts for the design of future radar systems were emphasized.

Papers presented at the Avionics Panel Symposium held in Toulouse, France 14–18 October 1985.

ISBN 92-835-0395-3

NATO OTAN
7 RUE ANCELLE · 92200 NEUILLY-SUR-SEINE
FRANCE

Telephone (1) 47 45 08 10 · Telex 610176

DISTRIBUTION OF UNCLASSIFIED AGARD PUBLICATIONS

AGARD does NOT hold stocks of AGARD publications at the above address for general distribution. Initial distribution of AGARD publications is made to AGARD Member Nations through the following National Distribution Centres. Further copies are sometimes available from these Centres, but if not may be purchased in Microfiche or Photocopy form from the Purchase Agencies listed below.

NATIONAL DISTRIBUTION CENTRES

BELGIUM
Coordonnateur AGARD — VSL
Etat-Major de la Force Aérienne
Quartier Reine Elisabeth
Rue d'Evere, 1140 Bruxelles

CANADA
Defence Scientific Information Services
Dept of National Defence
Ottawa, Ontario K1A 0K2

DENMARK
Danish Defence Research Board
Ved Idraetsparken 4
2100 Copenhagen Ø

FRANCE
O.N.E.R.A. (Direction)
29 Avenue de la Division Leclerc
92320 Châtillon

GERMANY
Fachinformationszentrum Energie,
Physik, Mathematik GmbH
Kernforschungszentrum
D-7514 Eggenstein-Leopoldshafen

GREECE
Hellenic Air Force General Staff
Research and Development Directorate
Holargos, Athens

ICELAND
Director of Aviation
c/o Flugrad
Reykjavik

ITALY
Aeronautica Militare
Ufficio del Delegato Nazionale all'AGARD
3 Piazzale Adenauer
00144 Roma/EUR

LUXEMBOURG
See Belgium

NETHERLANDS
Netherlands Delegation to AGARD
National Aerospace Laboratory, NLR
P.O. Box 126
2600 AC Delft

NORWAY
Norwegian Defence Research Establishment
Attn: Biblioteket
P.O. Box 25
N-2007 Kjeller

PORTUGAL
Portuguese National Coordinator to AGARD
Gabinete de Estudos e Programas
CLAFA
Base de Alfragide
Alfragide
2700 Amadora

TURKEY
Department of Research and Development (ARGE)
Ministry of National Defence, Ankara

UNITED KINGDOM
Defence Research Information Centre
Kentigern House
65 Brown Street
Glasgow G2 8EX

UNITED STATES
National Aeronautics and Space Administration (NASA)
Langley Research Center
M/S 180
Hampton, Virginia 23665

THE UNITED STATES NATIONAL DISTRIBUTION CENTRE (NASA) DOES NOT HOLD STOCKS OF AGARD PUBLICATIONS, AND APPLICATIONS FOR COPIES SHOULD BE MADE DIRECT TO THE NATIONAL TECHNICAL INFORMATION SERVICE (NTIS) AT THE ADDRESS BELOW.

PURCHASE AGENCIES

Microfiche or Photocopy	*Microfiche*	*Microfiche or Photocopy*
National Technical Information Service (NTIS) 5285 Port Royal Road Springfield Virginia 22161, USA	ESA/Information Retrieval Service European Space Agency 10, rue Mario Nikis 75015 Paris, France	British Library Lending Division Boston Spa, Wetherby West Yorkshire LS23 7BQ England

Requests for microfiche or photocopies of AGARD documents should include the AGARD serial number, title, author or editor, and publication date. Requests to NTIS should include the NASA accession report number. Full bibliographical references and abstracts of AGARD publications are given in the following journals:

Scientific and Technical Aerospace Reports (STAR)
published by NASA Scientific and Technical
Information Branch
NASA Headquarters (NIT-40)
Washington D.C. 20546, USA

Government Reports Announcements (GRA)
published by the National Technical
Information Services, Springfield
Virginia 22161, USA

Printed by Specialised Printing Services Limited
40 Chigwell Lane, Loughton, Essex IG10 3TZ

ISBN 92-835-0305-3

END

DATE

FILMED

12-86

DTIC